N-BODY SIMULATIONS OF INTERACTING GALAXIES

Dissertation

zur

Erlangung der naturwissenschaftlichen Doktorwürde
(Dr. sc. nat.)

vorgelegt der

Mathematisch-naturwissenschaftlichen Fakultät

der

Universität Zürich

von

Chiara Mastropietro

aus

Italien

Promotionskomitee

Prof. Dr. Ben Moore (Vorsitz)
Prof. Dr. Daniel Wyler

Zürich, 2005

Contents

List of Figures

List of Tables

Zusammenfassung

Diese Doktorarbeit präsentiert eine Untersuchung über die Effekte auf die Evolution von Galaxien durch die gravitative und hydrodynamische Wechselwirkung mit deren Umgebung. Satellitengalaxien, die in einem Orbit um das Halo der Hauptgalaxie sind und sich in einer dichten Umgebung befinden, erfahren gravitative Gezeitenkräfte durch die Hauptgalaxie, wechselwirken mit Substruktur und spüren hydrodynamischen Staudruck durch das umgebende gasförmige Medium, welches zum Abziehen des internen interstellaren Medium führt. All diese Prozesse induzieren morphologische und kinematische Veränderungen in der Satellitengalaxie, welche die Sternentstehung beeinflusst und zum Verlust von Materie führt. Das Resultat ist die Bildung von Stern- und Gasströmen, die in nahen Zwerggalaxien beobachtet werden.

Die Idee, dass Früh-Typ Galaxien das Resultat von morphologischen Transformationen von Spiralgalaxien und irregulären Galaxien sind, die von einem Galaxiencluster akkretiert werden, wird durch Beobachtungen und Erkenntnissen aus Simulationen unterstützt. Gemäss diesem Evolutionsszenario erwarten wir in der Nähe Galaxien in Clusters zu finden, die gerade eine morphologische Transformationsphase durchmachen und ihrer Scheibeneigenschaft teilweise immer noch erhalten ist. Die kürzliche Entdeckung von versteckten, nicht achsensymmetrischen und scheibenartigen Strukturen in hellen Zwerggalaxien und linsenförmige Galaxien (dE/dSph/dS0) in Virgo, Coma und Fornax weist darauf hin, dass sie Spät-Typ Vorgänger haben. Zusätzlich liegt der Rotationsgrad bei Werten von 0 bis nahezu 1, was man für eine Galaxie erwartet, die durch Rotation abgeflacht wird. In Kapitel 2 verfolgen wir die Entwicklung von Scheibengalaxien, welche ihren Orbit in einer Galaxiencluster-Umgebung haben, mit hochauflösenden N-Body Simulationen. Wir benutzen Galaxienmodelle mit kalten Dunkle Materie (CDM) Halos, welche ein steiles Dichteprofil haben, und strukturelle Parameter, wie sie von der Konkordanzkosmologie erwartet werden und lassen sie in ΛCDM Galaxiencluster evolvieren, wo das hierarchische Wachstum und Galaxien-Harassment selbstkonsistent modelliert werden. Die hohe Auflösung in unseren Simulationen erlaubt es uns, die detaillierte morphologische und kinematische Entwicklung der Satellitengalaxie zu verfolgen. Unsere Erkenntnis ist, dass die Galaxien signifikante morphologische Transformationen sogar in äusseren Teilen des Clusters durchmachen und sich durch die Hubble Sequenz von Spät-Typ Scheibengalaxien zu Zwergsphäroidgalaxien bewegen. Gezeitenschocks durch Dunkle Materie Substruktur und das mittlere Galaxiencluster-Potential sind beide wichtig und antreibend für die Entwicklung von Scheiben- zu Sphäroidstrukturen. Keine dieser Scheiben wird komplett zerstört und sie können daher nicht die Vorgänger von ultrakompakten Galaxien sein. Unscharf maskierte Bilder von simulierten Galaxien zeigen ähnliche versteckte Balken- und Spiraleigenschaften wie manche beobachteten Galaxien. Diese Strukturen verschwinden schrittweise, je mehr die Galaxien kinematisch aufgeheizt werden. Die projizierte Photometrie und Kinematik von unseren resultierenden Galaxien haben wir mit den neusten Daten vom Very Large Telescope und den hochauflösenden, spektroskopischen Untersuchungen

der Keck- und Palomar-Teleskope verglichen. Wir zeigen, dass die Kinematik (v/σ) der Sterne der resultierenden Galaxien ähnlich zu den Beobachtungen von dE/dSph Galaxien in Virgo und Fornax sind. Nur in den am ernsthaftesten zerrissenen Galaxien, welche die meiste Sternmaterie verlieren, werden die Orbits der Sterne komplett zufällig umgeordnet, während die meisten anderen Galaxien einen signifikanten Anteil an Rotationsbewegung beibehalten.

Während wir in Kapitel 2 nur reine gravitative Wechselwirkung auf die Satellitengalaxien betrachteten, analysieren wir in Kapitel 3 die gleichzeitigen Effekte von gravitativen und hydrodynamischen Kräften, die auf die Satellitengalaxie im Orbit um die Hauptgalaxie wirken. Einer der markantesten Hinweise auf eine Wechselwirkung zwischen den Magellanschen Wolken und der Milchstrasse ist der Magellansche Strom, ein zurückhängendes Filament von neutralem Wasserstoff, welches den Ursprung bei den Wolken hat und sich über ~ 100 Grad am südlichen Himmel erstreckt. Zudem muss die kombinierte Wechselwirkung zwischen diesen drei Galaxien einen starken Einfluss auf die morphologische Evolution der Wolken sowie ihre interne Kinematik und Sternentstehungsgeschichte haben. Mehrere Modelle wurden vorgeschlagen, um die Natur dieser Wechselwirkung zu studieren und die Hauptmechanismen, die für die Entstehung des Stroms verantwortlich sind, zu isolieren. Jedoch konnten weder reine Gezeiten- oder Staudruckmodelle gewisse Eigenschaften des beobachteten Stroms wie die graduelle Senkung der HI Kolonnendichte und den Mangel an Sternen im Strom oder die Entdeckung von neutralem Wasserstoff vor der grossen Magellanschen Wolke erklären. Aus Modellen der hierarchischen Strukturbildung erwartet man um die Milchstrasse ein ausgedehntes heisses Halo, welches im hydrostatischen Gleichgewicht mit dem Dunkle Materie Potential ist. Dieses gasartige Halo, das vom anfänglichen Kollaps übrig blieb, wird kontinuierlich durch die Akkretion von Satelliten mit der Zeit gespiesen. Die neusten Beobachtungsresultate haben die Existenz von heissem ($T \sim 10^6$ K) Gas weit jenseits der galaktischen Scheibe mit einer Dichte zwischen 10^{-5} und $10^{-4}\mathrm{cm}^{-3}$ bei einer Distanz, wie die der Grossen Magellanschen Wolke zum Galaxienzentrum, bestätigt. Die Wolken sind daher auf ihrem Orbit dem Staudruck durch die dünne Verbreitung von heissem Gas unterworfen. Zudem scheint die Morphologie der Magellanschen Wolken das Resultat einer komplexen Wechselwirkung zu sein, welche hydrodynamische Prozesse und Gezeiteneffekte beinhaltet.

Hier studieren wir nun zum ersten Mal die kombinierten Effekte von gravitativen und hydrodynamischen Kräften, die auf die Grosse Magellansche Wolke während ihrer Bewegung durch das galaktische Halo wirken, mit selbstkonsistenten Galaxienmodellen und hochauflösenden N-Body/SPH Simulationen. Wir modellieren das Dunkle Materie Halo sowie das ausgedehnte heisse Gas Halo sowie die stellare und gasförmige Scheibe beider Galaxien. Beide Galaxien sind in ΛCDM Dunkle Materie Halos mit steilen Dichteprofilen eingebettet. Gezeitenkräfte dehnen die Scheibe der Grossen Magellanschen Wolke was zur Bildung eines Balken, einer Wölbung und einem diffusen stellaren Halo führt, obwohl nur wenige Sterne ungebunden werden. Dieses stellare Halo könnte gewisse beobachtete Mikrolinseneffekte erklären. Als Konsequenz des asymmetrischen Potentials und der deformierten stellaren Scheibe, welche durch die Gezeitenwechselwirkung entstand, kann der Staudruck effizient Gas aus der Scheibe der Grossen Magellanschen Wolke abziehen, da die gravitative Rückstellkraft schwächer ist. Der Staudruck durch ein dünnes, ionisiertes Halo aus Gas reicht aus, um über $10^8 M_\odot$ Gas aus der Grossen Magellanschen Wolke zu entfernen, welches dann den grosskreisförmigen, zurückhängenden Strom um die Galaxie bildet. Die Kolonnendichte des abgelösten Gas fällt um zwei Grössenordnungen bei 100

Grad von der Grossen Magellanschen Wolke entfernt und die radiale Geschwindigkeit entlang des zurückhängenden Stroms stimmt gut mit den Beobachtungen überein. Die Grosse Magellansche Wolke ruft keine Reaktion in der Scheibe der Milchstrasse hervor. Die Gezeiten, die durch die Milchstrasse hervorgerufen werden, limitieren gravitativ die Grösse des Satelliten zu ungefähr 11 kpc. Nach vier Milliarden Jahren Wechselwirkung ist die Gasscheibe in der Grossen Magellanschen Wolke aufgrund des Staudrucks kleiner als die stellare Scheibe und die Grösse stimmt gut mit den beobachteten HI Daten überein.

In Kapitel 4 untersuchen wir die kombinierten Effekte von Gezeiten- und Staudruckkräften auf eine grosse Anzahl von Scheibengalaxien mit tiefer Oberflächenhelligkeit, die in einem Haupthalo wie dem der Milchstrasse im Orbit sind. Das Aufwühlen der Zwergscheibengalaxien durch die Gezeiten produziert Objekte, deren stellare Struktur und Kinematik jenen von Zwergsphäroidgalaxien ähnelt. Der Staudruck wird benötigt, um die ganze Gaskomponente abzuziehen. Gezeitenkräfte können dem Abziehen durch den Staudruck helfen, das gesamte Potential der Zwerggalaxie abzuschwächen. Aber sie führen auch zur Bildung von Balken, welche Gas nach Innen führt, was wiederum weiteres Abziehen schwieriger macht. Dieser Einwärtsfluss ist besonders effektiv, wenn sich das Gas radiativ abkühlen kann. Eine Kombination von Gezeitenkräften, Abziehen durch Staudruck und Aufheizen durch Ultraviolettstrahlung wird benötigt, um die verschiedenen Gasgehalte und Sternentstehungsgeschichten der Zwergsphäroidgalaxien in der Lokalen Gruppe zu verstehen.

Heutige Standardkosmologiemodelle mit Dunkler Materie sagen eine Vielzahl von Subhalos in der Lokalen Gruppe voraus, welche über eine Grössenordnung zu hoch ist im Vergleich zu der totalen Anzahl von beobachteten Satellitengalaxien. Viele Lösungen wurden vorgeschlagen, um die Diskrepanz zu erklären. Stoehr et al. 2002 machten den Vorschlag, dass gravitative Gezeiten ein Abflachung der zentralen Dichteprofile der Dunkle Materie Halos produzieren, was die effektive Konzentration der Satelliten reduziert und eine langsam steigende Rotationskurve ergibt. Dies würde den beobachteten Galaxien erlauben, in den massivsten Substrukturen innerhalb eines gegebenen Dunkle Materie Halos zu sein. Rückkopplungsprozesse würde die Sternentstehung in kleineren Objekten unterdrücken. In Kapitel 5 untersuchen wir wie die interne Struktur auf die Gezeitenwechselwirkung reagiert und untersuchen dabei die von Stoehr et al. 2002 vorgeschlagene Lösung. Wir führten Simulationen mit niedrig aufgelöste Satelliten aus kosmologischen N-Body Simulationen von Mutterhalos mit $N = 10^7$ Teilchen sowie mit hoch aufgelösten individuellen Subhalos, welche ihren Orbit in einem statischen Potential haben, durch. Wir finden, dass die zentrale Dichte der Satelliten mit steilen zentralen Dichteprofilen sogar nachdem über 99% der anfänglichen Masse abgezogen wurde, nicht durch Gezeiten verändert wird. Nehmen wir isotrope und tangential anisotrope Modell für die stellare Komponente an, können wir die beobachteten Geschwindigkeitsprofile von Fornax und Draco nur fitten, wenn das umgebende NFW Dunkle Materie Halo eine maximale Zirkulargeschwindigkeit im Bereich von 20–35 km s^{-1} haben. Falls die anfänglichen zentralen Dichteprofile der simulierten Subhalos steiler wäre (entweder von Anfang an oder durch adiabatische Kontraktion steiler) als diejenigen, die wir in unserer Arbeit annahmen, würden sogar noch tiefere Zirkulargeschwindigkeiten benötigt, um die Daten zu fitten. Dies bedeutet, dass die Gezeitenwechselwirkung nicht der Mechanismus sein kann, um die hellsten Zwerggalaxien in der Milchstrasse in die massivsten Subhalos in einem ΛCDM Universum einzubetten und die Fülle der galaktischen Satelliten mit den Vorhersagen aus den Dunklen Materie Szenarios abzustimmen. Modelle mit einer leichten tangentialen Anisotropie von stellaren

Objekten reproduzieren die beobachtete Form der Geschwindigkeitsdispersionsprofile für Fornax und Draco besser. Radial anisotrope Modelle überschätzen die zentrale stellare Geschwindigkeitsdispersion um einen Faktor ~ 2.

Summary

This thesis presents a study of the effects induced on galaxy evolution by gravitational and hydrodynamical interactions with the surrounding environment. Satellite galaxies orbiting in a dense environment experience gravitational tidal forces from the main halo, close encounters with other substructures and hydrodynamical ram pressure from the surrounding gaseous medium, which leads to the stripping of the internal inter-stellar medium (ISM). All of these processes induce morphological and kinematic transformations in the satellite, affecting its star formation history and removing mass thus producing the stellar and gaseous streams associated with some nearby dwarf galaxies.

The idea that early type galaxies are the result of a morphological transformation of spiral and irregular galaxies accreting into clusters is supported by some observations and simulation results. According to this evolutionary scenario we expect to find nearby cluster galaxies that are currently undergoing morphological transformation and retain part of their disk nature. The recent discovery of hidden non-axisymmetric and disk-like structures in bright Virgo, Coma and Fornax dwarf elliptical and lenticular galaxies (dE/dSph/dS0) indicates that they may have late-type progenitors. Furthermore, the degree of rotational support of these galaxies is found to vary from zero to a value close to one expected for a galaxy flattened by rotation. In Chapter 2 we follow the evolution of disk galaxies orbiting in a cluster environment using high resolution N-body simulations. We use galaxy models with cuspy CDM halos and structural parameters as expected in the concordance cosmological model and evolve them within a ΛCDM cluster where the hierarchical growth and galaxy harassment are modeled self-consistently. The high resolution achieved in our simulations permits us to follow the detailed morphological and kinematical evolution of the satellites. We find that most of the galaxies undergo significant morphological transformation, even at the outskirts of the cluster, and move through the Hubble sequence from late type disks to dwarf spheroidals. Tidal shocks with dark matter substructures and the mean cluster potential are both important at driving the evolution from disks to spheroidal structures. None of the disks are completely destroyed therefore they can not be the progenitors of ultra compact dwarf galaxies (UCDs). Unsharp masked images of the simulated galaxies show similar hidden bar and spiral features as some observed cluster galaxies. These structures gradually dissappear as the galaxies suffer more heating. The projected photometry and kinematics of our remnants are compared with the latest data from the Very Large Telescope (VLT) and the high resolution spectroscopic studies from the Keck and Palomar telescopes. We show that the kinematics (v/σ) of the stellar remnants is similar to the observations of Virgo and Fornax dE/dSph galaxies. Only within the most severely disrupted galaxies which lose most of their stellar mass, do the orbits of the stars become completely randomised, whilst of the remnants retain a significant amount of rotational motion.

While in Chapter 2 we focused on the effects of pure gravitational interactions on satellite galaxies, in Chapter 3 we analyse the simultaneous effects of gravitational and

hydrodynamical forces acting on a satellite orbiting in a main halo. The most prominent signature of an interaction between the Magellanic Clouds (LMC and SMC) and the Milky Way (MW) is given by the Magellanic Stream, a trailing filament of neutral hydrogen that originates from the Clouds and stretches for over ~ 100 degrees in the Southern Sky. Moreover, the combined interaction between these three galaxies must strongly influence the morphological evolution of the Clouds, as well as their internal kinematics and star formation history. Several models have been proposed in order to study the nature of this interaction and to isolate the main mechanism responsible for the formation of the Stream, but neither pure tidal or ram-pressure models can explain certain characteristics observed in the Stream, such as the gradual decrease of the HI column density and the lack of a stellar tidal feature or the discovery of neutral hydrogen in front of the LMC. The presence of an extended hot halo surrounding the MW and in hydrostatic equilibrium within the dark matter potential is expected within current models of hierarchical structure formation. This gaseous halo, left over from the initial collapse, would be continuously fueled by accretion of satellite galaxies over time. Recent observational results have confirmed the existence of a distribution of hot (T $\sim 10^6$ K) gas well beyond the Galactic disk, with a density between 10^{-5} and $10^{-4}\mathrm{cm}^{-3}$ at the LMC distance from the Galactic center. The Clouds are therefore subjected along their orbits to the ram pressure generated by this tenuous distribution of hot gas. Furthermore, the morphology of the Magellanic Clouds appears to be the result of a complex interaction that involves both hydrodynamical and tidal processes.

Here we study for the first time the combined effect of gravitational and hydrodynamical forces acting on the LMC as it moves within the Galactic halo, using fully self consistent galaxy models and high resolution N-body/SPH simulations. We model the dark and hot extended halo components as well as the stellar/gaseous disks of the two galaxies. Both galaxies are embedded in extended cuspy ΛCDM dark matter halos. Tidal forces elongate the LMC's disk, forcing a bar and creating a strong warp and diffuse stellar halo, although very few stars become unbound. The stellar halo may account for some of the observed microlensing events. As a consequence of the asymmetric potential and distorted stellar disk generated by tidal interactions, ram-pressure is efficient in stripping gas from the LMC's disk since the gravitational restoring force is weaker. Ram-pressure from a low density ionized halo is then sufficient to remove over $10^8 M_\odot$ of gas from the LMC's disk forming a great circle trailing stream around the Galaxy. The column density of the stripped gas falls by two orders of magnitude 100 degrees from LMC and the radial velocity along the trailing Stream agrees well with observations. The LMC does not induce any response in the Milky Ways disk, whilst the tides raised by the Milky Way gravitational limit the size the satellite to about 11 kpc. After four Gyrs of interaction the gas disk of the LMC is smaller than the stellar disk due to ram pressure and its size compares well with the observed HI data.

In Chapter 4 we investigate the combined effect of tides and ram-pressure forces on a large variety of low surface brightness disk satellites orbiting in a Milky Way primary halo similar to the one described in the previous chapter. Whilst tidal stirring of disk dwarfs produces objects whose stellar structure and kinematics resemble that of dwarf spheroidals, ram pressure stripping is needed to remove all of the gas component. Gravitational tides can aid ram pressure stripping by diminishing the overall potential of the dwarf, but they also induce bar formation which funnels gas inwards making subsequent stripping more difficult. This inflow is particularly effective when the gas can cool radiatively. A combination of tidal forces, ram pressure stripping and UV heating is required in order to explain the different gas content and star formation history of the dSphs in the Local Group.

The now standard cosmological cold dark matter model predicts a number of subhalos in the Local Group which is over an order of magnitude higher than the total number of observed satellite galaxies. Several solutions have been proposed in order to explain this discrepancy. Among them Stoehr et al. 2002 suggest that gravitational tides produce a flattening of the dark halo central density cusps, reducing the effective concentration of the satellites and producing slowly rising circular velocity curves. This would allow the observed Galactic satellites to be hosted by the most massive substructures within a given CDM halo. Feedback processes would suppress star formation in all the smaller objects. In Chapter 5 we investigate how a satellite's internal structure responds to tidal interactions, revisiting the solution proposed by Stoehr et al. 2002. We combined "low-resolution" satellites from cosmological N-body simulations of parent halos with $N = 10^7$ particles with high-resolution individual subhalos orbiting within a static host potential. We find that tides do not modify the central density structure of cuspy satellites even after over 99% of the initial mass is tidally stripped. Adopting isotropic and tangentially anisotropic models for the stellar component, we conclude that the observed velocity dispersion profiles of Fornax and Draco can be fitted only if the surrounding NFW dark matter halos have maximum circular velocities in the range 20–35 km s^{-1}. If the initial central density slopes of the simulated subhalos were steeper (either having intrinsically steeper inner slopes or becoming steeper as a result of adiabatic contraction) than the ones adopted in the work, even lower values of the circular velocity would be required to fit the data. This means that tidal interactions do not provide a mechanism for embedding the luminous dwarf galaxies of the Milky Way within the most massive subhalos in a ΛCDM universe, and, therefore, for reconciling the overabundance of Galactic satellites with CDM predictions. Finally, models with a slight tangential anisotropy of stellar orbits reproduce better the shape of the observed velocity dispersion profiles of both Fornax and Draco, whereas radially anisotropic models overestimate the central stellar velocity dispersion by a factor of ~ 2.

Chapter 1

Introduction

In this Chapter we explore the dynamics of interactions between galaxies and discuss how modern numerical computational techniques can be used to improve our understanding of the nature and evolution of these phenomena.

1.1 Gravitational encounters

Gravitational interactions between galaxies are far more common than one might think, assuming that the space density of galaxies is uniform. Galaxies group themselves in clusters, small groups or pairs: far from being isolated systems they formed and evolved in interaction with their environment and with neighbouring galaxies. The gravitational interactions produce distortions in the disks of the galaxies, giving rise to spiral arms, tidal tails and provoking outbursts of star formation. The morphology of the galaxy is therefore perturbed, even if the tides are not locally catastrophic: our Galaxy, for example, is interacting with the Magellanic Clouds and it is thought that this interaction was at its maximum about one billion years ago.

During an encounter the kinetic energy associated with the relative motion of the galaxies diminishes, because the internal energies increase. If the initial relative speed of the interacting systems is larger than a critical velocity v_f the galaxies reach the point of closest approach with sufficient orbital energy to escape to infinity, otherwise they will merge. If the initial speed is much larger than v_f the encounter alters both the orbits and the internal structure of the galaxies only slightly.

Apart from some rather special systems (Sridhar & Nityananda, 1990), analytic description of encounters between galaxies are possible only in limiting cases where the effects can be treated as perturbations. One such limit arises in fast encounters; another in encounters between galaxies of very different mass. In either case, tidal interactions pump energy into galaxies at expense of their relative motions.

1.1.1 Fast encounters

When galaxies collide with speeds much higher than their internal velocity dispersion – as in the case of rich galaxy clusters – the orbital motion of individual stars during the encounter can be neglected. In this limit, the encounter's effect is an increment of the velocity of each star, relative to the center of its galaxy, by an amount $\delta\mathbf{v}(\mathbf{r})$ which depends only on position. For fast encounters, the orbits of the galaxies can be approximated by straight lines; relative to the center of galaxy 1, let galaxy 2's position be given by the vector $(0, b, Vt)$, where b is the impact parameter (distance of closest approach), V is the relative velocity and t the duration of the encounter. If the ratios of the median radii of the two galaxies to the impact parameter are small (tidal approximation) the galaxies act on each other like point masses and a star at position $\mathbf{r} = (x, y, z)$ relative to the center of galaxy 1 suffers an impulsive velocity change, directed toward the point $(0, b, z)$, of magnitude $2GM_2/b'V$, where M_2 is the mass of the galaxy 2 and $b' = \sqrt{x^2 + (y - b)^2}$. Subtracting the motion of the center of mass of the galaxy and keeping only leading terms in an expansion around the point $(0, 0, 0)$ yields the velocity impulse

$$\delta\mathbf{v}(\mathbf{r}) = \frac{2GM_2}{b^2V}(-x, y, 0) \tag{1.1}$$

with respect to galaxy 1. The internal energy gained by a galaxy during an encounter is given by

$$\Delta E = \frac{1}{2}\int d\mathbf{r}\rho(\mathbf{r})|\delta\mathbf{v}(\mathbf{r})|^2 = \frac{4G^2{M_2}^2M_1}{3b^4V^2}\bar{r^2}, \tag{1.2}$$

where $\rho(\mathbf{r})$ is the galaxy mass density, M_1 is the mass of galaxy 1 and $\bar{r^2}$ is the mean-square radius of the perturbed system. The quantity ΔE is positive-definite, implying a one-way transfer of energy from the relative motion of the two galaxies to their internal degrees of freedom. If the energy absorbed by the interacting systems exceeds the energy of their initially-unbound orbit, then the galaxies will be bound together as a result of the encounter; however, this is only likely in relatively slow passages, which are not adequately described by the impulse approximation.

According to Equation 1.2, the internal, random energy gained in a fast, distant encounter increases sharply as the impact parameter b of the encounter decreases. This suggests that a few close encounters may pump more energy into a typical system than a large number of distant encounters.

1.1.2 Dynamical friction

The alternate limit where one galaxy is much smaller than the other is often discussed using Chandrasekhar's (1943) theory of dynamical friction. This theory figures in models of orbital evolution in interacting galaxies, including studies of "cannibalism" among cluster galaxies (Ostriker & Tremaine, 1975), accretion of satellites by the Milky Way (Tremaine, 1976), and the fate of the Magellanic Clouds (Murai & Fujimoto, 1980). Let's consider a body of mass M which is moving through an infinite population of stars of individual mass m, where $m << M$. The massive body acquires a parallel (respect to the initial velocity vector of the body M) velocity δv_p as well as a transverse velocity δv_t as a result of each encounter. The impulses resulting from successive encounters are partly correlated and accumulate linearly. As a result the changes δv_t sum to zero, while the changes in δv_p form a non-zero resultant. In consequence, the mass M suffers a steady deceleration. For field stars with an homogeneous and isotropic phase-space mass distribution function $f = f(|\mathbf{v}|)$, integrating the massive body acceleration over all encounters with impact parameter less than b_{max} gives

$$\frac{\mathrm{d}\mathbf{v}_M}{dt} = -16\pi^2G^2ln(\Lambda)M\frac{\mathbf{v}_M}{v^3{}_M}\int_0^{v_M}\mathrm{d}v\, v^2f(v), \tag{1.3}$$

where the Coulomb logarithm $\Lambda \sim b_{max}v^2/GM$. This equation describes a force of "dynamical friction" which opposes the massive body motion and slows it down with respect to the field star distribution. In the limit $M >> m$ assumed here, this deceleration is proportional to M but depends only on the mass density of field stars and not on their individual masses.

1.1.2.1 Orbit Decay

For slow encounters and mass ratios of order unity, self-consistent N-body simulations provide a fairly reliable way to study orbit decay. The basic physical mechanisms can be illustrated by encounters between simple spherical systems. In a head-on collision, each galaxy is gravitationally compressed as it passes through its partner, and rebound thereafter, tossing stars into loosely-bound orbits; the energy required to do this comes from the relative motion of the two galaxies (Toomre, 1974; Miller & Smith, 1980). In an off-axis encounter, the decay process is dominated by bodies which orbit within their respective galaxies in the same direction as the two galaxies orbit each other; these are promoted onto wider orbits, extracting both energy and angular momentum from the galaxies' relative motion (White, 1978; Navarro, 1990). Whether the encounter is head-on or off-axis, the net result is to excite internal motions within the galaxies at the expense of their relative orbit, which therefore decays.

Rotating disk components do not fundamentally alter the description of orbital decay. As White (1979) showed with simulated mergers of rotating spherical systems, orbits decay more rapidly if the spin and orbital angular momenta are parallel, and more slowly if they are anti-parallel. This is a simple consequence of the stronger tidal response produced in direct, as opposed to retrograde, encounters (see next section); direct passages pump more orbital energy into internal motions.

1.2 Tidal force

Repeated perturbations of the velocities of stars in a stellar system cause the orbits of the stars to diffuse in phase space. Hence we would expect orbits in system such as globular clusters and cluster galaxies to be smoothly populated. In particular, orbital diffusion would be expected to erase all sharp features in the spatial structures of these systems. On the opposite, observations indicate that globular clusters and many cluster galaxies have rather sharp edges. The origin of this apparent conflict of theory and observations lies in our neglect of the large-scale gravitational field of the galaxy or cluster of galaxies in which the system that experiences gravitational encounters orbits. In reality the field of the host system prunes the satellite system after each encounter, and thus prevents the satellite from swelling. Systems that are continuously pruned in this way have density profiles that plunge to zero at a finite radius r_t, the so called tidal radius of the satellite. The tidal radius of a spherical satellite of mass m orbiting beyond the outer edge of an host system of mass M, where $m << M$, is approximated by the Jacobi radius r_J, defined as (Binney & Tremaine, 1987)

$$r_J = (\frac{m}{3M})^{1/3}D. \tag{1.4}$$

The Jacobi radius provides only a crude estimate of r_t. Studies by Henon (1970) have shown that there can be trapped orbits about m with apocenters as large as $2r_J$ or more.

Thus we do not expect the stellar density $\rho(r)$ to drop abruptly to zero at r_J. However, the proportion of phase space occupied by bound orbits diminishes very rapidly beyond r_J, so we do expect ρ to decline steeply near r_J.

There is not direct generalization of the Jacobi limit in the case of non circular orbits. According to King (1962) in the case of elongated orbits the tidal limit is determined by conditions at the pericenter.

1.3 Close interactions and galaxy evolution

The role of galaxy interactions in driving activity and evolution of field spirals has been well documented through observational and theoretical studies. Models of interactions have demonstrated the basic dynamical response of galaxies to close encounters (Toomre & Toomre 1972; Negroponte & White 1982; Barnes 1988, 1992; Noguchi 1988; Barnes & Hernquist 1991, 1996; Mihos & Hernquist 1994, 1996). Close interactions can lead to a strong internal dynamical response in the galaxies, driving the formation of spiral arms and, depending on the structural properties of the disks, strong bar modes. These non-axisymmetric structures lead to compression and inflow of gas in the disks, elevating star formation rates and fueling nuclear starburst/AGN activity. If the encounter is sufficiently close, dynamical friction leads to an eventual merging of the galaxies, at which time violent relaxation destroys the dynamically cold disks and produces a kinematically hot merger remnant with many of the properties found in the field elliptical galaxy population (see Section, Barnes & Hernquist 1992). Numerical modeling of interactions has shown that gaseous inflow and central activity in an interacting disk is driven largely by gravitational torques acting on the gas — not from the companion galaxy, but by the developing non-axisymmetric structures (spiral arms and/or central bar) in the host disk (Noguchi 1988; Barnes & Hernquist 1991; Mihos & Hernquist 1996). This result argues that the structural properties of galaxies play a central role in determining the response to interactions. In particular, disks that are stable against the strong growth of disk instabilities will experience a weaker response, exhibiting modestly enhanced, disk-wide star formation (unless and until they ultimately merge). This stability can be provided by the presence of a centrally concentrated bulge (Mihos & Hernquist 1996) or a lowered disk surface density (at fixed rotational speed; Mihos, McGaugh, & de Blok 1997). In contrast, disk-dominated systems are more susceptible to global bar modes and experience the strongest levels of inflow and nuclear activity. Interacting and merging galaxies also show a wide variety of tidal features, from long thin tidal tails to plumes, bridges, and other amorphous tidal debris (see Figs. 1.1,1.2,1.3).

The evolution of this material was first described by the computer models of Toomre & Toomre (1972) and Wright (1972) (Fig. 1.4). Gravitational tides during a close encounter lead to the stripping of loosely bound material from the galaxies; rather than being completely liberated, this material ($> 95\%$) to its host galaxy (Hernquist & Spergel 1992; Hibbard & Mihos 1995). The outer portions of the tails contain the least bound material with the highest angular momentum. At any given time, material at the base of the tail has achieved turn-around and is falling back toward the remnant. Further out in the tail, material still expands away, resulting in a rapid drop in the luminosity density of the tidal tails due to this differential stretching. As a result, the detectability of these tidal features is a strong function of age and limiting surface brightness; after a few billion

Figure 1.1: The system of interacting galaxies NGC 4038-4039 known as Antennae. Optical image.

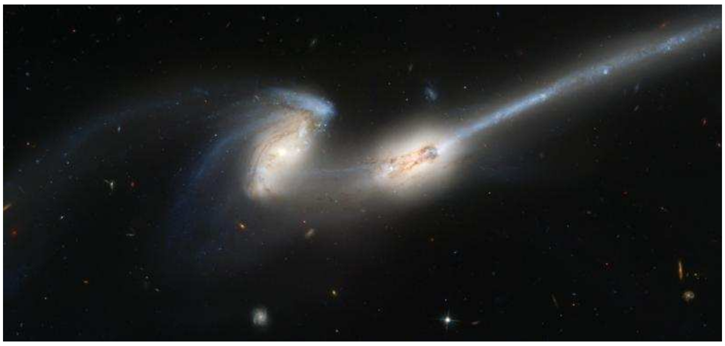

Figure 1.2: The galaxies NGC 4676 A and B known as the Mice. Optical image.

Figure 1.3: M51 (the Whirlpool galaxy) and its companion, NGC 5195. The bridge is clearly visible.

years of dynamical evolution, they will be extremely difficult to detect (Mihos 1995).

1.4 Mergers

When two galaxies of similar mass collide at a speed that is comparable with the internal velocities of the interacting systems, neither the dynamical friction approximation, nor the impulse approximation is valid. The results of numerical simulations suggest that a slow encounter between galaxies often leads to the two systems merging together. As a pair of galaxies spiral in towards merger, several dynamical effects are simultaneously active. In mergers of roughly equal-mass galaxies, orbits decay on a dynamical time-scale $\sim (G\bar{\rho})^{-1/2}$.

1.4.1 Spherical Systems

The simplest N-body simulations model the encounter of a pair of spherical galaxies. In head-on collisions, decay results from the gravitational compression arising when the two galaxies nearly coincide; this compression causes a slightly greater axial force to be felt between them as they try to separate than they experienced at corresponding distances during their approach (Toomre 1974; White 1978; Miller & Smith 1980). By stirring up the material in each galaxy at the expense of their orbital energy, this mechanism brings about the rapid merger of even the most centrally concentrated systems in only a few passages. In off-axis collisions, the collective response is dominated by those particles which orbit within their respective galaxies in the same direction as the two galaxies pass each other (White 1978, 1979; Roos & Norman 1979). Such particles are again promoted

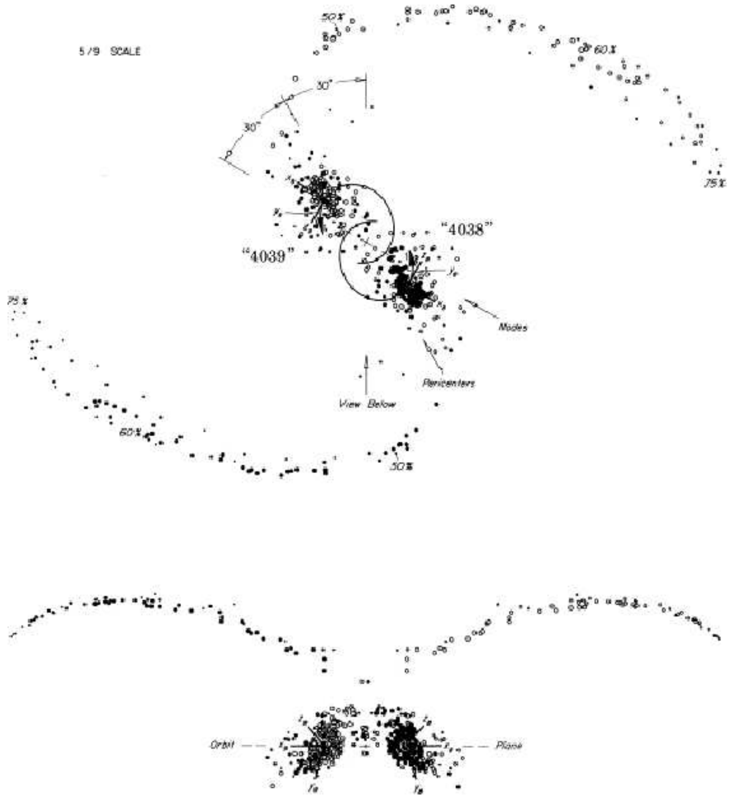

Figure 1.4: The Antennae galaxy: Toomre & Toomre's numerical simulation

.

onto less-bound orbits, receiving both binding energy and angular momentum from the relative motion of the two galaxies, and producing broad tail-like structures. Orbital decay is more rapid if the victim galaxies rotate internally in the same direction as their passage, since more of their constituents then match the angular speed of the perturber (White 1979).

Fluctuating gravitational fields during the merging process tend to transfer binding energy between different components of the system, but such fluctuations damp down before a complete redistribution takes place. The centers and outskirts of merger remnants remain therefore dominated by particles from the respective centers and outskirts of the interacting galaxies.

After a merger, the remnant relaxes progressively outward on a time-scale comparable to the local crossing time. The amount of material which escapes during the merger depends on the structure of the interacting galaxies as well as the parameters of their encounter. In general the escaping stuff comes from the outskirts of the original galaxies. The material which does not quite escape eventually phase-mixes to form an extended envelope around the body of the remnant, characterized by a r^{-4} density profile (Jaffe 1987; White 1987; McGlynn 1990).

Mergers of spherical galaxies produce remnants with fairly simple shapes and kinematics (White 1983). Head-on encounters result in prolate remnants with anisotropic velocity dispersions, whereas if the encounter is not quite head-on, the result is a slowly-tumbling triaxial object.

1.4.2 Disk / Halo Systems

Dark matter has been included in more recent models of merging disk systems. Mergers between equally-matched disk/halo galaxies were presented by Gerhard (1981), Farouki & Shapiro (1982), Negroponte & White (1983), Barnes (1988; 1992); in addition, Gerhard (1983a, b) and Barnes (1989) discussed models in which several disk/halo galaxies merge sequentially.

The dynamics of encounters between such galaxies are largely governed by the interactions of their extended dark halos; consequently even passages in which the visible components completely miss each other at first can lead to rapid orbital decay. The orbital angular momentum of the two halos is transferred to internal degrees of freedom, imparting spin and creating broad tidal tails. More tightly bound components, such as embedded disks and/or bulges, are not much braked by the tidal forces retarding the dark matter; instead, these components lose orbital angular momentum mostly by interacting with their own surrounding halos, once the latter have been decelerated (Barnes 1992). It is the interaction between such extended dark halos that brings two galaxies to a "screeching halt" and subsequent merger while the luminous tails extracted from their disks are still well-defined and visibly incriminating (Barnes 1988).

As in mergers of spherical systems, the incomplete violent relaxation of disk/halo models only blurs the original ordering in binding energy; the tightly-bound components which contained most of the luminosity in the original galaxies will be found near the center of the merger remnant. Luminous material dominates the central regions of merger remnants because the dense luminous parts of the infalling galaxies remain largely undisturbed until they finally encounter each other and merge within a now-common envelope of halo material (Barnes 1988).

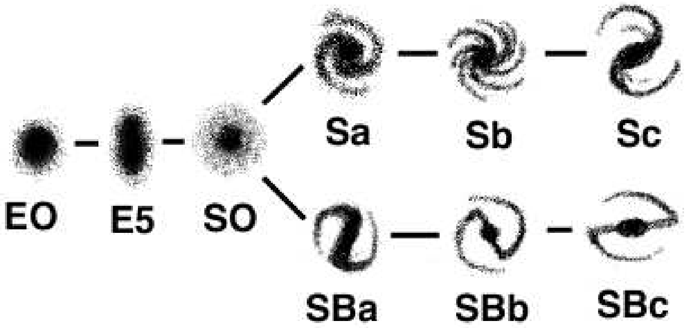

Figure 1.5: Hubble tuning fork diagram. Galaxies are classified according to their morphological appearances.

The shapes and kinematics of the remnants of disk/halo galaxy mergers are much more complex than those produced by mergers of spherical systems. For more details see White 1983b, Negroponte & White 1983, Barnes 1992 and Gerhard 1983a .

1.5 Galaxy evolution in dense environments

It is a remarkable feature that various properties of galaxies vary according to their environments. In 1926, Hubble classified galaxies according to their morphology along a tuning fork diagram (Fig. 1.5) which is is still commonly used to understand variety in galaxy morphology. However, little is known on the origin of this variety and its correlation with the galactic environment.

1.5.1 Observational evidences for environmental effects

1.5.1.1 The morphology-density relation and its evolution with redshift

The HST images (Fig 1.6 and Fig. 1.7) have revealed the presence of a large number of spiral galaxies in all distant cluster observed, in proportion that are much higher than in nearby clusters of similar richness (Dressler et al., 1994, 1997). This is reflected also in the evolution of the Morphology-Density (MD) relation, i.e. the observed correlation between the frequency of the various Hubble types and the local galaxy density, normally defined as the projected number density of galaxies within an area including its closets neighbours. In clusters in the local Universe, the existence of this relation has been known for a long time: ellipticals are frequent in high density regions, while the fraction of spirals is high in low density regions (Oemler, 1974; Butcher & Oemler, 1978; Dressler, 1980). At $z = 0.4 - 0.5$ an MD relation is already present, but it is quantitatively different from the relation at $z = 0$: the fraction of SO galaxies at $z = 0.5$ is much lower, at all densities, than in clusters at $z = 0$ (Fig. 1.8, Dressler et al. (1997)). The fraction of SOs in clusters appears to increase towards lower redshifts, while the proportion of spirals correspondingly decreases (Dressler et al. (1997); Fasano et al. (2000)). Interestingly, ellipticals are already as abundant at $z = 0.5$ as at $z = 0$. These findings strongly suggest that a significant fraction of the SO galaxies in clusters today have evolved from spirals at

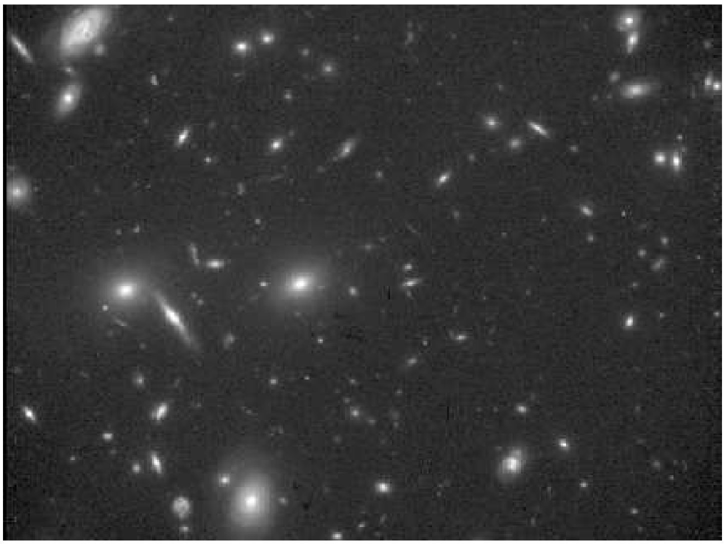

Figure 1.6: HST image of the cluster Abell 851, at $z = 0.41$. Note the high fraction of spirals and irregular galaxies.

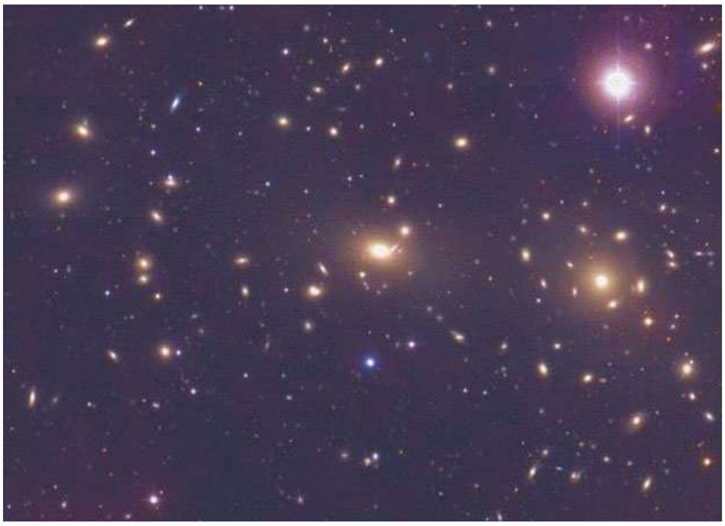

Figure 1.7: HST image of the center of the cluster Abell 1556 (Coma cluster), at $z = 0.032$. Most of the galaxies are ellipticals or early type systems.

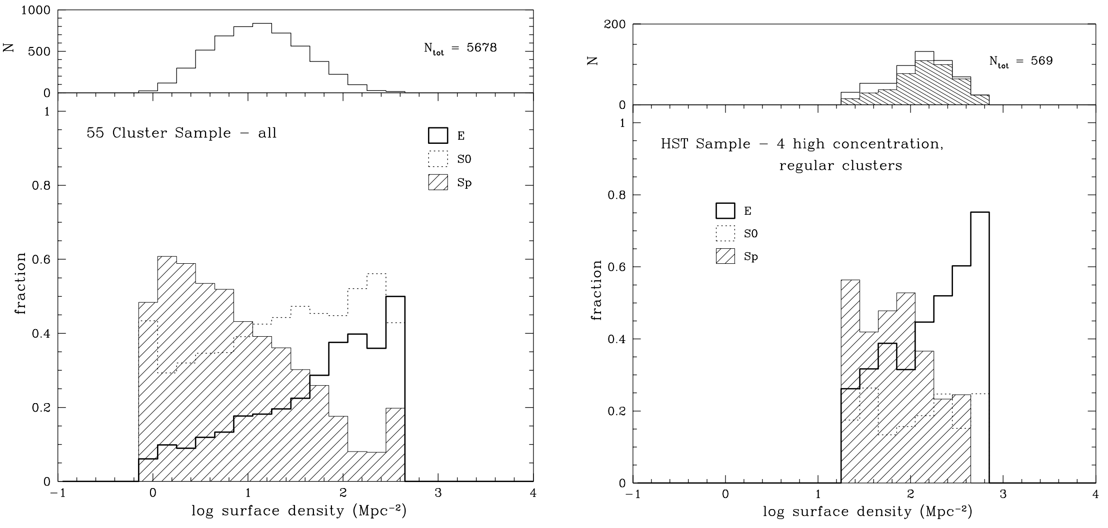

Figure 1.8: From Dressler et al. 1997. Left: morphology-density relation for 55 clusters at low redshift. Right: morphology-density relation for 4 regular clusters at $z \sim 0.45$.

relatively recent epochs. Adopting a more conservative distinction between "early-type" (Es+SOs) and late-type (spirals) galaxies, a similar evolution is found, with early type fraction decreasing at higher redshifts (van Dokkum et al., 2000; Lubin et al., 2002). First results at $z \sim 0.7 - 1.3$ seem to indicate that between $z = 0.5$ and $z = 1$ what changes in the MD relation is only the occurrence of early-type galaxies in the very highest density regions (Smith et al., 2005). Interestingly, an MD relation, originally found in the cluster cores, has been shown to be present across a wide range of environments, in all types of clusters, rich and poor, concentrated and irregular, with low and high L_X (Dressler, 1980; Balogh et al., 2002), in groups (Postman & Geller, 1984) and at large cluster radii (Treu et al., 2003), though the relation seems to vary from rich to less rich clusters (Dressler, 1980; Balogh et al., 2002).

1.5.1.2 Suppression of star formation in cluster regions

Similarly, there have been extensive evidence that cluster galaxies have smaller amount of star formation, with redder colors than field galaxies. It has been known for a long time that cluster regions lack emission line galaxies (Dressler et al., 1985). More generally, in the nearby universe the average star formation activity correlates with the local galaxy density: in higher density regions the mean star formation rate per galaxy is lower. This is not surprising, given the existence of the MD relation: the highest density regions have proportionally more early-type galaxies devoid of current star formation. Recently, many studies reported that star formation in the cores of clusters is much lower than in the surrounding field (Ferguson et al., 2000; Couch et al., 2001; Balogh et al., 2002).

In addition, it is becoming possible to specify the environment where star formation in galaxies starts to change. Abraham et al. (1996) reported that cluster members become progressively bluer as function of cluster-centric distance to 5 Mpc in A2390 ($z = 0.23$).

van Dokkum et al. (1998) found S0 galaxies in the outskirts of a cluster at $z = 0.33$. These S0s show a much wide scatter in their colors and are bluer on average than those in cluster cores, providing possible evidence for recent infall of galaxies from the field. Terlevich et al. (2001) reported that $U - V$ colors of early type galaxies are systematically bluer at outside the core of Coma cluster. Pimbblet et al. (2002) studied 11 X-ray luminous clusters ($0.07 < z < 0.16$) and found that the median galaxy color shifts bluewards with decreasing local galaxy density. Interestingly, the correlation between the mean SF and the local density extends to very low local densities: Lewis et al. (2002) showed that the star formation rate of galaxies decreases toward cluster cores at around one virial radius, and that such a correlation exists also outside of clusters. This seems to parallel the fact that an MD relation is probably existing in all environments.

1.5.2 Theoretical implications

In the field environment, interactions and mergers of galaxies are thought to be a prime candidate for driving evolution in galaxy populations. As we saw in the previous sections, major mergers of spiral galaxies may lead to the transformation of spirals into ellipticals (Toomre 1978; Schweizer 1982): the violent relaxation associated with a merger effectively destroys the galactic disks and creates a kinematically hot, $r^{1/4}$-law spheroid, while the concurrent intense burst of star formation may process the cold ISM of a spiral galaxy into the hot X-ray halo of an elliptical. These processes are not totally efficient, however, and leave signatures behind that identify the violence of the merging process: diffuse loops and shells of starlight, extended H I gas, significant rotation in the outskirts of the remnant, and dynamically distinct cores. While it is an open question as to what fraction of ellipticals formed this way, it is clear that at least some nearby field ellipticals — Centaurus A being a notable example (Schiminovich et al. 1994) — have had such violent histories.

The MD relation suggests two hypothesis regarding the origin of early type galaxies in clusters: either that disk galaxies do not form in regions that will become high density environments, or that these kind of galaxies do not survive unaltered in such environments. The lack of late type galaxies observed in distant clusters seems to support the latter scenario.

In clusters, a number of environmental effects may modify the dynamical response and evolution of interacting galaxies described in the previous sections. First, the relative velocities of interacting systems tend to be higher, although many low-velocity encounters still occur within smaller groups falling in from the cluster periphery. Indeed, galaxy clusters form not by accreting individual galaxies randomly from the field environment, but rather hierarchically through the infall of less massive groups falling in along filaments. These infalling groups have velocity dispersions that are much smaller than that of the cluster as a whole, permitting the slow, strong interactions normally associated with field galaxies. Second, the global tidal field of the cluster must also play a role in the evolution of interacting systems, stripping away the loosely bound tidal material and potentially adding energy to bound groups. The hot intracluster medium (ICM) can act to further strip out low-density ISM in galaxies, particularly the diffuse tidal gas ejected during collisions.

1.5.3 High speed encounters

The most obvious difference between interactions in the field and in the cluster environment is the collision speed of the encounter. While slow interactions are able to drive a strong dynamical response in disk galaxies, faster encounters result in a perturbation that is much shorter lived and less resonant with the internal dynamics of the disk. During slow encounters, both the disk and disk/bulge galaxy models develop dramatic bars and spiral arms, which can drive strong inflow and central activity. The lowered surface density of LSB models results in a weaker self-gravitating response (Mihos et al. 1997); a very small, weak bar is present, but the overall response is one of a persistent oval distortion, which would be much less able to drive gaseous inflow. In contrast, the response of the fast encounters depends more strongly on the structural properties of the galaxy. Pure-disk models develop a relatively strong bar mode, while disk/bulge systems sport a two-arm spiral pattern with no central bar. LSB models, on the other hand, lack the disk self-gravity to amplify the perturbation into any strong internal response. However, the vulnerability of LSBs lies not in their internal response to a single encounter, but rather in their response to repeated high-speed collisions in the cluster environment, which is much stronger (Moore et al. 1996; Lake et al. 1998).

Repeated fast encounters, coupled with the effects of the global tidal field, can drive a very strong response in cluster galaxies. For galaxy-like potentials, the amount of heating during an impulsive encounter scales like $\Delta E/E \sim r_p^{-2}$, where r_p is the impact parameter of the interaction, such that distant encounters impart less energy. However, this effect is balanced by the fact that under simple geometric weighting the number of encounters scales as r_p^2, so that the total heating, summed over all interactions, can be significant. Knebe et al. 2004 find that, on average, 30% of the satellite galaxy population experiences at least one encounter per orbit with another satellite galaxy. This result seems to be sensible to the age of the host halo, with a clear trend for more interactions in younger systems. There is a well defined correlation between the number of encounters and the distance from the cluster center – satellite galaxies closer to the center of the host experience more interactions – which simply reflects the increasing spatial density of satellites with decreasing radius within the main system. However the relative velocity of two galaxies during an encounter is higher closer to the cluster center, producing little structural damage and explaining the lack of correlation found between the total amount of heating that a satellite suffers after repeated encounters and its orbital parameters (Knebe et al. 2005). Interactions with other satellites account for $\sim 30\%$ of the total mass loss experienced by a satellite over its lifetime (Knebe et al. 2005).

These high-speed, "harassment-like" encounters are expecially effective at driving evolution in the low-luminosity cluster populations (Moore et al. 1996; Lake et al. 1998). The transformation sequence of a dwarf disk or dIrr galaxy begins with a violent bar instability. Subsequent perturbations cause the bar to lose angular momentum and it eventually collapses into a spheroidal system through a buckling type instability. During the early stages of the transformation, which takes roughly a cluster orbital time, the morphology of the galaxy may appear as a rotationally supported dS0 system. The nature of the dark matter is critical to the survival of galaxies in clusters. If galaxies had constant density cores of just a few kpc (or cuspy potentials with very low concentrations) then they would all be easily disrupted by the cluster potential. On the other hand, if galactic halos are cuspy and concentrated they would all survive in clusters and we would not expect to observe a significant component of diffuse light. The Ultra Compact Dwarfs recently found in the Fornax cluster are most likely the dense nuclei of nucleated dE galaxies that have been "overmerged" by gravitational interactions (Drinkwater et al. 2000). These tracer cores show that the central concentrations of the progenitor galaxies must have been low enough such that they have been completely disrupted by the present day.

A fundamental prediction from gravitational heating mechanisms is that dE's should be embedded within very low surface brightness tidal streams which streams should trace the orbital path of the progenitor galaxy. These kind of structures have been observed in a few nearby clusters (Fig. 1.9, Trentham & Mobasher 1998; Calcáneo-Roldán et al. 2000)). However, these arcs will only survive as discrete structures if the potential is quiet; substructure will dynamically heat these arcs, and eventually destroy them. Since the relaxation time is only short in the cluster cores the streams should survive relatively intact at the edge of clusters, but they should become well mixed near the cluster centers. The properties of the ICL in clusters, particularly the presence of substructure, may thus hold important clues about the accretion history and dynamical evolution of galaxy clusters. If much of the ICL is formed early in a cluster's dynamical history, before the cluster has been fully assembled, the bulk of the ICL will be morphologically smooth and well mixed by the present day, with a few faint tidal arcs showing the effects of late accretion. In contrast, if the ICL formed largely after cluster virialization, from the stripping of "quietly infalling" galaxies, the ICL should consist of an ensemble of kinematically distinct tidal debris arcs. Clusters that are dynamically younger should also possess an ICL with significant kinematic and morphological substructure.

1.5.4 Hydrodynamical mechanisms in dense environments

While tidal interactions directly perturb the morphology of a galaxy, hydrodynamical processes act on cluster galaxies evolution mainly affecting its star formation rate.

Ram pressure stripping (Moore et al. 1999, Quilis, Moore & Bower 2000) is effective at removing the entire gas supply from galaxies that pass through the cores of rich clusters (c.f. Fig. 1.10). Any galaxy passing through the core of a massive cluster will have its gas supply completely stripped by ram-pressure and viscous stripping on a timescale smaller than the core crossing time. The remaining dense molecular gas may recycle into the ISM and also be removed or consumed in a burst of star-formation due to the pressure increase as the galaxy reaches the cluster center. Disk galaxies with a deficit of cold gas or a morphological sign of gas removal are often observed near cluster centers (Vollmer et al. 2000; Volmer 2003). Especially, Haynes & Giovanelli (1986) showed that the frequency of HI deficient galaxies projected on the sky increases close to the center of the Virgo Cluster. Since the orbits of galaxies in clusters are nearly isotropic, which results in most of the galaxies orbiting through the dense inner region of the cluster (Ghigna et al 1998), the environment near rich clusters may also host galaxies that have suffered significant gravitational perturbations and have been partially stripped of gas by virtue of orbiting through the cluster core. About 10% of orbits will take galaxies through the core and to beyond twice the cluster virial radii (∼6 Mpc for Coma) and this could explain the suppression of star formation observed in some galaxies as far as several Mpc from the center of a cluster observed by different groups (Balogh et al. 1997; Kodama et al. 2001; Lewis et al. 2002).

On the other hand, star formation rates of galaxies may decrease gradually by stripping

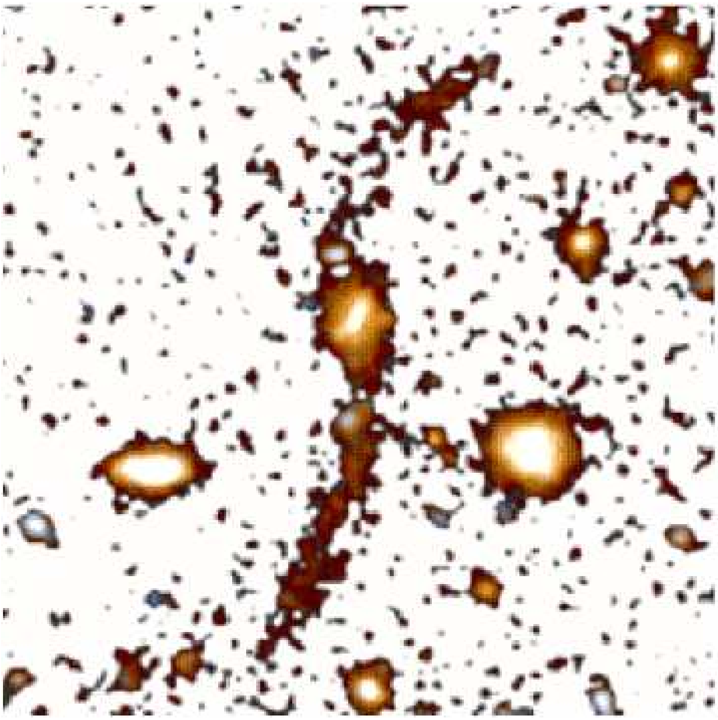

Figure 1.9: Symmetric stellar tidal stream from a disk galaxy that is orbiting in a galaxy cluster at $z = 0.5$ (MORPHS group).

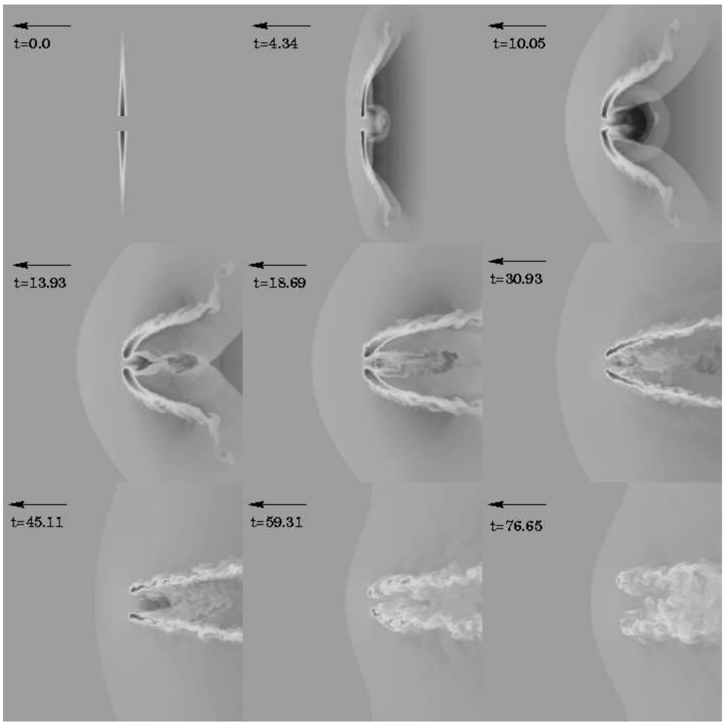

Figure 1.10: A high resolution Eulerian simulation of gas stripping of a galaxy falling into a gas density representative of the center of the Coma cluster at 3000 km/s (Quilis et al. 2000). The time unit is 10^6 years and each frame is on 50 kpc on a side.

of warm halo gas that would later infall on to the galactic disk, and be the source of cold gas and stars in the galactic disks (strangulation; Larson, Tinsley & Caldwell 1980; Balogh et al. 2001; Bekki et al. 2002). If only the warm gas is stripped, star formation may be allowed to continue by consuming the remaining cold disk gas but, without infalling gas from halo to replenish this supply, star formation will die out on timescales of a few Gyrs (Larson et al. 1980). Observationally, Finoguenov et al. (2003) found in the Coma cluster the filamentary gas where strangulation is likely to be happening and they predicted quiescent star formation in galaxy disks around the filament.

Another mechanism to slow down the star formation rate of galaxies is thermal evaporation of the cold gas in disk galaxies via heat conduction from the surrounding hot ICM (Cowie & Songaila 1977; Fujita 2004). Pressure triggered star formation, in which galactic clouds are compressed by the ICM pressure, can temporarily increase the star formation rate (Dressler & Gunn 1983; Evrard 1991; Fujita 1998).

1.5.5 The Local Group environment

The Local Group dwarf spheroidals are the extreme tip of the galaxy luminosity function, and as the shallowest potentials and faintest galaxies known they provide a strong test of our understanding of galaxy formation (Kormendy 1989). The Local Group morphology-density relation is similar to that of rich clusters in that the spheroidal galaxies with no diffuse gas are located close to the host galactic potentials of the Milky Way and M31. Again we can ask the question: do disks know not to form near the site of a massive potential or were they originally disks that have been transformed to spheroidals through interactions? Observationally this is unclear and a difficult question to answer since we can't observe Local Group progenitors at high redshifts.

However, a huge amount of detailed data exists for these faint Local Group galaxies (e.g. Grebel 2001), which must be reproduced by a successful model for their formation.

The dynamics of these systems indicate that their spheroidal shapes are due to random stellar motions and that rotational support is small. Many of these systems show evidence for continuous star-formation, or widely separated bursts, indicating that ram-pressure stripping by a hot Galactic halo component has not been completely efficient at removing their fuel. It also indicates that supernovae winds have not been effective at ejecting the bulk of the gas from these systems.

Galaxies are on average some 5 Gyrs older than galaxy clusters, which allows time for gravitational interactions to transform disks.

1.6 N-body simulations

As we saw in the previous chapter, much of our present understanding of galactic dynamics and interactions has emerged from numerical models of galaxies.

1.6.1 Gravity

A basic parameter which measures the capability of N-body codes to faithfully represent gravitational clustering is the width of their dynamical range for mass and length resolution. Fundamentally, solving gravity means solving Poisson's equation for the gravitational potential, ϕ, given a mass density, ρ: $\nabla^2\phi = 4\pi G\rho$ where G is the Newtonian gravitational constant. In a simulations with discrete bodies it is common to start from the explicit expression for the acceleration, $a_i = \nabla\phi$ on a given body in terms of the sum of the influence of all other bodies, $a_i = \sum_{i \neq j} GM_j/(r_i - r_j)^2$ where the r_i and M_i are the position and masses of the bodies respectively. Mass resolution is fixed by the total number of particles used. The gravitational force is softened on some scale $r < \epsilon$ to avoid problems with the integration and to minimize two-body scattering in cases where the bodies represent a collisionless system. ϵ is called the softening length of the system.

The dynamical range for length resolution is fixed by the ratio of the size of the simulation box to the softening scale for the computation of the gravitational force. The principal limitation on what can be achieved with these N-body models is the computational expense involved in calculating the forces acting on their particles. Because of the limits imposed by computational costs and computer memory, different strategies can be adopted in order to compromise between between numerical resource and extension of the dynamical range. Three main categories of N-body simulations can be devised, which essentially differ in their prescriptions for evaluating the gravitational force between particles.

Early N-body work such as studies of relatively small stellar systems were approached using a direct summation of the forces on each body due to every other body in the system **?**. Within this approach, the force softening scale is usually very small and the particle trajectories are calculated with great precision. This direct $\mathcal{O}(N^2)$ (N being the number of particles) approach is impractical for large numbers of bodies. Therefore, only a rather limited number of particles ($\lesssim 10^4$) is usually employed.

A popular scheme for larger N is the Particle-Mesh (PM) method which has long been used in electrostatics and plasma physics. The adoption of PM was strongly related to the realization of the existence of the $\mathcal{O}(N\,log\,N)$ Fast Fourier Transform (FFT) in the 1960's. The FFT is used to solve for the gravitational potential from the density distribution interpolated onto a regular mesh. In astrophysics sub-mesh resolution is often desired, in which case the force can be corrected on sub-mesh scales with local direct sums as in the Particle-Particle Particle-Mesh (P^{3}M) method. PM is popular in stellar disk dynamics, and P^{3}M has seen widespread adoption in cosmology. Working in Fourier space is not only more efficient, but it also allows efficient force error control through optimization of the Green's function and smoothing. Fourier methods are widely recognized as ideal for large, fairly homogeneous, periodic gravitating simulations. Multigrid has some advantages in parallel due to the local nature of the iterations. The Particle-Particle correction can get expensive when particles cluster in a few cells, while both multigrid and P^{3}M can adapt to address this via a hierarchy of sub-meshes.

A current popular choice is to use tree algorithms (Barnes & Hut 1986) which are inherently $\mathcal{O}(N\,log\,N)$. This approach recognises that details of the remote mass distribution become less important for accurate gravity with increasing distance. Thus the remote mass distribution can be expanded in multipoles on the different size scales set by a tree-node hierarchy. The appropriate scale to use is set by the opening angle subtended by the tree-node bounds relative to the point where the force is being calculated. The tree approach can adapt to any topology, and thus the speed of the method is somewhat insensitive to the degree of clustering. Once a tree is built it can also be re-used as an efficient search method for other physics such as particle based hydrodynamics.

A particularly useful property of tree codes is the ability to efficiently calculate forces for a subset of the bodies. This is critical if there is a large range of time-scales in a simulation and multiple independent time steps are employed. Multiple time steps are particularly important for current astrophysical applications where the interest and thus resolution tends to be focused on small regions within large simulated environments such as individual galaxies, stars or planets. Dynamical times can become very short for small numbers of particles. P^3M codes are faster for full force calculations but are difficult to adapt to calculate a subset of the forces.

The Fast Multipole Method (FMM) recognises that the applied force as well as the mass distribution may be expanded in multipoles. This leads to a force calculation step that is $\mathcal{O}(N)$ as each tree node interacts with a similar number of nodes independent of N and the number of nodes is proportional to the number of bodies. Building the tree is still $\mathcal{O}(N\,log\,N)$ but this is a small cost for simulations up to $N \sim 10^7$ (Dehnen 2000).

For the pure collisionless simulations performed in this thesis we used PKDGRAV the fully parallel multistepping N-body tree-code designed by Stadel 2001

1.6.2 Hydrodynamics and SPH

Astrophysical systems are predominantly at very low physical densities and experience wide-ranging temperature variations. Most of the material is in a highly compressible gaseous phase. In general this means that a perfect adiabatic gas is an excellent approximation for the system. Microscopic physical processes such as shear viscosity and diffusion can usually be neglected. High-energy processes and the action of gravity tend to create large velocities so that flows are both turbulent and supersonic: strong shocks and very high Mach numbers are common. Radiative cooling processes can also be important; however, the timescales can often be much longer or shorter than dynamical timescales. In the latter case isothermal gas is often assumed for simplicity. In many areas of computational astrophysics, particularly cosmology, gravity tends to be the dominating force that drives the evolution of the system. Visible matter, usually in the form of radiating gas, provides the essential link to observations. Radiative transfer is always present but may not significantly affect the energy and thus pressure of the gas during the simulation.

Fluid dynamics solvers can be broadly classified into Eulerian or Lagrangian methods. Eulerian methods use a fixed computational mesh through which the fluid flows via explicit advection terms. Lagrangian methods follow the evolution of fluid parcels via the full (comoving) derivatives. This requires a deforming mesh or a mesh-less method such as Smoothed Particle Hydrodynamics (SPH) (Monaghan 1992). Data management is more complex in these methods; however, advection is handled implicitly and the simulation tends to naturally adapt to follow density contrasts.

Smoothed Particle Hydrodynamics is an approach to hydrodynamical modeling developed by Lucy (1977) and Gingold & Monaghan (1977). It is a particle method that does not refer to grids for the calculation of hydrodynamical quantities: all forces and fluid properties are found on moving particles eliminating numerically diffusive advective terms.

The basis of the SPH method is the representation and evolution of smoothly varying fluid quantities whose value is only known at disordered discrete points in space occupied by particles. Particles are the fundamental resolution elements comparable to cells in a mesh. SPH functions through local summation operations over particles weighted with a smoothing kernel, W, that approximates a local integral. The smoothing operation provides a basis from which to obtain derivatives. Thus, estimates of density related physical quantities and gradients are generated.

A general smoothed estimate for some quantity f at particle i given particles j at positions $\vec{r}_j$ takes the form:

$$f_{i,\mathrm{smoothed}} = \sum_{j=1}^{n} f_j W_{ij}(\vec{r}_i - \vec{r}_j, h_i, h_j), \tag{1.5}$$

where W_{ij} is a kernel function and h_j is a smoothing length indicative of the range of interaction of particle j. It is common to convert this particle-weighted sum to volume weighting using $f_j m_j/\rho_j$ in place of f_j where the m_j and ρ_j are the particle masses and densities, respectively. For momentum and energy conservation in the force terms, a symmetric $W_{ij} = W_{ji}$ is required. For the hydrodynamical simulations presented in this thesis we used the code "Gasoline", (Wadsley et al. 2004) which is built on PKDGRAV framework and uses the kernel-average first suggested by Hernquist & Katz (1989),

$$W_{ij} = \frac{1}{2} w(|\vec{r}_i - \vec{r}_j|/h_i) + \frac{1}{2} w(|\vec{r}_i - \vec{r}_j|/h_j) \tag{1.6}$$

Gasoline employs a fairly standard implementation of the hydrodynamics equations of motion for SPH (Monaghan 1992). Density is calculated from a sum over particle masses m_j,

$$\rho_i = \sum_{j=1}^{n} m_j W_{ij}. \tag{1.7}$$

The momentum equation is expressed,

$$\frac{d\vec{v}_i}{dt} = -\sum_{j=1}^{n} m_j \left(\frac{P_i}{\rho_i^2} + \frac{P_j}{\rho_j^2} + \Pi_{ij} \right) \nabla_i W_{ij}, \tag{1.8}$$

where P_j is pressure, $\vec{v}_i$ velocity and the artificial viscosity term Π_{ij}.

In astrophysical systems the cooling timescale is usually short compared to dynamical timescales which often results in temperatures that are close to an equilibrium set by competing heating and cooling processes. In Gasoline a range of cases including adiabatic (no cooling), isothermal (instant cooling), and implicit energy integration are implemented. Hydrogen and Helium cooling processes have been incorporated. Ionization fractions are calculated assuming equilibrium for efficiency. Gasoline optionally adds heating due to feedback from star formation, an uniform UV background or using user defined functions.

Chapter 2

Morphological evolution of disks in clusters[1]

2.1 Abstract

The recent discovery of hidden non-axysimmetric and disk-like structures in bright Virgo dwarf elliptical and lenticular galaxies (dE/dSph/dS0) indicates that they may have late-type progenitors. Using N-body simulations we follow the evolution of disk galaxies within a ΛCDM cluster simulated with 10^7 particles, where the hierarchical growth and galaxy harassment are modeled self-consistently. Most of the galaxies undergo significant morphological transformation, even at the outskirts of the cluster, and move through the Hubble sequence from late type disks to dwarf spheroidals. None of the disks are completely destroyed therefore they can not be the progenitors of ultra compact dwarf galaxies (UCDs). The time evolution of the simulated galaxies is compared with unsharp-masked images obtained from VLT data and the projected kinematics of our models with the latest high resolution spectroscopic studies from the Keck and Palomar telescopes.

2.2 Introduction

Early type dwarfs (dE and dSO) are the most common type of galaxies in the nearby universe, yet their origin is still unknown. These galaxies are found nearly exclusively near bright galaxies and in groups or clusters. Their continuation or separation from the brighter elliptical sequence is currently debated (Graham, Jerjen & Guzmán, 2003; Gavazzi et al., 2004). Formation scenarios include mainly two different hypotheses: 1) dEs and dSOs are primordial galaxies, 2) they are the result of a morphological transformation of spiral and irregular galaxies accreting into the cluster. This latter idea is supported by some observations, i.e the relative number density of dwarf early type galaxies increases with the local galaxy density (Ferguson & Sandage, 1991), suggesting that the environment drives galaxy evolution. Kormendy & Freeman (2004) investigated the systematic properties of dark matter halos in late-type and dwarf spheroidal galaxies concluding that they form a single physical sequence as a function of the dark matter core mass. Moore, Lake & Katz (1998) have shown that galaxy harassment in clusters can transform spirals into spheroidals. Harassment can explain the morphological evolution of the small spiral

---

[1] This chapter (Mastropietro et al. 2005, astro-ph 0411648) is going to be published on MNRAS.

and irregular galaxies observed in clusters at redshift $z \sim 0.4$ (**?**) into dwarf ellipticals in the nearby universe (Moore et al., 1996). Moreover the radial velocities of early type galaxies in the Virgo cluster seem to indicate that these galaxies are not an old cluster population (Conselice, Gallagher & Wyse, 2001) but originate from infalling field galaxies. According to this evolutionary scenario we expect to find nearby cluster galaxies that are currently undergoing morphological transformation and retain part of their disk nature. Recent observations confirm that early type galaxies have a broad range of photometric and kinematical characteristics. Jerjen, Kalnajs & Binggeli (2000) and Barazza, Binggeli & Jerjen (2002) discovered hidden spiral structures and bar features in five bright dEs in the Virgo cluster, concluding that a sizeable fraction of all bright early type dwarfs hosts a disk component. Spirals and disks were also observed within dwarf spheroidal galaxies in the Coma (Graham, Jerjen & Guzmán, 2003) and Fornax clusters (De Rijcke et al., 2001). Furthermore, the degree of rotational support is found to vary from zero to a value close to one expected for a galaxy flattened by rotation (De Rijcke et al., 2001; Simien & Prugniel, 2002; Pedraz et al., 2002; Geha, Guhathakurta & van der Marel, 2003; van Zee, Skillman & Haynes, 2004).

The aim of this work is to follow the evolution of disk galaxies orbiting in a cluster environment using high resolution N-body simulations and to compare the final harassed remnants with the latest photometric and spectroscopic data. Previous studies have suffered from low resolution and they used idealised cluster models for the initial conditions. We aim to use sufficient resolution that we can follow the detailed morphological evolution and we evolve the galaxy models within a cluster selected from a cosmological simulation. In addition, the model has cuspy CDM halos and structural parameters as expected in the concordance cosmological model. This study complements that of Gnedin (2003) who studied the evolution of luminous early type disk galaxies within a cosmological context.

The paper is organised as follows. In § 2.3 we present the main characteristics of the galaxy models and the ΛCDM cluster used. The results of the three dimensional simulations are illustrated in § 2.4,while in § 2.5 and § 2.6 we report a projected photometric and kinematical analysis of the simulated remnants and the comparison with observations.

2.3 Simulations

All the simulations have been carried out using PKDGRAV, a parallel multistepping N–body tree–code designed for high force accuracy (Stadel, 2001).

The galaxy model is a multi–component system with a stellar disk embedded in a spherical dark matter halo and was constructed using the technique described by Hernquist (1993). The dark matter distribution initially follows a NFW (Navarro, Frenk & White, 1996, 1997) profile, which is adiabatically contracted in response to baryonic infall (Springel & White, 1999). The disk has an exponential surface density profile of the form:

$$\Sigma(R) = \frac{M_d}{2\pi {R_d}^2} \exp\left(-R/R_d\right), \tag{2.1}$$

where M_d and R_d are, respectively, the disk mass and radial scale length (in cylindrical coordinates), while the thin vertical structure is characterised by the scale height z_d which

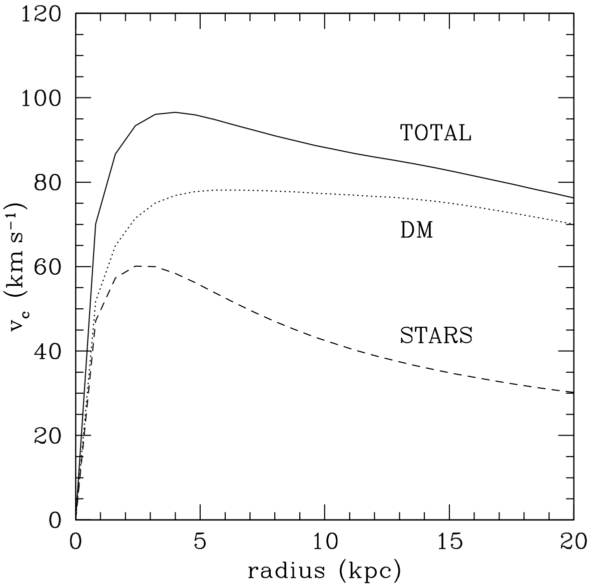

Figure 2.1: The rotation curve of the initial galaxy model. The stellar and dark matter contributions to the total rotation curve are indicated.

sets the “temperature” of the disk

$$\rho_d(R,z) = \frac{\Sigma(R)}{2z_d}\,\mathrm{sech}^2\,(z/z_d)\,. \tag{2.2}$$

The structural parameters of the disk and the halo are chosen so that the resulting rotation curve resembles that of a typical bulgeless late-type (Sc/Sd) disk galaxy (Courteau, 1997; Persic & Salucci, 1997). The model parameters are initialised following the same procedure as Mayer et al. (2002), which was based on the galaxy formation model of Mo, Mao, & White (1998).

The mass within the virial radius was set equal to 7×10^{10} M$_\odot$ and the fraction of mass in the disk is $\sim$ 6%. The contribution of the different components to the global rotation curve, assuming a disk scale length $R_d = 1.5$ kpc and a concentration $c = 10$ (where c is defined as $c = r_{vir}/r_s$, with r_{vir} and r_s respectively virial and scale radius of the NFW halo) is plotted in Fig. 2.1. The halo spin parameter, which sets the disk scale length in our modeling, is $\lambda = 0.045$, where λ relates the angular momentum J and the total energy E of a system with virial mass M_{vir} through the relation $\lambda = J|E|^{1/2}G^{-1}M_{vir}^{-5/2}$. The model has a central surface brightness $\mu_B = 22\,\mathrm{mag\,arcsec}^{-2}$, assuming an initial V-band mass to light ratio $\simeq 4$ Geha et al. 2002 and a $B-V$ color of 0.77 (van Zee, Barton & Skillman, 2004). The stellar disk satisfies the Toomre (Toomre, 1964) stability criterion, which requires, for a rotational supported disk

$$Q_{star}(R) = \frac{\sigma_R k}{3.36G\Sigma_s} > 1, \tag{2.3}$$

where σ_R is the radial velocity dispersion, κ is the local epicyclic frequency and Σ_s the stellar surface density. The efficiency of swing amplification of a disk perturbation with m-fold

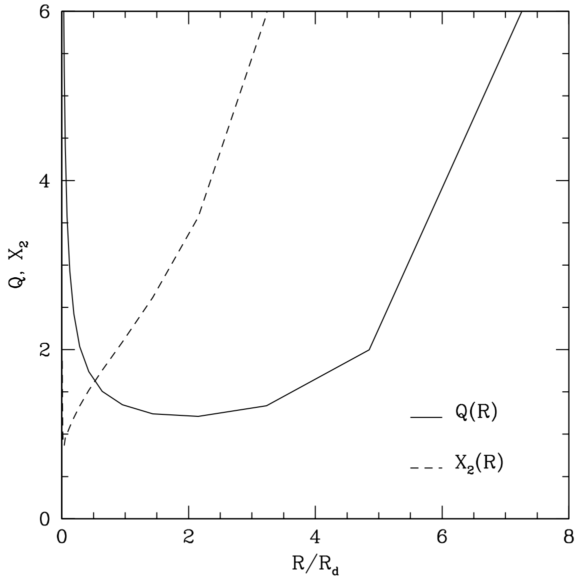

Figure 2.2: Q and X_2 parameters as function of radius (in units of the disk scale length R_d).

symmetry is governed by a combination of Q and the parameter $X_m = \kappa^2 R/(4\pi m G\Sigma_s)$ (Toomre, 1981). The radial profiles of Q and X_2 are indicated in Fig. 2.2.

Each galaxy is modeled with 10^6 particles, 10^5 of which are in the disk. The gravitational softening is set to 0.5 kpc for the dark halo and 0.1 kpc for the disk particles. The galaxies were evolved for ~ 5 Gyrs in a ΛCDM cluster with a mass at $z = 0$ comparable to that of Virgo ($M_{vir} = 3.1 \times 10^{14}$ M$_\odot$), concentration $c_{NFW} = 8.8$ and a virial radius R_{vir} of 1.8 Mpc. The cluster, selected from a 300 Mpc cube simulation (Diemand, Moore & Stadel, 2004b) with cosmological parameters $\Omega_\Lambda = 0.732$, $\Omega_m = 0.268$ and $\sigma_8 = 0.9$ (Spergel et al., 2003), was resimulated at high resolution and corresponds to the intermediate resolution cluster D9 of Diemand, Moore & Stadel (2004a). The number of particles within the virial radius is $\sim 6 \times 10^6$ and the softening length is 2.4 kpc.

At $z = 0.5$ we replaced 20 random cluster particles (10 within the virial radius and 10 within 20% of the virial radius) with the high resolution galaxy model. Only one galaxy model is used, in order to isolate the effects of orbit on the evolution. We assigned to the center of mass of each galaxy the same orbital position and velocity of the replaced particle. We replace particles rather than halos so as not to bias the results by omitting "overmerged" halos. Internal velocities and lengths were rescaled according to the redshift and cosmology. In particular the comoving velocities at a given redshift z are expressed in terms of the Hubble constant $H(z)$ through the relation

$$v = \frac{\dot{r}}{a} - H(z)\, x, \tag{2.4}$$

where r and x are the physical and comoving coordinate and a the scale factor $1/(1+z)$, respectively.

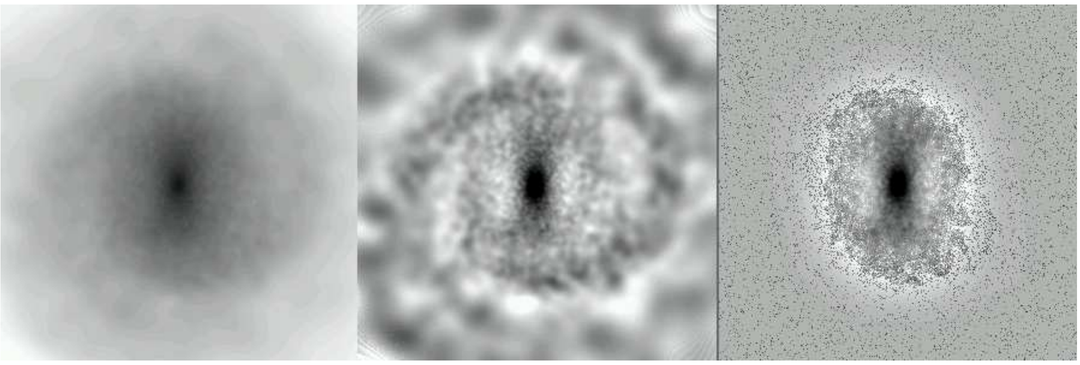

Figure 2.3: Unsharp masking technique applied to the stellar component of a simulated face-on galaxy (GAL5 of Table 2.1). The box size is $\sim$ 20 kpc. Left frame: smoothed stellar surface density produced from the the simulation output using BEAM by J. Stadel. Middle frame: the result of the unsharp masking on the former image, which reveals presence of a bar and a spiral pattern. Right frame: a noise filter is previously applied to the original surface density map, increasing the intensity of the gray channel for random selected pixels. As a result in the final unsharp image the low density structures disappear and only the bar and a ring feature are still visible.

2.4 Galaxy evolution

Among the initial sample of 20 galaxies, only 13 are still within the cluster virial radius at $z = 0$, while the others lie on bound orbits between R_{vir} and 1.5 R_{vir}. This result is consistent with the fact that about half of the halos which are presently at the outskirts of the cluster (up to $2R_{vir}$) have a pericenter smaller than R_{vir} (Moore, Diemand & Stadel, 2004).

The evolution of many of the galaxies within the cluster is quite violent and due to a sequence of strong gravitational encounters with substructures and with the global cluster potential. Most of the central galaxies lose a significant fraction of stars and undergo a complete morphological transformation from disks to spheroidal systems. In order to highlight the presence of hidden structures we applied to the stellar component of the simulation results the unsharp masking technique described in Barazza et al. 2002. This method consists of the following steps. The intensity of each pixel is replaced with the mean intensity of a given area around the pixel producing a smoothed image. The linear dimension of this area has to be close to the typical scale of the features that we want to uncover. The original image is then divided by the smoothed one. Fig. 2.3 illustrates the results of the unsharp masking applied to a galaxy of our sample, where the ESO's MIDAS task FILTER/SMOOTH is used for the image smoothing with a smoothing length of 30-40 pixels, corresponding to $\sim$ 2 kpc.

Fig. 2.4 represents the different phases of the evolution of a galaxy transforming into a dE. The first stage of the evolution is characterised by the formation of a strong bar (Moore, Lake & Katz, 1998) and an open spiral pattern in the disk. The spiral arms

Table 2.1: Final state of the remnants. The second column indicates, when available, the apocentric and pericentric distances of the last orbit. For each galaxy we list three dimensional (spherically averaged) tidal r_t and effective r_e radius (in kpc), dark matter M_h and stellar M_s mass (in units of $10^9 M_\odot$). The tidal radius is calculated using SKID (Stadel, 2001), while r_e is the radius containing half of the light. The last two columns indicate the axial ratios (respectively intermediate and short axis to major axis) measured within $2r_e$.

Galaxy	Apo-Peri	r_t	r_e	M_h	M_s	b/a	c/a
GAL1	200-90	8.5	2.0	2.6	2.3	0.79	0.40
GAL2	150-100	10.1	1.3	2.8	2.4	0.58	0.39
GAL3	650-60	16.6	2.7	13.0	4.2	0.98	0.18
GAL4	300-50	11.6	1.8	5.2	3.2	0.44	0.34
GAL5	630-100	19.4	1.9	7.6	3.3	0.62	0.27
GAL6	90-40	3.6	0.7	0.2	0.5	0.90	0.79
GAL7	75-210	11.0	1.8	4.2	3.3	0.55	0.31
GAL8	100-60	4.6	1.1	1.0	1.5	0.87	0.86
GAL9	120-70	7.9	1.1	1.5	1.8	0.66	0.54
GAL10	270-80	9.0	1.2	1.8	1.8	0.62	0.49
GAL11	1130-120	16.9	2.6	14.6	4.1	0.66	0.18
GAL12	720-210	14.7	2.6	18.8	4.1	0.45	0.23
GAL13	1720-450	16.8	2.9	21.6	4.2	0.34	0.22
GAL14	...-460	17.2	2.0	8.2	3.6	0.71	0.18
GAL15	...-900	17.4	2.6	19.2	4.2	0.41	0.28
GAL16	...-...	16.3	2.5	24.4	4.2	0.79	0.29
GAL17	2480-...	17.0	2.9	21.1	4.2	0.43	0.19
GAL18	...-...	15.6	2.6	21.0	4.2	0.38	0.22
GAL19	2290-...	15.2	2.7	19.5	4.2	0.41	0.25
GAL20	2810-...	15.0	3.0	19.6	4.2	0.77	0.17

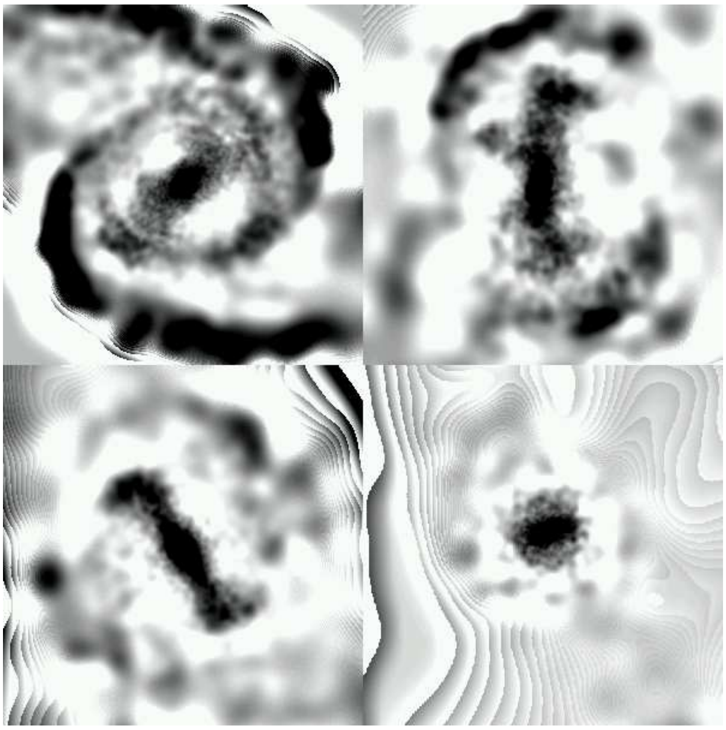

Figure 2.4: Morphological transformation (face-on projection) of a disk galaxy into a dwarf elliptical (GAL8 of Table 1). From the top left to the bottom right: at $t = 0.5$ Gyrs from the beginning of the simulation, and $t = 1.4, 2.4, 4.8$ Gyrs. The box size is $\sim$ 20 kpc. The step like structures visible at the edges of the galaxies are due to features present in the low density regions of the original smoothed stellar surface density maps, which are amplified by the unsharp masking.

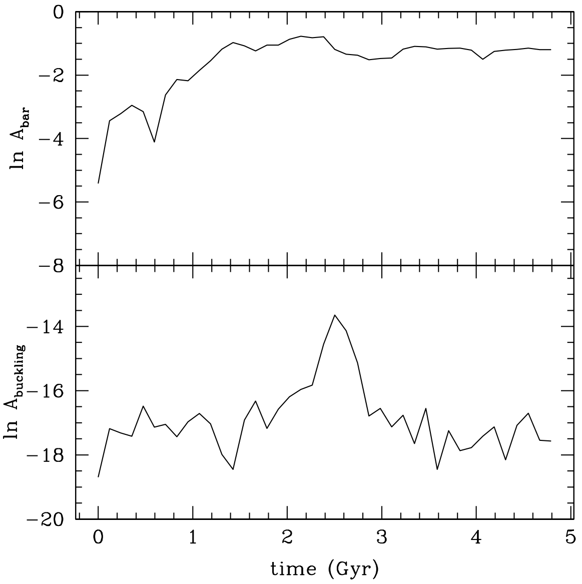

Figure 2.5: Evolution of a representative galaxy (GAL7 of Table 1). Top panel: strength of the bar. Bottom: buckling amplitude. The bar forms at $t = 1.1$ Gyrs and strongly buckles at $t = 2.4$ Gyrs.

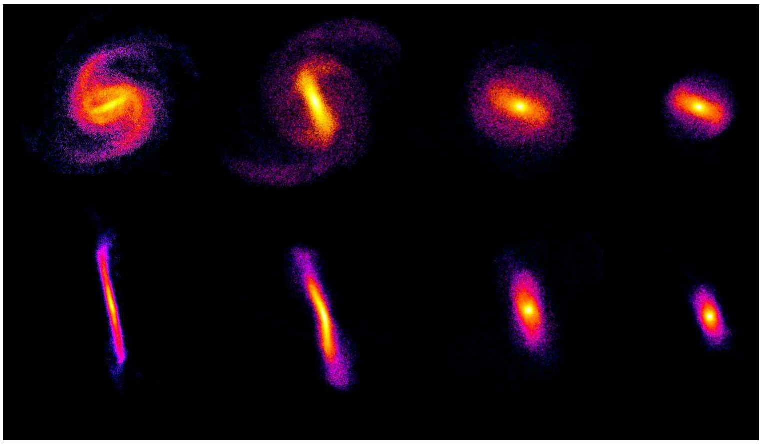

Figure 2.6: Evolution of the stellar surface density of GAL7 from $t = 1.4$ Gyrs to $t = 0$ Gyrs. The color scale is logarithmic. The top panels represent the face on projection while the corresponding edge on projection is shown on the bottom. The buckling phase, which has a peak at $t = 2.4$ Gyrs, does not destroy the bar but makes the central vertical structure of the galaxy thicker

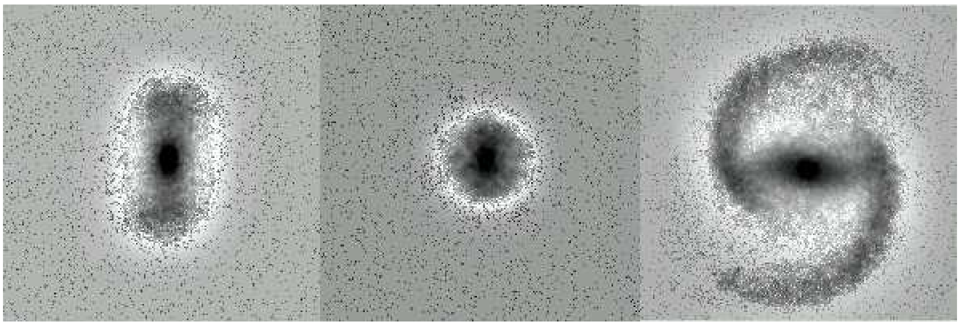

Figure 2.7: Three different final states of the harassed galaxies (unsharp nosified images). From the left to the right: bar-like galaxy (GAL7 of Table 2.1), spherical spheroid (GAL6) and spiral galaxy (GAL3). The addition of noises often hides ring structures surrounding the central bar, which is the case of the first remnant on the left. In order to point out the characteristic structure of the remnants we used two physical scales: the two images on the left have a box side of ~ 12 kpc while the box size of the spiral galaxy on the right is ~ 30 kpc.

are easily stripped while the remaining material forms a ring structure around the bar. The bar+ring phase is quite stable and is apparent in the final state of several of the remnant galaxies. Often the ring is not directly visible in the simulation output, but is clearly seen after applying the unsharp masking. When gravitational heating due to tidal interactions removes the remaining spiral and ring features, only a naked bar remains. The bar usually undergoes a strong buckling instability and as a result the central part of the galaxy becomes more spherical. The buckled bar is subjected to further tidal heating and loses mass from its edges, becoming rounder the more encounters it suffers and the longer it evolves near to the cluster centre. Fig. 2.5 illustrates the evolution of bar and buckling instabilities for a representative galaxy which is orbiting close to the center of the cluster at $z = 0$. A_{bar} and $A_{buckling}$ are the bar and buckling amplitudes, defined respectively as the Fourier decomposition of the phase of particles in the xy plane and of their vertical positions (Sparke & Sellwood, 1987)

$$A_{\rm bar} = \frac{1}{N}\left|\sum_j e^{2i\phi_j}\right| \tag{2.5}$$

and

$$A_{\rm buckling} = \frac{1}{N}\left|\sum_j z_j e^{2i\phi_j}\right|. \tag{2.6}$$

Fig. 2.6 shows a face and edge on projection of the same galaxy during the buckling phase where the bar appeared at $z = 0.3$.

Depending on the orbit and on the number of close encounters that the galaxy suffers, the morphological transformation of the stellar component can be complete and produce a pure spheroidal system, or can lead to the formation of a more elongated structure, which still retains disk and bar features (Fig. 2.7). For a few galaxies orbiting closest to the cluster center the tidal effects from the cluster potential become dominant and the evolution is very rapid. Fig. 8 shows the tidal tails generated by a strong impulsive encounter. The stripped mass is a significative fraction of the total stellar mass and the

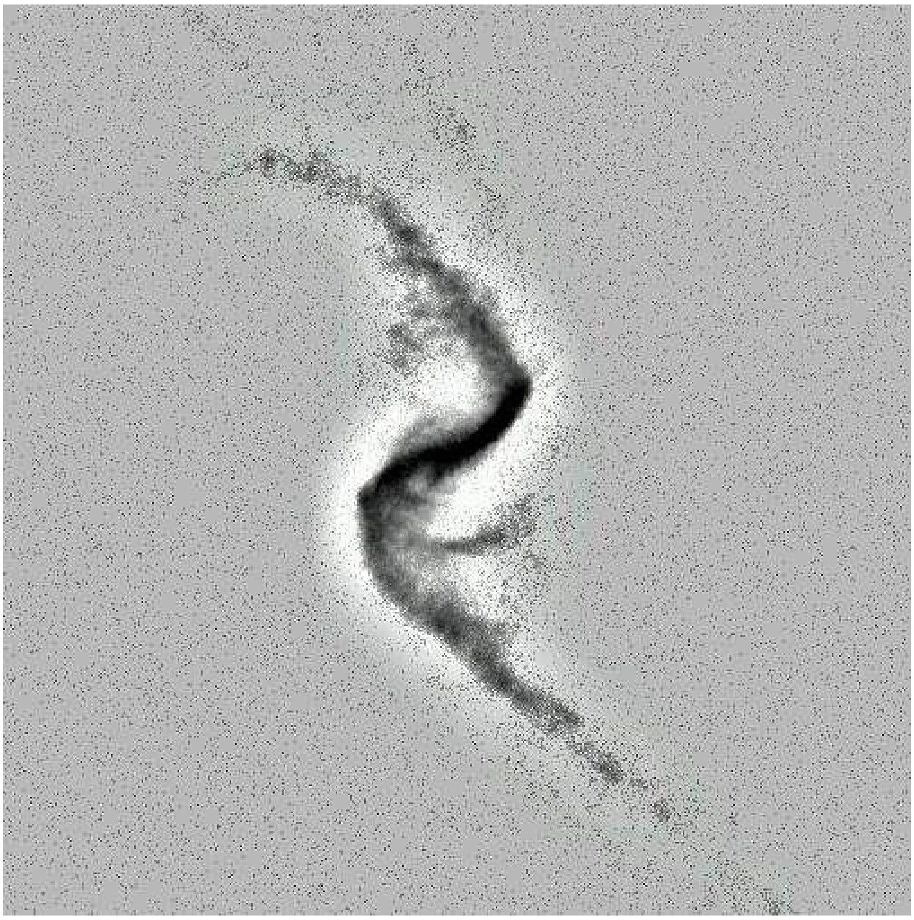

Figure 2.8: Tidal tails of GAL6 (Table 2.1) generated during a pericentric passage (unsharp noisified image). These smooth features are visible only for a short time (typically about 0.2-0.3 Gyr) since they are heated and evaporated by continued encounters with cluster substructures.

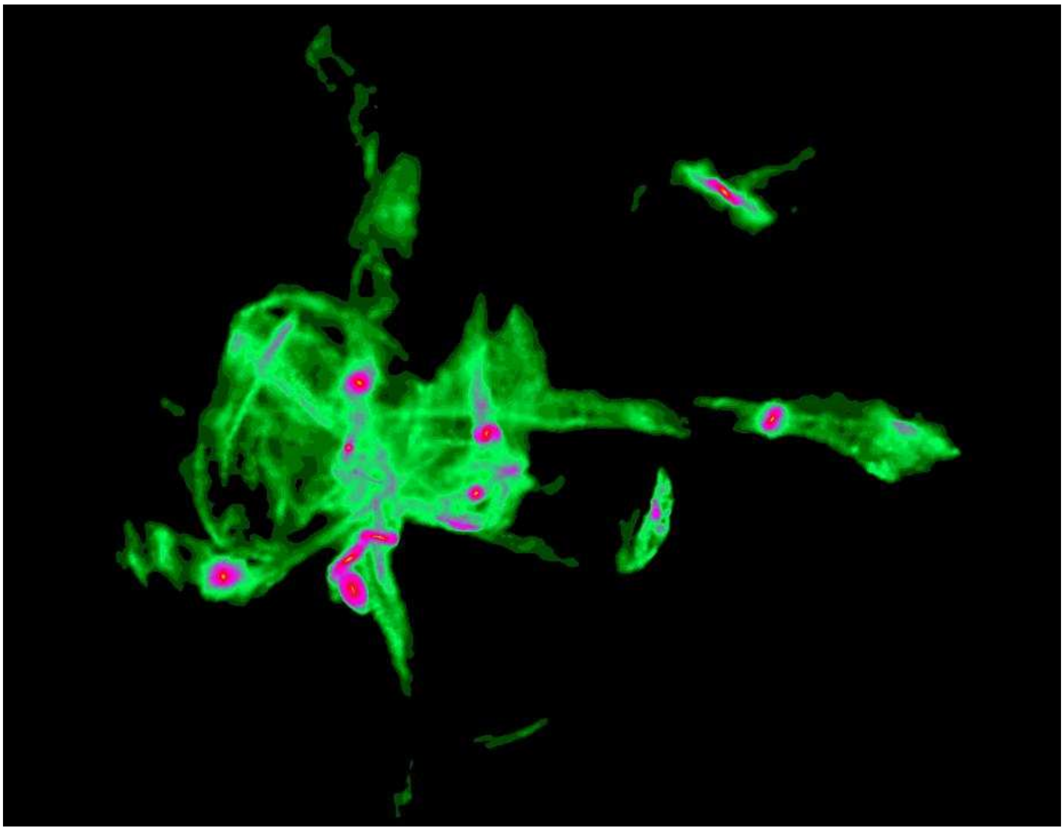

Figure 2.9: Intracluster light produced by tidal processes. The color contrast is chosen in such a way as to point out the low density regions (light green, corresponding to a surface brightness $\mu \lesssim 30$ mag arcsec^{-2}) and the traces of stellar streams.

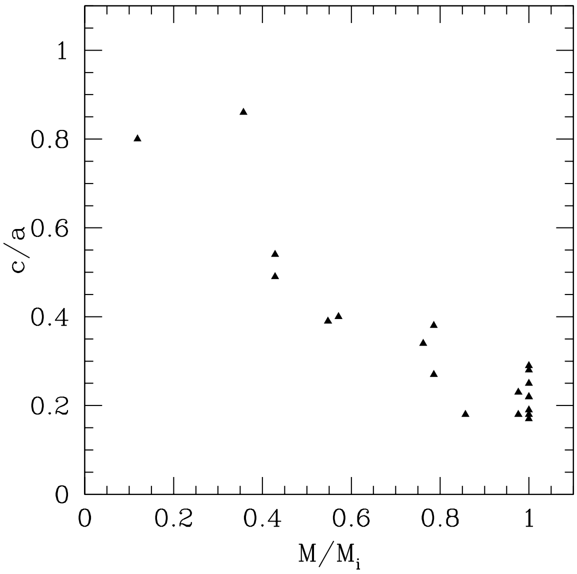

Figure 2.10: Final flattening of the remnants plotted versus the fraction of stellar mass within the tidal radius at $z = 0$.

surface density in the tails is comparable with that of the outer disk. We do not expect that these kind of structures will be easily observable in clusters, since their life time is quit short (≈ 0.2 Gyrs) due to numerous encounters with other substructures which heat and dissipate the stripped material. Stripped stars tend to create a diffuse distribution around the remnants (see Fig. 2.4) and in regions close to the center it is almost impossible to distinguish well defined stellar streams, even from the debris of a small fraction of the true number of dwarf galaxies in clusters.

Table 2.1 summarises the main properties of the remnant galaxies. The initial model has a virial radius of 85 kpc and the effective radius of the stellar distribution is 2.5 kpc, defined as the radius containing half of the light of the galaxy. While almost all the galaxies lose more than two thirds of the dark matter halo, galaxies located at outskirts of the cluster do not experience a significative amount of star loss, even if their stellar structure can be perturbed producing open spiral patterns and asymmetric features (last frame on the right of Fig. 2.7). For these remnants the reduction of the effective three–dimensional radius r_e is related to the formation of a bar that increases the central stellar density. On the other hand, galaxies orbiting closer to the cluster center lose up to 90% of their stellar mass and the decrease of r_e corresponds to a real decrease in the size of the stellar component. In a few cases the galaxy loses much more dark matter than stars and becomes baryon dominated in the central region. This is due to the fact that the orbits of the dark matter particles in the halo are more eccentric than those of the star particles and therefore reach the tidal radius more easily. Table 2.1 shows that the loss of stellar mass is not a simple function of the mean orbital radius or apocentric/pericentric distance from the cluster center, confirming the importance of harassment. According to Knebe et al. (2005) tidal interactions with other satellites account for about 30% of the total mass loss experienced by a satellite halo. The last two columns of Table 2.1 give the mean axial ratios within $2r_e$. There is a clear correlation between the c/a ratio (the flattening of the stellar component) and the final stellar mass. As shown in Fig. 10, massive stellar remnants have smaller c/a values and retain more of their initial disk nature, while galaxies that have lost most of their stars tend to be more spheroidal. The final state is always quite prolate, with the exception of GAL6 and GAL8 (the first two points in the upper left corner of Fig. 2.4) which are close to spherical. In the case of the less perturbed galaxies this is due to the fact that the radius $2r_e$ defines an area roughly corresponding to the bar region, while most of the other galaxies retain part of the radial anisotropy that originated during the bar phase (Mayer et al., 2001b). Fig. 2.11 illustrates the morphological and kinematic evolution of the stellar component of four representative galaxies of our sample. Each set of three panels represents the galaxy distance from the center cluster (top), the axial ratios (middle) and the ratio between the maximum rotational velocity v_{max} and the mean velocity dispersion $\bar{\sigma}$ (bottom) as a function of time. All these quantities are measured within 2 r_e. Both shapes and kinematics are not characterised by a smooth evolution, but present peaks and drops not necessarily connected to pericentric passages and indicative of tidal effects associated with close encounters with substructures. The initial steep decrease in the b/a ratio is instead related to the formation of the bar in the inner regions of the disk.

2.5 Photometric analysis

In order to compare the results of our simulations with observations and in particular with Barazza, Binggeli & Jerjen (2003), we selected the remnants within the virial radius at $z = 0$ (first 13 galaxies of Table 2.1) and projected them along a random line of sight.

The isodensity contours of the projected disks were fitted with ellipses using the MIDAS task FIT/ELL3. The ellipses centers, ellipticity and position angle were considered as free parameters of the fitting procedure. The isophotal contours of a representative galaxy (GAL9) are shown in Fig 2.5. Ellipticity and position angle profiles are plotted in Fig. 2.13, where the independent variable is the equivalent radius $r_p = \sqrt{a_p b_p}$, and a_p and b_p are the major and minor axis of the projected remnant. Even though there is not a well defined trend in the ellipticity profiles, galaxies which preserve a bar component are generally characterised by large ellipticities in the central 2-3 kpc and by a drop in the outer regions. Often the inner 0.5 kpc exhibits a very low ellipticity corresponding to a small nuclear component produced by buckling instabilities, whereas the external drop is more likely due to disk heating. Rounder systems have a wider range of profiles, with eccentricities that may even increase with radius, as in the case of GAL1.

The next step of this analysis consists in calculating the surface brightness profiles of the projected remnants. In order to derive a luminosity we need to assign a mass to light ratio. We expect that the ISM would be rapidly stripped by ram pressure effects such that star formation is truncated shortly after the galaxies enter the cluster environment. In this case, roughly 8 Gyrs from the beginning of the simulation, the stellar mass to light ratio will have increased by about a factor of $1.5 - 2$ (Mayer et al., 2001b). For this reason we used a B-band $M/L \sim 6$ for the final remnants. The cumulative light profiles were determined by integrating the light of each galaxy in elliptical apertures with increasing equivalent radius (MIDAS task INTEGRATE/ELLIPS) and fixed center, ellipticity and position angle. For these parameters we adopted their mean values within a

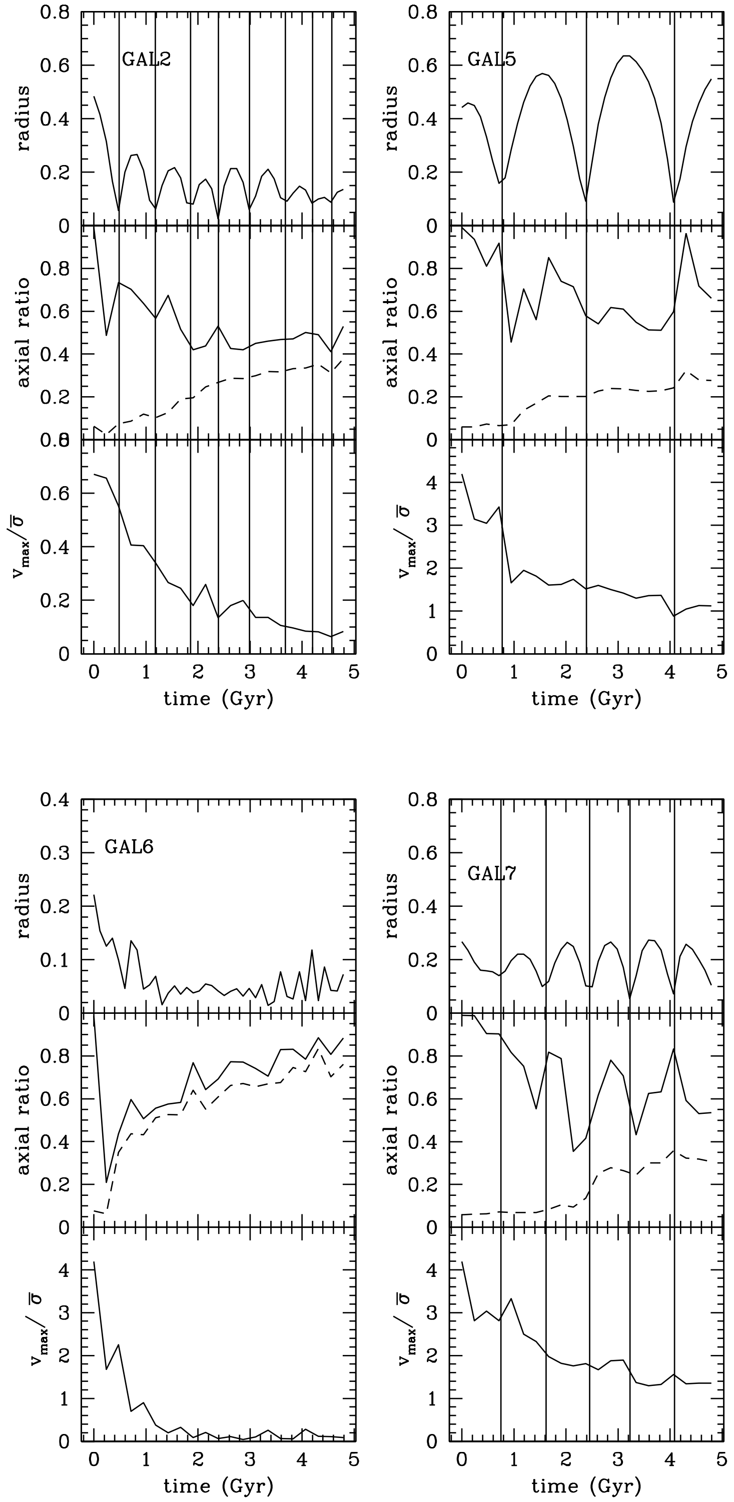

Figure 2.11: Each set of three vertical panels represents the morphological and kinematic evolution of a galaxy from Table 2.1: orbital radius (top panel), axial ratio (center) and anisotropy parameter (bottom). In the middle panel the solid line represents the intermediate/major axis ratio b/a while the dashed line is the short/major axis ratio c/a. The vertical solid lines indicate the pericentric passages. Note that the vertical scale of the top panel in GAL6 differs from the others.

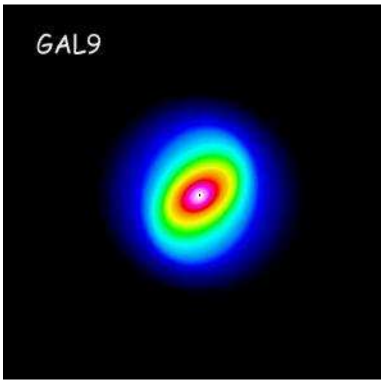

Figure 2.12: Elliptical contours of GAL9. A strong isophotal twist is evident in the outer region (see also Fig. 2.13).

Table 2.2: Effective radii (in kpc) of the projected remnants calculated using the integrated light curves. In most of the cases they do not deviate considerably from the values obtained for the three dimensional galaxies. A significative exception is GAL13, a disk system viewed almost edge on.

Remnant	r_{ep}	Remnant	r_{ep}
GAL1	1.9	GAL8	1.0
GAL2	1.7	GAL9	1.4
GAL3	2.7	GAL10	1.5
GAL4	2.4	GAL11	1.9
GAL5	2.3	GAL12	2.0
GAL6	0.6	GAL13	1.1
GAL7	1.5		

radius corresponding to half of the disk size, in order to avoid uncertainties in the isophote fitting procedure due to the low density external regions. In Table 2.2 we list the effective radius of each projected galaxy defined by r_{ep} which is the radius at which the cumulative light profile reaches half of the value that it has at the isophotal level of 28 mag arcsec^{-2} (upper B-band magnitude limit in Barazza et al. 2003).

The surface brightness profiles, obtained by differentiating the cumulative light curve with respect to the equivalent radius r_p (Barazza et al. 2003), are plotted in Fig. 2.13. The oscillation in the profiles of GAL3 and GAL12 reveals the presence of spiral arms viewed almost face on (Fig. 2.15), which enhance the local stellar density and produce abrupt changes in the position angle and eccentricity profiles.

The intensity profiles between 0.1 kpc (softening length for the stellar component) and the isophotal level of 27 mag arcsec^{-2} were fitted with a Sérsic profile

$$I(r) = I_0 e^{(-r/r_0)^{(1/n)}}, \tag{2.7}$$

where I_0 (central intensity), r_0 (scale length) and n (shape parameter) are the free parameters of the fit. For $n = 1$ the Sérsic model corresponds to an exponential law, while

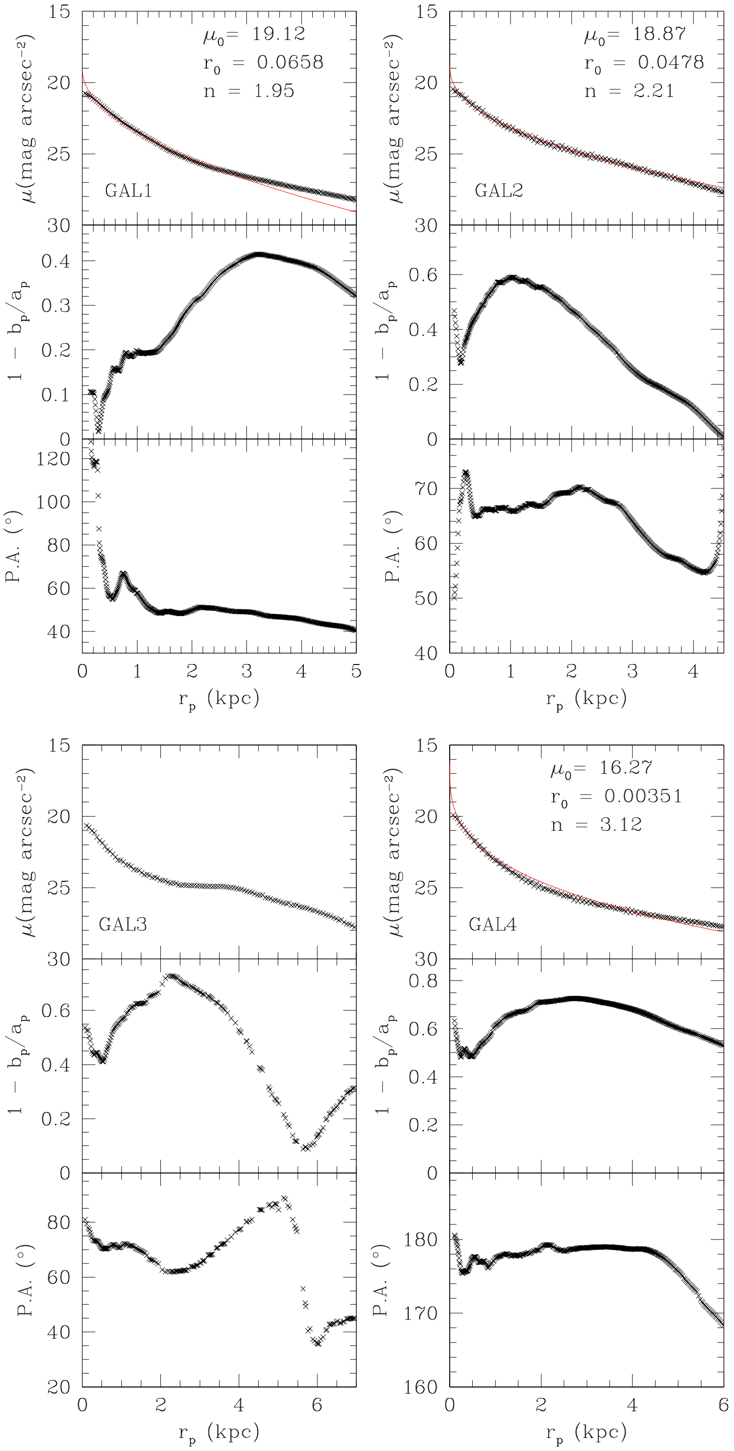

Figure 2.13: Each set of three vertical panels represents the photometric characteristics of a galaxy from Table 1: B-band surface brightness (top panel), ellipticity (center) and position angle profile (bottom). The coordinate r_p is the equivalent radius $r_p = \sqrt{a_p b_p}$, where a_p and b_p are the major and minor axis of the projected remnant. The Sérsic model is superimposed on the surface brightness profile (red solid line) and the corresponding best fit parameters are given in the top right of the panel. The central surface brightness μ_0 is expressed in mag arcsec^{-2}, r_0 is in kpc and the shape parameter n is a pure number which represents the deviation of the profile from an exponential law.

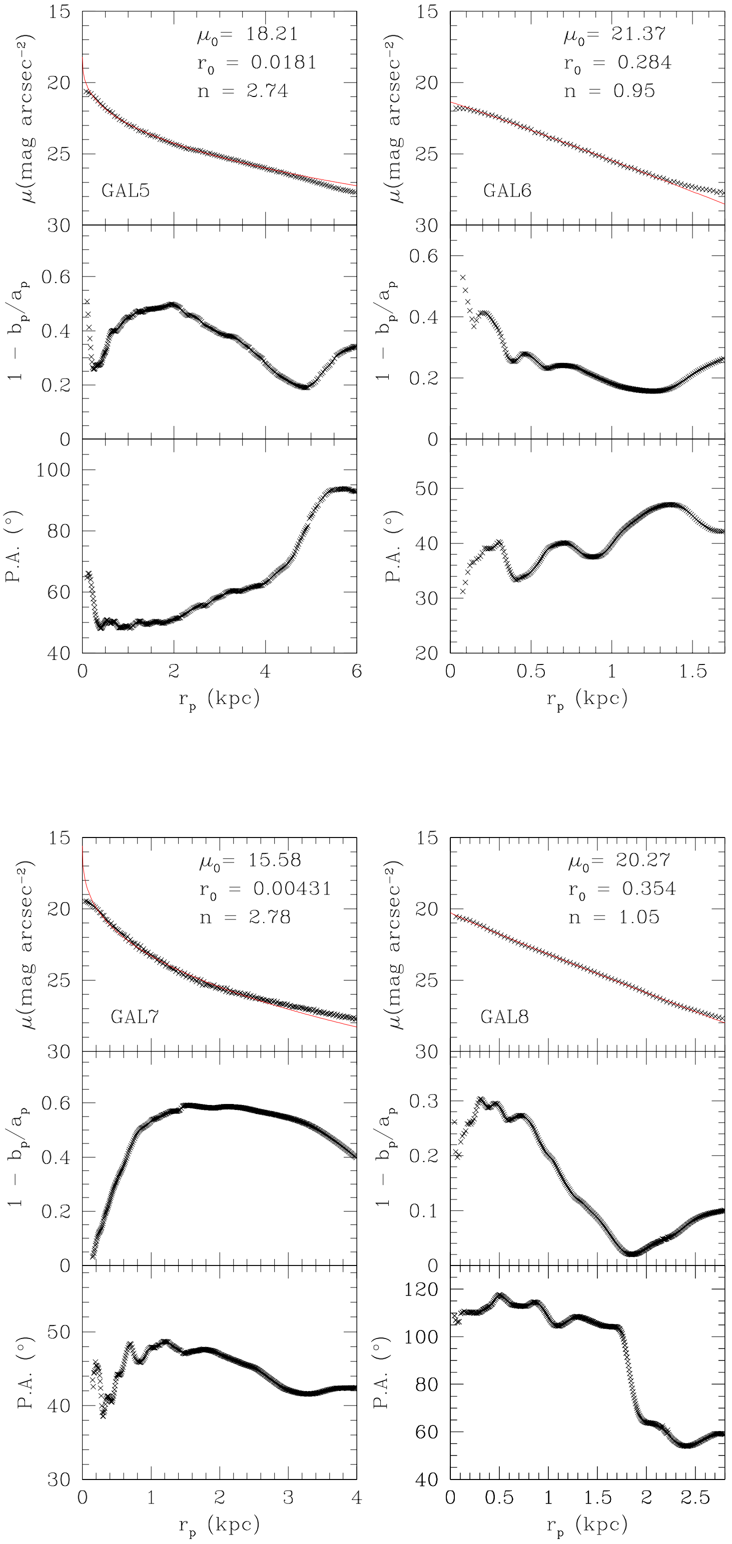

Figure 2.13: continued.

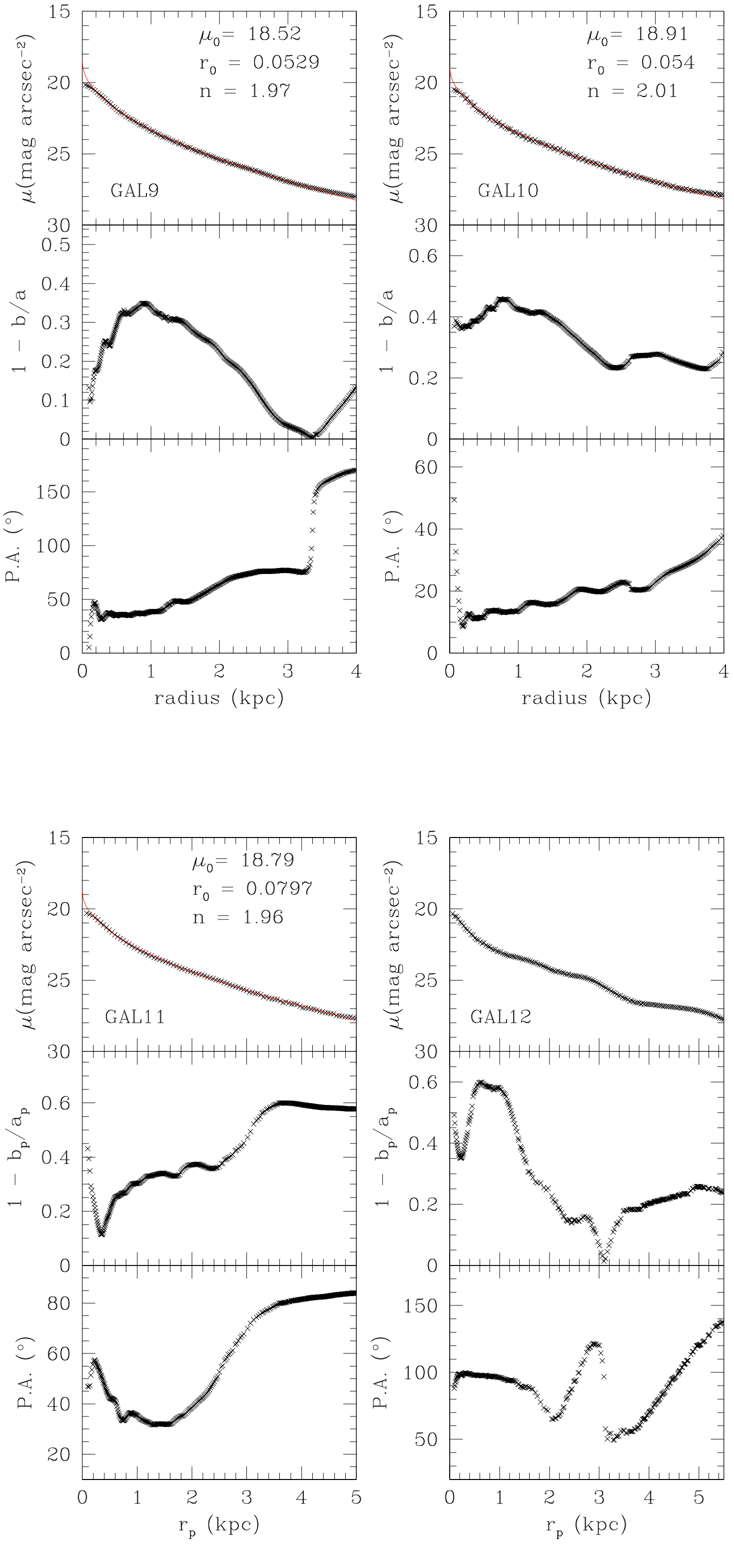

Figure 2.13: continued.

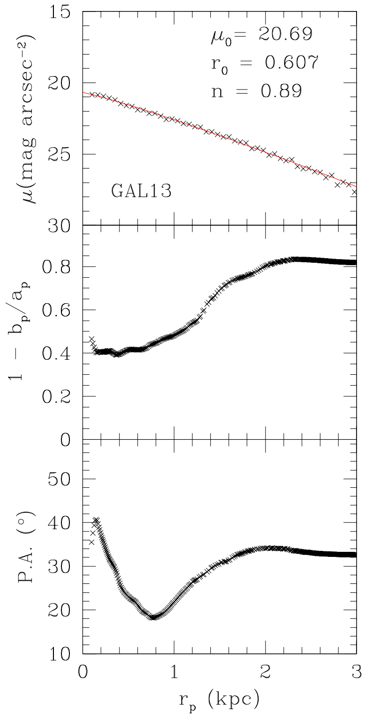

Figure 2.13: continued.

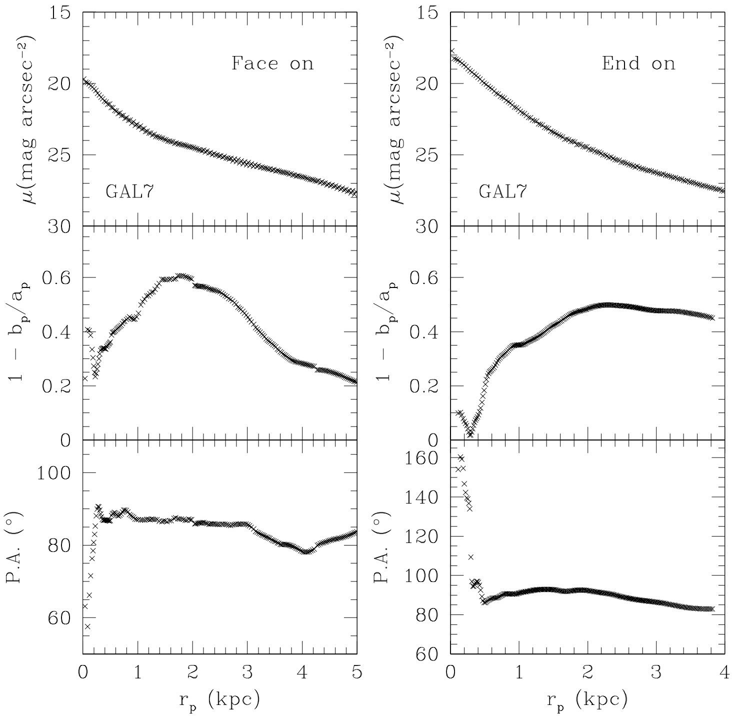

Figure 2.14: B-band surface brightness, ellipticity and position angle profiles of the face on and end on projections of GAL7.

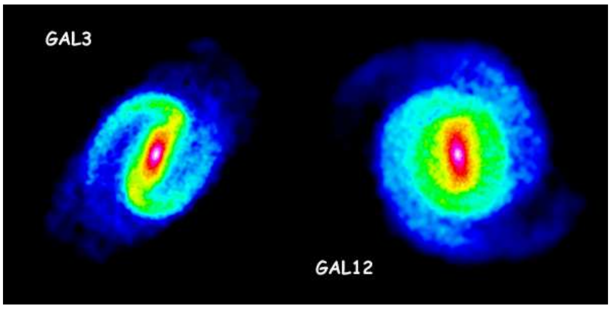

Figure 2.15: Surface density distribution of the two remnants presenting a nearly face on spiral pattern. The physical size of both the images is $\sim$ 12 kpc.

a shape parameter $n = 4$ is indicative of a de Vaucouleurs profile. Converting intensities to surface brightnesses, Equation **??** becomes

$$\mu(r) = \mu_0 + 1.086(r/r_0)^{(1/n)}, \tag{2.8}$$

where μ_0 is the surface brightness corresponding to I_0.

The fitting curves and parameters of those galaxies that it was possible to fit with a Sérsic model are indicated in Fig. 2.13. The range of surface brightness parameters agrees quite well with the observations of dwarf galaxies in Virgo. The central surface brightness of our remnants is on average slightly higher than the values observed in B-band by Barazza et al. 2003, who fitted Sérsic profiles over similar radial intervals, the scale lengths obtained from the fitting procedure are comparable with their results. Also note that the quoted central surface brightness values are Sercic fits extrapolated to $r = 0$. The actual values at our resolution limit are somewhat fainter (Table 2.3). Galaxies with the smallest values of the shape parameter n are not well fitted by a Sérsic profile in the central part. This is the case of GAL4 – apparently a pure spheroidal system with high ellipticity, in reality characterised by a disk component seen edge on – and of GAL7, which is still an asymmetric bar like system with a large central nuclear component with small ellipticity values. For GAL7 we also show surface brightness profiles, ellipticity and position angles for the face on and the end on projections (Fig. 2.14). The smallest central ellipticity is associated with the end on projection, where the bar is viewed along the major axis. Only the less massive remnants GAL6 and GAL8 have surface brightness profiles approaching to exponentials ($n \sim 1$).

2.6 Kinematics

We attempt to measure the kinematics of the remnants in a similar way as previous authors measuring dwarf galaxies in the Virgo cluster. We measure the kinematics of the 13 projected galaxies analyzed in § 2.5 using a 0.3 x 12 kpc slit, which corresponds, at the distance of Virgo (15.3 Mpc, Freedman et al. (2001)) to 3” x 40”. This radial range is comparable with the slit length adopted by van Zee et al. 2004 and allows us to observe in most of the galaxies the turnover of the rotation curve, while the thickness of the slit was set to the softening length of 0.1 kpc. The slit was positioned along the major axis of the projected remnant centered on the galaxy and star particles within the slit area were

Table 2.3: Parameters of the Sérsic fit: central surface brightness (in mag arcsec^{-2}), surface brightness at the softening radius, scale length (kpc) and shape parameter.

Galaxy	μ_0	μ (0.1 kpc)	r_0	n
GAL1	19.12	20.50	0.0658	1.953
GAL2	18.87	20.38	0.0478	2.208
GAL4	16.27	19.44	0.00351	3.115
GAL5	18.21	20.24	0.0181	2.740
GAl6	21.37	21.79	0.284	0.949
GAL7	15.58	18.95	0.00431	2.778
GAL8	20.27	20.60	0.354	1.054
GAL9	18.52	20.02	0.0529	1.972
GAL10	18.91	20.39	0.054	2.008
GAL11	18.79	20.01	0.0797	1.957
GAL13	20.69	20.83	0.607	0.885

binned into a grid. For each grid interval with more than 15 particles – excluding thus the most weakly bound particles at the edges of the system – we calculated the mean particle velocity (relative to the center of mass of the galaxy) and velocity dispersion along the line of sight. For the two smallest remnants GAL6 and GAL8 we increased the number of bins in order to obtain more precise velocity curves. The resulting kinematic profiles are indicated in Fig. 2.16, where for each galaxy the line of sight velocity (left panels) and velocity dispersion (right panels) are plotted as a function of the radial distance along the major axis. In most of the cases the remnants lose a large fraction of rotation velocity, but only for one galaxy (GAL6) we do not observe any significative rotation along the major axis. GAL8 shows a well defined symmetric rotation pattern although its peak velocities is only $\sim$ 7 km s^{-1}. GAL6 and GAL8 do not show evidences for structures or disk features and are spheroidal systems with a c/a ratio larger (Table 2.1) than the other remnants and surface brightness profiles well fitted by exponential laws. Moreover, they are quite small ($M_s \leq 1.5 \times 10^9 M_\odot$) baryonic dominated galaxies presently orbiting at $\approx$ 100 kpc from the cluster center.

Is the lack of rotation observed in GAL6 due to a projection effect, i.e. we are looking at the face on projection of a rotating system, or is it physically significative? Fig. 2.17 illustrates the kinematic profiles of GAL6 and GAL8 for different inclinations of the remnant: from the top to the bottom $i = 0°$, which corresponds to a face-on projection, $i = 45°$ and $i = 90°$ (edge-on). The last panel on the bottom represents an end-on galaxy, with inclination $i = 90°$ and the three dimensional major axis aligned with the line of sight. GAL6 shows traces of rotation only for $i = 0$, with a maximum rotational velocity $v_{max} = 3.7\,\mathrm{km\,s^{-1}}$, while the other projections have not well defined rotation curves and values of $v_{max} \lesssim 2.7\,\mathrm{km\,s^{-1}}$. In the case of non-rotating galaxies we estimated an upper limit for v_{max} by differentiating the average velocities on each side of the major axis and dividing by two (Geha, Guhathakurta, & van der Marel, 2002). In the calculation of v_{max} for $i = 0°$ and $i = 90°$ we excluded points with velocity dispersion larger than $80\,\mathrm{km\,s^{-1}}$, representing stars close to the tidal radius of the remnant, which projected motion respect to the center of mass is due to stripping processes and not to rotation. On the other hand

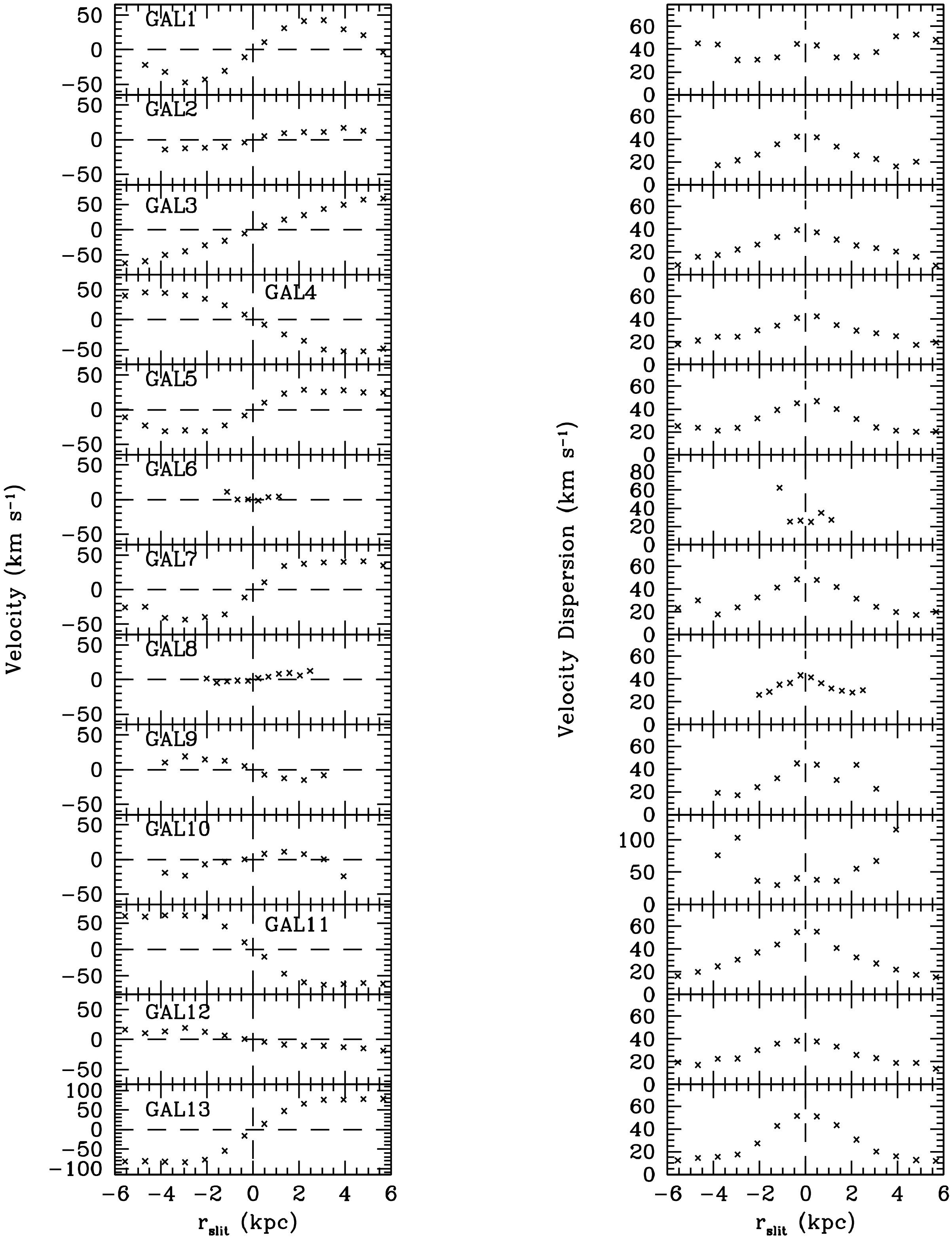

Figure 2.16: Projected kinematic profiles of the remnants within the cluster virial radius at $z = 0$. The line of sight velocity (left panels) and the velocity dispersion (right panels) are plotted as a function of the radial distance along the major axis.

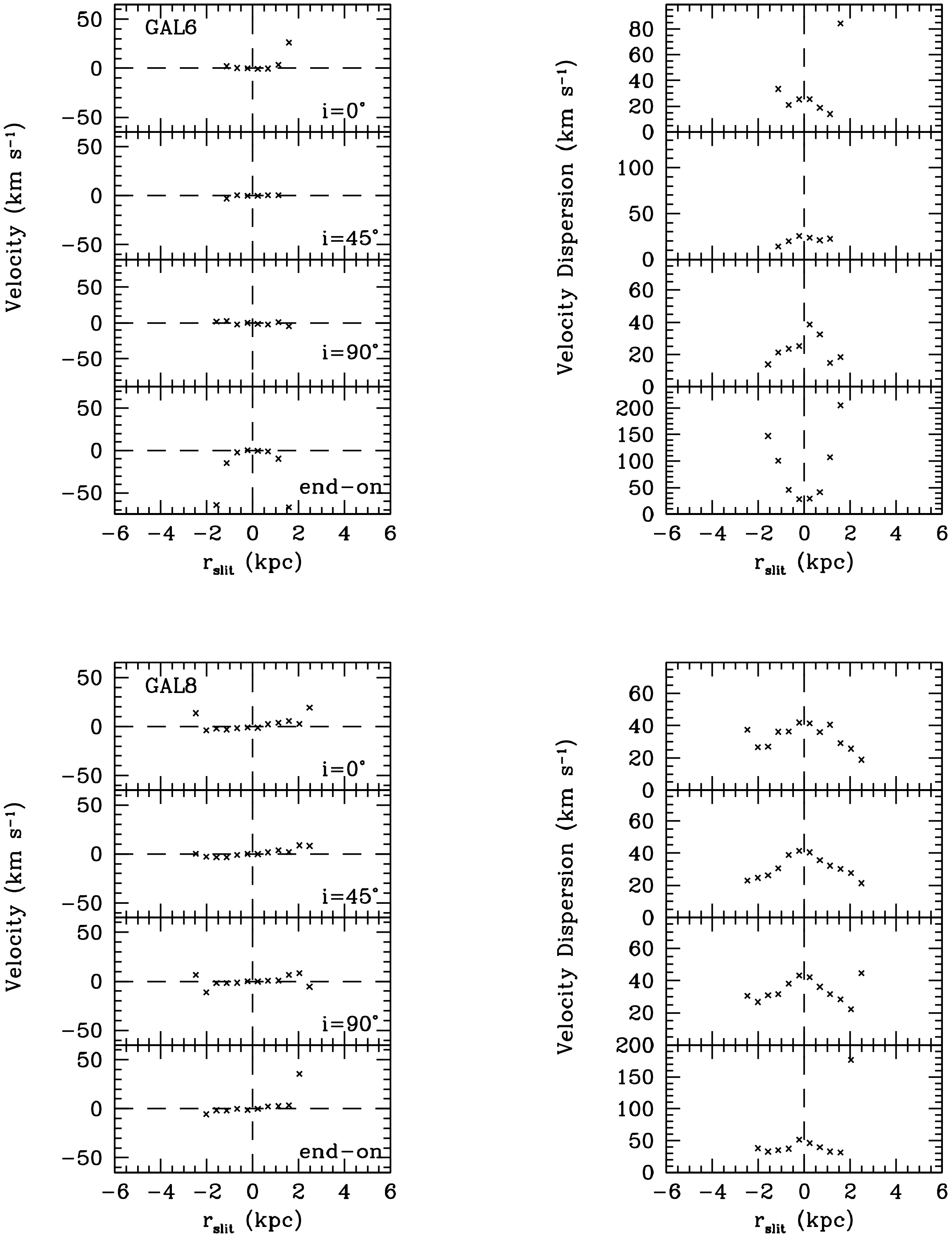

Figure 2.17: Projected kinematic profiles of GAL6 and GAL8 for $i = 0°$ (face-on orientation), $i = 45°$, $i = 90°$ (edge-on) and $i = 90°$ with the three dimensional major axis aligned with the line of sight (end-on projection). The line of sight velocity (left panels) and the velocity dispersion (right panels) are plotted as a function of the radial distance along the projected major axis.

GAL8 has always a well defined rotation pattern and there is not a preferential direction with zero rotation. Among the other galaxies characterised by low rotation velocities (see Fig. 2.16), GAL2, GAL9 and GAL10 are more massive systems if compared with the two spheroids GAL6 and GAL8, but have still high c/a values, while the low line of sight velocity of GAL12 is not related to a morphological transformation but is simply due to the fact that it is a spiral galaxy viewed face on (Fig. 2.15).

On the basis of this limited sample we expect non-rotating and slowly rotating dwarfs to have internal and environmental properties substantially different from the rotating ones. In particular the former seem to be the product of a violent morphological transformation accelerated by the proximity of the cluster center. This result is apparently in contradiction with Geha et al. 2003 who finds no relationship between the amount of rotation and the morphology or the orbital properties of the galaxies in their sample.

From Fig. 2.16 it appears evident that although the galaxies lose significant amounts of mass, the velocity dispersion can rise up to $50\,\mathrm{km\,s^{-1}}$ in the central 1-2 kpc. This is due to the bar formation and the transformation of circular to more radial orbits. The velocity dispersion profiles are typically decreasing at larger radii but they rise again in those galaxies for which the slit semi-length approaches or exceeds the tidal radius.

As the ratio between rotational velocity and velocity dispersion decreases, the galaxy loses rotational support and the flattening becomes dominated by anisotropic pressure. The degree of rotational support can be expressed in terms of the anisotropy parameter $(v/\sigma)^*$ (Binney, 1978), defined as

$$(v/\sigma)^* = \frac{v/\bar{\sigma}}{\sqrt{\epsilon(1-\epsilon)}}, \tag{2.9}$$

where v is the rotational velocity, $\bar{\sigma}$ and ϵ the mean projected velocity dispersion and ellipticity. The theoretical prediction for a rotationally flattened spheroidal is given by $(v/\sigma)^* \sim 1$ (Binney & Tremaine, 1987) and is represented in Fig. 2.18 by a continuous solid line. Galaxies well below this curve have significant velocity anisotropy.

In order to compare our results with observations, we plotted in Fig. 2.18 the ratio of the maximum rotational velocity v_{max} to the mean velocity dispersion $\bar{\sigma}$ within a radius of 6 kpc versus the mean isophotal ellipticity calculated in the same radial range. In the same plot we show the observational results for most of the dwarf galaxies in Virgo with published kinematics. We also plot the data for dwarf galaxies in the Fornax cluster by De Rijcke et al. (2003). Some of the galaxies in Fig. 2.18 (VCC 543, VCC 917, VCC 1036, VCC 1261 and VCC 1308) were observed by both Geha et al. 2003 and van Zee et. al 2003, using the Keck II and Palomar telescope. The observations of van Zee et. al 2003, which cover a larger radial extent due to the aperture size, gives to significantly higher values of v_{max} respect Geha et al. 2003. This appears to be due to the fact that the smaller slit used by the latter authors only samples the inner rising part of the rotation curve and does not include the maximum value. For example VCC 917 and VCC 1308, classified as non-rotating galaxies (both with $v_{max} = 0.4$ km s^{-1}) by Geha et al. 2003, have $v_{max} > 10$ km s^{-1} according to van Zee et al. 2003, while the rotation curves of the slowly rotating dwarfs VCC 543 and VCC 1036 ($v_{max} = 13$ and 14 km s^{-1} in Geha et al. 2003) peak beyond 15" with $v_{max} > 40$ km s^{-1}. Most of the simulated remnants have a similar range of ellipticities and $v_{max}/\bar{\sigma}$ as the observed dwarfs, even if it is clear that we have some difficulties in reproducing galaxies with a degree of rotational support close to zero. On the other hand it is possible that the low $v_{max}/\bar{\sigma}$ ratio of some galaxies is due to the small

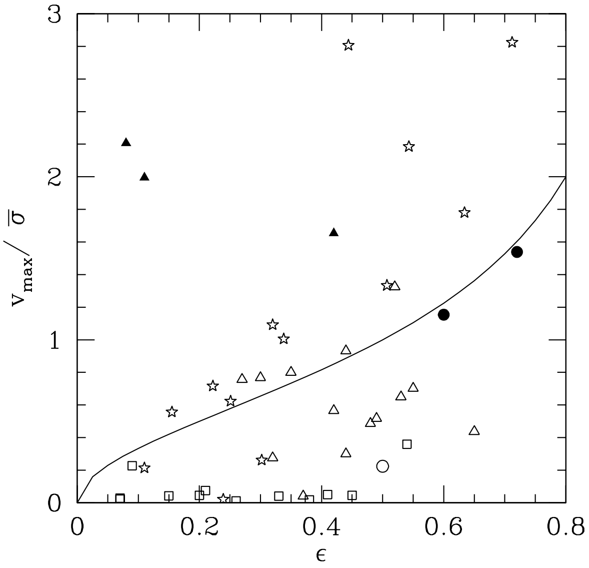

Figure 2.18: The ratio of the maximum rotational velocity v_{max} to the mean velocity dispersion $\bar{\sigma}$ plotted versus the mean isophotal ellipticity. Stars represent the simulated sample, while open triangles, open squares, filled triangles and open circles show observational data from van Zee, Skillman & Haynes (2004), Geha, Guhathakurta & van der Marel (2003), Pedraz et al. (2002) and Bender & Nieto (1990), respectively. For galaxies observed both by Geha, Guhathakurta & van der Marel (2003) and van Zee, Skillman & Haynes (2004) we assumed the values of v_{max} and $\bar{\sigma}$ provided by the latter work. Filled circles indicate data relative to dwarf spheroidals in the Fornax cluster from De Rijcke et al. (2003). The solid line represents the theoretical prediction for a galaxy flattened by rotation from Binney & Tremaine (1987).

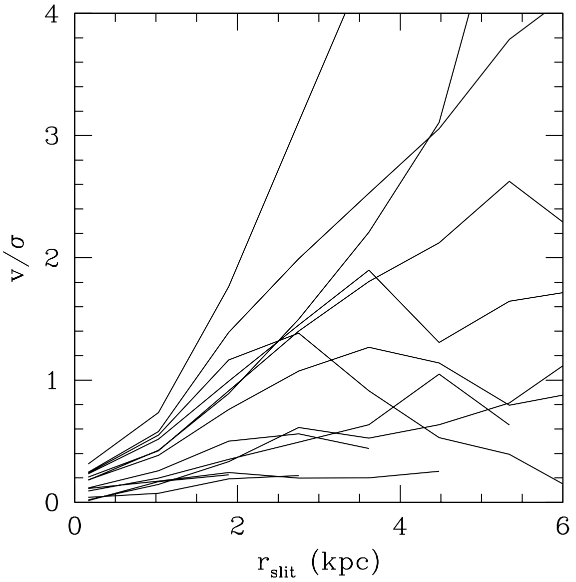

Figure 2.19: v/σ ratio as a function of the radial distance along the major axis for the 13 projected remnants of Fig. 2.16.

radial range covered by the observations. In order to understand how much the slit length influences the results, in Fig. 2.19 we plotted the v/σ ratio of the projected remnants as a function of the radial distance along the slit. In most of the cases v/σ increases with radius (with the remarkable exception of GAL1 whose rotational support drops beyond $r = 2.5$ kpc). Using a 4 kpc slit we would find 10 galaxies below $v_{max}/\bar{\sigma} = 1$, 6 of which with $v_{max}/\bar{\sigma} < 1$ and 3 well below $v_{max}/\bar{\sigma} = 0.1$, which is the upper limit assumed by Geha et al. 2003 for non-rotating dwarfs. Increasing the slit length up to 8 kpc, the number of galaxies with a low degree of rotational support is still quit high (7 galaxies with $v_{max}/\bar{\sigma} < 1$ and 4 with $v_{max}/\bar{\sigma} < 0.5$), but only GAL6 has still a $v_{max}/\bar{\sigma} \sim 0$, as in the case of the adopted slit length of 12 kpc.

2.7 Conclusions

We follow the evolution of late type disk galaxies as they evolve within a hierarchically forming galaxy cluster using N-body simulations. We use a single galaxy model to explore the effects of cluster-centric position and orbit. Our resolution is such that we can compare with Keck and Palomar kinematics and VLT imaging data. We find that:

(i) The cluster environment can be responsible for triggering bar and buckling instabilities.

(ii) Tidal shocks with dark matter substructures and the mean cluster potential are both important at driving the evolution from disks to spheroidal structures. However, galaxies within the inner 100 kpc suffer the most complete transformation.

(iii) None of the disks are completely destroyed therefore we do not expect to create UCD galaxies by progenitor disks with cuspy dark halos.

(iv) More tidal heating leads to more mass loss which leads to rounder galaxies.

(v) The kinematics (v/σ) of the stellar remnants is similar to observations of Virgo and Fornax dE/dSph galaxies. Only the most severely disrupted galaxies which lose most of their stellar mass become completely pressure supported. Most of the remnants retain a significant amount of rotational motion.

(vi) Unsharp masked images of the galaxies show similar hidden bar and spiral features as some cluster galaxies. These gradually dissapear as the galaxies suffer more heating. Our results could be rescaled in time and mass to make statements about possible disk progenitors entering group or even galactic environments. The next step is to self-consistently follow the evolution of galaxies as they form and evolve in different environments.

2.8 Acknowledgements

We would like to thank Jürg Diemand for providing the cosmological cluster simulation. We are grateful to Alister Graham, Andrea Macciò, Fabio Barazza, Marla Geha, Frank van den Bosch and Stelios Kazantzidis for useful discussions. The numerical simulations were performed on the Zbox (http:/www.theorie.physik.unizh.ch/stadel) supercomputer at the University of Zürich. CM and RP are supported by the Swiss National Science Foundation. VPD is supported by a Brooks Fellowship at the University of Washington.

Chapter 3

The gravitational and hydrodynamical interaction between the Large Magellanic Cloud and the Galaxy [1]

3.1 Abstract

We use high resolution N-Body/SPH simulations to study the hydrodynamical and gravitational interaction between the Large Magellanic Cloud and the Milky Way. We model the dark and hot extended halo components as well as the stellar/gaseous disks of the two galaxies. Both galaxies are embedded in extended cuspy ΛCDM dark matter halos. We follow the previous four Gyrs of the LMC's orbit such that it ends up with the correct location and orientation on the sky. Tidal forces elongate the LMC's disk, forcing a bar and creating a strong warp and diffuse stellar halo, although very few stars become unbound. The stellar halo may account for some of the microlensing events observed towards the LMC. Ram-pressure from a low density ionised halo is then sufficient to remove $1.4 \times 10^8 M_\odot$ of gas from the LMC's disk forming a great circle trailing stream around the Galaxy. The column density of stripped gas falls by two orders of magnitude 100 degrees from LMC and the radial velocity along the trailing Stream agrees well with the observations. The LMC does not induce any response in the Milky Way disk. On the contrary, the tides raised by the Milky Way determine the truncation of the satellite at about 11 kpc. After several Gyrs of interaction the gas disk of the LMC is smaller than the stellar disk due to ram pressure and its size and morphology compares well with the observational data.

3.2 Introduction

The Milky Way - Magellanic Cloud system provides us with a close up view of a complex ongoing galaxy interaction. Gravitational and hydrodynamical forces from the Galaxy are reshaping its largest satellites and creating the spectacular Magellanic Stream (hereafter

---

[1] This chapter (Mastropietro et al. 2005, astro-ph 0412312) is going to be published in MNRAS.

MS). The MS is a trailing filament of neutral hydrogen that originates from the Magellanic Clouds and stretches for over ~ 100 degrees in the Southern Sky and is the most prominent signature of an interaction between the Clouds and the Milky Way. The combined interaction between these three galaxies must strongly influence the morphological evolution of the Clouds, as well as their internal kinematics and star formation history. A resonant interaction between the Galaxy and the LMC could even be sufficient to excite the warp observed in the Galactic disk (Weinberg, 1995, 1998).

Several models have been proposed in order to study the nature of this interaction and to isolate the main mechanism responsible for the formation of the Stream. These models have become increasingly refined over the years. The first gravitational tidal models took into account just the binary interaction between the LMC and MW (Lin & Lynden-Bell, 1977; Murai & Fujimoto, 1980), but later models included one or more close interactions between the Clouds themselves during the last orbit (Gardiner, Sawa, & Fujimoto, 1994; Lin, Jones, & Klemola, 1995; Gardiner & Noguchi, 1996; Yoshizawa & Noguchi, 2003; Connors et al., 2004; Bekki & Chiba, 2005).

The strongest argument which has been used to argue for a tidal origin for the MS is provided by the discovery of neutral hydrogen in front of the LMC (Putman et al., 1998), although the amount of material in this feature is just a fraction of the mass of the MS (Putman et al., 2003a). However there are some characteristics of the Stream that tidal models cannot explain. In particular they fail in reproducing the gradual decrease of the HI column density and the lack of a stellar tidal feature (Mathewson et al., 1979; Brueck & Hawkins, 1983; Guhathakurta & Reitzel, 1998). Stars are expected to be stripped by gravitational forces along with the gas, although Weinberg (2000) suggests that the stellar debris would have a different distribution respect to the gaseous Stream and form a diffuse envelope around the LMC. Traces of the tidal interaction could be associated with the the giant stars observed by Majewski et al. (1999) around the Magellanic Clouds.

A hydrodynamical interaction has also been invoked to explain the Stream. Mathewson et al. (1987) proposed that gas is swept away from the intra-cloud region and decelerated by random collisions with high velocity clouds (HVC). This model requires unrealistic densities for the HVCs in the MW halo in order to justify the high number of encounters that should generate the Stream and does not explain the column density gradient. Continuous stripping models (Meurer, Bicknell & Gingold, 1985; Sofue, 1994; Moore & Davis, 1994) propose a scenario in which gas is stripped by ram-pressure forces from the outer regions of the Clouds through an interaction with a distribution of hot gas in the halo or an extended ionised disk. A satellite moving with a relative velocity v respect to this external medium of density ρ experiences a pressure $P = \rho v^2$ which can be sufficient to remove part of the neutral gas from the disk. Together with the difficulties in creating a continuous leading arm – although the stripped material decelerated by ram pressure forces could fall on smaller orbits and lead the Clouds (Sofue, 1994; Moore & Davis, 1994) – ram pressure models are thought not to be able to reproduce the large amount of gas observed in the Stream ($\sim 2 \times 10^8 M_\odot$ according to Putman et al. 2003a).

The presence of an extended hot halo surrounding the MW and in hydrostatic equilibrium within the dark matter potential is expected by current models of hierarchical structure formation (Maller & Bullock, 2004). This gaseous halo, left over from the initial collapse, would be continuously fuelled by accretion of satellite galaxies over time. Recent observational results have confirmed the existence of a distribution of hot ($T \sim 10^6$ K) gas well beyond the Galactic disk, with a radius larger than 70 kpc in order to explain some ionisation features discovered in the MS (Sembach et al, 2003; Putman et al., 2003b). Constraints from dynamical and thermal arguments fix the density of the gaseous halo in a range between 10^{-5} and $10^{-4}\mathrm{cm}^{-3}$ at the LMC distance from the Galactic center. The Clouds are therefore subjected along their orbits to the ram pressure generated by a tenuous distribution of hot gas and the Magellanic System itself seems to be the result of a complex interaction that involves both hydrodynamical and tidal processes.

The aim of this work is to study for the first time the simultaneous effect of gravitational and hydrodynamical forces acting on the LMC as it moves within the Galactic halo, using fully self consistent galaxy models. In particular we are interested in the formation and evolution of the Magellanic Stream and in the dynamical changes in the internal structure of the LMC due to the interaction with the MW. We ignore the SMC owing to its small mass ($\sim 10\%$ of the LMC), neglecting the possibility of a close encounter between the two Clouds and the consequence of additional loss of mass. This approximation would lead to an underestimation of the amount of HI in the Stream.

This chapter is structured as follows. In Section 4.1 we present the main characteristics of the galaxy models that we use. The results of test wind tube simulations are discussed in Section 3.4. In Section 3.5 we analyse the results of the interacting runs regarding the Stream and the LMC disk.

3.3 Galaxy Models

The initial conditions of the simulations are constructed using the technique described by Hernquist (1993). Both the Milky Way and the Large Magellanic Cloud are multi-component systems with a stellar and gaseous disk embedded in a spherical dark matter halo. The density profile of the NFW (Navarro, Frenk & White, 1997) halo is adiabatically contracted due to baryonic cooling (Springel & White, 1999). Stars and cold ($T = 10^4$K) gas in the disk follow the same exponential surface density profile of the form

$$\Sigma(R) = \frac{M_d}{2\pi {R_d}^2} \exp\left(-R/R_d\right), \tag{3.1}$$

where M_d and R_d are the disk mass and radial scale length (in cylindrical coordinates) respectively, while the thin vertical structure is characterised by the scale height $z_d \sim \frac{1}{5}R_d$:

$$\rho_d(R,z) = \frac{\Sigma(R)}{2z_d} \operatorname{sech}^2\left(z/z_d\right). \tag{3.2}$$

The MW model comprises of two further components: a stellar bulge and an extended hot gaseous halo. The bulge has a spherical Hernquist (Hernquist, 1990) profile:

$$\rho_b(r) = \frac{M_b}{2\pi} \frac{r_b}{r(r_b + r)^3} \tag{3.3}$$

where M_b is the bulge mass and r_b its scale length.

Although the presence of an extended corona of hot gas seems to be the most likely explanation for the detection of OVI and OVII absorption lines associated with HI structures (MS, some HVCs, Outer Spiral Arm, Complex A, Complex C, according to Sembach

Table 3.1: Galaxy models: for each component mass (in units of $10^{10}M_\odot$) and scale radius (kpc) are indicated. R_d and r_b are defined as in Eq. (1) and (3), while the scale radius of the NFW profile which characterizes both the DM and the hot halo is $r_s = r_{vir}/c$, where r_{vir} and c are the halo virial radius and concentration respectively. The last three columns refer to high resolution runs and report number of particles, mass particle (in units of $10^5M_\odot$) and softening length (kpc).

MW	Mass	Scale radius	N	m	ϵ
Bulge	0.73	0.70	10^4	7.3	0.1
Gaseous disk	0.46	3.53	10^5	0.46	0.1
Stellar disk	4.10	3.53	10^5	4.10	0.1
DM halo	104.0	18.2	10^6	10.4	0.5
Hot halo	1.0	18.2	5×10^5	0.20	0.5
LMC	Mass	Scale radius	N	m	ϵ
Gaseous disk	0.11	1.66	10^5	0.11	0.1
Stellar disk	0.11	1.66	5×10^4	0.22	0.1
DM halo	2.38	6.02	6×10^5	10.4	0.5

et al. 2003), its density structure is still uncertain, particularly at large distances from the Galactic center. These ionization features suggest a mean density of the gaseus halo (n_h) within 80 kpc of $\sim 10^{-4} - 10^{-5}\text{cm}^{-3}$ (Sembach, 2003). Stanimirovic (2002) provides similar values for the density at 45 kpc ($n_h \lesssim 3 \times 10^{-4}\text{cm}^{-3}$) in order to explain the confinement mechanism of the MS clouds through pressure support from the hot halo. Another constraint comes from the detection of Hα emission along the MS which cannot be explained solely by photoionisation from the Galactic disk (Putman et al., 2003b) and could be induced by the interaction with a relative dense ($n_h > 10^{-4}\text{cm}^{-3}$ at 50 kpc) gaseous environment (Weiner & Williams, 1996). With a density higher than 10^{-4}cm^{-3} Quilis & Moore (2001) are able to reproduce, using hydrodynamical simulations, the head-tail structure and the compression fronts associated with HVCs, in the case of either pure gas clouds or gas embedded within a dark matter halo. A significantly lower value for the upper limit of the halo density ($n_h < 10^{-5}\text{cm}^{-3}$) is found by Murali (2000) by requiring the survival of the cloud MS IV for 500 Myrs against evaporation. However we emphasise the fact that the evaporation time strongly depends on the temperature of the gaseous halo (Cowie & McKee, 1977) and a choice of $T \sim 10^6$K, three times lower than the value used by Murali, increases by almost a factor fifteen the lifetime of MS IV, making the survival of the cloud possible at a density of even 10^{-4}cm^{-3}. At larger distances from the Galactic center constraints on the halo density are poor, although Blitz & Robishaw (2000) derive a value of $2.5 \times 10^{-5}\text{cm}^{-3}$ at a distance of 200 kpc by applying ram pressure stripping to dwarf spheroidal galaxies within the Galactic halo.

We model the hot halo with a spherical distribution of gas which traces the dark matter profile within the virial radius and is in hydrostatical equilibrium inside the Galactic potential. Assuming an isotropic model, the halo temperature at a given radius r is determined by the cumulative mass distribution $M(r)$ of the dark, stellar and gaseous

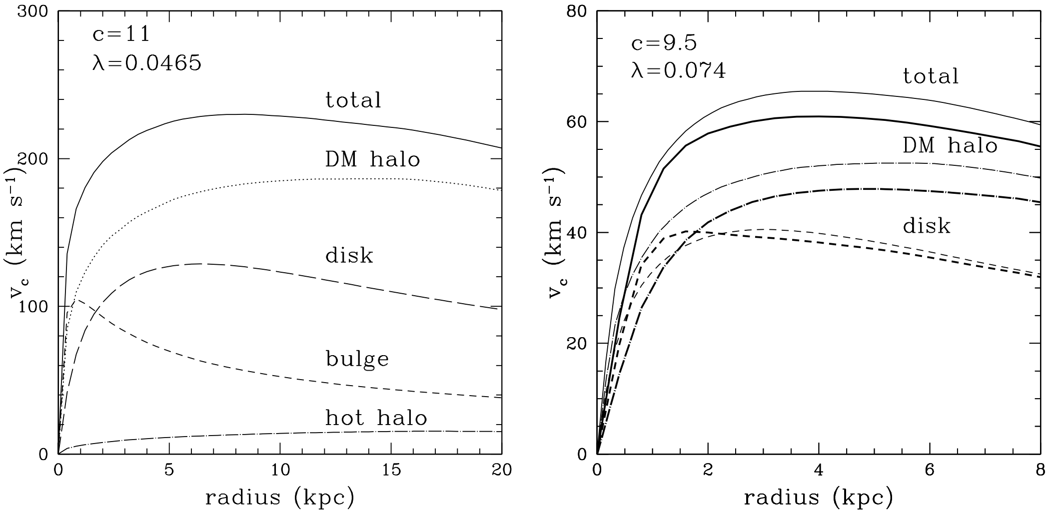

Figure 3.1: Left panel: MW rotation curves. On the top left spin and concentration parameter are indicated. Right panel: LMC rotation curves. Thin lines represent the rotation curves of the initial model, while thick lines refer to the satellite evolved for 4 Gyrs in interaction with the MW. On the top left spin and concentration parameter of the initial model are indicated.

components of the MW beyond r and by the density profile $\rho_h(r)$ of the hot gas:

$$T(r) = \frac{m_p}{k_B}\frac{1}{\rho_h(r)}\int_r^\infty \rho_h(r)\frac{GM(r)}{r^2}\,dr\,, \tag{3.4}$$

where m_p is the proton mass, G and k_B are the gravitational and Boltzmann constants. The halo gas is completely ionised at a mean temperature of 10^6 K. We normalise the density profile using a hot halo mass of $M_h = 10^{10}M_\odot$, which corresponds to a mean density of $2 \times 10^{-5}\text{cm}^{-3}$ within 150 kpc and 8.5×10^{-5} at 50 kpc. With the assumption that the gas traces the dark matter we overestimate by a factor of three the ionised gas density near the disk, however this is not important for the current study.

Our Milky Way model (Table 3.1) is similar to model A_1 of Klypin, Zhao, & Somerville (2002) and was selected in order to match observational data at the present time. About 4 Gyrs ago, when we start studying the evolution of the LMC, the dark and gaseus halo masses of the Galaxy may have been quite different. However we expect that most of the dark halo mass was probably already in place at $z = 2 - 3$, since galaxy formation simulations suggest that large disk galaxies had the last major merger quite early in order for a large enough disk to form by $z = 0$. The evolution of the gaseus halo is poorly known but work in progress suggests its density could have been higher than the value adopted in this paper.

The masses and the scale lengths adopted for the LMC model (Table 3.1) reproduce quite well the peak of the rotation curves inferred by Kim et al. (1998) and van der Marel et al. (2002). As we will see in Section 3.5, the interaction with the MW does not affect significantly the stellar and dark matter mass in the inner 8–9 kpc of the LMC (which is the interval covered by HI and carbon star data) and consequently the global rotation curve within this radial range. In order to take in account the loss of cold gas from the disk of the satellite, we assumed an initial amount of gas in the disk which is $\sim 2-3$ times larger than HI observed to be associated with the LMC (Kim et al., 1998; Putman et al., 2003a; Brüns et al., 2005).

Fig. 3.1 shows the rotation curves of the different components of the two galaxies. The concentration c and the spin parameter λ (Mo, Mao, & White, 1998) are indicated at the top left of each panel. The concentration is defined as $c = r_{vir}/r_s$, where r_{vir} and r_s are the virial and the scale radius of the NFW halo, whereas the spin parameter relates the angular momentum J and the total energy E of an halo with a virial mass M_{vir} through the relation $\lambda = J|E|^{1/2}G^{-1}M_{vir}^{-5/2}$. The disk of the satellite galaxy has, within the scale radius, a central mass surface density of $\sim 70\,\mathrm{M_{\odot}pc^{-2}}$, which corresponds to a B-band surface brightness of $\sim 23\,\mathrm{mag\ arcsec^{-2}}$, if we adopt a mass to light ratio of two.

The thickness of the disks is set such that Toomre's (Toomre, 1964) stability criterion is satisfied, which requires, for a stellar disk

$$Q_{star}(r) = \frac{\sigma_R k}{3.36 G \Sigma_s} > 1, \tag{3.5}$$

where σ_R is the radial velocity dispersion, k is the local epicyclic frequency and Σ_s the stellar surface density. For a gaseous disk Equation 3.5 becomes:

$$Q_{gas}(r) = \frac{v_s k}{\pi G \Sigma_g} > 1, \tag{3.6}$$

where v_s is the sound velocity and Σ_g the surface density of the gas.

All the simulations we now discuss were carried out using GASOLINE, a parallel tree-code with multi-stepping (Wadsley, Stadel & Quinn, 2004). The high resolution runs have 2.46×10^6 particles, of which 3.5×10^5 are used for the disks and 5×10^5 for the hot halo of the MW (Table 1). The gravitational spline softening is set equal to 0.5 kpc for the dark and gaseous halos, and to 0.1 kpc for stars and gas in the disk and bulge components. All the runs are adiabatic, except those treated in Section 4.2.1, which include radiative cooling.

3.4 Test simulations

The mass resolution of the simulations strongly influences the ram pressure process. In particular, if the particles of the hot external medium are too massive, they do not flow smoothly on to the disk, but produce scattering and numerical holes, artificially increasing the stripping effeciency. In order to study these effects, we perform several test simulations in which we place the model LMC galaxy within a "wind tunnel" and vary the mass of the hot halo particles for a fixed resolution of the LMC disk.

The first set (H1, H2 and H3) of runs simulates the passage of the satellite at the perigalacticon, which is the point along the orbit where ram pressure is most efficient due to the high values of ρ_h and v. The volume of the wind tunnel is an oblong of base equal to the diameter of the LMC and height $h = vt$, where v is the velocity of the satellite at the perigalacticon ($250\,\mathrm{km\,s^{-1}}$) and t is set $\sim$ 2 Gyrs ($\sim$ the inferred orbital time for the LMC). We represent the hot gas as a flux of particles moving with a velocity v along the z axis, parallel to the angular momentum of the disk. The hot particles have an initial random distribution, a temperature $T = 10^6$K and a number density $n_h = 8 \times 10^{-5}\mathrm{cm}^{-3}$. The box has periodic boundary conditions in order to restore the flow of hot gas that leaves the oblong. The disk particles have the same mass m_{disk} as in the high resolution interacting runs (see Table 2), while the mass ratio with the particles in the oblong m_h/m_{disk} is 1:10, 1:2 and 1:1. Gas is removed from the disk if the ram pressure produced by the hot halo of the MW is greater than the restoring force per unit area provided by the disk of the satellite. The condition for ram pressure stripping is expressed by (Gunn & Gott, 1972)

$$\rho_h v^2 > 2\pi G \Sigma(R) \Sigma_g(R), \tag{3.7}$$

where v is the velocity of the galaxy with respect to the surrounding medium, ρ_h is the density of the hot halo of the MW and $\Sigma_g(r)$ is the cold gas surface density at the radius R. Σ represents the gravitational surface mass density of the disk. The minimum radius given by Equation 3.7 is the final stripping radius R_{str} beyond which the ISM can be removed from the galaxy. The halo component does not contribute to the restoring force initially, since in the case of a face on impact any force associated to a spherical potential is perpendicular to the wind pressure. As the gas is stripped out from the disk in the z direction, the disk gravity decreases while the projection of the radial halo gravity force in the z direction rises (Schulz & Struck, 2001). This effect is particularly important in the case of low ram pressure regimes as the ones we are interested in here. The condition for stripping expressed in Equation 3.7 implicitly assumes instantaneous stripping from the disk and discrete ram pressure stripping events such that the loss of mass approaches an asymptotic limit. If instead ram pressure is a continuous process with time scales comparable with the orbital time of the satellite, the stripping radius calculated analytically underestimates the physical size of the gaseous disk. Such a continuous ram pressure stripping occurs here not because of turbulent or viscous stripping but because the gas at the edge of the disk heats up responding to the compression exerted by the outer medium and can therefore become unbound by increasing its energy despite the ram pressure wind being constant. Timescales of both Kelvin-Helmoltz instabilities and artificial viscous forces are close to 10 Gyr because of, respectively, stabilisation due to the cuspy halo potential of the LMC and the high mass resolution employed, and are therefore negligible over the timescales explored here.

Equation 3.7 expresses the condition for stripping in the midplane of the disk, where the restoring force from the disk is maximum. In order to provide a numerical definition for the stripping radius we can assume that particles which lie in the midplane of the disk are those included in a thin (with a thickness ~ 2 softening lengths) layer parallel to the disk plane. We estimate R_{str} as the radius which contains 99% of the LMC gas particles in the midplane of the disk. We excluded thus a small fraction of particles located at large radial distance from the center of the galaxy due to heating by the external hot medium. The mass of gas that remains in the disk can be computed summing the disk particles inside a cylinder of radius R_{str} and thickness 1 kpc. The mass of gas bound to the satellite at a time t is instead not directly related to R_{str}, but is determined by the potential of the dark halo. We calculate it balancing kinetic, thermal and potential energy in concentric spherical shells centered on the LMC, defining the gas tidal radius r_g as the radius of the most distant bound shell.

The mass of cold gas stripped from the LMC's disk M_{str} decreases as we decrease the mass of the halo particles: in H1 M_{str} is ~ 1.6 times larger than in H3 (Table 3.4). Mass

Table 3.2: LMC wind tunnel simulations. For each run the density ρ_h (in units of $10^{-5}\mathrm{cm}^{-3}$) of the hot medium and the velocity v ($\mathrm{km\,s}^{-1}$) of the satellite are indicated. The resolution of each model is expressed in terms of the mass ratio m_h/m_{disk} between halo and disk particles. N is the number of hot particles, while the last four columns give the ram pressure stripping radius R_{str} (in kpc) and the mass stripped from the disk M_{str} (in units of $10^8 M_\odot$), the gas tidal radius r_g (kpc) and the mass of gas unbound to the galaxy M_{unb} ($10^8 M_\odot$). In the case of edge on galaxies the stripping radius R_{str} is the average value between the two sides of the disk. All the values are calculated at $t = 2$ Gyrs.

Run	Model	ρ_g	v	m_h/m_{disk}	N	R_{str}	M_{str}	r_g	M_{unb}
H1	face on	8	250	10	0.37	4.0	4.11	6.7	2.84
H2	face on	8	250	2	1.86	5.3	2.76	7.5	1.32
H3	face on	8	250	1	3.2	5.5	2.52	7.8	1.0
L1	face on	3.5	175	2	0.54	6.6	2.09	8.3	0.58
L2	face on	3.5	175	1	1.07	6.8	2.02	8.5	0.44
L3	face on	3.5	175	0.5	2.14	6.9	1.99	8.6	0.42
E1	edge on	8	250	2	1.86	5.5	2.74	7.7	1.32
E2	edge on	3.5	175	2	1.07	6.2	2.32	8.1	0.79

resolution also determinates the shape of the front edge and influences the morphology of the gaseous disk. Fig. 3.2 shows the gas density in the disk after 2 Gyrs for the H1, H2 and H3 runs. Numerical effects in the low resolution run are quite evident: the massive hot particles produce particle – particle interactions with gas in the galaxy, creating holes and discontinuities along the front edge of the disk. The spiral pattern is partially destroyed and the disk looses its symmetry. Scattering reduces the stripping radius by a factor of 1.4 and produces a sharp truncation, while the effect of pure ram pressure is much more gradual, since halo particles stream around the disk. Finally, the removed gas forms an asymmetric and turbulent tail. The high resolution H3 run appears very symmetric with a flat and uniform edge and a regular stream, which flows around the disk and creates a low density region behind (Fig. 3.3). As previously noticed by several authors (Quilis, Moore & Bower, 2000; Quilis & Moore, 2001; Schulz & Struck, 2001), a bow shock forms in front of the disk, increasing the local ICM temperature from 10^6 to 2.5×10^6 degrees. The intermediate run H2 is similar to H1, although the gas tail is more pronounced and the amount of stripped gas is less than 10% larger. The resolution (mass ratio of 1:2) of the H2 run is to be a good compromise between the necessity of solving the gas dynamics and the number of particles to use in a full production simulation.

The runs L1, L2 and L3 have a gas density ($\rho_h = 3.5 \times 10^{-5}\mathrm{cm}^{-3}$) and satellite velocity (175 $\mathrm{km\,s}^{-1}$) similar to our final LMC's orbit with apocentric distance $\sim$ 50 kpc and apo/peri ratio $\sim 2.5 : 1$ (see section 4.1). Reducing the ram pressure by a factor of three decreases the stripped mass by $\sim$ 20%, while the amount of unbound gas is almost 60% smaller. This indicates that a lower ram pressure is still efficient in stripping gas from the disk, but part of the removed material is now bound to the satellite by the dark halo gravity. The simulations were computed using three different resolutions, with m_h/h_{disk}

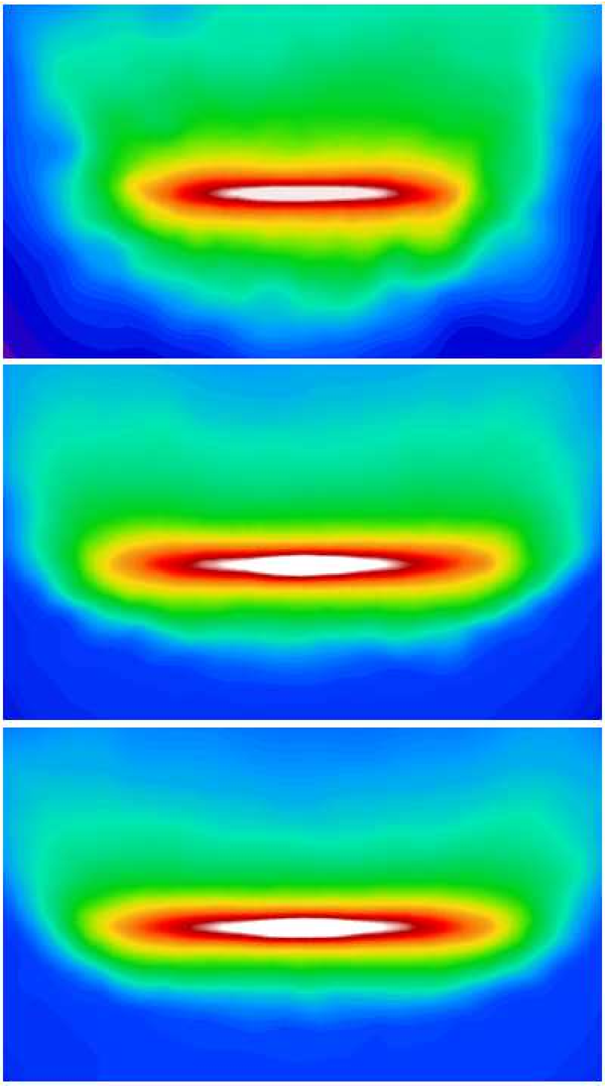

Figure 3.2: From the top to the bottom: column density distribution for the LMC test models H1, H2, H3. The scale is logarithmic with blue corresponding to the density of the hot halo gas. The effects of resolution are clearly apparent in the upper panel.

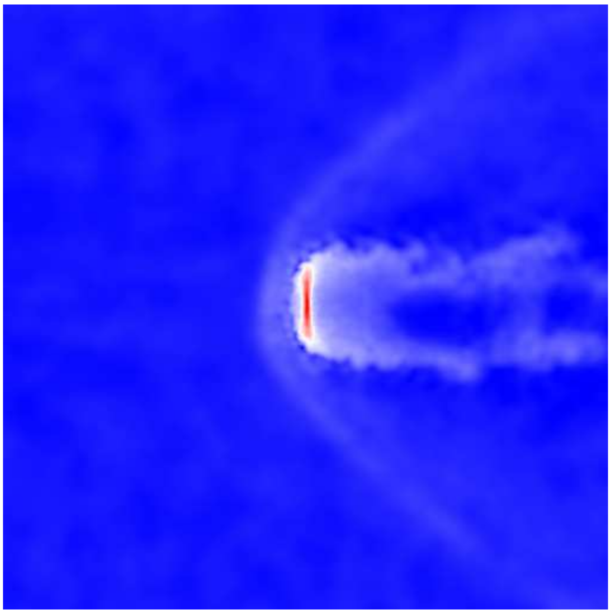

Figure 3.3: H3 run: density distribution of gas in a thin slice perpendicular to the LMC disk. The satellite is moving face on toward the left side of the picture while a shock front forms in the external medium in front of the disk.

equal to 2, 1 and 0.5. The stripped mass converges for $m_h/m_{disk} < 1$.

The dependence of ram pressure on the satellite orientation is not a simple function of the angle between the disk plane and the orbital velocity (Vollmer et al., 2001) and can depend on the ram pressure and the structure of the satellite (Abadi, Moore & Bower, 1999; Quilis, Moore & Bower, 2000; Schulz & Struck, 2001; Marcolini, Brighenti & D'Ercole, 2003). In the simulations E1 and E2 the galaxy is moving edge on through the hot gas. Comparing the amount of stripped mass of E1 and E2 with the results of the corresponding face on runs H2 and L1, it is clear that the stripping is not very sensitive to disk orientation. This is consistent with the conclusions of Marcolini, Brighenti & D'Ercole (2003), who observe that ram-pressure stripping sensitively depends on the inclination angle of the disk only in regimes of strong winds. In the case of relatively large dwarfs (the LMC total mass lies between their models MD and LG) subject to weak ram pressure forces, as in the MW halo case, the central region of the disk is essentially unaffected for any inclination of the galaxy and the outer parts are similarly stripped in face-on and edge-on runs. These results imply that the amount of gas in the Stream will only slightly depend on the initial inclination of the LMC disk and on the precession eventually induced by tidal forces from the MW.

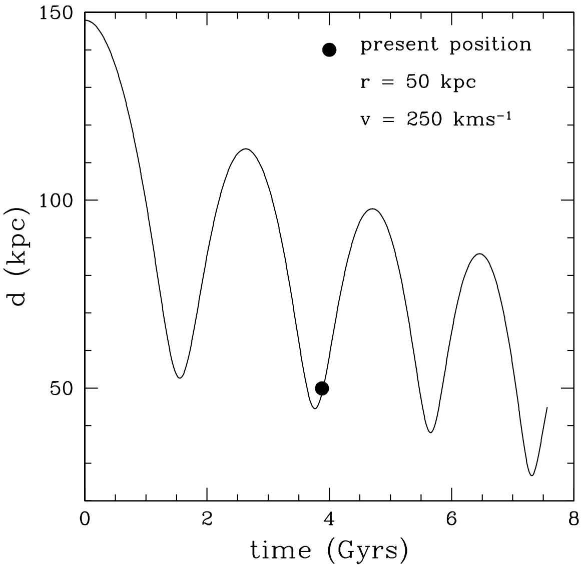

Figure 3.4: Orbital separation for the MW – LMC system

3.5 Interacting runs

3.5.1 Orbital parameters

The morphology of the Stream indicates that the orbit of the LMC is nearly polar and counter–clockwise, as seen from the Sun, while kinematical data (van der Marel et al., 2002) imply that the present position at $\sim$ 50 kpc from the Galactic Center, is close to the perigalacticon. Since the mass ratio between the MW and its satellite is about 50:1, we expect that the effects of the dynamical friction are not negligible on time scales comparable with the orbital period. On the other hand, at each pericentric passage the LMC loses mass from tidal stripping, increasing its decay time: dynamical friction becomes less effective as the satellite approaches the Galaxy (Colpi, Mayer & Governato, 1999).

Dynamical friction implies that we can not precisely make a backwards integration of the LMC's orbit, therefore we make several low resolution test simulations (3×10^5 particles) in order to find the correct starting point for the LMC 4 Gyrs in the past such that it ends up with the present distance, velocity and orientation on the sky. We find orbital parameters close to the ones obtained by Gardiner, Sawa, & Fujimoto (1994) and Gardiner & Noguchi (1996). In particular the orbital plane is perpendicular to the Galactic disk, the present eccentricity (defined as $(r_{apo} - r_{per})/(r_{apo} + r_{per})$, with r_{apo} and r_{per} apogalacticon and perigalacticon distances) and the orbital period are respectively 0.44 and $\sim$ 2 Gyrs. The orbital separation between the MW and the LMC is plotted in Fig. 3.4 for the past 4 Gyrs and 4 Gyrs into the future. The satellite is currently at 50 kpc from the Galactic center and is moving away from the perigalacticon (at 45 kpc) with a modulus of the velocity of $250\,\mathrm{km\,s^{-1}}$. Its Local Standard of Rest velocity v_{LSR}, i.e. the radial velocity seen from the Sun, is 270 km s^{-1}, while the present position in Galactic coordinates is (b,l)=($-30°$, 277°). All these values are quite close to those provided by observations. In particular the observed v_{LSR} is 274 km s^{-1} according to Luks & Rohlfs (1992) and Hardy, Suntzeff & Azzopardi (1989) while (b, l)= $(-32.89°, 280.46°)$ from Tully (1988). Fig. 3.4 evidences that plot the LMC orbit is slowly sinking, with each apogalactic distance $\sim 20\%$ smaller than the previous one. We will show in the next subsection that the change in the orbital parameters due to dynamical friction strongly affects the tidal forces and rate of ram pressure stripping.

In choosing the initial inclination and position of the line of nodes we make the approximation that they do not change during the interaction. In particular we adopt the values from van der Marel et al. (2002): respectively $i = 34.7°$ and $\Theta = 129.9°$. This choice could partially influence the final stellar structure of the disk, but not the ram pressure stripping process, as seen in the previous section.

3.5.2 The Stream

The close interaction with the MW strongly perturbs the entire structure of the satellite. In particular during the 4 Gyrs preceding the present epoch the LMC loses $\sim 80\%$ of its dark halo, and is currently tidally truncated at a radius of 11 kpc, consistent with the values provided by analytic calculations (Weinberg, 2000; van der Marel et al., 2002) and with observations of the outer regions of the disk (Irwin, 1991; van der Marel, 2001). The contribution of the dark matter halo to the final rotation curve within 8 kpc from the center decreases by ~ 5 km s^{-1} and the disk component predominates in the inner region (right panel of Fig. 3.1).

While all the stars within the tidal radius are likely to be gravitationally bound, this is not true for gas. In fact, part of the gas that lies within the tidal radius can have enough thermal energy to escape from the potential well of the galaxy. Fig. 3.5 illustrates the evolution of the baryonic mass as function of time. The dotted and solid curve refers to the stellar and gaseus component respectively while the dashed curve represents the gas within the tidal radius which is actually bound to the LMC.

After two perigalactic passages the satellite looses roughly $\sim 12\%$ of its gas and $\sim 4\%$ of stars. A pure tidal stripping model would remove similar amounts of both stars and gas unless the initial gas disk was significantly more extended. The larger amount of stripped gas is due primarily to ram–pressure stripping: the rate at which gas is lost increases as the LMC approaches perigalacticon (the solid vertical lines in the plot), corresponding to higher densities of the diffuse halo gas and to higher velocities of the satellite along the orbit.

Stars are stripped from the LMC only during the last perigalacticon, since the previous perigalactic passage is too far from the MW to produce significative tidal shocks and to perturb the stellar structure of the satellite. The present stellar distribution (bottom panel of Fig. 3.5.2) indicates that the disk is becoming elongated, forming a trailing and a small leading arm (with surface density $\sim 3 \times 10^{-3} M_{\odot} pc^{-2}$), but most of the stars stripped from the disk are still bound to the LMC and form a large spheroidal component.

Contrary to the stars, gas is stripped during the first passage at perigalacticon, forming a continuous stream that lies in a thin plane (width ~ 25 kpc) perpendicular to the disk of the MW (Fig. 3.6) and between 50 and 75 kpc from the Galactic center. Fig. 3.5.2 (upper panel) represents the distribution of stripped gas in an Aitoff projection. Our simulations predict that the MS forms a great polar circle, but most of the gas is lost recently and it is now at an angular distance between 10° and 120° from the LMC. The

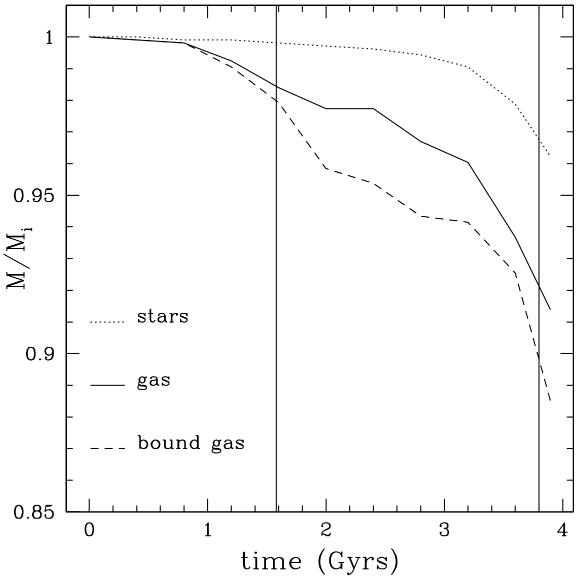

Figure 3.5: Fraction of stars and gas bound to the satellite during the last 4 Gyrs. Both the gas within the tidal radius and the bound gas are plotted. M_i is the initial mass of each disk component. The vertical solid lines indicate the perigalactica.

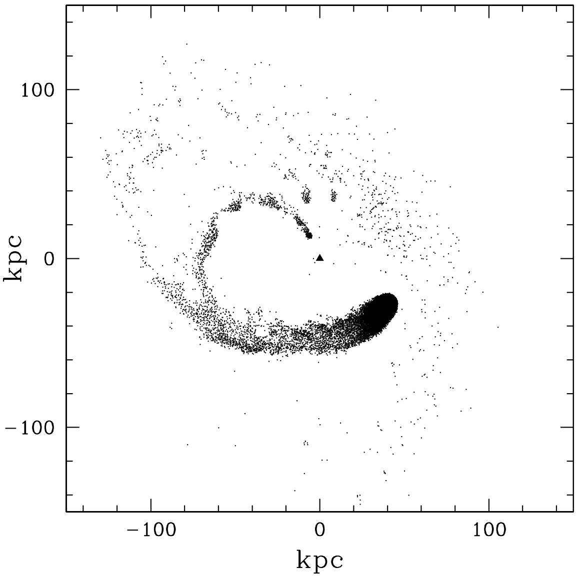

Figure 3.6: Final distribution of gas from the LMC disk in a plane perpendicular to the Galactic plane

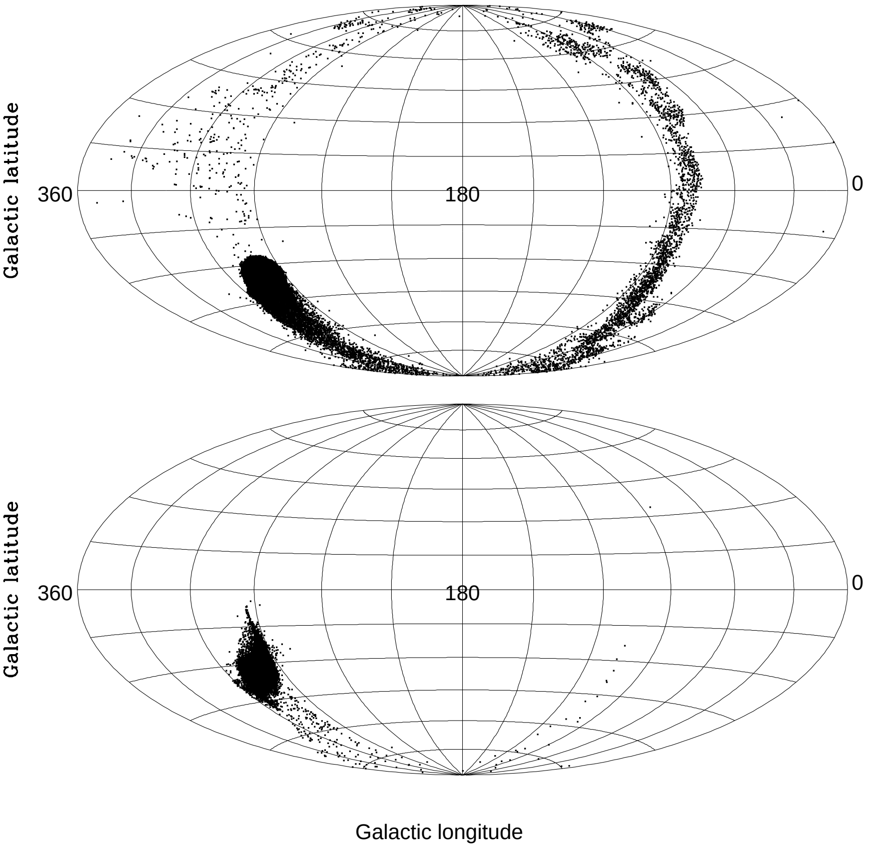

Figure 3.7: Present distribution of gas (top) and stars (bottom) from the LMC disk in Galactic coordinates.

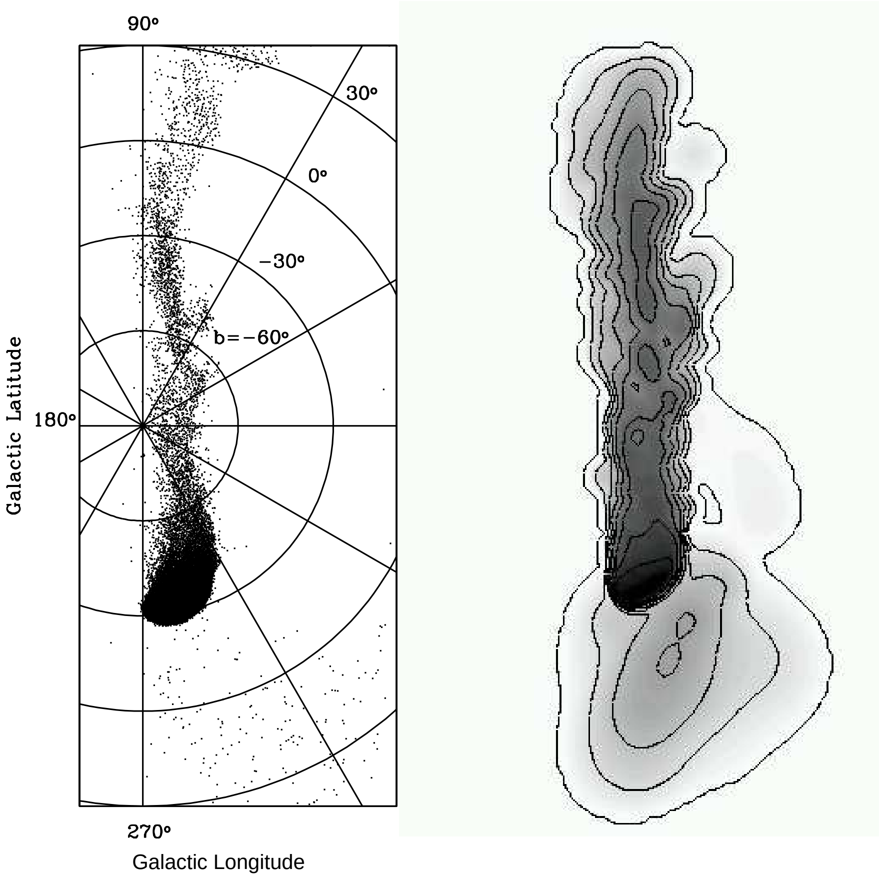

Figure 3.8: Left panel. Polar projection of the simulated stream in Galactic coordinates. Right panel. Hydrogen column density along the Stream. Same projection and scale as in Fig. 9. The intensity values are on a logarithmic scale with black corresponding to the highest dense regions within the LMC disk. The column density contours are 0.05, 0.15, 0.45, 1.35, 4.05, 12.15, 36.45 and 109.35 $\times 10^{19}\mathrm{cm}^{-2}$. The resolution limit in Putman et al. (2003a) is $\sim 2 \times 10^{18}\mathrm{cm}^{-2}$, close to our second outermost level.

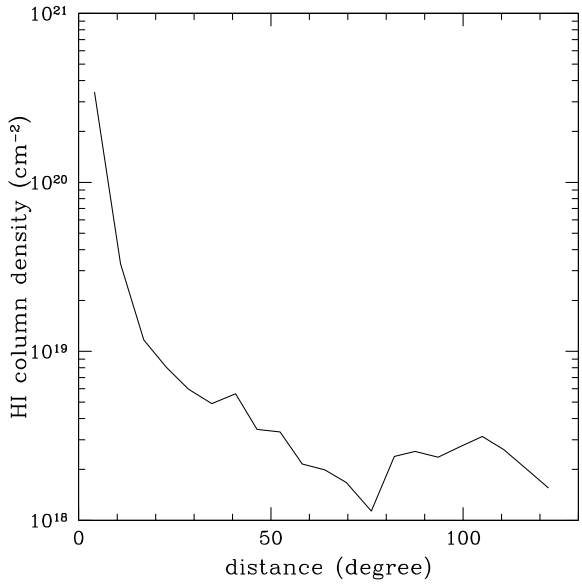

Figure 3.9: Hydrogen column density along the Stream. The system of coordinates is chosen in order to have the LMC at 0 degrees.

location of the Stream in the Southern Galactic hemisphere is comparable with the values of b and l provided by observations. The material which lies in the Northen hemisphere was stripped from the satellite during the first orbit and is presently falling to the Galactic center. In particular the tail of this extended stream is intersecting the actual position of the satellite at $b \sim -30°$. It actually appears on the sky as a leading feature and could in principle reproduce observations of the leading arm of the Magellanic Stream. Its column density is however significantly lower than the observed one. The location of this gas is more clearly visible in Fig. 3.8, which shows a polar projection of the Stream. The right panel of Fig. 3.8 also indicates the hydrogen column density gradient along the Stream, calculated assuming 72% HI abundance. The gas in the "leading region" presents a density peak between $b = -30°$ and $b = 30°$ and at $l \sim 285°$, but more material lies at larger longitudes and less negative latitudes, altougth the local density seems to be lower. Unfortunately, due to the thermodynamical model adopted, the gas does not cool and condense in to individual clouds, but particles at the very end of the Stream thermalise with the external hot medium influencing both morphology and kinematics. Moreover the resolution adopted in the simulation does not permit us to resolve this area with more than 10^3 gas particles.

The column density of the gas located where we expect to find the trailing arm gradually decreases along the length of the Stream moving from the LMC to $(b, l) \sim (20°, 80°)$. At a fixed angular distance from the LMC the structure of the Stream is not uniform but has some well defined high density regions. Within 120° from the satellite the decrease in density is by nearly two orders of magnitude along the Stream (Fig. 3.9) and is comparable with the gradient in column density observed in the trailing arm moving from the head of the Stream ($3.3 \times 10^{19}\mathrm{cm}^{-2}$ at an angular distance of $\sim 10°$ from the LMC) to MS VI ($3.6 \times 10^{18}\mathrm{cm}^{-2}$). This decrease in density is due to the combination of two

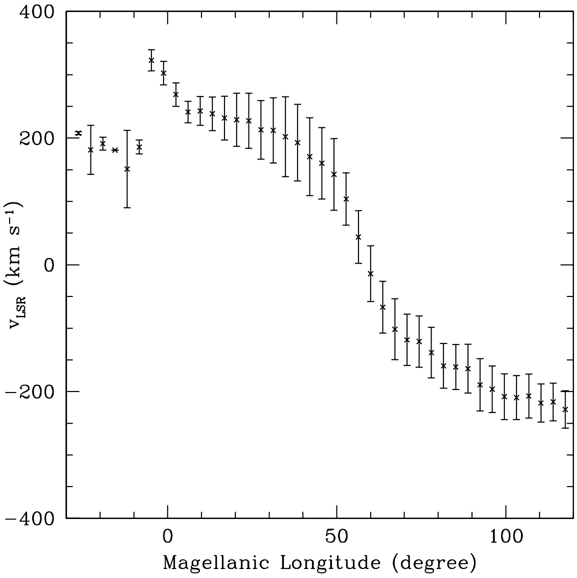

Figure 3.10: Radial velocity of the simulated Stream in the Local Standard of Rest as a function of the Magellanic Longitude. Each point represents the mean velocity within an angular interval of 3.5° along the MS. The error bars show the standard deviation in each interval.

factors. The gas close to the head of the Stream is pulled from the disk during the last perigalacticon, when the stripping rate is maximum, whereas the tip is ~ 1 Gyr old and corresponds to an apogalactic passage. Moreover, the tail is formed by the first material stripped from the outer and low density regions of the exponential disk. This decrease in column density is a remarkable success for the ram-pressure scenario since tidal models generically produce streams with surface densities that fall off much more slowly (Moore & Davis, 1994; Gardiner & Noguchi, 1996).

The mass of the stripped gas ($1.4 \times 10^8 M_\odot$, almost 90% of which within the same angular distance from the LMC covered by observations) is similar to the observed amount of neutral hydrogen in the Stream by Putman et al. (2003a) ($2 \times 10^8 M_\odot$). The total amount of unbound gas after 4 Gyrs is comparable with the gas stripped in one orbital time from an LMC model in a test tube simulation with densities and velocities characteristic of a perigalactic passage. This means that the tidal forces acting on the satellite contribute to ram pressure processes: as a consequence of the resulting asymmetrical potential and distorted stellar disk, it is easier to strip more gas from the LMC's disk since the gravitational restoring force is weaker. Thus even a low density gaseous Galactic halo is able to remove a significant amount of gas from the LMC. The difference in the characteristic time scales of hydrodynamical and gravitational forces explains why a gaseous leading arm does not form through tidal stripping: gas is removed quite early from the outer regions of the LMC disk that during the second passage at the perigalacticon starts forming a leading arm feature.

Fig. 3.10 represents the Local Standard of Rest radial velocity of the Stream versus the Magellanic longitude (l_M) within an angular range similar to the one explored by observations (Putman et al., 2003a; Brüns et al., 2005). The Magellanic coordinate system adopted is the same used by (Putman et al., 2003a) and previously described by Wakker (2001). The Magellanic longitude 0° corresponds to the center of the LMC. The Local Standard of Rest velocity is calculated assuming a solar circular rotation around the Milky Way of 220 km s^{-1}. The LMC is characterised by a mean radial velocity of 270 km s^{-1} (the steep increment of v_{LSR} around $l_M = 0$ is due to the rotation of the LMC disk), while moving through larger Magellanic longitudes along the Stream the velocity slows down to 0 km s^{-1} at $\sim$ 60° from the Cloud and to high negative values ($\sim$ -250 km s^{-1}) at $l_M \sim 120°$. The velocity gradient along the Stream is almost 600 km s^{-1}, not far from the velocity range observed in HIPASS data (Fig. 12 could be compared with the analogous Fig. 3 from Brüns et al. (2005)). The points located at negative Magellanic longitudes represent the gas lying in the "leading region". The mean radial velocity of this area is $\sim$ 180 km s^{-1}, with a clear gap respect to the velocity of the LMC, whereas the Leading Arm feature is observed at low relative velocities to the Cloud, with a mean v_{LSR} of 250 km s^{-1}. As we discussed previously, we do not expect to reproduce correctly the kinematics of this region since the gas is already thermalized with the hot surrounding medium.

3.5.2.1 Adiabatic versus cooling runs

We have presented results from simulations that do not include radiative cooling. As discussed in Section 3.4 , in this case the gas in the disk of the LMC will increase its temperature as it is strongly compressed by the outer medium. In the adiabatic regime the gas can only lose energy by expansion, which requires a long timescale, and can become easily unbound due to this input of thermal energy. We have run a simulation with radiative cooling adopting a standard cooling function for primordial gas (hydrogen and helium). The resolution is the same as in the high resolution adiabatic interacting simulation. This run does not include star formation or supernovae feedback. The gas quickly heats up to $\sim 10^5$ K due to shock heating, the peak of the cooling curve, then cools down on a timescale much shorter than the dynamical time, shrinking in radius compared to its original location. After a few cycles of heating and cooling the disk is significantly smaller and the gas sits deeper in the potential well and as a result no gas is stripped. However, what we are witnessing is probably the result of overcooling since we are neglecting the effect of star formation, namely heating from supernovae feedback and radiation from massive stellar associations. The LMC in particular shows widespread intense star formation across its disk and bar. In reality a multi-phase ISM will result that will be enable the gaseous disk to be in pressure equilibrium with the outer medium. Until we can effectively model this multi-phase medium, we believe that the results of the adiabatic simulations are closer to reality.

3.5.3 The LMC disk

The Galactic disk remains unperturbed during the interaction, while the morphology of the satellite changes drastically. In particular we will focus on the changes in the stellar and gaseous structure of the LMC.

Our initial model has a pure exponential stellar disk with a thin vertical structure and no bar component.

After 4 Gyrs from the beginning of the simulation almost the entire stellar component is still bound to the satellite, but less than 90% of the stars lie in the thin disk, which is

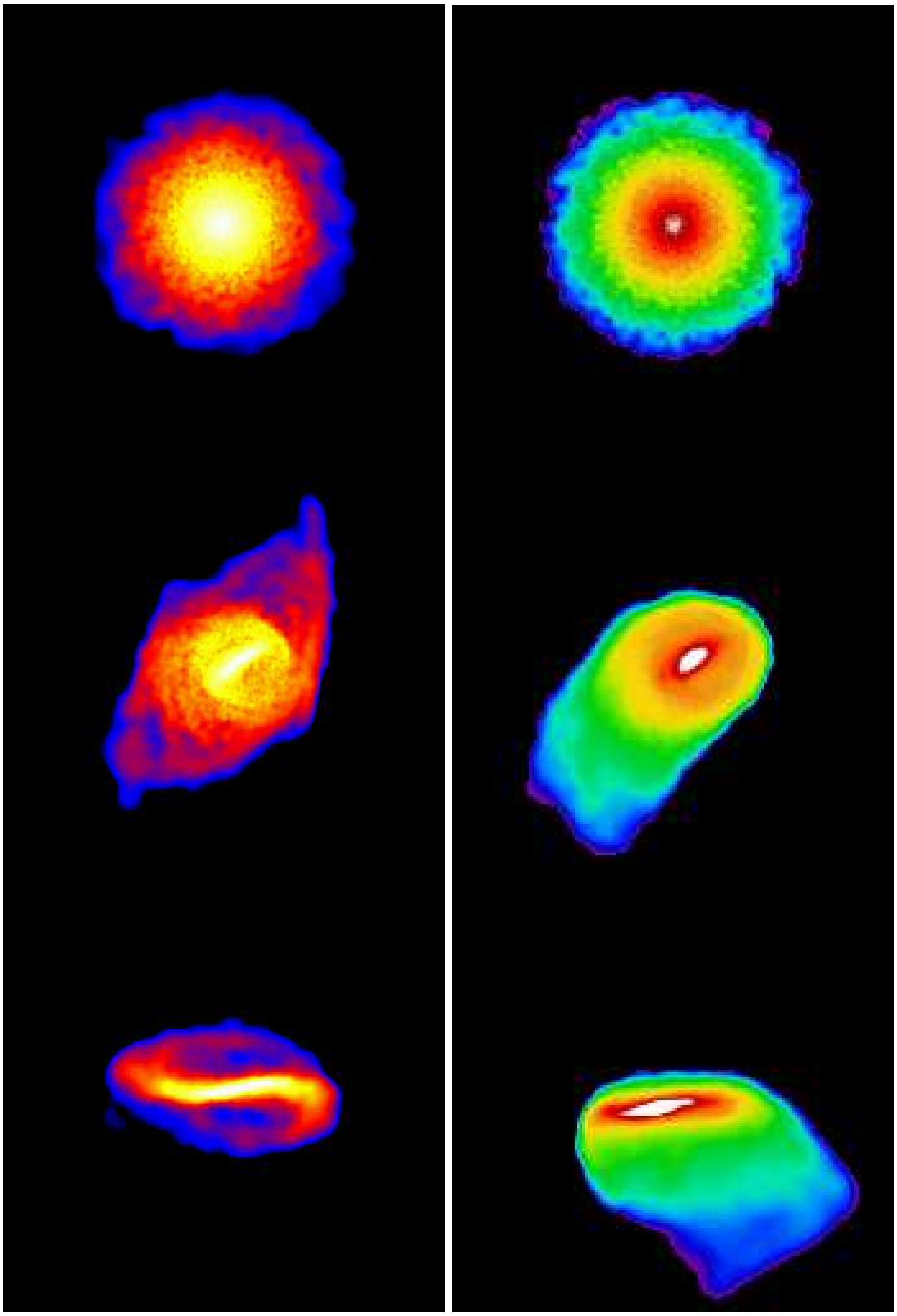

Figure 3.11: LMC stellar surface density (left) and gas column density (right). From the top to the bottom: initial conditions, final face on and edge on projection. Colour scales are logarithmic. In the left panels white corresponds to a stellar density of $10^2 M_\odot \mathrm{pc}^{-2}$ and blue to $10^{-2} M_\odot \mathrm{pc}^{-2}$. In the right panels white indicates a gas column density of $10^{22}\mathrm{cm}^{-2}$ and violet $10^{19}\mathrm{cm}^{-2}$. The first part of the Stream is visible.

surrounded by a stellar spheroid with a radius of ~ 11 kpc (left panels of Fig. 3.11). The structure of this spheroidal component is quite complex, since a strong warp that wraps 180° around the LMC is superimposed on the underlying low density stellar distribution. This final configuration is similar to the one obtained by Bekki & Chiba (2005). The warp forms after the first passage at the perigalacticon and involves a large fraction of the stellar particles. It extends ~ 5 kpc out of the thin disk and is aligned with the major axis of the satellite. The existence of a warp is inferred by Kim et al. (1998) from the gas velocity field in the disk of the LMC, by van der Marel & Cioni (2001) and Olsen & Salyk (2002) using the apparent magnitude of different classes of stars as a distance indicator. The diffuse spheroidal component has an average surface density of $\sim 5 \times 10^{-2} M_{\odot}\mathrm{pc}^{-2}$, which becomes one order of magnitude larger if we consider only the warp region. The warp deformation is partially directed along the line of sight and could have implications for the microlensing results, increasing the optical depth caused by self–lensing (Zaritsky & Lin, 1997; Zhao & Evans, 2000). The LMC's disk appears elongated, with a mean ellipticity $\epsilon = 0.38$ (where $\epsilon = 1 - q$ and q is the axial ratio), in a direction roughly aligned with the Galactic center and perpendicular to the Stream. These values agree very well with the observations provided by van der Marel (2001). Within the inner 6–7 kpc of the model LMC a strong and asymmetric bar forms after the first perigalacticon.

The isodensity contours of the face-on disk were fitted with ellipses using the MIDAS task FIT/ELL3. The ellipse centers, ellipticity and major axis position angle were considered as free parameters of the fitting procedure. The results of this projected analysis are illustrated in Fig. 3.12. The first plot on the top (solid line) shows the B-band surface brightness profile of the present face-on LMC, for which the best fitting exponential curve has a scale length of 1.5 kpc. The dashed line is the original exponential disk, with a scale length of ~ 1.7 kpc. The second and third panels illustrate the variation of the position angle and eccentricity as a function of radius. The position angle is almost constant in the central 4 kpc of the disk and presents a sharp twist beyond this radius, which corresponds to the transition between the bar region and the outer density contours characterized by ellipticities $\lesssim$0.2. At radii $\gtrsim 8$ kpc the disk appears more elongated, with a further increase in ellipticities and a twist of $\sim 50°$ in the position angle. The last plot on the bottom indicates the drift of the countour centers in the plane of the disk, which moves consistent with observations (van der Marel, 2001) by almost 1 kpc.

Fig. 3.13 illustrates the kinematic profiles of three different orientations of the LMC disk observed today: from the top to the bottom face-on, edge-on and end-on projections. The peak in the velocity dispersion in the central 6–8 kpc is mainly due to the bar formation, while the external regions appear to be dominated by an hot tidally perturbed component with $\sigma_p \sim 20$ km s^{-1}.

The gaseous disk is completely dominated by stripping processes (right panels of Fig. 3.11). It retains a symmetric structure only within the central 12 kpc, in connection with the thin component of the stellar disk. Within this radius we do not observe a significative displacement between the center of the stellar distribution and the gaseus disk. The ram pressure stripping radius after 4 Gyrs is ~ 6 kpc, a factor of three smaller than the initial disk radius and compatible with the results provided by HIPASS data (Putman, Gibson & Smith, 1998).

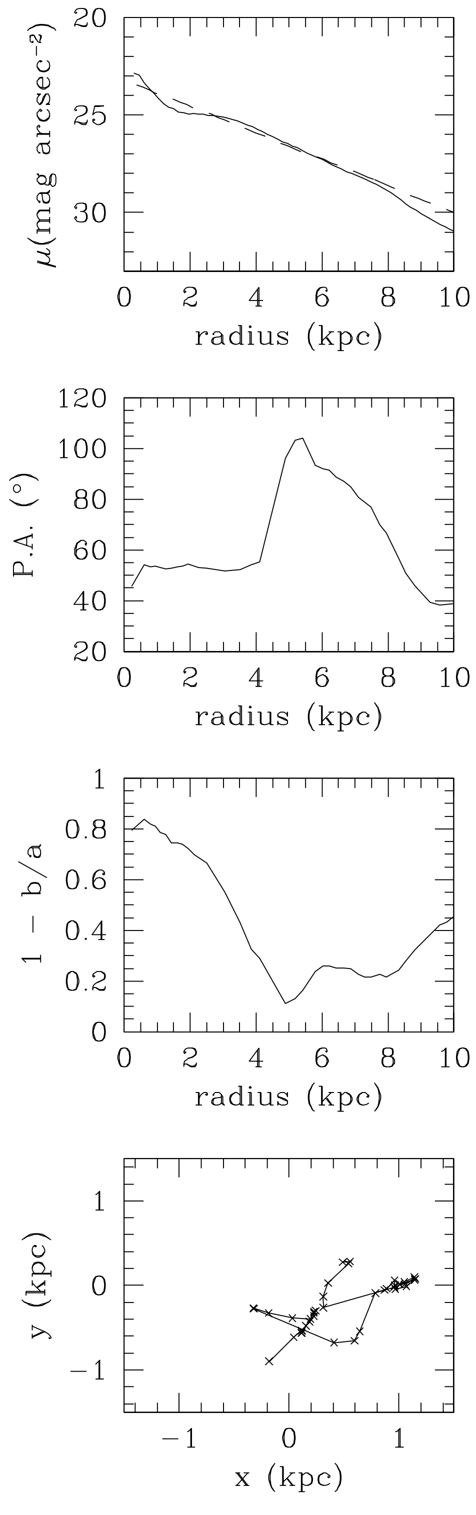

Figure 3.12: Photometric analysis of a face-on projection of the LMC disk. From the top to the bottom: B-band surface brightness, major axis position angle and ellipticity profiles. The last plot on the bottom represents the drift of the ellipse center in the plane of the disk.

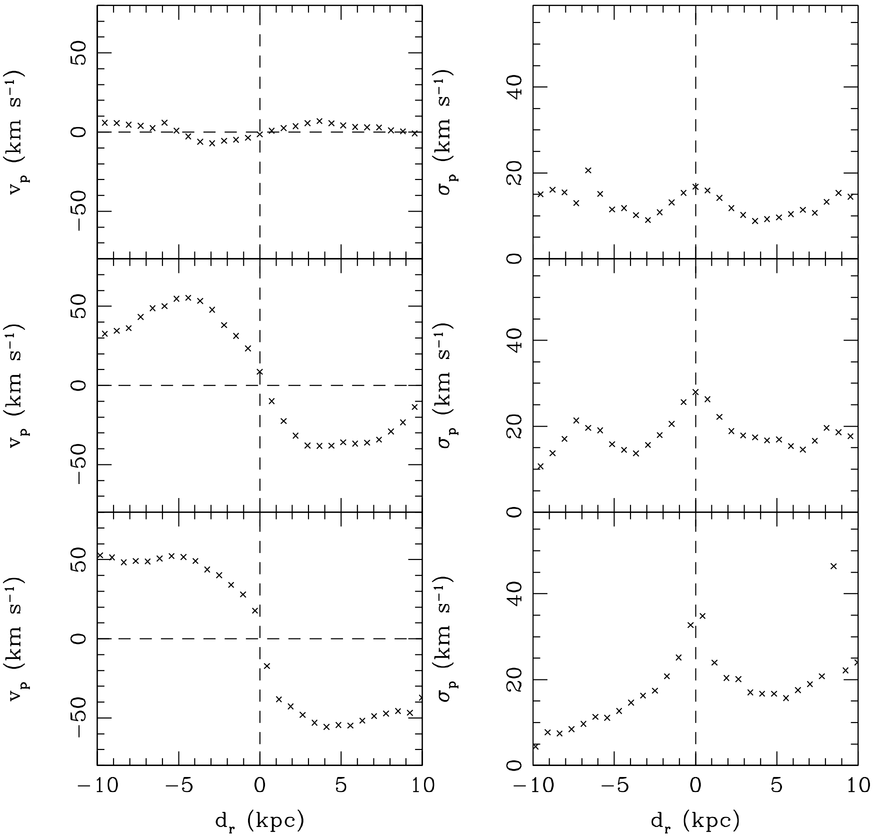

Figure 3.13: Projected velocity (left) and velocity dispersion (right) profiles for three different orientations of the LMC disk. From the top to the bottom: face-on, edge-on and end-on.

3.6 Conclusions

We have carried out high resolution gravitational/hydrodynamical simulations of the interaction between the LMC and Milky Way. As the LMC spirals inwards towards the Galaxy it suffers ever increasing gravitational tidal forces and hydrodynamical stripping. Our simulations cover the previous 4 Gyrs of the orbit of the LMC such that at the final time it ends up at its correct location within the Galactic halo and with the observed inclination. We find that the combined effects of gravity and ram-pressure stripping can account for the majority of the LMC's kinematical and morphological features and the morphology of Magellanic Stream.

Our model of the hot gaseous halo places a total of $10^{10} M_{\odot}$ of ionised hydrogen within the dark matter halo of the Galaxy. The density at 50 kpc is $\approx 8 \times 10^{-5}$ atoms/cm^3. This is sufficient to remove over $10^8 M_{\odot}$ of gas from the LMC, close to the observed mass of the Stream, although the interaction between the LMC and the Galaxy is not likely the only source of the MS gas. In fact the complexity of the HI geometry in the region surrounding the Magellanic Clouds suggests that a close encounter between the Clouds and gas stripped from the SMC contributed not negligibly to the formation of the Stream.

The gas stripped from the LMC disk forms a great circle, or a polar ring, around the Galaxy, consistently with the recently discovered extension of the Stream into the Northern Hemisphere by Braun & Thilker (2004). Less material was stripped during the pericentric passage 4 Gyrs ago since dynamical friction has moved the Clouds closer today. Thus we can reproduce the observed decrease in column density along the Stream. Very few stars are tidally removed from the LMC, but its disk becomes severely warped due to the tidal interaction. This creates a diffuse halo of stars within the LMC that may have been observed as self-lensing events. The disk of stars is elongated by 2:1 oriented towards the Galactic centre in agreement with the observations of van der Marel (2001).

Several improvements to our simulations could be made in order to study this fascinating interacting system in more detail. More detailed modelling of the star-formation and internal ISM of the LMC is necessary in order to study the role of gas stripping on star-formation, and the role of star-formation and the multiphase ISM on the stripping process. Including the interaction with the SMC which could supply a significant amount of gas to the Stream and may be responsible for the Magellanic bridge and the leading arm. Including a more realistic treatment of the gas physics in order to study the detailed structure of the stripped gas and its interaction with the halo gas as it infalls through the galactic halo.

3.7 Acknowledgements

We would like to thank Mary Putman, Tobias Kaufmann, Andrea Macciò and Luigi Mancini for useful discussions. The numerical simulations were performed at the University of Zürich on the Zbox (http:/www.theorie.physik.unizh.ch/stadel) supercomputer. CM is supported by the Swiss National Science Foundation.

Chapter 4

Simultaneous ram pressure and tidal stripping: how dwarf spheroidals lost their gas[1]

4.1 Abstract

We perform high-resolution N-Body+SPH simulations of gas-rich dwarf galaxy satellites orbiting within a Milky Way-sized halo and study for the first time the combined effects of tides and ram pressure. The structure of the galaxy models and the orbital configurations are chosen in accordance to those expected in a ΛCDM Universe. While tidal stirring of disky dwarfs produces objects whose stellar structure and kinematics resembles that of dwarf spheroidals after a few orbits, ram pressure stripping is needed to entirely remove their gas component. Gravitational tides can aid ram pressure stripping by diminishing the overall potential of the dwarf, but tides also induce bar formation which funnels gas inwards making subsequent stripping more difficult. This inflow is particularly effective when the gas can cool radiatively. Assuming a low density of the hot Galactic corona consistent with observational constraints, dwarfs with $V_{peak} < 30$ km/s can be completely stripped of their gas content on orbits with pericenters of 50 kpc or less. Instead, dwarfs with more massive dark haloes and $V_{peak} > 30$ km/s lose most or all of their gas content only if a heating source keeps the gas extended, partially counteracting the bar-driven inflow. We show that the ionizing radiation from the cosmic UV background at $z > 2$ can provide the required heating. In these objects most of the gas is removed or becomes ionized at the first pericenter passage, explaining the early truncation of the star formation observed in Draco and Ursa Minor. Galaxies on orbits with larger pericenters and/or falling into the Milky Way halo at lower redshift can retain significant amounts of the centrally concentrated gas. These dwarfs would continue to form stars over a longer period of time, especially close to pericenter passages, as observed in Fornax and other dSphs of the Local Group. The stripped gas breaks up into individual clouds pressure confined by the outer gaseous medium that have masses, sizes and densities comparable to the HI clouds recently discovered around M31.

---

[1] This chapter (Mayer et al. 2005, astro-ph 0504277 was submitted to MNRAS

4.2 Introduction

The origin of dwarf spheroidal galaxies (dSphs) is a long standing subject of debate. These galaxies are gas poor or completely devoid of gas and are the faintest galaxies known. Objects matching the definition of dSphs are found both in galaxy clusters and in groups, but it is certainly the Local Group the place where dSphs have been better studied thanks to their proximity.

Two main formation paths have been proposed explain their origin, nature of nurture. In one scenario these faint galaxies could be the result of cosmic reionization and stellar feedback quenching gas accretion and star formation in low mass haloes (Dekel & Silk 1986; Thoul & Weinberg 1996; Bullock, Kravtsov & Weinberg 2000; Ferrara & Tolstoy 2000; Benson et al. 2002a, 2002b; Somerville 2002; Susa & Umemura 2004). However, there is no obvious signature of reionization in the star formation history of these galaxies (Grebel & Gallagher 2004), which in many cases continued to form stars over more than 10 Gyr, and for some dSphs the most recent inferred halo masses are likely too large ($10^8 - 10^9 M_{\odot}$, see Kleyna et al. 2002; Wilkinson et al. 2004; Kazantzidis et al. 2004) for supernovae winds to remove most of the baryons (Mori, Ferrara & Madau 2002; Mayer & Moore 2004; Read & Gilmore 2004).

In addition, these models do not naturally explain why dSphs share some structural similarities with equally faint but gas-rich, much younger disk-like galaxies, dwarf irregulars (dIrrs), notably their exponential light distribution. Furthermore they do not give rise to the morphology-density relation observed in groups and clusters, namely the fact that dSphs tend to be concentrated towards the central galaxies while dIrrs are found at much larger distances, nor they explain the dichotomy between dominance of rotation for the stars of most dIrrs and dominance of pressure support for those of dSphs. Various environmental effects have been scrutinized to explain similarities and differences between the two types of galaxies postulating that dSphs are somehow transformed dIrrs. Ram pressure stripping of gas from dwarf irregular-like progenitors caused by a hot diffuse gaseous corona surrounding the Milky Way has been proposed as a way to explain the low gas contents of dSphs together with the similar stellar light distributions of the two types of dwarfs (Einasto et al. 1974; Faber & Lin 1983; Grebel, Gallagher & Harbeck 2003), and has also been considered as the origin of HI clouds possibly associated with some dSphs and transitional dIrrs/dSphs like Phoenix (Blitz & Robishaw 2000; Gallart et al. 2001). Van der Bergh (1996) has argued that the correlation between galactocentric distance and gas content in dSphs is a signature of ram pressure stripping. Tidal stripping of dwarf irregulars has also been considered as an alternative way of removing gas from the dwarfs (e.g. Ferguson & Binggeli 1994).

Recently, high resolution N-Body/SPH simulations were used to show that tides do not only remove gas and stars but can also reshape the stellar components of a dwarf disky galaxy resembling a dwarf irregular (Mayer et al. 2001a,b). This “tidal stirring” can turn a rotationally supported disk into a pressure supported spheroidal stellar system by means of bar formation and a subsequent buckling instability. The mechanism is particularly effective for satellites of massive galaxies that are strongly tidally shocked owing to the plunging orbits expected in CDM models and works for systems having a variety of dark halo profiles, including cuspy profiles (Mayer et al. 2002). The transformation is not necessarily associated with intense tidal mass loss; indeed, objects with very high-mass-to light ratios, thus embedded in dense, massive dark halos, can still be reshaped from the instabilities induced by tidal shocks albeit losing minimal mass (Mayer et al. 2001b).

A problem of this model, however, is that tides cannot remove completely the gas from the disky progenitors of dSphs; the low gas fractions of dSphs can be explained by only invoking rapid consumption from star formation of the remaining gas in a series of tidally triggered bursts associated with bar-driven gas inflows (Mayer et al. 2001b). However, although intermittent star formation is observed in some dSphs (Gallart et al. 1999; Hernandez, Gilmore & Valls-Gabaud 2000), the star formation rates needed to completely consume the gas are well in excess of those implied by reconstructions of the star formation histories of dSphs using detailed color-magnitude diagrams (Mayer et al. 2001b). Moreover, Draco and a few other dSphs do not show extended star formation histories, instead seem to have ceased star formation about 10 Gyr ago (Grebel et al. 2004).

It is likely that both gravitational tides and hydrodynamical processes play a role (Gavazzi et al. 2001). For example, ram pressure could act simultaneously with tides and increase the efficiency of gas removal (Mayer & Wadsley 2003). Recent 2D and 3D grid-based hydrodynamical simulations of ram pressure stripping of disk-like dwarfs in poor groups show that ram pressure alone can remove most of the gas in dwarf galaxies with halo circular velocities lower than 30 km/s (Marcolini, Brighenti & D'Ercole 2003). However, these and other simulations (Mori & Burkert 2000) do not use models of dwarf galaxies directly based on the Λ CDM model and do not include the effect of tides. The effectiveness of both ram pressure and tidal stirring will also depend on the orbital history of the dwarfs, and this is where the cosmological framework comes into play. For example dwarfs that fell into the primary halo at very high redshift likely had orbits with smaller pericenters relative to those falling later on (Mayer et al. 2001b), thus suffering stronger tidal shocks, and possibly also stronger ram pressure in a denser gaseous corona, while being exposed to the effect of the cosmic UV background (Bullock, Kravtsov & Weinberg 2000; Somerville 2002; Barkana & Loeb 1999; Shaviv & Dekel 2003). Indeed cosmological simulations of galaxy formation incorporate all such mechanisms but their resolution is still too coarse to allow a study of their effects at the scale of the tiny dwarf spheroidals (Governato et al. 2004).

In this paper we will study for the first time the combined effects of ram pressure and tidal stirring using high resolution three dimensional N-Body+SPH simulations of dwarf galaxies orbiting within the Milky Way dark halo and gaseous corona. We will use galaxy models and orbits consistent with the predictions of ΛCDM simulations. The simulations include also radiative cooling as well as heating and ionization from the cosmic UV background radiation. The main goal of the present work will be to establish whether these two mechanisms can explain the present-day low gas content of dSphs if these galaxies are the descendants of gas-rich dwarfs with structure similar to today's dIrrs.

4.3 Initial Conditions

4.3.1 Galaxy models

Models comprise an exponential disk of gas and stars embedded in a live NFW halo for the dwarf, and a live NFW halo plus hot gas distribution with the same density profile for the primary galaxy. Halo virial parameters (mass, radius, circular velocity) are consistent with the LCDM model. Although we believe that the Milky Way halo has a virial velocity

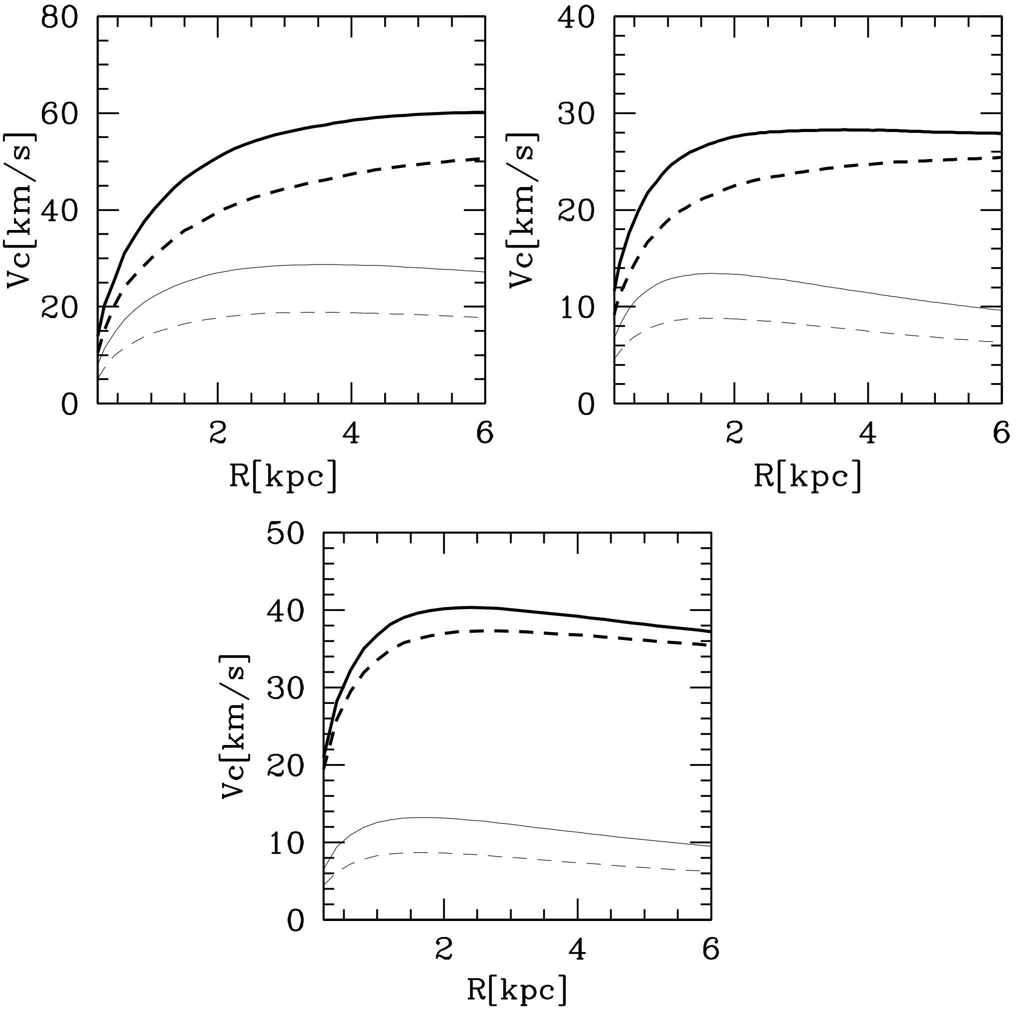

Figure 4.1: Initial rotation curves of the dwarf galaxy models.The lines show, respectively, the total rotation curve (thick solid), the contribution of dark matter (thick dashed), that of stars (thin solid) and that of gas (thin dashed). From top left to bottom, models V60c4, V30c4 and V40c20 are shown.

Table 4.1: Parameters of the full interaction (FI) simulations. Column 1: Name of model Column 2: Peak circular velocity of the satellite (km/s) Column 3: Satellite halo concentration Column 4: Disk scale length (kpc) Column 5: Apocenter distance (kpc) Column 6: Pericenter distance (kpc) Column 7: Thermal physics (AD=adiabatic, RC=radiative cooling, RCUV=radiative cooling + cosmic UV background). All runs include tides and ram pressure except those referred to as TD which do not include ram pressure. Column 8: name of run (HR stands for high resolution, see text). Column 9: initial gas mass (in units of $10^6 M_\odot$) Column 10: final gas mass (in units of $10^6 M_\odot$)

Model	V_{peak}	c	R_h	r_{apo}	r_{peri}	physics	Run	M_{gas_i}	M_{gas_f}
V60c4	62	4	2.2	250	50	AD	Rc4aAD	450	55
V60c4	62	4	2.2	250	50	AD	Rc4aADHR	450	60
V60c4	62	4	2.2	250	50	RC	Rc4aRCHR	450	380
V60c4	62	4	2.2	250	50	RCUV	Rc4aRCUV	450	290
V28c4	25	4	1.1	250	50	TD(AD)	Rc4bTD	45	20
V28c4	25	4	1.1	250	50	AD	Rc4bAD	45	0
V28c4	25	4	1.1	250	50	RC	Rc4bRC	45	9.5
V28c4	25	4	1.1	150	30	RC	Rc4cRC	45	0
V40c20	42	20	0.5	150	30	TD(AD)	Rc20TD	46.5	22.2
V40c20	42	20	0.5	150	30	AD	Rc20AD	46.5	0
V40c20	42	20	0.5	150	30	RC	Rc20RC	46.5	3.55
V40c20	42	20	0.5	150	30	RCUV	Rc20RCUV	46.5	0.65
V40c20	42	20	0.5	250	50	AD	Rc20bAD	46.5	0
V40c20	42	20	0.5	250	50	RC	Rc20bRC	46.5	10

$V_{vir} = 140 - 160$ km/s (Klypin, Zhao & Somerville 2002) we use a slightly larger value, $V_{vir} = 180$ km/s, in order to have $V_{peak} = 230$ km/s at about 10 kpc from the center without including a disk component. We choose a concentration $c = 10$ for the MW halo, this being typical for LCDM halos at a scale of $\sim 10^{12} M_{\odot}$ (Bullock et al. 2001). With our choice of parameters the shape of the rotation curve is quite flat out to 100 kpc and the resulting halo mass within 100 kpc is $\sim 8 \times 10^{11} M_{\odot}$, consistent with the orbital dynamics of the Magellanic Clouds and distant dSphs (Lin, Jones & Klemola 1995; Dehnen & Binney 1998). Overall our halo model resembles model A3 in Klypin, Zhao & Somerville (2002), which matches simultaneously most of the known observational constraints within the framework of the LCDM model. The hot gas is in hydrostatic equilibrium within the halo potential and its temperature is $\sim 10^6$ K at 50 kpc, consistent with OVI, OVII and X-ray absorption measurements in the Galactic halo (Sembach et al.2003). Assuming an isotropic model, the halo temperature at a given radius r is determined by the cumulative mass distribution $M(r)$ of the dark, stellar and gaseous components of the MW beyond r and by the density profile $\rho_h(r)$ of the hot gas:

$$T(r) = \frac{m_p}{k_B} \frac{1}{\rho_h(r)} \int_r^{\infty} \rho_h(r) \frac{GM(r)}{r^2}\, dr\,, \tag{4.1}$$

where m_p is the proton mass, G and k_B are the gravitational and Boltzmann constants. Its density at 50 kpc from the center is 8×10^{-5} atoms/cm^3 (see also Mastropietro et al. 2004). At a distance of $\sim$ 100 kpc or more, where the dwarf galaxies that we have simulated spend most of the time while orbiting within the primary halo (see below), the hot halo density is $< 10^{-5}$ atoms/cm^3. Such a hot diffuse halo is also a natural expectation of the current LCDM paradigm of structure formation (White & Frenk 1991; Governato et al. 2004; Sommer-Larsen, Portinari & Goetz 2003; Maller & Bullock 2004).

The multi-component dwarf galaxy models are built using the technique developed by Hernquist (1993) and later refined by Springel & White (1999) (for further details on the modeling see also Mayer et al. 2002). They comprise an exponential disk of gas and stars embedded in an NFW halo. We used three dwarf models with $V_{peak} = 28$, 42 or 62 km/s km/s and concentration $c = 4$ (the first two models) and $c = 20$ (the third model). The choice of halo concentration can be quite flexible since cosmological simulations show a large scatter of such property at small mass scales, mostly due to a large spread in halo formation times (Bullock et al. 2001). The rotation curves of the models are reported in Fig. 4.1; while the rotation curves of models V60c4 and V30c4 are slowly rising in agreement with those of todays' dwarf irregulars, that of model V40c20 rises quite steeply owing to the much higher halo concentration. A steep rotation curve is a more appropriate choice for the progenitors of Draco or Ursa Minor that have very high central dark matter densities (see Mayer et al. 2001b; Hogan & Dalcanton 2000).

Lokas (2002) and Kazantzidis et al. (2004) have shown that dSphs kinematics suggests they are embedded in halos with $V_{peak} \sim 20 - 35$ km/s. We used even larger values of V_{peak} in our initial conditions since these can later decrease as a result of tidal mass loss, by roughly a factor of 2 according to the recent cosmological simulations by Kravtsov, Gnedin & Klypin (2004).

The galaxy models have disks of mass $\approx 4\%$ of the total mass, lower than the universal baryon fraction but quite typical for present-day LSB or dIrr galaxies (Jimenez et al. 2003). Following, Mo, Mao & White (1998), the exponential scale length R_h of the disk is determined by the spin parameter and concentration c of the halo; we use $\lambda = 0.043$ for models Rc4a and Rc4b, and $\lambda = 0.08$ for model Rc20a,b (the mean spin of cosmological halos is $\lambda \sim 0.05$, see e.g. Gardner 2001, and 20% of halos have spins as high as 0.1 due to the log-normal shape of the probability distribution of halo spins). The disk sizes in models V28c4 and V40c20 are the same (the higher spin parameter compensates for the higher halo concentration) and, since also the disk mass is the same by choice, we can isolate the role of halo concentration (or, equivalently, V_{peak}) by comparing the two models. Note that all the models have a central surface brightness of 23 mag arcsec $^{-2}$ in the B band for a stellar-mass-to light ratio of 2, typical of dIrrs and dwarf spirals (see de Blok & McGaugh 1997). Galaxies with these low disk mass fractions are stable to bar formation in isolation irrespective on halo concentration (Mayer & Wadsley 2004). However they can become bar unstable when tidally perturbed by a much more massive halo.

We use 3×10^5 particles for the dark halos of the dwarfs and 3×10^4 particles for both the stellar and the gaseous disk of the dwarf. The Milky Way halo is modeled with 10^6 dark matter particles, while 5×10^5 particles are used for the superimposed gaseous halo (the mass of hot halo particles is $8 \times 10^4 M_{\odot}$). Each simulation has a total of $\sim 1.8 \times 10^6$ particles, which makes them quite computationally demanding. Two runs employing model V60c4 were repeated with increased resolution in the disk of the dwarf, (2×10^5 particles for both its stellar and its gaseous component, see Table 4.1). The choice of putting a large fraction of the total number of particles in the primary halo is motivated by the desire of minimizing spurious two-body heating between halo particles and those of the disks of the dwarfs (Moore, Katz & Lake 1996; Mayer 2004).

We use a fairly large gravitational softening for the gas and dark matter particles in the primary system, $\varepsilon = 2$ kpc to minimize discreteness noise in the potential. For the dwarf models instead, the softening is $\varepsilon = 0.3 R_h$ for halo particles and $\varepsilon = 0.1 R_h$ for star and gas particles, where R_h is the disk scale length (see Table 4.1).

4.3.2 Simulations

The dwarf galaxy satellites are placed on bound eccentric orbits in the primary halo. In Mayer et al. (2001b) we explored a wide range of orbital eccentricities and initial disk inclinations. Tidally induced transformation was found to be essentially independent on disk inclination (with only purely retrograde encounters versus purely prograde encounters showing significant differences). We also found that the orbital time, and not the orbital eccentricity, is the most sensitive orbital parameter for causing the transformation since it determines both the strength and number of tidal shocks. Here we choose orbits with an apocenter to pericenter ratio of 5, corresponding to the mean value for satellites in cosmological simulations (Ghigna et al. 1998, Gill et al. 2004), and we consider apocenters of 250 or 150 kpc (the pericenter being 50 or 30 kpc) corresponding to orbital times of, respectively, 3.2 and 1.3 Gyr. The dwarf galaxies start at apocenter and are evolved for 3 to 5 orbits with their disks initially inclined 60 degrees with respect to their orbital plane. Different mean orbital distances radii could be associated to satellites infalling into the Milky Way halo at different cosmic epochs (Mayer et al. 2001b; Kravtsov et al. 2004; Gill et al. 2004), say at $z > 1$ or $z < 1$, for, respectively, the smaller and larger orbital time.

The simulations were performed with the parallel Tree+SPH code GASOLINE (Wadsley, Stadel & Quinn 2004). The internal energy of the gas is integrated using the asymmetric formulation, that gives results very close to the entropy conserving formulation

Table 4.2: Parameters of the wind tunnel (WT) simulations. Column 1: Model Galaxy (see Table 1). Column 2: Gas physics (AD=adiabatic, RC=radiative cooling). Column 3: Angle between z-axis of the disk and direction of the flow. Column 4: Mass remaining in the disk at after 5×10^8 years (in units of $10^7 M_\odot$). Column 5: Stripping radius in kpc. Column 6: Stripping radius (in kpc) predicted using analytical prediction (see text). Column 7: name of run (LR stands for "low resolution", see text).

Model	gas physics	i	M_{fin}	R_{strip_1}	R_{strip_2}	RUN
V28c4	AD	0	0	0	0	T1c4a
V28c4	AD	90	0	0	0	T2c4a
V28c4	RC	0	0	0	0	T3c4a
V28c4	RC	45	0	0	0	T4c4a
V28c4	RC	90	6	0	0	T5c4a
V60c4	AD	0	57	4.25	5.8	T1c4b
V60c4	AD	30	66	4.25	5.8	T2c4b
V60c4	AD	60	64	4.25	5.8	T3c4b
V40c20	AD	0	4.38	1.58	1.6	T1c20
V40c20	AD	0	3.6	1.5	1.6	T1c20LR
V40c20	RC	0	6.2	1.75	1.6	T2c20
V40c20	RC	90	7.85	2	1.6	T3c20

(Springel & Hernquist 2003) but conserves energy better. In simulations without radiative cooling the gas can heat or cool only by adiabatic compression or expansion. Dissipation in shocks is modeled using the quadratic term of the standard Monaghan artificial viscosity. The Balsara correction term is used to reduce unwanted shear viscosity (Balsara 1995). A detailed description of the SPH code is given in Wadsley et al. 2004.

We perform both adiabatic runs and runs with radiative cooling. We use a standard cooling function for a primordial mixture of hydrogen and helium (the metallicity in dSphs is indeed much lower than solar, with $-1 <<\text{Fe/H}>< -2$, see Gallagher, Grebel & Harbeck 2003). Cooling shuts off below 10^4 K. The initial temperature of the gaseous disks is 8000 K for the most massive model ($V_{max} = 62$ km/s) and slightly lower for the other lighter models.

The purpose of running adiabatic simulations is two-fold; first, it helps in understanding the interplay between thermodynamical and mechanical effects of ram pressure as we shall see in the following section, and second heating by external radiation fields or stellar feedback, especially in low mass objects as those considered in this paper, might overtake radiative cooling and create a hot phase that would essentially behave as an adiabatic gas (Thacker & Couchman 2000; Marcolini et al. 2003; Springel & Hernquist 2003). Therefore radiative cooling and adiabatic runs can be regarded as two extreme cases crudely bracketing the conditions of the real interstellar medium in which a hot and a cold phase will coexist at all times. Finally, in a few runs with cooling we also include a uniform external radiation field which models the cosmic UV background arising at high redshift. This is implemented using the Haardt & Madau (1996) model which includes photoionizing and photoheating rates produced by QSOs and galaxies starting at $z = 7$. We implicitly assume that the dwarf enters the Milky Way halo at $z = 7$. The ionizing flux remains quite high until $z = 2$, therefore the dwarf is exposed to the radiation for a duration of ~ 5 Gyr.

We complement our "full interaction" runs (hereafter FI runs), so called because they include both tides and ram pressure, with wind tunnel simulations aimed at studying the effect of ram pressure alone.

The volume of the simulations is a tube with rectangular section, having a base equal to the diameter of the dwarf model (out to its virial radius) and height $h = vt$, where v is the typical velocity of the satellite at pericenter in the FI runs ($290\,\mathrm{km\,s^{-1}}$) and t is set ~ 0.5 Gyrs ($t_{enc} = R_{peri}/V_{peri}$, where t_{enc} is the time the dwarf spends near pericenter of the orbits in the FI runs). We represent the hot gas as a flux of particles moving with a velocity v along the longest axis of the tube, this being parallel or at an angle with the angular momentum of the disk depending on the run. The hot particles have an initial random distribution, a temperature $T = 10^6$K and a number density $n_h = 8 \times 10^{-5}\mathrm{cm}^{-3}$. We use periodic boundary conditions in order to restore the flow of hot gas that leaves the tube. We will indicate these as WT runs (where WT stands for wind tunnel). These experiments allow to resolve the background gas flow with very high resolution, thus limiting numerical artifacts like the spurious stripping induced by transfer of momentum in two-body collisions between the hot halo particles and the gas particles in the disk of the dwarf (Abadi, Moore & Bower 1999).

The mass of the gas particles is equal to that used for the dwarfs in the FI runs, i.e. $8 \times 10^4 M_\odot$, for the runs employing our largest dwarf model, V60c4, while it is 8 times lower for the runs employing the other two models, V28c4 and V40c20, since these have correspondingly lighter disks. The (adiabatic) runs with models V28c4 and V40c20 where repeated with a lower resolution of the background flow, equal to that of the FI runs. The total number of particles used in the hi-res WT runs thus varies from 10^6 in runs with models V28c4 and V40c20 to 2×10^5 in runs with model V60c4.

4.4 Results

Table 4.1 and 4.2 report the results of the FI and WT runs. Dwarf galaxies undergo severe stripping owing to the combined action of tides and ram pressure. The overall mass loss varies depending on the dwarf galaxy model, in particular the depth of its potential well, on its orbit and on the gas physics (the balance between cooling and heating). Dwarfs can retain $20 - 50\%$ of their initial gas content or be completely stripped. Ram pressure stripping occurs very rapidly as the galaxy approaches pericenter for the first time. A bow shock is visible (Fig. 4.2) and reflects the fact that the dwarfs near pericenter are moving at mildly supersonic velocities in the hot halo owing to their eccentric orbits (the Mach number is ~ 1.5).

The tidal shock at first pericenter passage deforms the disk to an extent that depends on how deep is the potential well of the galaxy. Symmetric stellar tidal tails develop but but the gas generally trails the galaxy since ram pressure sweeping dominates (compare gas and stars in Fig. 4.3). The dark halo loses most of its mass in all cases and the overall depth of the potential well is reduced which increases the efficiency of gas removal. The stars develop a bar instability due to the strong tidal perturbation (Fig. 4.3) which drives a radial gas inflow (Mayer et al. 2001b). This inflow counteracts the reduction of the

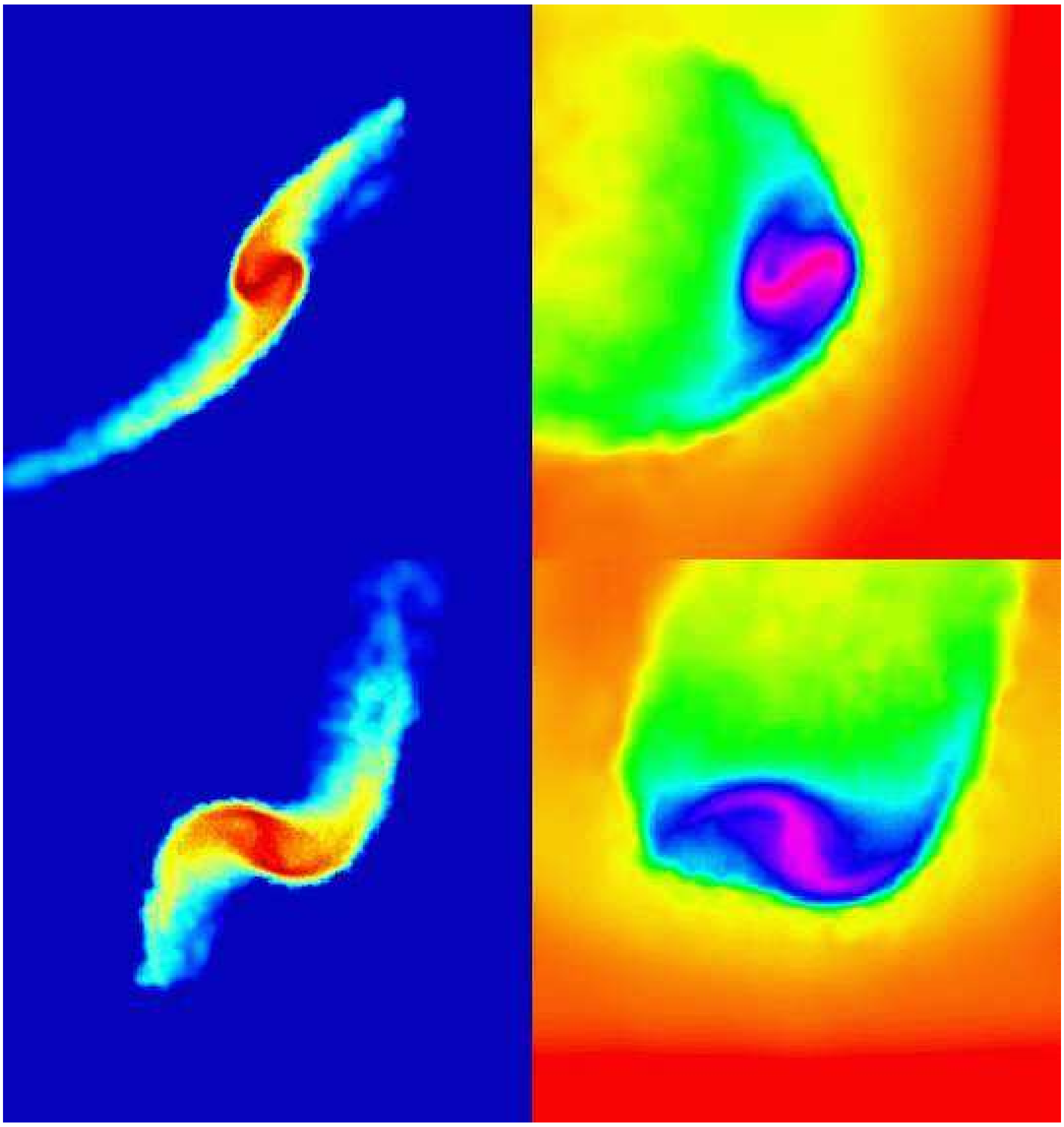

Figure 4.2: Color coded logarithmic density maps for run Rc4aADHR. Projections along (top) and perpendicular to the orbital plane (bottom) are shown for the stars (left) and for the gas component (right). Snapshots are taken at $T = 1.7$ Gyr, while crossing pericenter for the first time. Boxes are 100 kpc on a side for the stars and 30 kpc on a side for the gas (a smaller box is used for the gas to show its structure in greater detail). The two color maps are such that colors go, respectively, from blue to red through yellow (stars) and from red to magenta through yellow and green (gas) going from lower to higher densities.

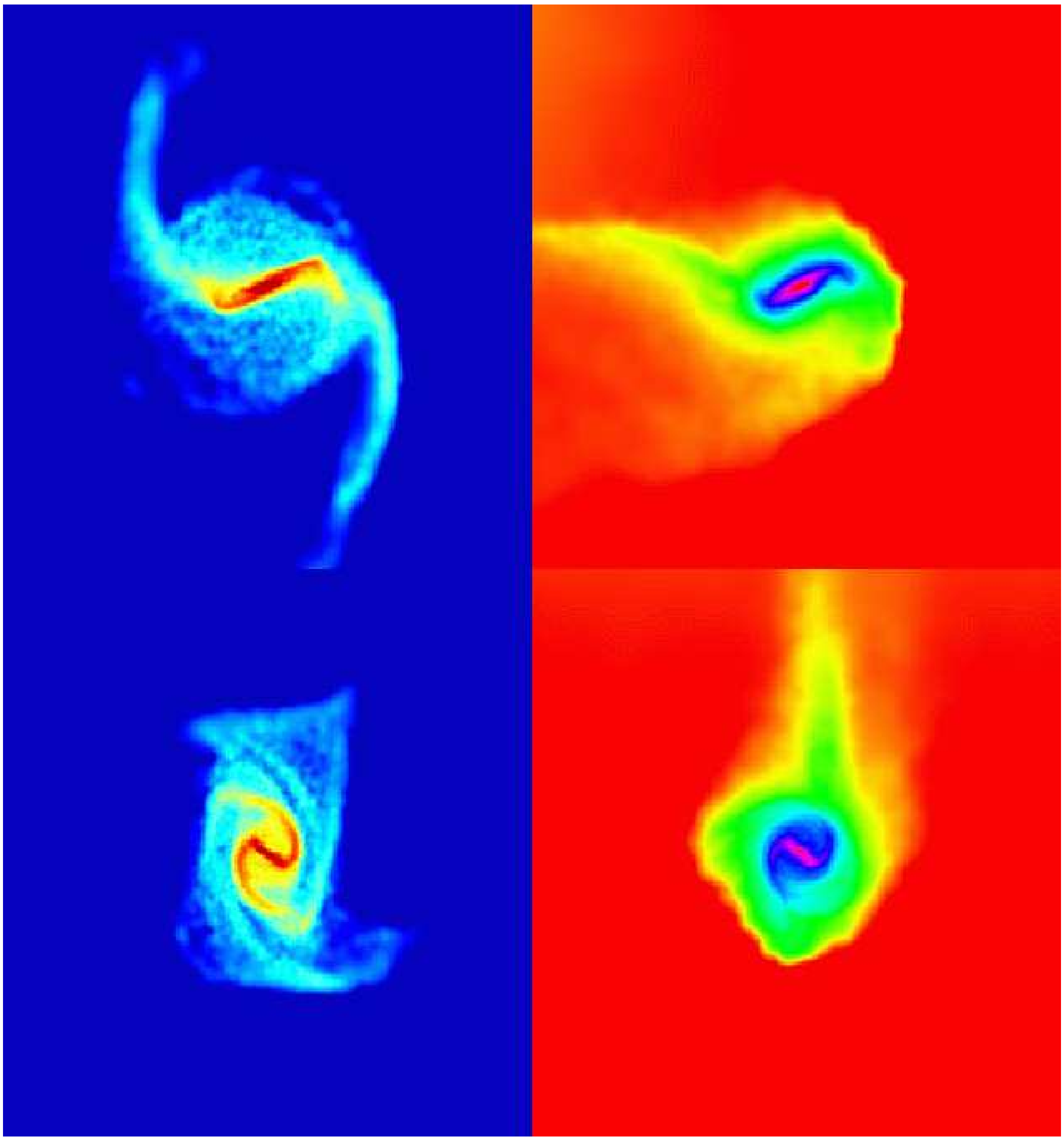

Figure 4.3: Color coded logarithmic density maps for run Rc4aADHR. Projections along (top) and perpendicular to the orbital plane (bottom) are shown for the stars (left) and for the gas component (right). Snapshots are taken at $T = 3$ Gyr, after first pericenter passage. Boxes are 50 kpc on a side.

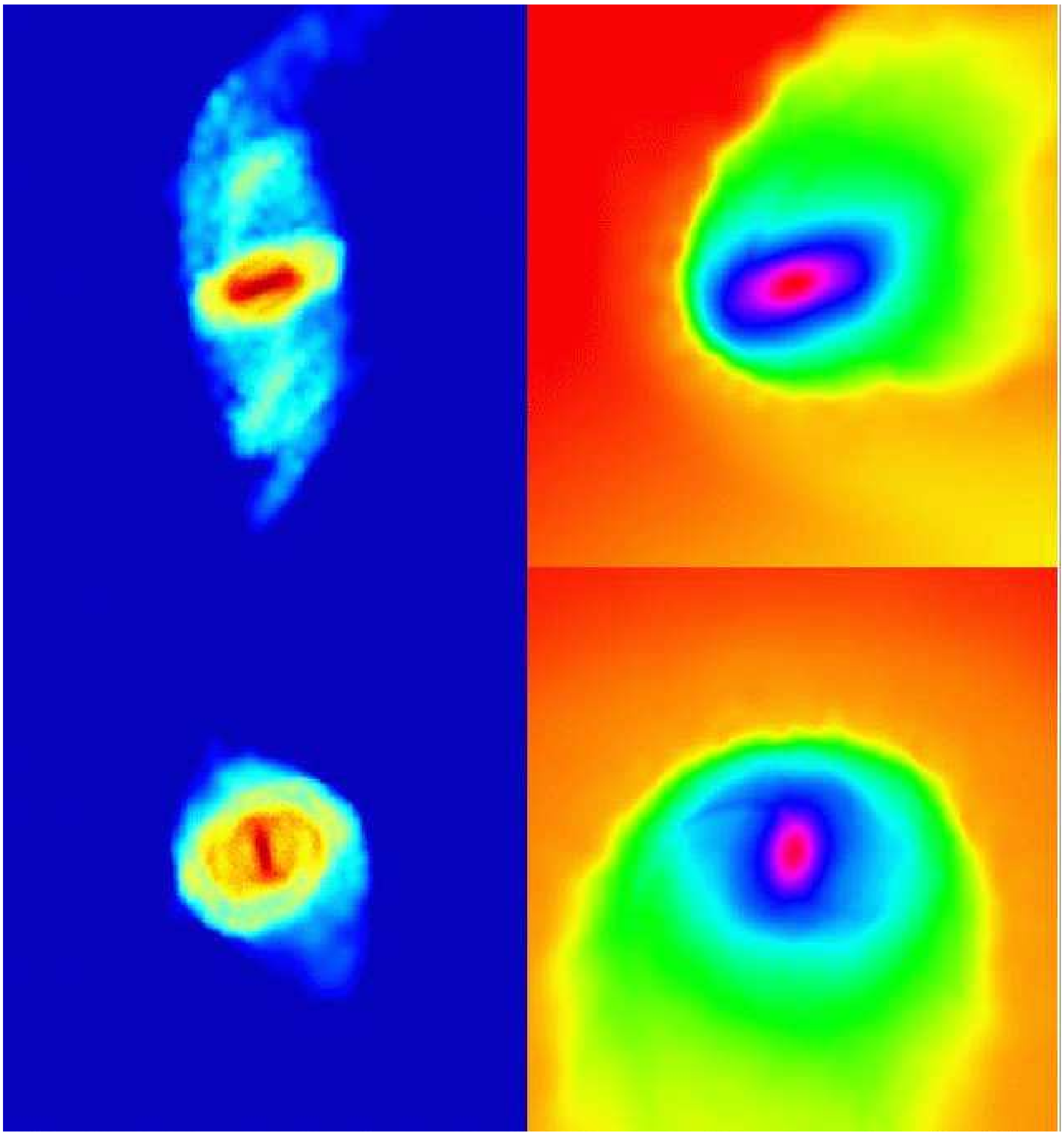

Figure 4.4: Color coded logarithmic density maps for run Rc4aADHR. Projections along (top) and perpendicular to the orbital plane (bottom) are shown for the stars (left) and for the gas component (right). Snapshots are taken at $T = 6$ Gyr, after the second pericenter passage. Boxes are 50 kpc on a side for the stars and 25 kpc on a side for the gas.

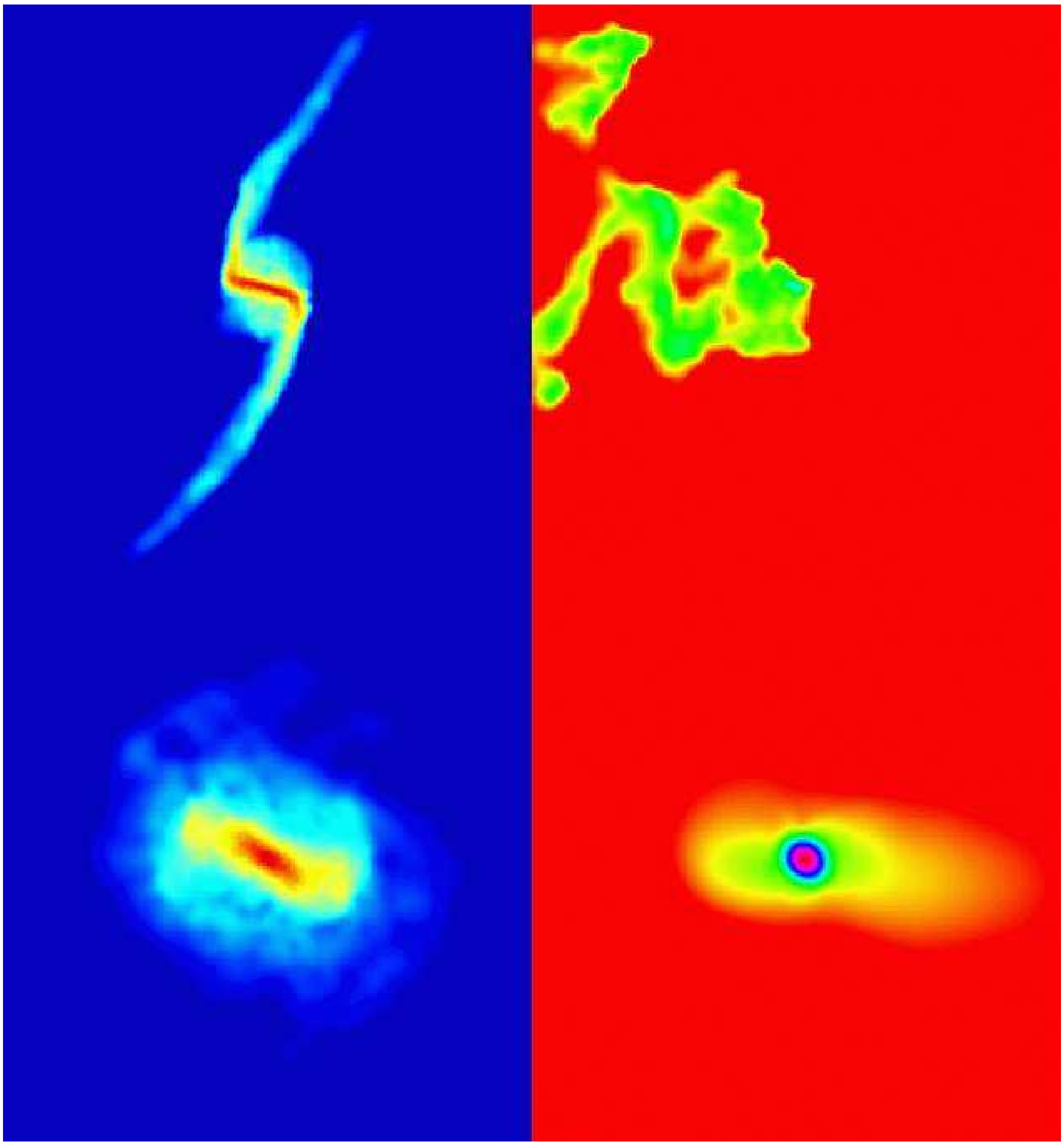

Figure 4.5: Color coded gas density (right) and stellar logarithmic density maps (left) for run Rc4bRC. Projections along the orbital plane are shown in a box of 30 kpc on a side at $T = 1.7$ Gyr (top) and in a box of 10 kpc on a side at $t = 6$ Gyr (bottom) after the second pericenter passage. All boxes are centered on the center of mass of the bound stars. Re-accretion of gas between the two different times has clearly occurred (the gas distribution is completely displaced from the stars at $T = 1.7$ Gyr).

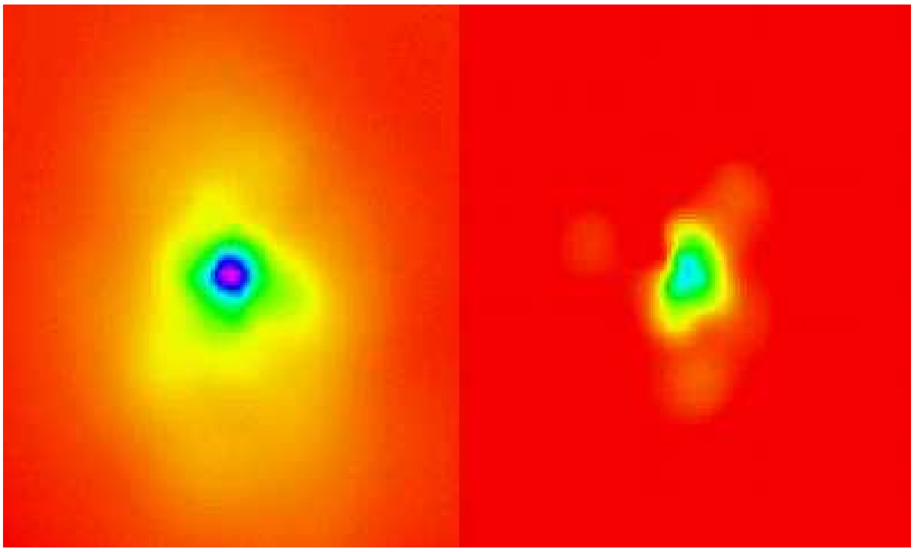

Figure 4.6: Color coded logarithmic gas density maps for run Rc20RC (left) and for run Rc20RCUV (right) at $t = 5$ Gyr, after three pericenter passages. The projection along the orbital plane is shown. The boxes are 10 kpc on a side and are centered on the center of mass of the bound stars. Clearly the gas remaining in the dwarf is much less and much more diffuse when UV heating is added.

mean restoring force by moving some gas deeper towards the center of the dwarf where it is harder to strip (note the central density concentration in Fig. 4.4-4.6). As a result on subsequent orbits ram pressure stripping continues but with much lower intensity.

In what follows we will describe the results quantitatively by analyzing the gas mass loss in FI and WT runs as well as the fate of the stripped gas.

4.4.1 Gas mass loss

4.4.1.1 Wind tunnel (WT) runs

Fig. 4.7- 4.10 show the evolution of the gas component of the dwarfs.

In the absence of an external perturbation the stellar disks are stable to bar formation.

Removal of gas begins immediately; a bow shock develops and some gas in the disk rises above the disk plane slightly more than 10^7 years. This is evident in the early truncation of the gas surface density profiles (see Fig. 4.12). The stripped gas is diffuse in adiabatic runs whereas it breaks into clumps pressure confined by the external medium in the cooling runs (see Fig. 4.8). The evolution of the temperature of the gas is shown in Fig. 4.11. As the hot halo pushes the gas out of the disk it also rises its temperature to $\sim 10^5$ K as a result of compression. If radiative cooling is included the gas quickly cools down to 10^4 K; cooling occurs on a timescale shorter than 10^7 years since the gas is heated to temperatures at which the cooling rate is maximum. Occasionally gas particles that did not gain enough momentum to leave the disk fall back towards the midplane as they cool down (compare for example Fig. 4.7 and 4.8 for run T2c20 - the disk appears more intact at a later time). The distribution of the gas becomes slightly more concentrated towards the midplane of the disk (see the evolution of the surface density profiles in Fig. 4.12), and subsequent stripping is harder. In adiabatic runs, instead, the heated gas remains hot and expands; the gas disk thickens and it is stripped more easily than in the cooling runs (see Fig. 4.8) as its own pressure support makes it less bound to the disk potential. No stripped gas falls back to the disk. We consider as "stripped" all the gas that is removed from the stellar disk.

Table 4.2 also includes the stripping radii found in the simulations, defined as the minimum distance from the center of the dwarf at which gas particles are stripped.

Some of the WT runs were performed twice, using a resolution of the background flow equal or higher than that of the FI runs employing the same model (see Section **??**); we found differences within 20% for the gas mass loss and even less for the stripping radii.

Table 4.2 reports the gas mass in the disk measured after 0.2 Gyr. The difference in the amount of stripped mass between runs with and without cooling is visibly higher than that between runs adopting different disk inclinations; indeed inclination effects are appreciable only when extreme cases are compared, namely an edge-on versus a face-on run (where the disk inclination is intended relative to the direction of motion of the background gas flow). We note that for the most massive model, V60c4, we have performed only adiabatic runs since our main goal here is to estimate the maximum amount of mass that can be stripped by ram pressure alone. The difference between runs with and without radiative cooling is smaller in terms of stripping radii than it could be guessed from the difference in the amount of stripped mass (Table 4.2). The reason is that the distribution of gas in the cooling runs becomes more concentrated (thus a given radius contain more mass) as we noted before.

Our results show that model V28c4 is completely stripped in all cases (e.g. Fig. 4.9) except when cooling and an inclination of 90 degrees with respect to the flow are used at the same time (both choices go in the direction of minimizing stripping). Instead the models V60c4 and V40c20 always retain a significant amount of gas. This indicates that if the progenitors of dSphs once had massive halos corresponding to $V_{peak} \sim 50$ km/s, as suggested by recent cosmological simulations (Kravtsov, Gnedin & Klypin 2004), ram pressure alone was not able to remove their gas early on unless the halo density was once significantly higher than 10^{-4} atoms cm^{-3}. On the other end, these results also suggest that efficient gas removal from ram pressure could have happened at some later stage if tides were able to weaken the potential well of the dwarf bringing V_{peak} down to ~ 30 km/s. Interestingly, an NFW halo with $V_{peak} \sim 30$ km/s or lower does fit the present-day velocity dispersion of dSphs (Lokas 2002; Kazantzidis et al. 2004). We will come back to this in the following sections

We tried to compare our numerical results with simple analytical estimates of the effectiveness of ram pressure stripping. Gas is removed from the disk of the dwarfs if the ram pressure force is greater than the restoring force per unit area provided by the disk and halo of the dwarf. The condition for ram pressure stripping for an axisymmetric disk system is expressed by (Gunn & Gott 1972)

$$\rho_h v^2 > 2\pi G \Sigma(R) \Sigma_g(R), \tag{4.2}$$

where v is the velocity of the galaxy with respect to the surrounding medium, ρ_h is the density of the hot halo of the MW and $\Sigma_g(r)$ is the cold gas surface density at the radius R. Σ represents the surface mass density of the disk. The minimum radius given by Equation 4.2 is the final stripping radius R_{str} beyond which the ISM can be removed from the galaxy.

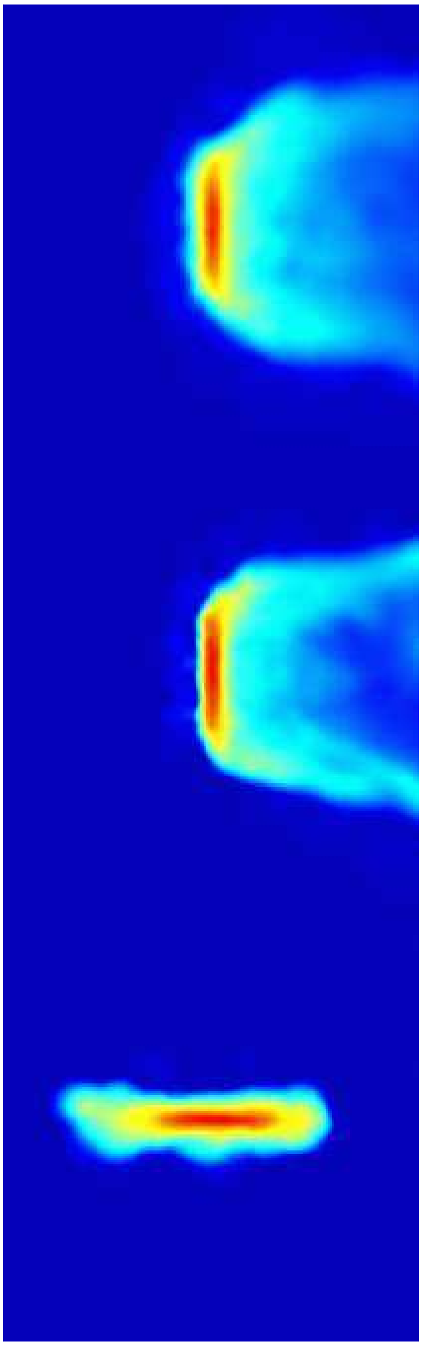

Figure 4.7: Color coded logarithmic gas density map for three wind tunnel (WT) runs. From top to bottom, an edge-on view after $t = 0.05$ Gyr of the gas disk in runs T1c20, T2c20, T3c20. The background gas flows along the horizontal axis from left to right (from right to left in the bottom panel). Boxes are 10 kpc on a side.

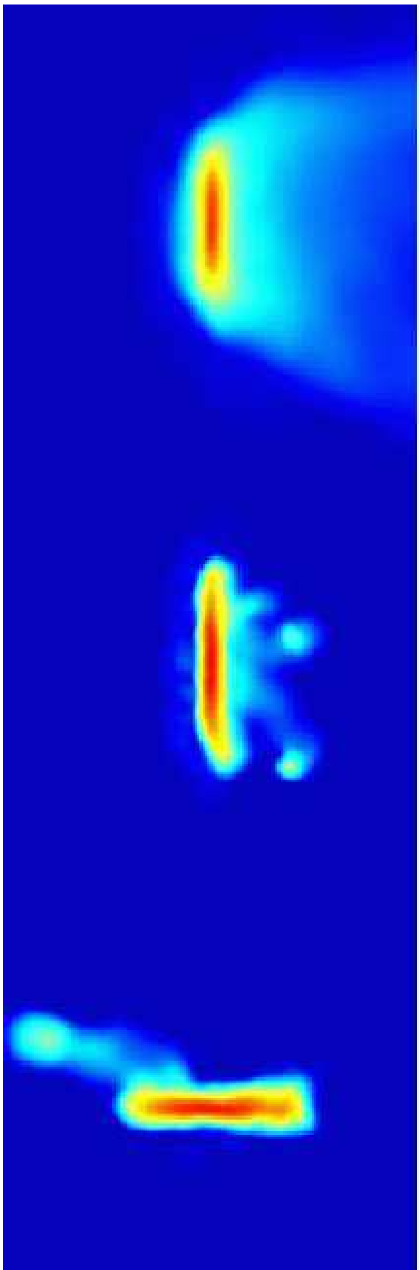

Figure 4.8: Color coded logarithmic gas density map for three wind tunnel (WT) runs. From top to bottom, an edge-on view after $t = 0.3$ Gyr of the gas disk in runs T1c20, T2c20, T3c20. The background gas flows along the horizontal axis from left to right (from right to left in the bottom panel). Boxes are 10 kpc on a side.

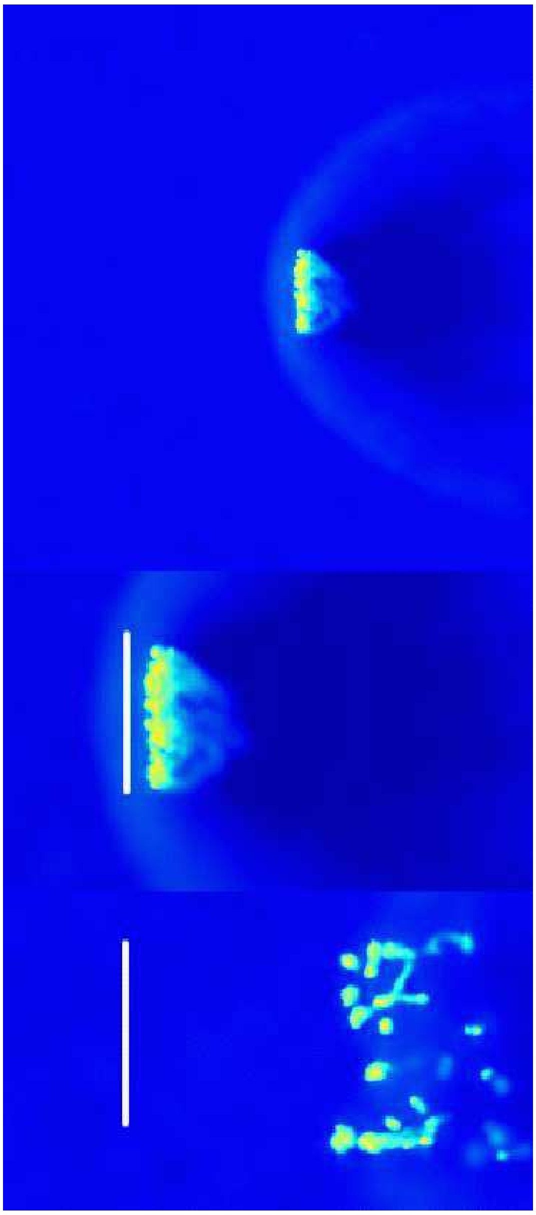

Figure 4.9: Color coded logarithmic gas density map for the gas of the dwarf in run T2c4b. On top the output after $t = 0.05$ Gyr is shown in a box of 30 kpc on a side. The bow shock is clearly visible. In the middle panel we show a zoom-in of the same snapshot (the box is 10 kpc along the longest axis). The bottom panel shows a zoom-in of a snapshot taken after t=0.3 Gyr (the box is also 10 kpc along the longest axis). The white vertical bar shows the location of the stellar disk. Complete gas stripping occurs in this case. The background gas flows along the horizontal axis from left to right.

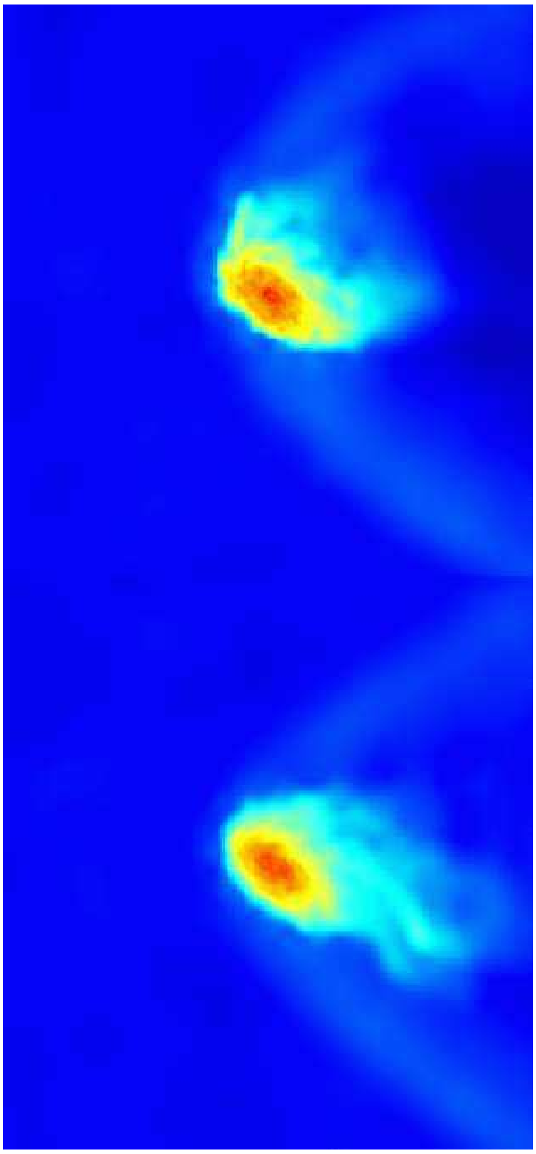

Figure 4.10: Color coded logarithmic gas density map for the gas of the dwarf in run T2c4b. From top to bottom, the outputs after $t = 0.05$ Gyr and $T = 0.3$ Gyr are shown. The boxes are 30 kpc on a side. The background flow is along the horizontal axis from left to right.

Equation 4.2, however, neglects the contribution from dark matter to the restoring force (see Gavazzi et al. 2001). In all of our models the dark matter content is high even near the disk; we will simply account for that by replacing $\Sigma(R)$ with $\Sigma_{dm} + \Sigma_b(R)$, where Σ_{dm} is the surface mass density of the dark matter in a slab with height comparable to the disk thickness and $\Sigma_b(R)$ is the surface mass density of the baryons within the same slab (in our models the gas component always gives a non negligible contribution to the disk mass). This formula describes the instantaneous stripping of gas. We found it difficult to use this prescription as to reflect both the complex interplay between mechanical and thermodynamical effects seen in the simulations and the fact that the stripping is not exactly instantaneous but continues for some time (typically it saturates after ~ 0.2 Gyr). In particular, $\Sigma_g(r)$ is strongly time dependent due to the action of heating and cooling as we noted above. We find that a reasonable prediction can be obtained if we choose not the initial $\Sigma_g(r)$ but that at the time the gas begins to heat up (as little as 10^6 years after the beginning of the simulations). The predicted stripping radius (see Table 4.2) can be slightly larger than that in the simulations (even for runs with cooling). However, the prediction is always close to the stripping radius measured in the simulations at earlier times, i.e. when the approximation of a single, instantaneous stripping event is better satisfied.

4.4.1.2 Full Interaction (FI) runs

In these runs the dwarf galaxy evolves under the combined action of tides and ram pressure. The mass loss as a function of time for a number of runs is shown in Figure 13. At any given time we identify as bound to the dwarf the gas with temperature $T < T_{vir}$ (where T_{vir} is the initial virial temperature of the halo of the dwarf, in the range $\sim 3 \times 10^4 - 10^5 K$ depending on the model) and which is located within the bound stellar component. We checked that by using this definition one essentially selects the gas that is gravitationally bound to the dwarf.

The angle between the direction of the flow in the hot halo and the plane of the disk is continously changing because of the orbit of the galaxy and since the disk inclination relative to the orbit changes as the dwarf is tidally torqued by the primary. We compare the gas mass losses observed in FI runs with those occurring in the face-on WT runs which yield the highest possible gas mass loss due to ram pressure only. In general galaxies lose more gas compared to WT runs (compare Table 4.1 and Table 4.2 for both adiabatic and cooling runs). However, as we found previously, only in some of the runs (mostly those employing model V28c4) is the dwarf completely stripped of its gas content (see Table 4.1). Furthermore, while with tides added a dramatic increase in the stripping is always observed in adiabatic runs, stripping can be unexpectedly less effective in cooling runs (compare run Rc4bRC in Table 4.1 with all the “c4a” runs in Table 4.2).

This happens because the tidally induced bars funnel $20-40\%$ of the initial gas content of the disk within a radius smaller than the initial disk scale length of the dwarf.

The gas shocks through the bar as it loses angular momentum and heats up. In adiabatic runs this heat cannot be dissipated quickly and the gas ends up more extended.

In cooling runs the gas loses rapidly its thermal energy and there is not enough pressure to stop its inflow. As a result gas profiles become much more concentrated in cooling runs and a larger amount of gas ends up deeper in the potential well where it is harder to strip (Fig. 4.14-4.15). In runs which include the heating from the UV background the gas remains more extended than with just radiative cooling (Fig. 4.6) and stripping is much more efficient, with gas mass losses closer to those of adiabatic runs.

Despite the complex interplay between bar instability and thermal physics, it turns out that the fractional amount of stripped mass correlates well with the initial V_{peak} of the satellite on a given orbit, both with and without cooling (for example compare run Rc4cRC and run Rc20RC in Table 4.1, or run Rc4aRCUV and run Rc4bRC). For the same initial V_{peak}, orbits with smaller pericenter lead to a larger reduction in the V_{peak} due to more numerous and stronger tidal shocks (Fig. 4.17). This favours ram pressure stripping as it lowers the gravitational restoring force. Furthermore, on orbits with a pericenter of 30 kpc the maximum halo gas density is about a factor of 3 higher relative to the case with a pericenter of 50 kpc, and this also favours ram pressure stripping. As a consequence gas mass loss is significantly larger and faster in runs using a more plunging orbit (Table 4.1).

Estimating the stripping radius from formula 4.2 is somewhat meaningless in these runs because the depth and shape of the potential of the dwarf is continously changing due to the action of tides and the distribution of the bound gas also changes with time. Nonetheless, it is noteworthy that the stripping radius estimated using formula 4.2 with the parameters of the initial models is from 2 to 3 times larger than the radius at which most of the bound gas sits in the FI runs after the first pericenter passage, hence after bar formation and inflow. This is because the remaining bound gas is that material which flows to the center of the bar.

One interesting feature of cooling runs is that sometimes re-accretion of gas is observed. This is clearly shown by the sequence in Fig. 4.5 (compare the location of the stars and the gas at the two different times) and also shows up in some of the curves of the mass loss (top panel in Fig. 4.13). This happens when gas is stripped from the disk near pericenter but does not have enough momentum to escape the galaxy. As the galaxy moves towards apocenter, where relative velocities are lower, the gas falls back onto the disk. This is not observed in adiabatic runs because gas that has been removed from the disk quickly becomes hotter than the virial temperature of the dwarf halo.

We repeated several of these simulations without a gaseous halo to isolate the efficiency of gas removal by tides alone. The amount of gas stripped is a factor of 3 to 6 less than the simulations which include ram pressure stripping, depending on the radiative cooling (Fig. 4.13).

When compared with the WT runs where only ram pressure is included, tides strip from similar to appreciably lower amounts of mass (lower panel of Fig. 4.13). The relative increase of stripping when ram pressure is added to tides is maximum for model V40c20, that has the steepest rise of the dark matter density in the center (see Fig. 4.1). This reflects the different physical scalings of ram pressure and tidal forces. In these highly concentrated halos the response to tidal shocks is nearly adiabatic near the center (Taffoni et al. 2003; Kazantzidis et al. 2004), hence stripping is expected to be minimal inside $R_{v=v_{peak}}$. However, this is applicable only to stripping induced by tidal shocks; the timescale on which istantaneous ram pressure acts is instead much smaller than that of tidal shocks, $< 10^7$ years (we follow Mori & Burkert 2000 for parameters of e.g. run Rc20V60RC) against $\sim 10^8$ years ($\sim R_{peri}/V_{peri}$). Such timescale is also smaller than the local gas orbital time even in a highly concentrated halo ($> 10^7$ years) hence the response of the galaxy to ram pressure is impulsive instead of adiabatic. On the other end, the other models, having low concentration haloes, respond more impulsively to tides in the first place, so that the increase in stripping efficiency is not so dramatic.

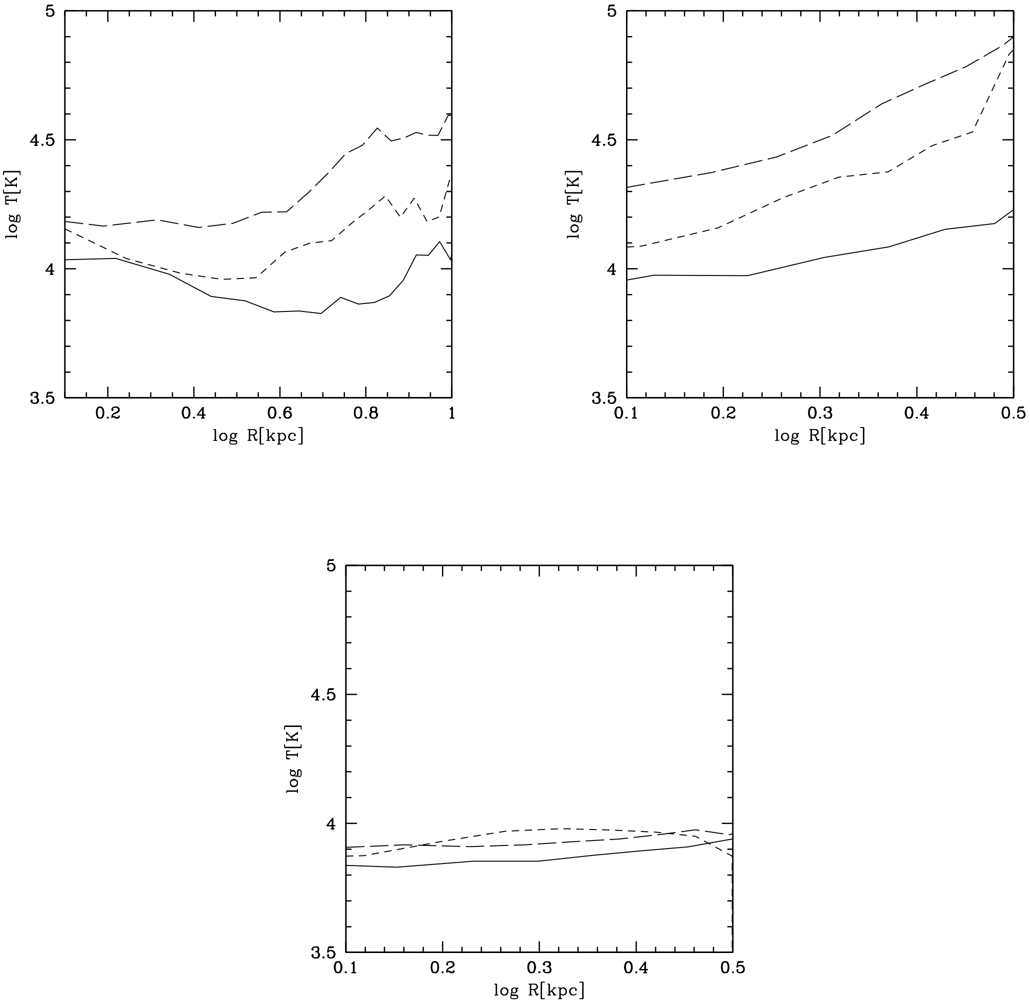

Figure 4.11: Evolution of temperature profiles of the gas in WT runs. Profiles are azimuthally averaged in a cylinder with height twice that of the stellar disk (R is the cylindrical radius). The solid line is for $t = 0.02$ Gyr, the short-dashed line for $t = 0.1$ Gyr and the long-dashed line for $t = 0.3$ Gyr. From left to right, run T1c4b, T1c20 and T2c20 are shown

.

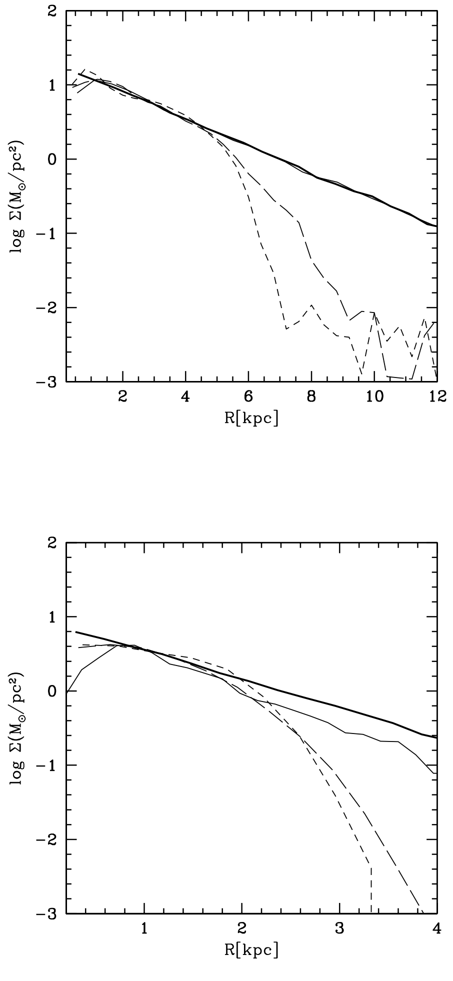

Figure 4.12: Evolution of density profiles of the gas in WT runs. Profiles are azimuthally averaged in a cylinder with height equal to that of the stellar disk (R is the cylindrical radius). The thick solid like is for $t = 0$, the thin solid line for $t = 0.02$ Gyr, the short-dashed line for $t = 0.1$ Gyr and the long-dashed line for $t = 0.3$ Gyr. From left to bottom, runs T1c4b, T3c4b, T1c20 and T2c20 are shown

.

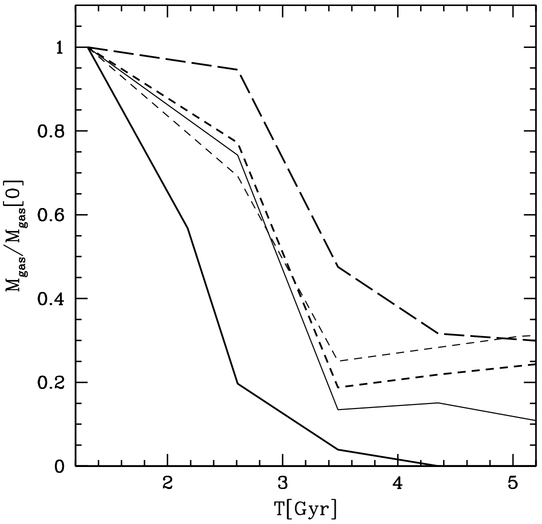

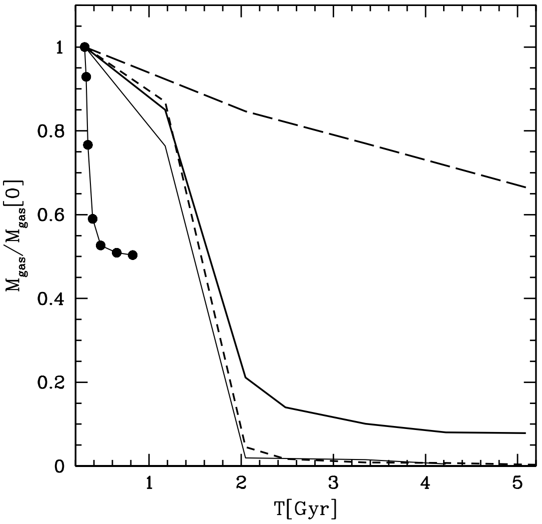

Figure 4.13: Time evolution of the bound gas mass for FI runs using model V60c4, V28c4 (top) and runs using model V40c20 (bottom). Top: run Rc4aAD (thin solid line), Rc4aRCUV (thin short-dashed line), Rc4bTD (long-dashed line),Rc4bAD (thick solid line), Rc4bRC (thick short-dashed line). Bottom: run Rc20TD (long dashed line), Rc20AD (thin solid line), Rc20RC (thick solid line line), Rc20RCUV (short dashed line). The line with dots shows the mass loss rate (due to ram pressure only) for one of the WT runs, T1c20 (see Table 4.2 – the curve stops at less than 1 Gyr since WT runs were run for a short timescale since stripping saturates very early on.

In these simulations the peak velocity of the rotation curve of the satellites, V_{peak}, drops by $20-50\%$ after several orbits (Fig. 4.17) while in cosmological simulations it often decreases by more than a factor of 2 over several Gyr (Kravtsov et al. 2004, but see Ghigna et al. 1998). Such difference may be due to the limited number of orbital configurations here explored (some of the satellites in Kravtsov et al. (2004) have pericenters even smaller than 30 kpc) and/or to the fact that cosmological runs do not include baryons and do not have enough force and mass resolution to follow the complex disk evolution, especially bar formation and the resulting gas inflows that can produce a remarkable increase in the central density (our force resolution is 5 times better than the best published cosmological simulations with baryons). These issues will be investigated systematically in a forthcoming paper (Kazantzidis, Mayer et al., in preparation).

In summary, the final gas fractions drops to $0-50$ % of the initial gas content for galaxies on orbits with pericenter of 50 kpc, with 10% being a typical fraction, and to as low as $0-6$ % of the initial values for galaxies on an orbit with pericenter of 30 kpc (see Table 4.1). In the runs that include the effect of the cosmic UV background even when there is gas left inside the dwarf this is ionized, and the observational upper limit on the mass of neutral hydrogen in dSphs, $M_{HI} < 0.01\ M_s$, where M_s is the stellar mass, is fully satisfied. The gas will be able to recombine later on as the cosmic background fades away, but the local ultraviolet radiation flux from the Milky Way or M31 might be enough to keep it ionized even at low redshift (Maschenko, Carignan & Bouchard 2004). The current upper limits on the total amount of gas in dSphs including the ionized component, are much higher, $M_g < 0.1 M_s$ (Gallagher et al. 2003) , and are satisfied in the final states of the dwarfs for the majority of our runs. Hence a combination of ram pressure and tidal stripping succeeds in explaining how dwarf spheroidals have little or no neutral hydrogen today. On any given orbit, dwarf models with higher V_{peak} are stripped less severely and, in particular, our most massive model, V60c4, ($V_{peak} = 62$ km/s), always retains a substantial amount of gas. This is consistent with the fact that bright dwarf elliptical (dEs) satellites of M31, like NGC205, whose central velocity dispersion, $\sigma = 30-45$ km/s, is comparable to that of the evolved states of model V60c4, do have some amount of neutral gas (Mateo 1998).

When neutral gas remains in the dwarfs, most of it will be rapidly turned into stars as it reaches very high densities due to the effect of the bar, and bursts localized near the center of the dwarf are expected at pericenter passages. as described in Mayer et al. (2001a). Hence we predict that the higher the mass of the dwarf (not its luminosity) the more extended its star formation history should be.

For dwarfs that start out with similar masses, our simulations suggest that the outcome will vary depending on their orbit.

A signature in the star formation history of the dwarfs is expected at the epoch when it underwent the first close approach within the Milky Way. This can be either a burst or a marked depression of the star formation depending on whether just a fraction or most of the gas is removed from the dwarf galaxy.

4.4.2 Kelvin-Helmholtz instabilities and turbulent stripping

Gas that survives istantaneous ram pressure can be stripped by the Kelvin-Helmholtz (KH) instability developing at the interface between the gas of the dwarf galaxy and the ISM (Nulsen 1982; Murray et al. 1993, Quilis et al. 2000). This is also known as turbulent stripping since the gas reaches a turbulent state as the instability develops. In order to develop KH instabilities require a sharp boundary to exist between the two fluids. Even at the high resolution adopted here SPH is hardly capable of resolving KH instabilities mostly because the artificial viscosity and the fact that densities are smoothed in SPH both contribute to "blur" any sharp interface. An approximate "effective" local kinematical viscosity can be calculated as $\nu = \alpha c_s h/8$, where α is the coefficient of the linear term in the artificial viscosity, c_s is the sound speed and h is the SPH smoothing length (Lufkin et al. 2004). The Reynolds number is then $Re \sim Lv_{gal}/\nu$, where L is the typical size of the object moving in an external medium (the disk of the dwarf here) and v_{gal} is the speed at which it is moving; this number is strictly a function of position (since ν is a function of position) and is in the range $20 - 100$ in our runs (the highest Reynolds numbers occur in the highest resolution WT runs). This is of course much lower than the Reynolds numbers typical of turbulent flows (up to 10^4). Aside from numerical issues that might hamper the development of KH instabilities in the simulations we can ask whether turbulent stripping is likely to be important for dwarf galaxies moving in a very diffuse halo as those that we are modeling here. Mori & Burkert (2000) found that spherical dwarf galaxies moving at a few thousand km/s in a dense cluster hot halo will be stripped on a timescale significantly smaller than the crossing time of the galaxy in the cluster. Following Mori & Burkert (2000) we use the following equation to obtain an estimate of the expected characteristic timescale for stripping by KH instabilities including the stabilizing effect of gravity (which is mainly provided by the dark halo potential in our models);

$$\begin{aligned}\tau_{\rm KH} &= \frac{FM_0}{\dot{M}_{\rm KH}}, \qquad (4.3)\\ &= 2.19\times 10^9 \left(\frac{F}{0.1}\right)\left(\frac{M_0}{10^9 M_\odot}\right)^{\frac{1}{7}}\left(\frac{n_h}{10^{-4}{\rm cm}^{-3}}\right)^{-1}\\ &\qquad \times\left(\frac{v_{\rm gal}}{10^3{\rm km\ s}^{-1}}\right)^{-1}\ {\rm yr}.\end{aligned}$$

The equation assumes spherical symmetry, which is a reasonable assumption since our galaxies are dominated by a spherical dark matter halo. In the equation M_0 is the CDM halo mass within the radius R_{strip} down to which galaxies are stripped in the WT runs (see Table 4.2, these simulations offer a cleaner test case since they include only ram pressure), $F = M_{bar}/M_0$ is the mass ratio between the baryons and the CDM halo within the same radius, and $\dot{M}_{\rm KH} = \pi R^2_{strip}\rho_h v_{\rm gal}$ is the mass loss rate from the galaxy through KH instabilities (ρ_h is the hot halo density and v_{gal} is the velocity of the galaxy through the hot halo). For the gas densities ($\sim 10^{-4}$ atoms cm^{-3}) and velocities occurring at pericenter the timescale for KH stripping is, respectively, 4 Gyr for model V40c20 and 10 Gyr for model V60c4, these being the model galaxies in which instantaneous ram pressure is not capable of removing all the gas. For the gas densities and velocities where the satellites spend most of their time, namely at distances larger than 100 kpc, the KH stripping timescale is at least several Hubble times.

Shear viscosity in a laminar flow ($Re < 30$) can also produce a slow stripping of the gas with timescales and mass loss rates comparable to those of KH stripping in the turbulent regime (Nulsen 1982). Physical viscosity is not included in our treatment of SPH and therefore this viscous stripping mode is missing. Spurious viscous stripping from the artificial viscosity term is limited by our reasonably high resolution and the

Balsara correction. The characteristic viscous time is $\tau = L^2/\nu$ is ~ 10 Gyr, which means viscosity effects are negligible given that the important timescales, those related to ram pressure and tidal shocks, are much smaller (between 10^7 and 10^8 years). Tittley, Pearce & Couchman (2001) have shown that SPH can alter the magnitude and scaling with density of hydrodynamical drags because of the way pressure forces among neighboring cold and hot background particles are calculated (in essence the cross section of an object moving in a hot medium can be artificially enhanced or decreased). However, the effect is particularly severe, enhancing the drag over the expected value, only in the subsonic regime, whereas our galaxies all move at slightly supersonic velocities.

In summary, our simulations have enough resolution to overcome artificial viscous stripping but cannot model correctly turbulent stripping yet. However, although SPH is often blamed for its inability to model hydrodynamical turbulence we recall that published grid simulations are of similar quality when it comes to the ability to model turbulence – Marcolini et al. (2003) find Reynolds numbers similar to what we find.

4.4.3 Dark and baryonic contents of the remnants: can we explain Draco?

In FI runs the stellar disk is stripped and transformed into a spheroidal system by means of tidal heating and bar-buckling instabilities as described in Mayer et al. 2001a,b. The ratio M_{dark}/M_{bar} between dark matter mass and baryonic mass in the final objects varies between 3 and 12, the highest values occurring in runs with model V40c20. In remnants with the highest dark matter contents or highest central concentration of gas the buckling instability is weaker, with the result that the bar-like shape is preserved. The trend with gas concentration is consistent with the findings of Debattista, Mayer et al. (in preparation) for isolated bar-unstable galaxies with gas. However, in reality the central gas would form stars and its distribution will become less concentrated.

The final central v/σ of the stars is below 0.5, thus compatible with those of dSphs, and the central final velocity dispersions are in the range $10 - 30$ km/s.

We can ask whether the remnants of model V40c20, can reproduce the overall properties of Draco, one of the most extreme dSphs in terms of low luminosity and high M/L.

In adiabatic runs the gas is completely stripped after the first pericenter passage. The observed truncation of the star formation history in Draco could be thus interpreted as the result of its infall into the Milky Way halo. However, in runs with cooling some gas is retained. Assuming a star formation rate comparable to that deduced for Draco and Ursa Minor by Hernandez et al. (2000), $100 - 200 M_\odot$/Myr, we obtain that the remaining gas in run Rc20RC will be turned into stars in about 5 Gyr, leaving a dwarf completely devoid of gas. But this implies a fairly extended star formation history, contrary to what observed for Draco, and the amount of gas that needs to be turned into stars is non-negligible, $\sim 6 \times 10^6 M_\odot$; if we sum such mass to the remaining bound stellar mass we get $5 \times 10^7 L_\odot$. For a mass-to-light ratio ~ 4, as typical of old stellar populations we would get a luminosity $\sim 10^7 M_\odot$, i.e. 50 times higher than the V band luminosity of Draco (Odenkirchen et al. 2001).

Since the largest fraction of the final bayonic mass is contributed by the initial stellar mass in the model (tidal stripping is moderate in highly concentrated haloes) an excessive final luminoisty would result also in adiabatic runs. As for the dark matter content one would obtain $M/L = \sim 50$, as high as typical estimates for M/L in Ursa Minor and comparable to the lower limits for M/L in Draco (Mateo 1998; Wilkinson et al. 2004). The final projected central velocity dispersion, $\sim$ 15 km/s, is consistent with the peak velocity dispersion of Draco (Wilkinson et al. 2004). The central dark matter density measured for the stirred dwarf at the end of the simulation, $0.065 M_{\odot}/pc^3$ is also in rough agreement with the value estimated for Draco ($\sim 0.1 M_{\odot}/pc^3$). Thus run Rc20RC produces a model with roughly the right dark matter content but an excessive baryonic content. Adding heating and photoionization from a uniform UV background (run Rc20RCUV) aids gas removal and leaves essentially no neutral gas after a few Gyr. In this case the star formation history, as in the adiabatic runs, would have been essentially truncated after the first close encounter with the Milky Way. Nevertheless, the total stellar mass of the dwarf would still yield a luminosity about an order of magnitude higher than that of Draco.

The final luminosity depends on the initial stellar and gas content of the model, which was chosen to be fairly representative of the baryonic content of todays' dIrrs. Although Draco likely had a halo massive enough to resist gas removal from supernovae feedback or photoionization, the progenitors from which it assembled at very high redshift were certainly much smaller and were likely affected by these mechanisms. Hence one can imagine that the main progenitor of Draco had a baryon fraction much lower the one we used here. In such a scenario, however, environmental effects would not have played the primary role in setting the current high M/L of Draco. One alternative explanation is to imagine that Draco was a mostly gaseous disky dwarf by the time it entered the Milky Way, with minimal star formation having taken place. Such a low star formation rate can be simply the result of an extended, relatively high angular momentum disk being almost everywhere Toomre stable and below the density threshold necessary for star formation to happen, as observed today in some dIrrs and LSB galaxies (Verde, Oh & Jimenez 2002). To explore this possibility we have run a simulation in which the initial model has the same structural properties of model V40c20 except that now as much as 90% of the disk is gaseous. A weaker stellar bar forms given the lower stellar mass which produces a weaker gas inflow, and a larger relative fraction of the disk mass is stripped by ram pressure. In an adiabatic run all the gas is stripped after two pericenter passages, leaving a gas-free remnant that roughly matches the luminosity of Draco after $\sim$ 3 Gyr. In a run with cooling and the cosmic UV radiation of order $10^5 M_{\odot}$ of gas remain in the dwarf, but all this gas is ionized and no star formation would be possible, and even in this case the final stellar mass would be comparable to that of Draco.

4.4.4 Fate of stripped gas

The stripped gas has a very different fate in the adiabatic and in the cooling runs. In the adiabatic runs it ends up quite diffuse and hot ($T > 10^5$K) and quickly thermalizes and mixes with the gas in the MW halo. When cooling is allowed the gas along the tails fragments into dense clouds and sheet-like structures pressure confined by the ambient medium. This is shown in Fig. 4.18.

These clouds remain cold ($T < 10^5$ K) until they are dissolved as they sink deeper in the potential well due to gas drag. Sinking of the gaseous tails is marginal in the adiabatic runs because the stripped gas is too diffuse to experience significant drag. Fragmentation is suppressed in the first place in adiabatic runs because the density of the gas along the tails is too low for the cloud to reach pressure equilibrium within the hot ambient medium. In the simulations with UV heating, clouds are also present, although they are slightly

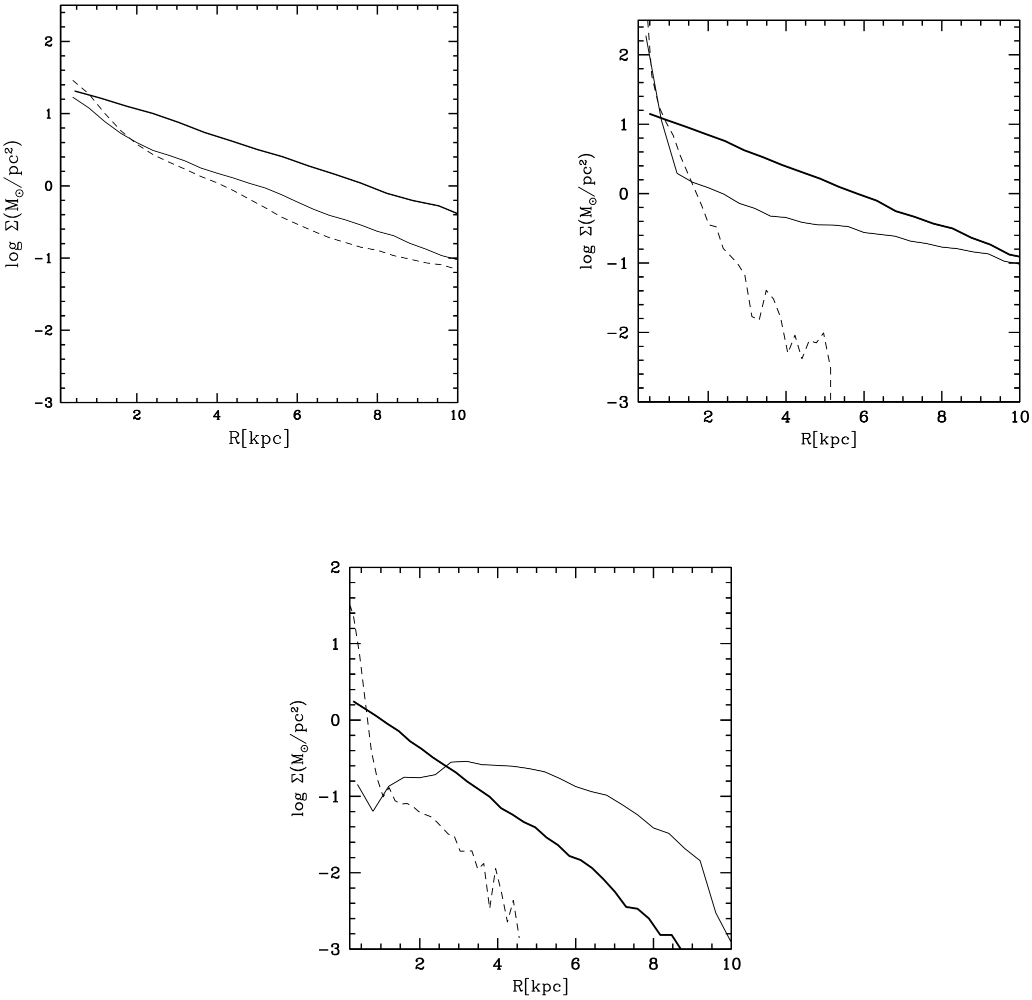

Figure 4.14: Evolution of gas surface density profiles in FI runs. The thick solid line is used for the initial profile, the thin solid line is used for the profile at T=3 Gyr (after first pericenter passage), and the dashed line is used for the profile at T=6 Gyr (after second pericenter passage). From top left to bottom, the runs Rc4aAD, Rc4aRCUV, and Rc4bRC are shown. The unusual shape of the profile at intermediate times in the bottom panel reflects the fact that gas is displaced from the galaxy at this point (see also Fig. 4.5).

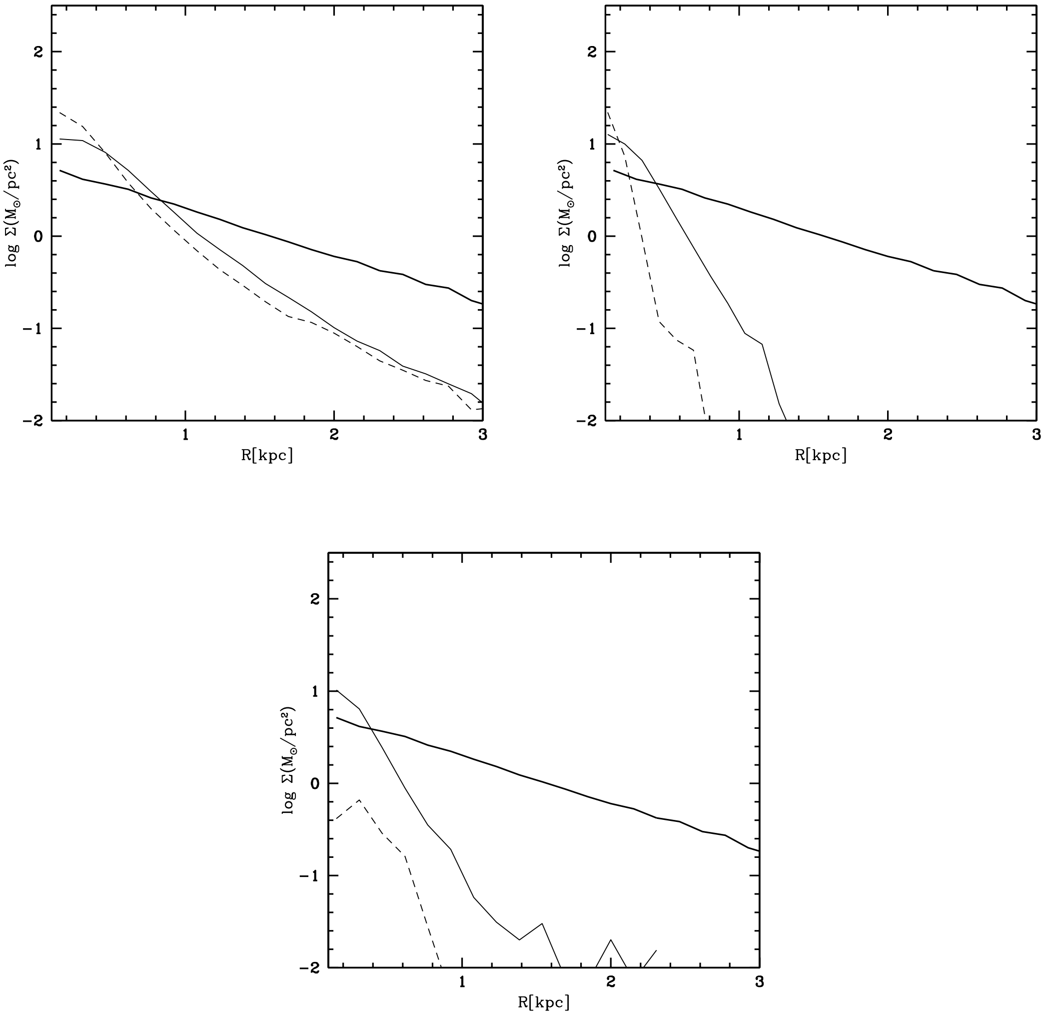

Figure 4.15: Evolution of gas surface density profiles in FI runs. The thick solid line is used for the initial profile, the thin solid line for the profile after first pericenter crossing (T=1 Gyr) and the dashed line for the profile after second pericenter passage (T=3 Gyr). From top left to bottom , run Rc20TD, Rc20RC, and RC20RCUV are shown.

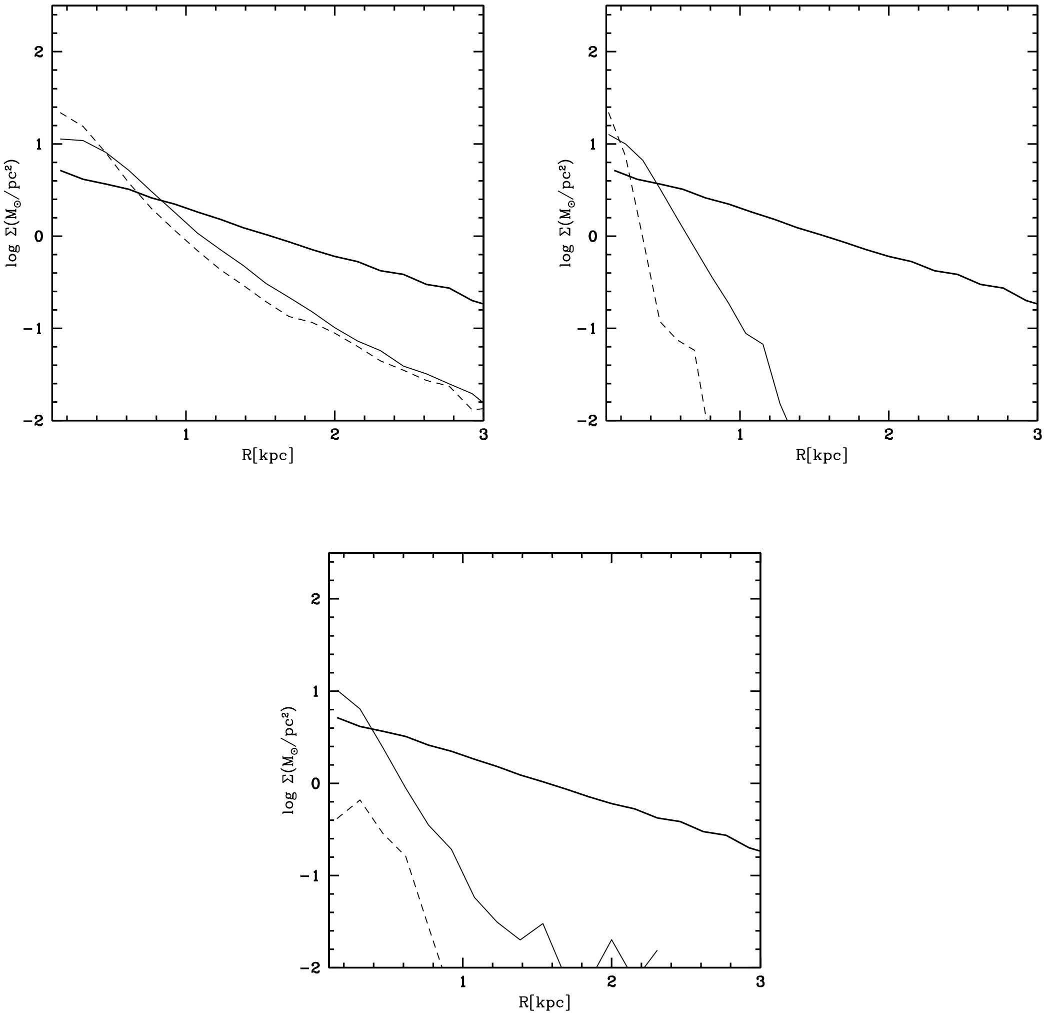

Figure 4.16: Evolution of gas surface density profiles in FI runs. The thick solid line is used for the initial profile, the thin solid line for the profile after first pericenter crossing (T=1 Gyr) and the dashed line for the profile after second pericenter passage (T=3 Gyr). From left to right, run Rc20TD, Rc20RC, and RC20RCUV are shown.

more diffuse and hotter (see Fig. 4.18).

Individual clouds survive for a timescale of $\sim 10^8$ years. The dissolution of the clouds is due to a combination of ram pressure and tidal disruption, but spurious evaporation due to artificial viscosity and discreteness effects (particle-particle collisions) may be important, especially for the smallest clouds that are close to the resolution limit (we consider a cloud to be unresolved if it contains less than 64 particles, i.e. twice the number of neighboring particles used in the SPH calculation). We calculate that ablation of the clouds due to Kelvin-Helmoltz stripping would occur on timescales comparable to the dissolution timescales observed in the simulations.

A single stripped satellite produces tens of blobs with masses in the range $10^4 - 10^6 M_\odot$ and sizes in the range $0.5 - 5$ kpc.

These blobs could explain the cold HI fragments identified by Thilker et al. (2004) around M31. These clouds have column densities ($\sim 10^{20}$ cm^{-2}) and masses (if placed at roughly the distance of M31) of $10^5 - 10^6 M_\odot$, similar to the most massive among our clouds. They have different velocities with respect to the systemic velocities, which lead Thilker et al. to suggest that they could hardly be tidal debris of disrupted dwarfs. However, a spread in velocities arises naturally because of the drag exerted by the diffuse gaseous halo. We measure velocities differing by up to a factor of 2 among the clouds in our simulations.

The variety of shapes of the clouds detected by Thilker et al. ,from nearly spherical to elongated filaments, is also reproduced by our simulations (Fig. 4.18). The clouds do not appear tidally disturbed because they are pressure confined. However, their origin is partly tidal since they are the result of the combined removal of gas by tides and ram pressure. Although our simulations lack low temperature cooling (by molecules and metals) the heating from the cosmic or local UV radiation should keep their temperature and densities close to the values observed in the simulations. However, since many of the clouds are just above our resolution limit we feel that it is premature to draw firm conclusions concerning their structure. Nonetheless the simulations strongly suggest a connection with HI fragments and possibly other gaseous structures observed in the Local Group like some of the high velocity clouds (HVCs) and the Magellanic Stream (see also Mastropietro et al. 2004).

4.5 Summary and Conclusions

The combination of ram pressure and tidal forces can produce systems resembling gas poor dwarf spheroidals from disk-like progenitors. Here we summarize our findings:

- Ram pressure alone can remove completely the gas only in dwarfs having halos with $V_{peak} < 30$ km/s. This is consistent with the results found by Marcolini et al. (2003) using different initial conditions and a different numerical technique.

- Compressional heating arising as the dwarf travels through the outer medium can significantly enhance ram pressure stripping by producing a more extended gas distribution. As a result, stripping is more effective in adiabatic runs than in cooling runs since in the latter such heating is dissipated.

- The combination of tides and ram pressure is in general more effective at removing gas from the dwarfs than ram pressure alone and always significantly more effective

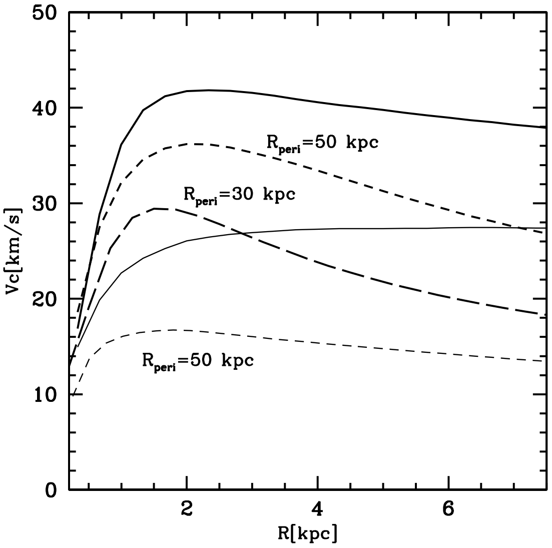

Figure 4.17: Evolution of the rotation curves of the dwarfs (including the contributions of both dark matter and baryons) in run Rc20TD (thick lines)and run Rc4aTD (thin lines). The solid lines represent the initial conditions while the short-dashed show the curves after 3 orbits, corresponding to $t = 4$ Gyr and $t = 10.2$ Gyr, respectively. The thick long-dashed line shows the curve for run Rc20bAD after $t = 10.2$ Gyr. Pericenter distances for the various orbits are indicated in the plot. Note that runs Rc20TD and runs Rc20bAD employ the same initial dwarf model but different orbits.

than tides alone. Tidal stripping lowers V_{peak} and thus the depth of the potential well of the dwarf.

- Tidally induced bar formation opposes ram pressure stripping by driving a large fraction of gas towards the center where it is harder to strip at subsequent pericenter passages. This counteracting effect is stronger when radiative cooling is included and explains why in a few cases the addition of tides does not increase the amount of stripped mass.
- Low baryonic contents and high mass-to-light ratios comparable to those of many dSphs can be obtained as a result of ram pressure and tidal stripping. However heating sources, such as the cosmic UV background arising during reionization, are required in order to obtain a very low gas fraction in a halo as massive as that in which Draco is probably embedded.
- The gaseous stream produced by the stripped dwarfs fragments into several cold clouds pressure confined by the outer medium. These clouds have properties reminiscent of gaseous structures possibly associated with the Local Group, including some of the HVCs and the HI fragments recently detected around M31.

We have considered only two types of orbits in this paper. Since proper motions of dSphs are poorly constrained (recent HST-based measurement still have a quite large error, e.g. see Piatek et al. 2003 for Carina) there is still quite some freedom in choosing the initial orbits. For example evolving model V40c20 on an orbit with smaller pericenter, say between 10 and 20 kpc, would enhance both tidal stripping and ram pressure. More eccentric orbits would lead to higher pericentric velocities which greatly increases the efficiency of ram pressure stripping. Furthermore, the progenitors of dSphs might have suffered both tidal and ram pressure stripping already before entering the Milky Way halo (Kravtsov et al. 2004). Hence our results should be regarded as quite conservative.

As we noted above, the initial orbits and initial masses of the dwarfs are both factors that the determine the final dark-to-baryonic mass ratio and other properties of the remnants. Therefore, the fact that Fornax and Draco have similar masses, as inferred from their velocity dispersions (Kazantzidis et al. 2004), but differ by more than a factor of 10 in their luminosity, can be explained in two ways. Either the progenitors of these two dwarfs started out with very different relative amounts of dark matter and baryons, for reasons related to their formation history and not to the environment, or they descend from very similar progenitors having comparable dark and baryonic masses, but evolved differently because they entered the primary halo at a different epoch and on different orbits.

The ionizing radiation at high redshift also plays a role in determining the efficiency of ram pressure stripping, and its effect again will be stronger for dwarfs infalling at higher redshift. It is a natural consequence of structure formation in hierarchical models that subhaloes that are found closer to the center of the primary system at $z = 0$ are typically those that fell earlier into the potential well of the primary system. Based on their current distances one would conclude, for example, that Fornax is likely a more recent addition to the Milky Way system, and would have suffered fewer and weaker pericenter passages, relative to Draco. It retained some gas after the first one or two orbits, a condition usually satisfied in those of our simulations that have the largest pericenter, and underwent a few

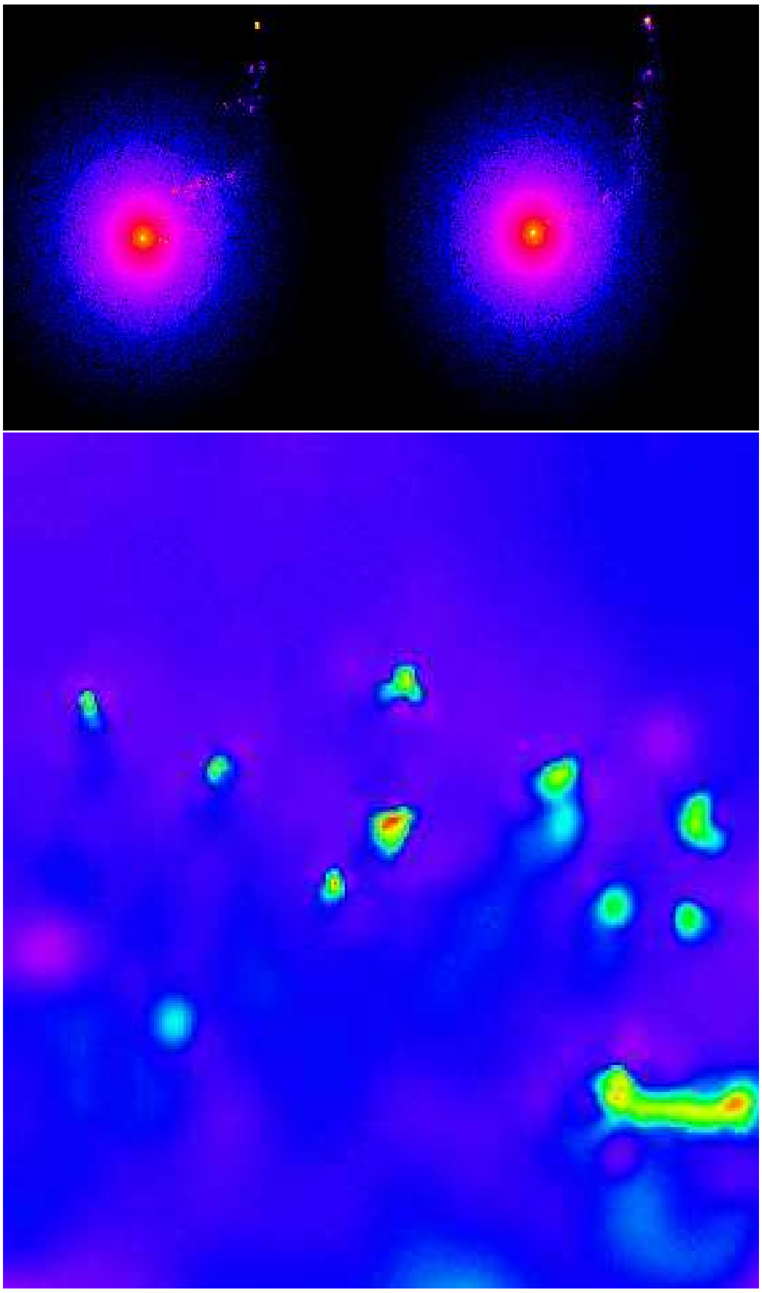

Figure 4.18: Top: color coded density map (brighter colors for higher densities) showing a box of 200 kpc on a side, slightly offset from the center of mass of the Milky Way+satellite system, for run Rc20RC (left) and run Rc20RCUV (right) at $t = 1.5$ Gyr. A gaseous trail fragmenting into clouds is visible. Bottom: color coded temperature map of one small region of the gaseous stream in run Rc20RC (the box has a size of about 40 kpc on a side) showing the detailed structure of the clouds.

bursts over the past few Gyr (Mayer et al. 2001b). Instead, Draco entered earlier on a tighter orbit and lost almost all its gas at the first pericenter passage, thus ending star formation early. We note that for the orbits with a pericenter of 30 kpc pericenter crossing occurs 0.7 Gyr after the dwarf enters the Milky Way halo. If the dwarf begins its infall at $z = 6 - 7$, i.e ~ 1 Gyr after the Big Bang, this leaves about ~ 2 Gyr to form stars before gas removal occurs, consistent with the estimated time span for the star formation history of Draco (Grebel & Gallagher 2004). While the infall time of the progenitor of Draco is clearly a free parameter, our results show that these simple assumptions produce a scenario that fits a number of observational constraints.

It is important to keep in mind that the Milky Way halo model used here is based on data at $z = 0$ and the components that we assumed as fixed do indeed evolve through cosmic time. At high z, as the dwarfs began their route towards the Milky Way, the dark halo and gaseous halo masses may have been quite different. However, ΛCDM galaxy formation simulations suggest that large disk galaxies had the last major merger quite early on in order for a large enough disk to assemble by $z = 0$, which means most of the dark halo mass was probably already in place at $z = 2 - 3$. The evolution of the gaseous halo in ΛCDM simulations has not been investigated yet but work in progress suggests its density at several tens of kiloparsecs could have been ten times higher than the value adopted in this paper.

In our simulations ram pressure stripping is most effective close to pericentric passages. This reflects the fact that we have assumed a smooth density distribution for the hot halo. If the halo has a complex multiphase structure as predicted by some models (Maller & Bullock 2004) the dwarfs would move through a clumpy medium and could undergo intense ram pressure stripping even far from pericenter if they encounter a dense and massive cloud. Galaxy formation simulations which follow the build-up and evolution of the gaseous halo at very high resolution with a proper treatment of the multi-phase ISM will eventually be able to address this aspect. However, current cosmological simulations can hardly capture the effect of ram pressure on satellite galaxies even in the case of a smooth halo because of the limited resolution and owing to uncertainties in the star formation and feedback processes which concur to determine the gas fraction in satellite galaxies.

Therefore nowadays simulations such as those discussed in this paper represent a necessary counterpart to cosmological runs and provide the only means to test the physical effect of environmental mechanisms in a robust way.

The numerical simulations were carried out on the zBox supercomputer at the University of Zurich and on LeMieux at the Pittsburgh Supercomputing Center.

Chapter 5

Density profiles of cold dark matter substructure: Implications for the missing-satellites problem[1]

5.1 Abstract

The structural evolution of substructure in cold dark matter (CDM) models is investigated combining "low-resolution" satellites from cosmological N-body simulations of parent halos with $N = 10^7$ particles with high-resolution individual subhalos orbiting within a static host potential. We show that, as a result of mass loss, convergence in the central density profiles requires the initial satellites to be resolved with $N = 10^7$ particles and parsec-scale force resolution. We find that the density profiles of substructure halos can be well fitted with a power-law central slope that is unmodified by tidal forces even after the tidal stripping of over 99% of the initial mass and an exponential cutoff in the outer parts. The solution to the missing-satellites problem advocated by Stoehr et al. in 2002 relied on the flattening of the dark matter halo central density cusps by gravitational tides, enabling the observed satellites to be embedded within dark halos with maximum circular velocities as large as 60 $\mathrm{km\,s^{-1}}$. In contrast, our results suggest that tidal interactions do not provide the mechanism for associating the dwarf spheroidal satellites (dSphs) of the Milky Way with the most massive substructure halos expected in a CDM universe. Motivated by the structure of our stripped satellites, we compare the predicted velocity dispersion profiles of Fornax and Draco to observations, assuming that they are embedded in CDM halos. We demonstrate that models with isotropic and tangentially anisotropic velocity distributions for the stellar component fit the data only if the surrounding dark matter halos have maximum circular velocities in the range $20 - 35$ $\mathrm{km\,s^{-1}}$. If the dSphs are embedded within halos this large then the overabundance of satellites within the concordance ΛCDM cosmological model is significantly alleviated, but this still does not provide the entire solution.

My personal contribute to this paper was oriented to reproduce the observed kinematics of the dwarf spheroidals, assuming that they are embedded in the potential wells of our cuspy tidally stripped satellites, and to constrain the maximum mass or circular velocity of their host halos. I fitted the observed line of sight velocity dispersion profiles of Draco and

---

[1] This chapter is published in: Kazantzidis et al. 2004b, ApJ, 608, 663

Fornax dSphs adopting isotropic and anysotropic models for the stellar component and an NFW profile with different concentrations and peak velocities for the dark matter halo. Radially anisotropic models always overestimate the central stellar svelocity dispersion by a factor of ~ 2, while isotropic and tangentially anisotropic models match the observed data only for values of v_{peak} much smaller than those suggested by Stoehr et al. 2002.

5.2 Introduction

The concordance Lambda cold dark matter (ΛCDM) cosmological model for structure formation has been remarkably successful in explaining most of the properties of the universe on large scales and at various cosmic epochs. Recent results from microwave background experiments and large redshift surveys have highlighted the ability of this model to reproduce observations as diverse as the abundance and clustering of galaxies and clusters and the statistical properties of the Lyα forest within constraints set by measurements of the primordial fluctuation spectrum, observations of distant Type Ia supernovae, and gravitational lensing statistics (e.g., Phillips et al. 2001; Jaffe et al. 2001; Percival et al. 2001; Hamilton & Tegmark 2002; Croft et al. 2002; Bahcall et al. 2003; Tonry et al. 2003; Spergel et al. 2003). However, on non-linear scales the ΛCDM model has been neither convincingly verified nor disproved, and several outstanding issues remain unresolved.

Specifically, the rotation curves of dwarf and low surface brightness galaxies are better fitted by shallower dark matter density profiles and lower concentrations than those predicted by the standard model (e.g., Flores & Primack 1994; Moore 1994; Burkert 1995; McGaugh & de Blok 1998; de Blok et al. 2001, de Blok, McGaugh & Rubin 2001; de Blok & Bosma 02; McGaugh et al. 2003; Simon et al. 2003). However, cuspy dark matter distributions may be consistent with the rotation curve data once systematic uncertainties are considered, such as non-circular motions due to the presence of a bar (Valenzuela & klypin 2003; Rhee et al. 2004). Fast rotating bars require dark matter densities on galactic scales significantly lower than the theoretical predictions (Debattista & Sellwood 2000) and fluid dynamical models based on observations of barred galaxies support the same conclusion (Weiner et al. 2001). The inner Galaxy mass profile is marginally consistent with having dark matter in the central region (Binney & Evans 2001). On cluster scales, gravitational lensing observations are similarly suggestive of a discordance between the measured shallow dark matter density inner slopes and the predicted by numerical simulations cusps (Sand et al. 2002; Sand et al. 2004). Nevertheless, hydrodynamical calculations of cluster formation have yet to be carried out and compared in detail with the observational data.

Among the most puzzling discrepancies on small scales is the so-called substructure problem. ΛCDM predicts a number of subhalos within the Local Group with maximum circular velocities in the range $V_{\max} \sim 10-30 \ \mathrm{km\,s^{-1}}$, which is about 2 orders of magnitude higher than the total number of observed satellite galaxies (kauffmann et al. 1993; Moore et al. 1999; Klypin et al. 1999). A number of possible solutions has been proposed to alleviate this problem. One class of solutions is related to radical modifications of the fundamental ΛCDM paradigm itself, including allowing for a finite dark matter particle self-interaction cross section that enhances the satellite destruction within galactic halos (Spergel & Steinhardt 2000), reducing the small-scale power with a warm dark matter candidate (e.g., Avila-Reese et al. 2001; Eke et al. 2001; Bode et al. 2001), changing the shape of the primordial power spectrum (Kamionkowski & Liddle 2000; Zentner & Bullock 2002), introducing an interaction between dark matter particles and photons (Bœhm et al. 2002) or resorting to the decay of a charged particle to suppress the small-scale power spectrum (Sigurdson & Kamionkowski 2004).

A second class of solutions relies on the inability of low mass satellites to form stars, by either supernova feedback, photoionization, or reionization. Indeed, baryon dissipation, star formation, and radiative feedback mechanisms must have a decisive effect on the properties of the final observed system, and it has been suggested that suppression of gas collapse and/or cooling by a photoionizing background at high redshift can dramatically reduce the number of visible satellites with $V_{\rm vir} < 50$ km s^{-1}, possibly reconciling the observations with the model predictions (Bullock et al. 2000; Benson et al. 2002a; Benson et al. 2002b) Nonetheless, these semi-analytical calculations adopt a simple description of the radiation physics and disagree with recent numerical simulations showing that even very small dwarf galaxies with circular velocities of the order of $V_{\rm vir} \sim 30$ km s^{-1} or even lower can self-shield themselves from the UV background and form some stars (Susa & Umemura 2003). Feedback processes may also violate the strong correlation between baryonic mass and virial velocity, as emphasized by Mayer & Moore 2004.

Recently, another way of relieving the missing satellites problem has been advocated by Stoehr et al. (2002, hereafter S02). These authors argue that the observed Galactic satellites are hosted by the most massive substructures within a given CDM halo. In this case, feedback processes suppress star formation in all smaller objects, and the "luminosity function" of the dwarf spheroidal galaxies (dSphs) is consistent with the "mass function" of the subhalos. This represents a somewhat simpler scenario than forming stars in a random 10% of the satellites over a larger mass range. However, in order to achieve this renormalization of the observed satellite mass/circular velocity function, S02 claimed that the observed velocity dispersions of the dSphs do not correlate with the maximum circular velocities, $V_{\rm max}$, of their dark matter halos in the way originally assumed by Moore et al. (1999) and Klypin et al. (1999) when they identified the substructure problem.

As an illustrative example, consider the case of the dSph Fornax, with an observed stellar central velocity dispersion of $\sigma_\star \sim 10$ km s^{-1} (Mateo 1998). The circular velocity of the surrounding dark matter halo at the location of the dwarf can be of the order of $V_{\rm c} = a\sigma_\star \sim 15 - 20$ km s^{-1}, depending on the particular assumptions made to infer such quantities from observations. For example, an isothermal halo model with a flat circular velocity profile, as adopted by Moore et al. (1999), would yield $V_{\rm c} = \sqrt{2}\sigma_\star = 14.1$ km s^{-1}. Provided that the circular velocity profile is still slowly rising in the region where the visible dwarf galaxy resides, $V_{\rm c}$ may substantially underestimate $V_{\rm max}$. This would clearly allow the dwarf galaxies to be embedded in dark halos with very large maximum circular velocities in the range of $V_{\rm max} = 50 - 60$ km s^{-1}. However, such slowly rising circular velocity profiles seem to be in notable disagreement with previous studies suggesting that the standard ΛCDM halos corresponding to the dSphs are expected to be very concentrated, which naturally leads to steeply rising circular velocity profiles (Bullock, Kravtsov & Weinberg 2001).

S02 suggested that the satellites experience significant mass redistribution in their centers as a result of tidal interactions, leading to shallower inner density profiles and smaller effective concentrations than those of comparable isolated halos. However, the subhalos in their cosmological simulations contained just a few thousand particles and the softening lengths they used were comparable to the entire extent of some of the dSphs they wanted to resolve. These authors corroborated their results by comparing them with the higher resolution N-body simulations of Hayashi et al. (2003, hereafter H03), who employed individual cuspy model satellites disrupting in a static primary potential and found the same shallow inner density profiles as a result of tides. Nonetheless, the later models have the major shortcoming that they do not constitute equilibrium configurations, since they are constructed by approximating the exact velocity distribution at any given point in space with a Maxwellian. When evolved in isolation, these models relax rapidly to an inner density slope much shallower than the originally intended one, and any results obtained should be treated with care (Kazantzidis, Magorrian, & Moore 2004a).

In this chapter, we investigate how a satellite's internal structure responds to tidal interactions, revisiting the solution to the missing-satellites problem proposed by S02. Our study uses N-body cosmological simulations of renormalized systems, in which the subhalos have up to 15 times more particles than those used by S02. Note, however, that Stoehr et al. (2003) confirmed the results of S02, using a simulation with a factor of 9 more particles. Furthermore, we investigate the tidal disruption of individual cuspy substructure halos, employing $N = 10^7$ particles, 100 times the mass resolution of H03, to minimize numerical effects (Moore et al. 1996; Diemand et al. 2004a). Our primary goal is to examine the change in the internal structure of the substructure at scales comparable to the actual sizes of the luminous dwarf galaxies as they suffer tidal shocks and gravitational stripping. The models we adopt for the individual satellite simulations are self-consistent realizations and thus ideal for the sensitivity of this particular study. As we illustrate below, tides do not modify the central density structure of cuspy satellites and therefore the missing satellites problem can not be solved in this way.

This chapter is organized as follows. In § 5.3, we discuss our cosmological and individual satellite simulations and present our results regarding the internal structural evolution of the substructure. In § 5.4, we model the kinematics of the Draco and Fornax dSphs on the basis of the findings of our simulations, and in § 5.5 we discuss the implications of our results. Finally, in § 5.6 we summarize our main findings and conclusions.

5.3 Numerical Simulations

All the simulations carried out in this chapter were performed with PKDGRAV (Stadel 2001). The time integration conserved energy to better than 0.15% in all cases, which is adequate for the kind of numerical simulations presented in this chapter. The energy must be conserved at such a level that the dynamics of the regions of interest can be meaningfully probed. We have also explicitly checked that our results are not compromised by choices of force-softening, time-stepping, or opening angle criteria in the treecode. In what follows and unless otherwise explicitly stated, we consider as our framework the concordance flat ΛCDM cosmological model with present-day matter and vacuum densities $\Omega_{\mathrm{m}} = 0.3$ and $\Omega_\Lambda = 0.7$, respectively, dimensionless Hubble constant $h = 0.7$, present-day fluctuation amplitude $\sigma_8 = 0.9$, and index of the primordial power spectrum $n = 1.0$. Note also that in the remainder of this chapter we use the terms "satellites," "subhalos," and "substructure" indistinguishably.

Table 5.1: Structural and numerical parameters of the satellite models

Model (1)	N (2)	c (3)	$r_{\rm s}$ (h^{-1} kpc) (4)	$V_{\rm peak}$ ($\rm km\,s^{-1}$) (5)	$r_{\rm peak}$ (h^{-1} kpc) (6)	$\epsilon_{\rm sat}$ (h^{-1} kpc) (7)
LR	5×10^5	9	5.4	41.5	11.7	0.511
HR1	10^7	21	2.3	51.3	5.0	0.021
HR2	10^7	9	5.4	41.5	11.7	0.021

5.3.1 Substructure in a Fixed External Potential

In this section, we investigate the structural evolution of CDM substructure, using N-body simulations of satellites orbiting within the gravitational potential of a static primary. The satellites are modeled using the Navarro, Frenk & White (1997, hereafter NFW) density profile, under the assumptions of spherical symmetry and isotropic velocity dispersion tensors. These models are constructed using the procedure described in Kazantzidis et al. (2004), which produces self-consistent equilibria that do not suffer from numerical instabilities present in other schemes, such as those that approximate the exact velocity distribution at any given point in space by a Gaussian.

The NFW density profile is given by

$$\rho(r) = \frac{\rho_{\rm s}}{(r/r_{\rm s})(1+r/r_{\rm s})^2} \qquad (r \leq r_{\rm vir}) \ , \tag{5.1}$$

where the characteristic inner density $\rho_{\rm s}$ and scale radius $r_{\rm s}$, are sensitive to the epoch of halo formation and tightly correlated with the halo virial parameters, via the concentration, $c \equiv r_{\rm vir}/r_{\rm s}$, and the virial overdensity, $\Delta_{\rm vir}$. Since the NFW density profile corresponds to a cumulative mass distribution that diverges as $r \rightarrow \infty$, we introduce an exponential cutoff for $r > r_{\rm vir}$. The latter sets in at the virial radius and turns off the profile on a scale $r_{\rm decay}$, which is a free parameter and controls the sharpness of the transition:

$$\rho(r) = \frac{\rho_{\rm s}}{c(1+c)^2} \left(\frac{r}{r_{\rm vir}}\right)^{\epsilon} \exp\left(-\frac{r-r_{\rm vir}}{r_{\rm decay}}\right) (r > r_{\rm vir}). \tag{5.2}$$

In order to ensure a smooth transition between equations (5.1) and (5.2) at $r_{\rm vir}$, we require the logarithmic slope there to be continuous. This implies

$$\epsilon = -\frac{1+3c}{1+c} + \frac{r_{\rm vir}}{r_{\rm decay}}. \tag{5.3}$$

The satellites' virial mass is equal to $M_{\rm sat} = 1.4 \times 10^{10}\, h^{-1} {\rm M}_{\odot}$, corresponding to a circular velocity at the virial radius of $V_{\rm vir} = 35 \ {\rm km\,s^{-1}}$ for the adopted ΛCDM model. However, a dark matter halo of a given mass and size does not have a unique NFW profile. Indeed, the parameter that controls the shape of the density profile is the concentration

c, and higher values of concentration correspond to a larger fraction of the virial mass being contained in the inner regions of the halo. For a given mass, the measured scatter in this parameter reflects mainly the different formation epochs (Bullock et al. 2001a; Eke et al. 2001; Wechsler et al. 2002). For the adopted ΛCDM model, the median concentration value for an object of this mass scale is $c_{\rm sat} = 21$, with the 2σ deviation given by $c_{\rm sat} \sim 11 - 40$ (Bullock et al. 2001a).

Here we present results for two high-resolution simulations ($N = 10^7$) of subhalos having concentration parameters equal to $c_{\rm sat} = 21$ (HR1) and $c_{\rm sat} = 9$ (HR2). We consider these two significantly different values of the concentration to single out readily how the evolution of the satellites' structure depends on this parameter. We note that values as small as $c_{\rm sat} = 9$ for the mass scale of our satellites are possible within models with a lower fluctuation amplitude σ_8. In order to demonstrate the need for such a high mass resolution, we run a simulation using a lower resolution of $N = 5 \times 10^5$ particles with the lower value of the concentration $c_{\rm sat} = 9$ (LR). We emphasize that even the latter run uses a factor of 5 more particles than the highest-resolution simulations of H03.

For the low resolution run, we choose a spline softening length of $\epsilon = 0.511 h^{-1}$ kpc. This value corresponds to an equivalent Plummer softening length equal to that of the highest resolution cosmological simulation, GA2, of S02. For models HR1 and HR2, we choose a gravitational softening of $\epsilon = 0.021 h^{-1}$ kpc, comfortably smaller than the typical sizes of the dSph satellites of the Milky Way which constitute the ultimate target of the present study. Numerical and structural parameters of all models are summarized in Table 5.1. Columns (1), (2) and (3) give the satellite galaxy model, number of particles and concentration. Columns (4), (5), (6) and (7) give the scale radius, maximum circular velocity, radius where the circular velocity peaks, and softening length. Note that the virial mass of all satellite models is $M_{\rm sat} = 1.4 \times 10^{10}\, h^{-1}{\rm M}_\odot$. For all the runs, we followed the time evolution of the density, $\rho(r)$, and circular velocity, $V_{\rm c}(r)$, profiles of the satellites. We explore below how these evolve depending on the structural properties of the subhalos and on the numerical resolution.

The orbits of the satellites are influenced only by the external, spherically symmetric static tidal field, which is represented by the logarithmic halo potential,

$$\Phi = \sigma^2 \ln(R^2 + R_{\rm c}^2) \ , \tag{5.4}$$

where σ is the one dimensional velocity dispersion and $R_{\rm c}$ is the core radius. We use $\sigma = 127.3$ km s^{-1} and $R_{\rm c} = 0.7 h^{-1}$ kpc, resulting in a circular velocity profile that flattens out already at ~ 3 kpc and reaches an asymptotic value of $v_0 = \sqrt{2}\sigma \sim 180$ km s^{-1}. This modeling gives a total mass within 100 kpc of the center of the fixed potential equal to $M_{R<100\ {\rm kpc}} = 5.25 \times 10^{11}\, h^{-1}{\rm M}_\odot$. This value is at the upper limit of estimates for the mass of the Milky Way from satellite motions (Kochanek 1996) and dynamics of the Magellanic Clouds (Lin et al. 1995), and it is within the range of models for the Milky Way proposed in the context of ΛCDM (Klypin et al. 2002). This choice serves our primary aim, which is to investigate the change of the satellites' internal structure in a regime in which the tidal shocks are very strong. Note also that the total mass within the pericenter of the orbit is equal to $M_{R<25\ {\rm kpc}} = 1.3 \times 10^{11}\, h^{-1}{\rm M}_\odot$.

The orbits of the Milky Way dSphs are currently poorly constrained observationally. Nevertheless, their current distances, which give an indication of the apocenter of their orbits, coupled with studies of the orbital properties of cosmological halos, can be used to constrain the orbital parameters of the satellites. In particular, the model satellites are placed on an eccentric orbit with an apocenter radius of $r_{\rm apo} = 105h^{-1}$ kpc and $(r_{\rm apo}/r_{\rm per}) = (6/1)$, close to the median ratio of apocentric to pericentric radii found in high resolution cosmological N-body simulations (Ghigna et al. 1998; Tormen et al. 1998). The center of the external potential is always set to be $(x, y, z) = (0, 0, 0)$. We begin all our simulations by placing the satellites at apocenter, and we integrate the orbits forward for 7 Gyr. This timescale corresponds to more than three orbital periods ($T_{\rm orb} \sim 2.25$ Gyr) in the chosen orbit and already represents a significant fraction of the cosmic time. Our approach neglects the effects of the dynamical friction and the response of the primary to the presence of the satellite. However, this choice is justified given the difference in the mass (almost a factor of 50) and size of the two systems and the anticipated rapid and substantial mass loss owing to tides (see also Taffoni et al. 2003).

The tidal field alters the structure of the satellites through a combination of strong tidal shocks occurring at each pericentric passage and gradual mass loss throughout the orbital evolution. In the top panels of Figures 5.1 and 5.2, we present the evolution of the density (*left*) and circular velocity (*right*) profiles of the bound remnant of the initial models HR1 and HR2, respectively. After allowing the satellites to pass past the pericenter for the first time, we show the profiles at every odd quarter of the orbit between apocenter and pericenter. These profiles are plotted from the force resolution (2ϵ) outward. The choice of how to determine the bound remnants' center is crucial for our intended analysis, since quantities such as the spherically averaged density and circular velocity profiles are quite sensitive to the center's definition. In this study, we identify the center adopting the most bound particle method, which agrees very well with the center of mass recursively calculated using spherical regions of decreasing radius. Indeed, we confirmed that both methods give converging results by comparing the resulting density profiles for some of our stripped satellites. This comparison yielded identical profiles for the remnants at all radii between our force resolution and the tidal radius for all the cases we tried.

We determine the mass that remains self-bound as a function of time using the following iterative scheme: in the rest frame of the most bound particle, we calculate the binding energies of all the other particles, using the tree-based gravity calculation performed by PKDGRAV, and we remove all those with positive binding energy. This calculation of binding energies and subsequent removal of unbound particles is repeated until no more particles can be removed or no bound remnant is found (i.e., all particles are removed). In practice, this iterative procedure converges rapidly and ensures that the true bound entity will be identified. Note that this technique is essentially the same one used by most group finding algorithms, such as the publicly available SKID (Stadel 2001), which we use for the substructure in the cosmological simulations analyzed in § 5.3.2, where removing the background potential is more difficult, but it has the advantages of (1) using a tree structure for the potential calculation which requires of the order of $O(N \log N)$ operations instead of $O(N^2)$, where N is the number of particles in the remnant, and (2) having a parallel implementation for very large N. In this way, we can handle a much larger number of particles than would be possible with SKID, and at a fraction of the computational burden.

In the above analysis, we used equal-size logarithmic bins. Different number of bins were used, depending on the stage of the orbital evolution, ensuring that in each case we have a sufficiently large number (> 1000) of particles in each bin. This choice of binning simply minimizes the noise in the resulting profiles. The central density of model HR2 decreases between the initial and final values by almost a factor of 3 more than

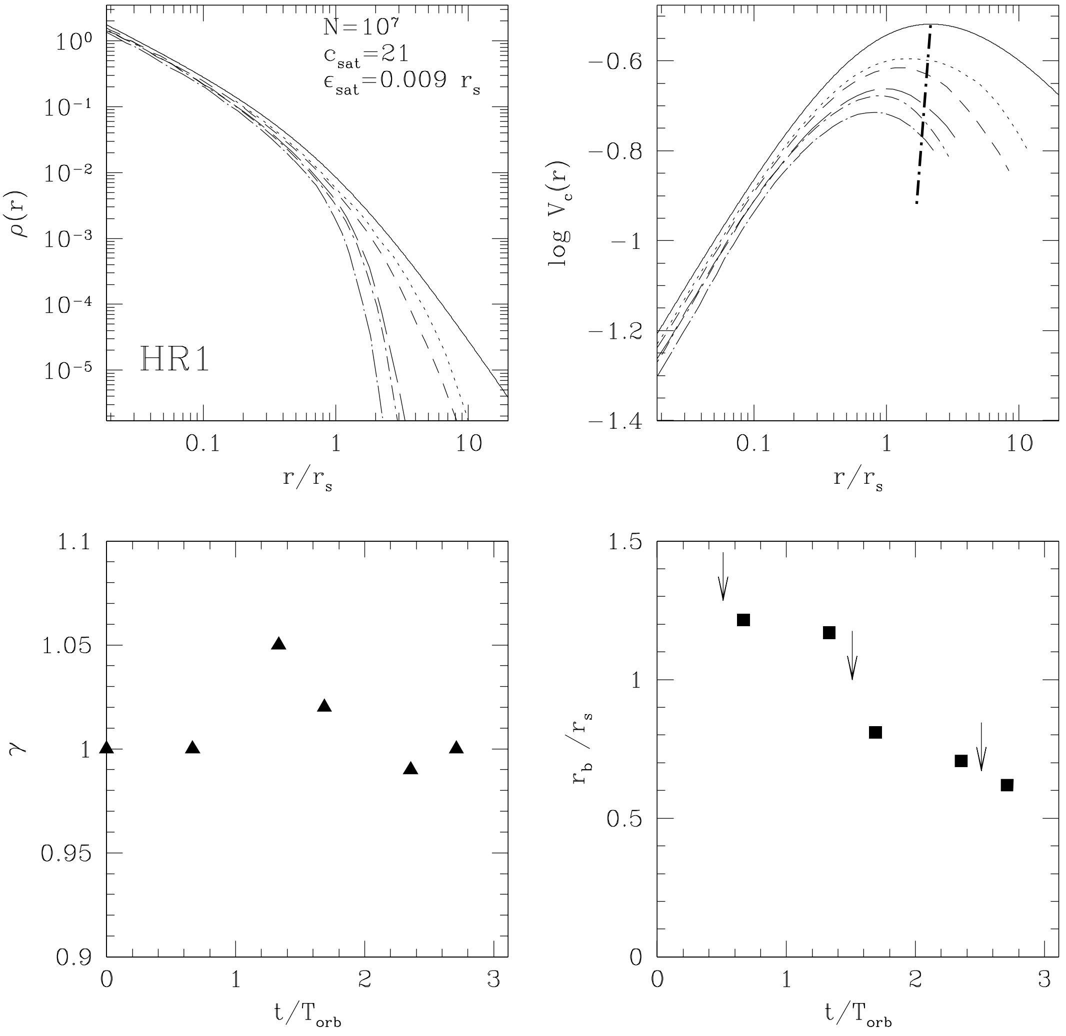

Figure 5.1: *Top:* Evolution of the density (*left*) and circular velocity (*right*) profiles of the bound mass for the high resolution model HR1. The number of particles, N, the concentration parameter, $c_{\rm sat}$, and the softening length, ϵ, are indicated (*upper right-hand corner*). The scale radius of this model is $r_{\rm s} = 2.3h^{-1}$ kpc. The orbital evolution shown corresponds to approximately three orbital periods ($T_{\rm orb} \sim 2.25$ Gyr). Profiles are shown at every odd quarter of the orbit between apocenter and pericenter, after allowing the satellites to pass the first pericenter, and are plotted from the force resolution (2ϵ) outward. The lines from top to the bottom, in order of decreasing central density, show the profiles at $t = (0, 0.67, 1.33, 1.69, 2.36, 2.71)\,T_{\rm orb}$. The density and circular velocity are given in units of $M_{\rm sat}/r_{\rm s}^3$ and $(GM_{\rm sat}/r_{\rm s})^{1/2}$, respectively. The thick dotted line indicates the expected relation between $V_{\rm max}$ and $r_{\rm max}$ for field halos (see text for details). *Bottom:* Evolution of the central density slope γ (*left*) and break radius $r_{\rm b}$ (*right*) of the fitting formula (eq. [5.5]) that describes the structure of our subhalos. The latter fit parameter is expressed in units of the scale radius, $r_{\rm s}$, of the initial model. Downward arrows indicate the pericentric passages. The substructures maintain the same steep central density slope down to the limit of our force resolution as they get tidally stripped. Tides, however, shift inward the break radius $r_{\rm b}$ of the fitting function. Note the considerable change in $r_{\rm b}$ after each pericentric passage.

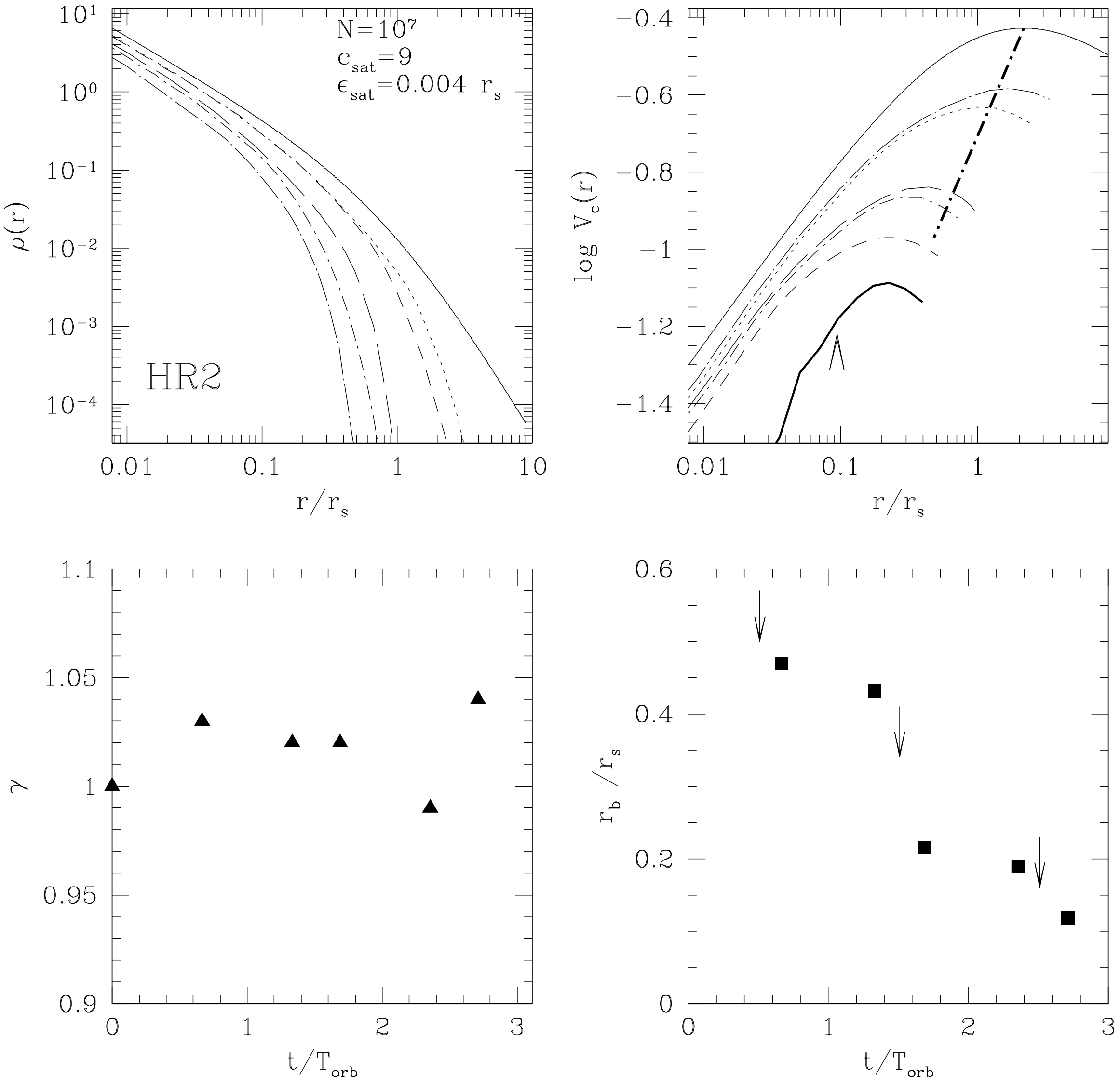

Figure 5.2: Same as Figure 5.1, but for model HR2. The scale radius is $r_s = 5.4h^{-1}$ kpc. Compared to model HR1, the decrease in the central density and maximum circular velocity, $V_{\max}$, is significantly more pronounced, because of the higher binding energy for more concentrated models. Tidal interactions truncate this model at smaller physical radii than in model HR1, which is reflected in the evolution of the break radius (*bottom right*). The thick solid line shows the circular velocity profile of the low resolution satellite (LR) at $t = 2.71\,T_{\rm orb}$. Even though this timescale is the same as the one corresponding to the last curve in the high-resolution run, the low resolution satellite has lost substantially more mass, and its central slope indicates a shallower inner density profile. Upward arrow indicates the softening used in the low resolution simulation.

the decrease in model HR1 over the same timescales. This is due to the fact that the initial concentrations are quite different. The concentration parameter of model HR1 is considerably higher than that of HR2, and thus the former model is more resilient to tidal heating. The same effect is clearly seen on the evolution of the circular velocity profiles. In particular, the overall change in the $V_{\rm max}$ is significantly more pronounced in model HR2 than in model HR1 for the same timescales. The thick dotted lines in the top right panels of Figures 5.1 and 5.2 indicate the expected relation between $V_{\rm max}$ and the distance at which the maximum circular velocity, $r_{\rm max}$, occurs for *field halos* (Colín et al. 2004). The latter is a measure of the concentration of the satellites. Tidal stripping moves the subhalos to the left of the expected relation, so that for a given $V_{\rm max}$ these systems have smaller $r_{\rm max}$ and hence higher effective concentrations than field halos. For example, after ~ 6 Gyr the $V_{\rm max}$ and $r_{\rm max}$ of the $c_{\rm sat} = 9$ satellite decrease by a factor of 3.5 and 8.5, respectively. For the same change of $V_{\rm max}$, however, one would expect $r_{\rm max}$ to vary by just a factor of 3 from the relation for field halos. The higher relative densities of heavily stripped halos may account for the fact that Draco, being considerably closer to the Milky Way, has a mass-to-light ratio higher than that of Fornax, despite their similar stellar velocity dispersions.

The density structure of our subhalos can be described through the following simple formula

$$\rho(r) \propto r^{-\gamma} \exp(-\frac{r}{r_{\rm b}}) \ , \tag{5.5}$$

where γ denotes the central slope of the substructure density profile and $r_{\rm b}$ an effective "break" radius describing the outer cutoff imposed by the tides. In the bottom panels of Figures 5.1 and 5.2, we show the evolution of these two fitting parameters. Note that $r_{\rm b}$ is expressed in units of the scale radius, $r_{\rm s}$, of the initial models. The robustness of the aforementioned binning procedure was verified by comparing these results against those when the particles were binned in spherical shells with the same number of particles in each bin. In this case, we choose as bin center the average radius of all particles in the given bin, and we assign equal statistical weight to each radial bin. The two procedures yielded almost identical values for γ and $r_{\rm b}$ for the entire orbital evolution. Note that in the bottom panels of Figures 5.1 and 5.2, we present our results adopting the latter binning procedure, and the same is also true for results shown in Figure 5.3.

The bottom left panels of Figures 5.1 and 5.2 demonstrate that tidal effects do not serve to reduce the central density cusp down to the limit of our force resolution. This is a fundamental result of this chapter that is independent of the concentration of the satellites and valid for their entire orbital evolution. Most of the tidally stripped mass is removed from the outer parts of the subhalos, steepening the outer density profiles and shifting the break radius $r_{\rm b}$ inward. This just reflects the fact that tides truncate the satellite models at increasingly smaller physical radii. The two bottom right panels illustrate that the lower concentration satellite (HR2) gets truncated at smaller radii than its higher concentration counterpart. In both models, the break radii experience the biggest decrease after each pericentric passage, but this decrease is more pronounced in model HR2. Between pericenters the break radii decrease in a smoother manner.

Even though this result is also verified in the lower resolution model LR when we compared the density profiles, it is interesting to note that the same is not true for the circular velocity profiles. Indeed, convergence in the latter profile is significantly more problematic, and this is highlighted in the top right panel of Figure 5.2, where the circular

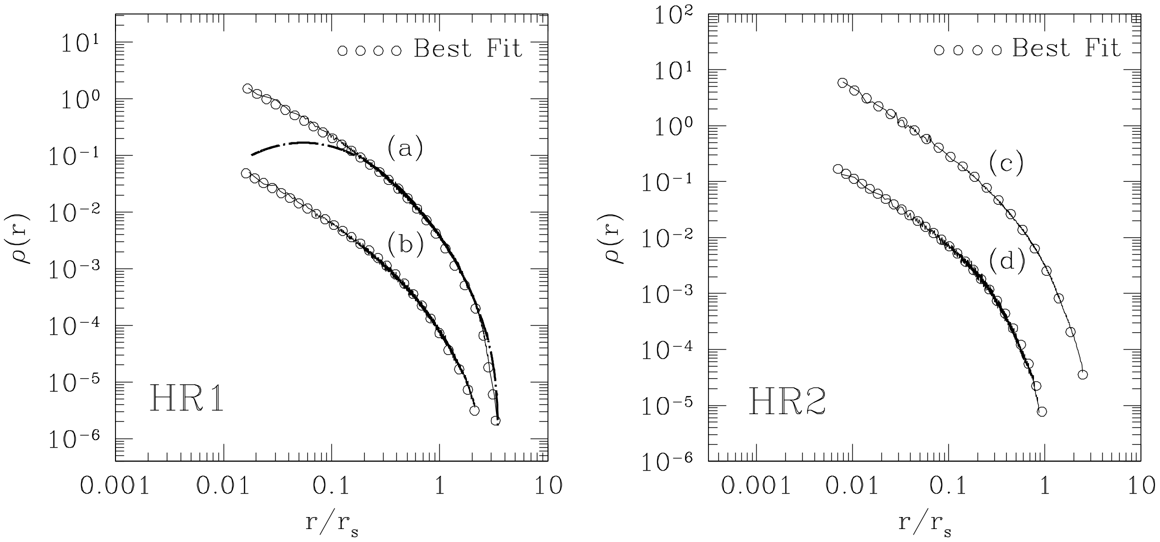

Figure 5.3: Density profiles of substructure halos from our individual satellite simulations (*solid curves*), together with fits to the density structure obtained using eq. (5.5) (*circles*). The profiles are shown for models HR1 (*left*) and HR2 (*right*) and for two different timescales in the orbital evolution. In both panels, the density profiles corresponding to the lower curves are vertically shifted downward by 1.5 dex for clarity. Curves (a) and (b) correspond to $t = 1.69\,T_{\rm orb}$ and $t = 2.71\,T_{\rm orb}$, respectively. These curves are best described by fitting parameters $(\gamma, r_{\rm b}/r_{\rm s}) = (1.02, 2.69)$ and $(\gamma, r_{\rm b}/r_{\rm s}) = (1.00, 2.06)$, respectively. Curves (c) and (d) correspond to $t = 1.33\,T_{\rm orb}$ and $t = 2.36\,T_{\rm orb}$ and the best fit parameters are $(\gamma, r_{\rm b}/r_{\rm s}) = (1.02, 0.43)$ and $(\gamma, r_{\rm b}/r_{\rm s}) = (0.99, 0.19)$, respectively. The fits are satisfactory over 4 orders of magnitude in density and 2 orders of magnitude in radius and for satellites having concentration parameters that differ by more than a factor of 2. The thick dotted line shows the density profile corresponding to the parabolic circular velocity fitting formula proposed by S02 with $a = 0.45$, the median value of their best fits to substructure halos (see text for details).

velocity profile of the low resolution satellite is shown for comparison at $t = 2.71\,T_{\rm orb}$ (*thick solid line*). The downward arrow indicates the softening used in this simulation. The circular velocity profile of a model satellite having a factor of 20 fewer particles than its high-resolution counterpart and evolved on the same orbit is significantly lower and has a steeper inner gradient. This is entirely due to resolution effects. The fact that the convergence in the circular velocity is harder to attain is not surprising, since it is a cumulative quantity (see also below,§ 5.3.2). This warns against using the circular velocity to compute the structural properties of satellites, as done in S02.

Figures 5.1 and 5.2 indicate that the inner satellite regions corresponding to subkiloparsec scales are much less affected by the tides than the outer ones. In particular, the satellite with $c_{\rm sat} = 21$ suffers almost no change, even in the value of the central density. Subhalo particles that have orbital times shorter than the shock duration will be only marginally affected by the shock itself. This is known as adiabatic correction (Weinberg 1995). Especially for the satellite with the highest central density ($c_{\rm sat} = 21$), the adiabatic correction to the impulse approximation is extremely important, as it reduces significantly the predicted amount of shock heating. We can calculate the variation of the kinetic energy of a particle located at some distance r from the center of the satellite, ΔE, due to impulsive heating at each pericentric passage in the extended mass distribution of a primary isothermal halo (see also Mayer et al. 2002; Taffoni et al. 2003). Gnedin, Hernquist, & Ostriker (1999) have shown that for orbits as eccentric as those considered here, we can approximate the trajectory of the satellite with a straight line path and write

$$< \Delta E >= \frac{1}{2}\left(\frac{GM_0}{R_{\rm per}^2 V_{\rm per}}\right)^2 \frac{r^2\pi^2}{3}\left(\frac{R_{\rm per}}{R_{\rm max}}\right)^2 (1+\omega\tau)^{-2.5} \ , \tag{5.6}$$

where M_0 and $R_{\rm max}$ are the total mass and radius, respectively, of the primary halo, which are assumed equal to the mass and radius within the apocenter of the satellite's orbit, and $V_{\rm per}$ is the satellite's velocity at the pericenter of the orbit. These parameters are equal to $M_0 = 8.4 \times 10^{11}\ h^{-1}{\rm M}_{\odot}$, $R_{\rm max} = 105h^{-1}$ kpc, and $V_{\rm per} = 345$ km s^{-1}. The last term in the product is the first-order adiabatic correction with ω and τ being the orbital frequency for a particle at radius r and the duration of the tidal shock, respectively.

For a particle at a distance of $r = 0.7h^{-1}$ kpc from the center of the satellite, ΔE without the adiabatic correction is roughly equal to 20% of its binding energy, $E_{\rm bind}$, after three tidal shocks. Instead, $\Delta E/E_{\rm bind}$ is already greater than 1 at a radius of $r = 1.75h^{-1}$ kpc, despite the fact that the tidal radius of the satellite is much larger. However, once the adiabatic correction is included, the ratio $\Delta E/E_{\rm bind}$ is reduced by nearly 90%, explaining why the satellite is barely affected by the tidal shocks in its inner regions. Note that in order to incorporate the effect of the adiabatic correction in the simulations, one needs to model the inner regions of the subhalo quite accurately. This means resolving down to sub-kiloparsec scales in the first place and also avoiding non-equilibrium initial conditions or coarse mass resolution. The latter could affect the orbital frequencies of the dark matter particles, which might well end up in a region of phase space that is not protected by the adiabatic invariance anymore (this problem is reminiscent of the difficulty that N-body simulations of low resolution have in resolving resonances in stellar systems; see Weinberg & Katz (2002)).

Figure 5.3 shows the density profiles for two different timescales in the orbital evolution of models HR1 and HR2 (solid curves). Fits to the density structure of the substructure halos using equation (5.5) and obtained by χ^2 minimization are also shown, as circles. Model HR1 (*left*) is plotted at $t = 1.69\,T_{\rm orb}$ and $2.71\,T_{\rm orb}$, which correspond to ~ 0.4 Gyr after the satellite has concluded its second and third pericentric passages, respectively. Model HR2 (*right*) is plotted at $t = 1.33\,T_{\rm orb}$ and $2.36\,T_{\rm orb}$, which correspond to ~ 0.4 Gyr before the conclusion of the satellite's second and third pericentric passages, respectively. Note that for clarity we offset the lower curves in both panels by 1.5 dex. Clearly, the structure of our stripped satellites is reasonably well reproduced by the proposed fitting formula. We should note that this formula works well in the case of the lower concentration satellite for the entire orbital evolution. On the other hand, the case of the $c_{\rm sat} = 21$ satellite is somehow slightly different. The fitting function works better for the last stages of the orbital evolution, at which the satellite has suffered significant mass loss. This is just reflecting the resilience to tidal stripping of the high concentration satellite during the early stages of the evolution and the fact that the mass loss is more gradual compared to the low concentration model, even from the outer regions. Finally, for comparison we show the density profile resulting from the fitting formula proposed by S02 (*thick dotted line*) to describe the structure of their subhalos (see their eq. [1]), plotted down to the limit of our force resolution. The values for $r_{\rm max}$ and $V_{\rm max}$ in their formula are taken directly from the particular subhalo. In addition, we adopt a value for the parameter a in their equation that is equal to the median of their best fits, $a = 0.45$. Compared to the density profiles describing the structure of our satellites, the latter profile has a substantially shallower slope on scales comparable to the sizes of the dSphs. Interestingly, the density reaches even negative values at a finite radius, demonstrating that its use should be avoided.

5.3.2 Substructure in Hierarchical Cosmological Simulations

In this section, we present results from a set of high resolution ΛCDM cluster simulations (Diemand et al. 2004b). The initial conditions are generated with the GRAFIC2 package (Bertschinger 2001). We begin with a 300^3 particle cubic grid with a comoving cube size of 300 Mpc (particle mass $m_{\rm p} = 2.6 \times 10^{10}\, h^{-1}{\rm M}_\odot$). At $z = 0$ we identify several clusters for resimulating at higher resolution, using refinement factors of 6, 9, and 12 in length (216, 729, and 1728 in mass), so that the mass resolution is $m_{\rm p} = 1.5 \times 10^7\, h^{-1}{\rm M}_\odot$ in the highest resolution run. We label these three runs as R6, R9 and R12, after their refinement factors. At $z = 0$ the refined cluster contains 1.8×10^6 particles within the virial radius in run R6, 6×10^6 in R9, and 1.4×10^7 in R12. Note that we define the virial radius of the clusters, $R_{\rm vir}$, to be the distance from the center at which the mean enclosed density is $178\Omega_{\rm m}^{0.45} \approx 103.5$ times the critical value $\rho_{\rm crit}$ (Eke et al. 1996). The softening length is comoving from the start of the simulation ($z \simeq 40$) to $z = 9$. From $z = 9$ until the present we use a physical softening length of 2.1, 1.4, and $1.05 \times 10^{-3} R_{\rm vir}$ for R6,R9, and R12 respectively.

In the top panels of Figure 5.4, we show the density (*left*) and circular velocity (*right*) profiles of two distinct substructure halos simulated at two different resolutions. In simulation R9 (*solid lines*), the two subhalos contain $N = 3.4 \times 10^4$ and $N = 1.4 \times 10^4$ particles, respectively, whereas in simulation R6 (*dashed lines*) the same subhalos contain a factor of 3.375 fewer particles. The vertical dotted lines show the adopted force resolution. Densities are expressed in units of the present critical density for closure, $\rho_{\rm crit} = 3H_0^2/8\pi G$, and the virial radius of the parent halo is equal to $R_{\rm vir} = 1.225 h^{-1}$ Mpc. The profiles of the cosmological satellites are to be trusted only up to the resolution limit set by two body relaxation (Diemand et al. 2004A). We note that the convergence of the circular velocity profiles is much weaker than that of the density profiles at different resolutions, in agreement with the results presented in § 5.3.1. As the circular velocity is a cumulative quantity, numerical effects show up at comparatively larger radii, where the density profiles have already converged, biasing the circular velocity profiles. Therefore, one should be especially cautious when using the circular velocity profiles obtained at one particular resolution to provide fitting functions to systems whose typical scales fall below such resolution, as done in S02.

In the bottom panels of Figure 5.4, we present results regarding substructure halos taken from our highest resolution simulation (R12). The density profiles of two heavily stripped subhalos before entering the primary halo (*dashed lines*) and at present (*solid lines*) are shown in the bottom left panel. These satellites have of the order of $N = 2 \times 10^4$ particles before entering the host. The subhalo denoted "(i)" is shown at $z_{\rm in} = 0.80$ and at present just before the second pericentric passage ($r_{\rm min} = 0.21 R_{\rm vir}$). The second subhalo, denoted "(ii)," is offset by 1 dex to avoid overlap and is shown at $z_{\rm in} = 0.94$ and at present just before the *fourth* pericentric passage ($r_{\rm min} = 0.15 R_{\rm vir}$). The thick solid lines indicate two critical values for the inner slope, $\rho(r) \propto r^{-1}$ and $\rho(r) \propto r^{-1.5}$. This plot illustrates

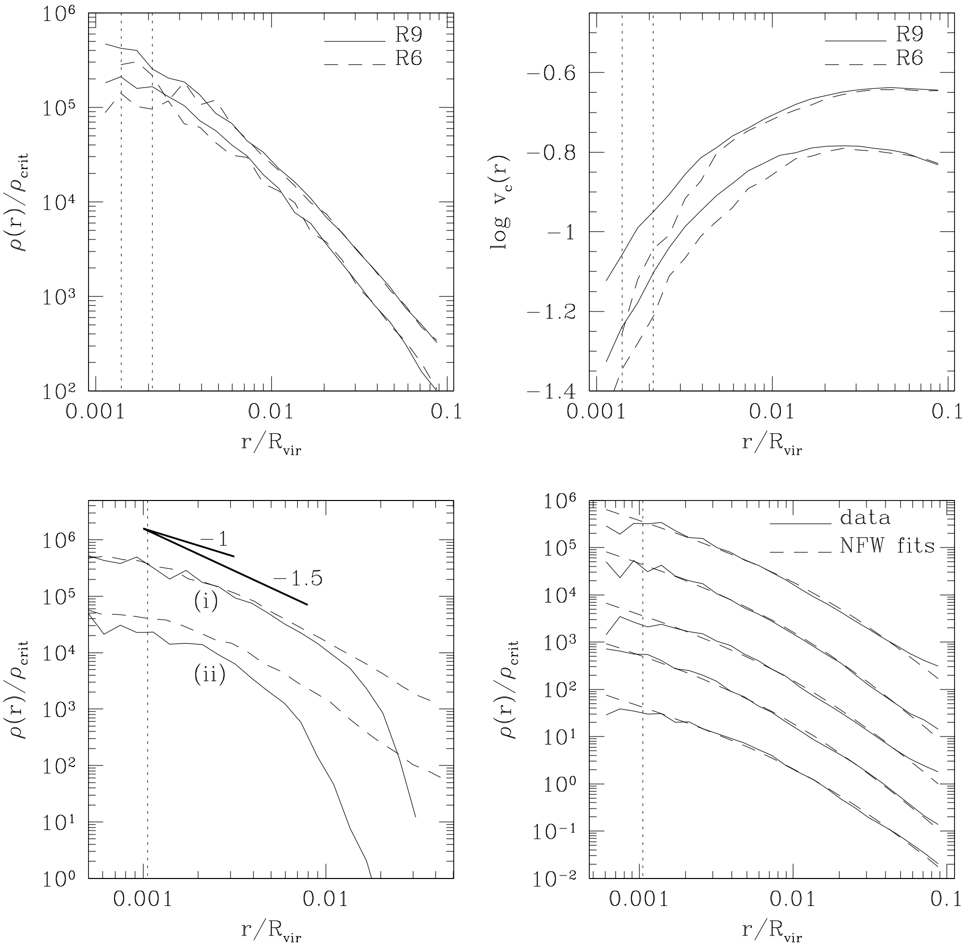

Figure 5.4: *Top:* Density (*left*) and circular velocity (*right*) profiles of two subhalos simulated at two different resolutions. Circular velocities are expressed in units of the maximum circular velocity of the parent halo. In simulation R9 (solid lines), the subhalos contain 3.4×10^4 and 1.4×10^4 particles, while in R6 (dashed lines) they contain a factor of 3.375 fewer particles. The convergence in the circular velocity profiles between the two resolutions is significantly slower on account of the cumulative nature of this quantity. This demonstrates that it is erroneous to use the circular velocity to compute the structural properties of substructure. *Bottom left:* Density profiles of two heavily stripped substructure halos in simulation R12 before entering the primary halo (*dashed lines*) and at present (*solid lines*). Subhalo (i) is shown at $z = 0.80$ and just before the second pericentric passage. Subhalo (ii) is shown at $z = 0.94$ and just before the fourth pericentric passage and is offset by 1 dex to avoid overlap. The numbers near the thick solid lines indicate the power slope of those lines. Both subhalos have of the order of $N = 2 \times 10^4$ particles before entering the host. The cosmological subhalos maintain their steep inner density slope even after several pericentric passages. *Bottom right:* Density profiles of the five most massive halos in simulation R12 (solid lines). The best-fit NFW profiles are also plotted (*dashed lines*). To avoid overlap the lower four density profiles are vertically shifted by 1, 2, 3, and 4 dex from the top to the bottom. These five halos are resolved with more than 2×10^5 particles. In all panels the vertical dotted lines show the adopted force resolution.

that the substructures maintain the steep inner density slope that they had before entering the primary halo, even after several pericentric passages. These heavily stripped satellites have outer profiles consistent with an exponential cutoff. Even though these cosmological simulations are state-of-the art by the current standards, the resolution in these stripped satellites is still too low for us to draw robust conclusions regarding the evolution of their inner structure.

Finally, the bottom right panel of Figure 5.4 shows the density profiles of the five most massive substructure halos in this simulation (*solid lines*) together with the best fit NFW profiles (*dashed lines*). To avoid overlap, the lower four density profiles are each vertically shifted by 1 dex from each other. These five halos are resolved with more than $N = 2 \times 10^5$ particles, and their density profiles are described reasonably well by the NFW profile. These halos entered the host system quite late and have typically made only one orbit; however, these most massive halos represent the ones that would be associated with the dSphs, according to S02. We can plausibly trust their central structure to $0.002 R_{\rm vir}$, which corresponds to about 500 pc when scaled to the Galaxy. At this radius the density profiles are still cuspy, with central slopes between -1 and -1.5.

We end by emphasizing that the behavior of the satellites in the time-dependent cosmological tidal field is not obviously similar to that our individual subhalos exhibit when evolved in a static host potential. The latter are spherical systems with isotropic velocity dispersion tensors, whereas the cosmological satellites presented here are in general triaxial, anisotropic systems, and they suffer additional artificial heating from background particles and physical heating from encounters with other substructures. It is remarkable, therefore, that our findings regarding the way that tidal interactions affect the central density cusps converge in these two radically different regimes: the inner density profiles remain cuspy to the resolution limit of the simulations.

5.4 Dwarf Spheroidal Kinematics in CDM Subhalos

Cosmological numerical simulations confirm that isolated halos in the mass range $10^7 - 10^{10} {\rm M}_\odot$ have central cusps not shallower than $\rho(r) \propto r^{-1}$, on scales comparable to the ones probed by the stars in the dSph satellites (Moore et al. 2001; Colín et al. 2004). Our results in § 5.3 indicate that an initial cuspy satellite will retain its cusp in the presence of a tidal field. Therefore, it is an interesting exercise to attempt to reproduce the observed kinematics of the dSphs assuming cuspy dark matter distributions, and to constrain the maximum mass or circular velocity of their host halos. The advantage of our approach lies in the fact that we have sufficient numerical resolution, and therefore there is no need of extrapolating the inner density slopes to scales smaller than the force resolution, as done by S02.

The dynamics of a spherically symmetric stellar distribution embedded in a spherical dark matter potential can be described by the lowest order Jeans equation, assuming that the two components are in equilibrium and that there are no net streaming motions (e.g., rotation):

$$\frac{{\rm d}}{{\rm d}r}(\rho \sigma_{\rm r}^2) + \frac{2\beta}{r} \rho \sigma_{\rm r}^2 + \rho \frac{{\rm d}\Phi}{{\rm d}r} = 0 \tag{5.7}$$

(BT87), where $\rho(r)$ and $\sigma_{\rm r}(r)$ are the density profile and the radial velocity dispersion of the tracer stellar population, respectively, $\Phi(r)$ is the underlying dark matter gravitational

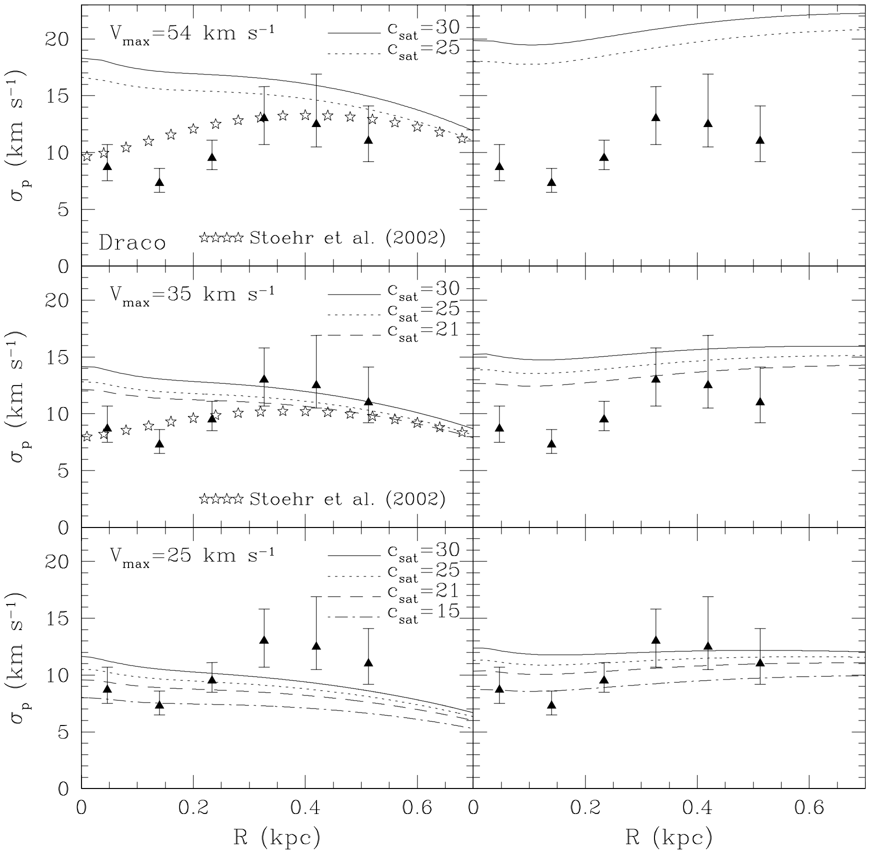

Figure 5.5: Observed line-of-sight velocity dispersions for the dSph Draco (*triangles*), compared with those predicted for stellar systems embedded in dark matter halos with structure similar to the ones of our simulated subhalos. Each pair of panels refers to a single value of $V_{\rm max}$, while the various lines correspond to different values of $R_{\rm max}$ in the same range as in S02 (see text for details). The three plots on the left show results assuming a tidal radius for Draco equal to the *optical radius* measured by Odenkirchen et al. (2001) and also adopted by S02. The panels on the right show results for the same range of parameters, but for tidal radii 3 times as large. The filled points correspond to the results obtained assuming the parabolic fits to the circular velocity profiles adopted by S02. From top to bottom, the results for $V_{\rm max} = 54$, 35, and 25 km s^{-1} are shown. Globally, the observed velocity dispersion profile is better reproduced by subhalos with $V_{\rm max} = 25$ km s^{-1} and assuming a significantly larger than the nominal tidal radius.

potential, and β describes the velocity anisotropy of the stars. The solution of the Jeans equation (5.7) with the boundary condition $\rho(r) \to 0$ at $r \to r_{\rm t}$ for β=const reads

$$\rho\sigma_{\rm r}^2 = r^{-2\beta} \int_r^{r_{\rm t}} r^{2\beta} \rho \frac{{\rm d}\Phi}{{\rm d}r}\, {\rm d}r \ , \tag{5.8}$$

where $r_{\rm t}$ is the tidal radius of the stellar component.

However, the quantity that can be measured and compared with observations is the line-of-sight velocity dispersion, $\sigma_{\rm p}$, at projected distance R from the center of the dwarf, which is given by

$$\sigma_{\rm p}^2(R) = \frac{2}{I(R)} \int_R^{r_{\rm t}} \left(1 - \beta\frac{R^2}{r^2}\right) \frac{\rho\, \sigma_{\rm r}^2(r,\beta)\, r}{\sqrt{r^2 - R^2}}\, {\rm d}r \tag{5.9}$$

(Binney & Mamon 1982; BT87), where $I(R)$ is the surface distribution of the tracer population:

$$I(R) = 2 \int_R^{r_{\rm t}} \frac{r\, \rho(r)}{\sqrt{r^2 - R^2}}\, {\rm d}r. \tag{5.10}$$

We solve equation (5.9) using the customary King profile for the stellar population of the dSph galaxies,

$$\rho_\star(r) \propto \frac{1}{z^2}\left[\frac{1}{z}\cos^{-1}(z) - (1 - z^2)^{1/2}\right] \tag{5.11}$$

(King 1962), where $z \equiv [1 + (r/r_{\rm c})^2]/[1 + (r_{\rm t}/r_{\rm c})^2]$ and $r_{\rm c}$ denotes the core radius of the profile. For Fornax and Draco, we use the parameters from Mateo (1998) and Odenkirchen et al. (2001), respectively, similarly as in S02. Note that the normalization in equation (5.11) is not important for the purpose of our analysis, since it cancels out. Motivated by the structure of our simulated subhalos from the cosmological simulations, we assume that the dark matter halos associated with the dwarf galaxies follow the NFW density profile. This provides a lower limit to the recovered velocity dispersions, since there is evidence in favor of steeper central density cusps on these scales (e.g., Moore et al. 2001). Our results are not sensitive to the presence of the exponential cutoff, since the fitting formula of equation (5.5) differs appreciably from the NFW density profile only near the break radius $r_{\rm b}$. This is larger than the tidal radii of the stellar components of the dSphs, where the integral in equation (5.9) has to be truncated anyway. In addition, we checked that any eventual differences in the resulting projected stellar velocity dispersions were negligible even when we considered models with stellar tidal radii significantly larger than the nominal values (see below).

We consider halos having both a maximum circular velocity, $V_{\rm max}$, and a corresponding radius, $R_{\rm max} = R(V_{\rm max})$, within the range considered by S02. In practice, for each value of $V_{\rm max}$ there is only a limited range of halo concentrations such that $R_{\rm max}$ is consistent with the values measured by S02 for their subhalos. In Figures 5.5 and 5.6, we show the results of the comparison for Draco and Fornax, respectively, assuming isotropic stellar orbits. The observed velocity dispersion profiles are reproduced from Mateo (1998) for Fornax and from Kleyna et al. (2002) for Draco. In some of these panels, where the relative information is available, we overplot the results obtained adopting the parabolic fitting function of the form proposed by S02 for their subhalos (*filled points*). We remind the reader that the density profiles corresponding to this parabolic function have substantially shallower inner slopes at scales comparable to the sizes of the dSphs than the profiles describing the density structure of our satellites. Each pair of panels refers to a single

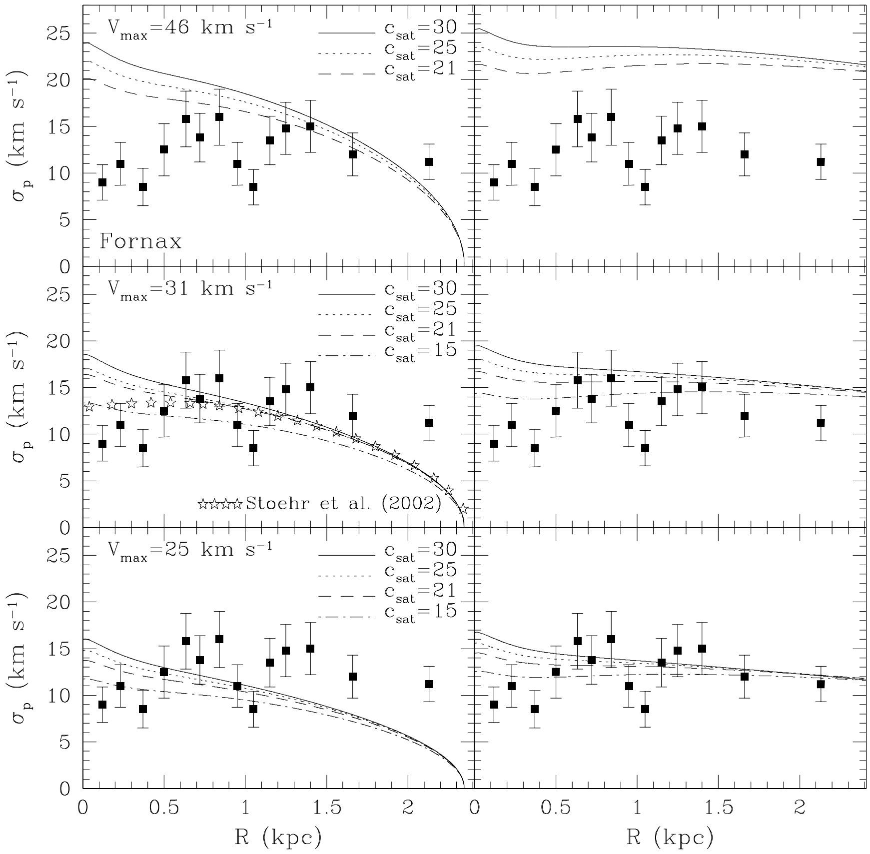

Figure 5.6: Same as Figure 5.5, but for the dSph Fornax (*squares*). The three plots on the left show results assuming a value for the tidal radius taken from the review of Mateo (1998). From top to bottom, the results for $V_{\max} = 46$, 31, and 25 $\mathrm{km\,s^{-1}}$ are shown. Similarly to the case of Draco, the stellar velocity dispersion is better reproduced by subhalos with $V_{\max} = 25$ $\mathrm{km\,s^{-1}}$ and assuming a tidal radius 3 times larger than the nominal value (*right*).

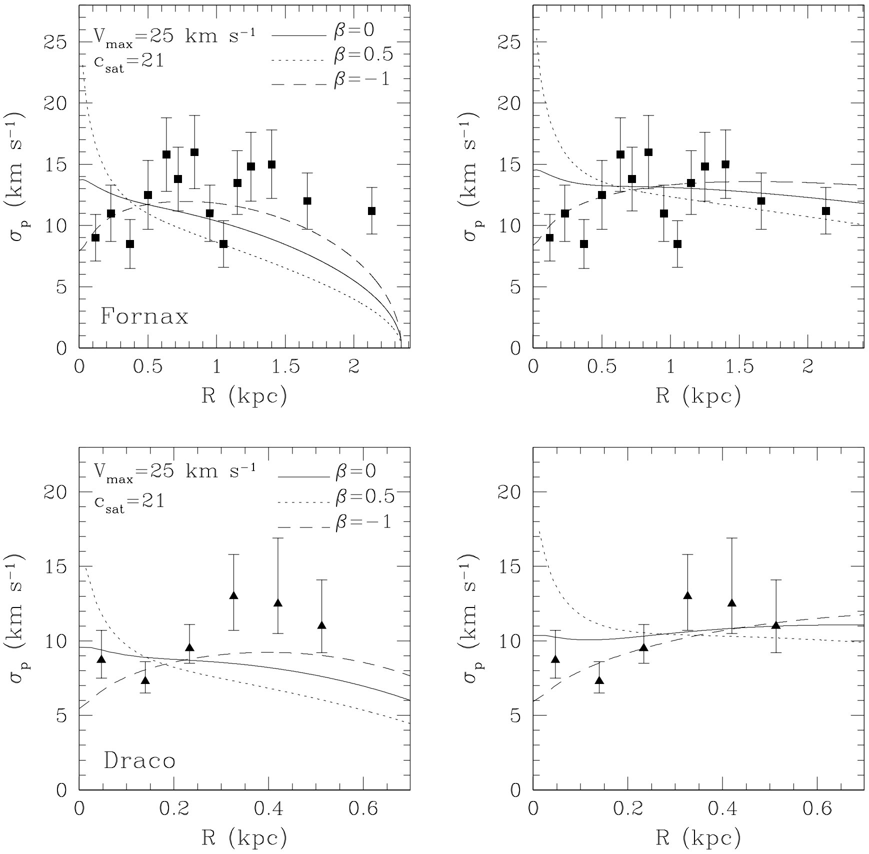

Figure 5.7: Kinematics of Fornax (*top*) and Draco (*bottom*), compared with those expected for stellar systems embedded within NFW subhalos with $V_{\max} = 25\ \mathrm{km\,s^{-1}}$. Different values for the anisotropy parameter β in the velocity distribution of the stellar component have been considered. The solid lines correspond to isotropic models, whereas the dotted and dashed lines to radially and tangentially anisotropic models, respectively. The plots on the left show results for values of the tidal radii of the stellar component equivalent to those used by S02, while the plots on the right correspond to tidal radii 3 times as large. Models with mildly tangentially anisotropic distribution of stellar orbits better reproduce the observed velocity dispersion profiles of both Draco and Fornax. Radially anisotropic models overestimate the central stellar velocity dispersion and make the curves decrease more steeply with distance, contrary to the trend in the observational data.

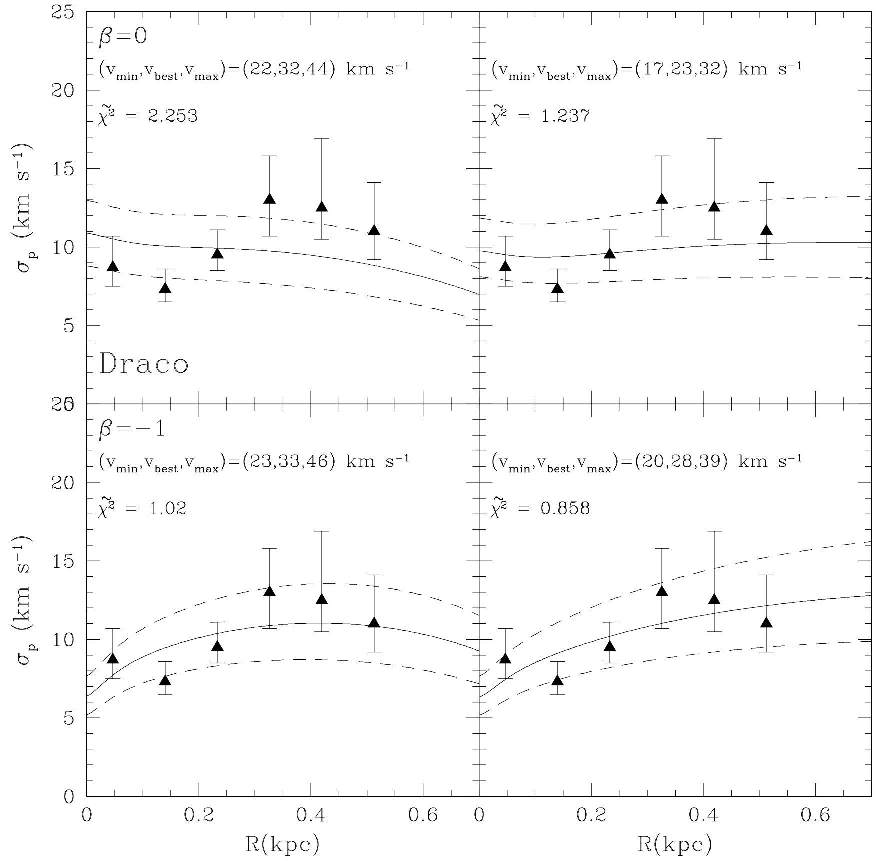

Figure 5.8: Best fit models (*solid lines*) and 3σ intervals (*dashed lines*) for the kinematics of Draco, assuming isotropic (*top*) and tangentially anisotropic (*bottom*) models for the stellar distribution. The stars are embedded in the potential wells of our stripped satellites and follow a King profile. The panels on the left show results adopting a tidal radius equal to the nominal value, whereas the panels on the right show results for tidal radii 3 times as large (see text for details). Keeping the concentration parameter fixed ($c = 21$), we fit by χ^2 minimization the maximum circular velocity $V_{\rm max}$. The best fit value of $V_{\rm max}$ corresponds to $\rm v_{best}$, whereas $\rm v_{min}$ and $\rm v_{max}$ bracket the 3σ intervals. The quality of the fits in terms of the reduced χ^2 is also indicated for the different cases. Subhalos with $V_{\rm max}$ in the range $20 - 35\ {\rm km\,s^{-1}}$ provide the best fit to the data, while $V_{\rm max} > 40\ {\rm km\,s^{-1}}$ are 3σ or more away from the best fit.

value of $V_{\max}$. The three panels on the left show results assuming a tidal radius equal to that adopted by S02, while the panels on the right assume tidal radii 3 times as large.

It is immediately apparent that subhalos with $V_{\max} \sim 50$ km s^{-1} would yield velocity dispersions significantly above the observed values for both Fornax and Draco, once the cuspy density profiles consistent with the structure of our satellites were used. The discrepancy becomes even worse if we allow the stellar component to have a tidal radius larger than the nominal value estimated by fitting the star counts to a King profile. Recent observational studies of Draco show no evidence of tidal tails, lending support to the view that the optical radius is only a lower limit to the true physical boundary of the system (Odenkirchen et al. 2001; Kleyna et al. 2002; Piatek et al. 2002; Klessen et al. 2003), and this might also be true for the majority of the dSphs. By considering subhalos with $V_{\max} \sim 30$ km s^{-1}, we match satisfactorily only the velocity dispersion data points at the outermost radii, which have the largest error bars. Subhalos with $V_{\max} = 25$ km s^{-1} reproduce the observed stellar velocity dispersions reasonably well for the entire range of parameters considered. This conclusion is in disagreement with that reached by S02, simply because of their use of a parabolic fitting function, and suggests that there is no room for entirely solving the substructure problem by simply changing the way the velocities are mapped. Globally, the observed velocity dispersion profile is better reproduced by assuming a larger tidal radius, even though the predicted profiles always tend to be slightly flatter than the data.

The situation can be improved significantly by adopting a weakly tangentially anisotropic velocity distribution for the stars, as shown in Figure 5.7. Indeed, for $\beta = -1$ (*dashed lines*), subhalos with $V_{\max} = 25$ km s^{-1} are nicely consistent with most of the data points for both Draco and Fornax. Note that a mildly tangentially anisotropic distribution of stellar orbits was required by Kleyna et al. (2002) in their best fit models to the kinematics of Draco. Moreover, Lokas (2002) finds that the steeper the dark halo inner density cusp, the more tangential a stellar velocity distribution is required to fit the data for both Draco and Fornax. Interestingly, modeling based on high-resolution Keck spectroscopy of six Virgo dwarf elliptical galaxies having an average line-of-sight velocity dispersion in the range $\sigma \sim 25 - 50$ km s^{-1} also yields for most of them best fit models to their kinematics that are consistent with mildly tangentially anisotropic orbits (Geha et al. 2002). Radially anisotropic models with $\beta = 0.5$ (*dotted lines*) overestimate the central stellar velocity dispersion by a factor of ~ 2 and lead to steeply declining velocity dispersion profiles, contrary to the trend in the observational data. As in the case of the isotropic orbits, if we assume a tidal radius 3 times larger (*right*) the match to the stellar velocity profiles becomes better.

In Figures 5.8 and 5.9, we present the best fit models (*solid lines*), together with the 3σ intervals (*dashed lines*) for Draco and Fornax respectively, assuming isotropic (*top*) and tangentially anisotropic (*bottom*) models. In each case, we fix the value of the concentration parameter and fit, by χ^2 minimization the maximum circular velocity $V_{\max}$ with the two different values for the tidal radius of the stellar component. Note that for Draco the best fit is calculated taking into account that the error bars are asymmetric. The fixed concentration parameter we used ($c = 21$) is consistent with nearly all the profiles of the subhalos in S02. Higher concentration models would imply lower values of $V_{\max}$, and therefore our choice is conservative. This more detailed analysis shows that subhalos with $V_{\max}$ in the range $20 - 35$ km s^{-1} provide the best fit to the data and also that the high values favoured by S02, $V_{\max} > 40$ km s^{-1}, are 3σ or more away from the best fit.

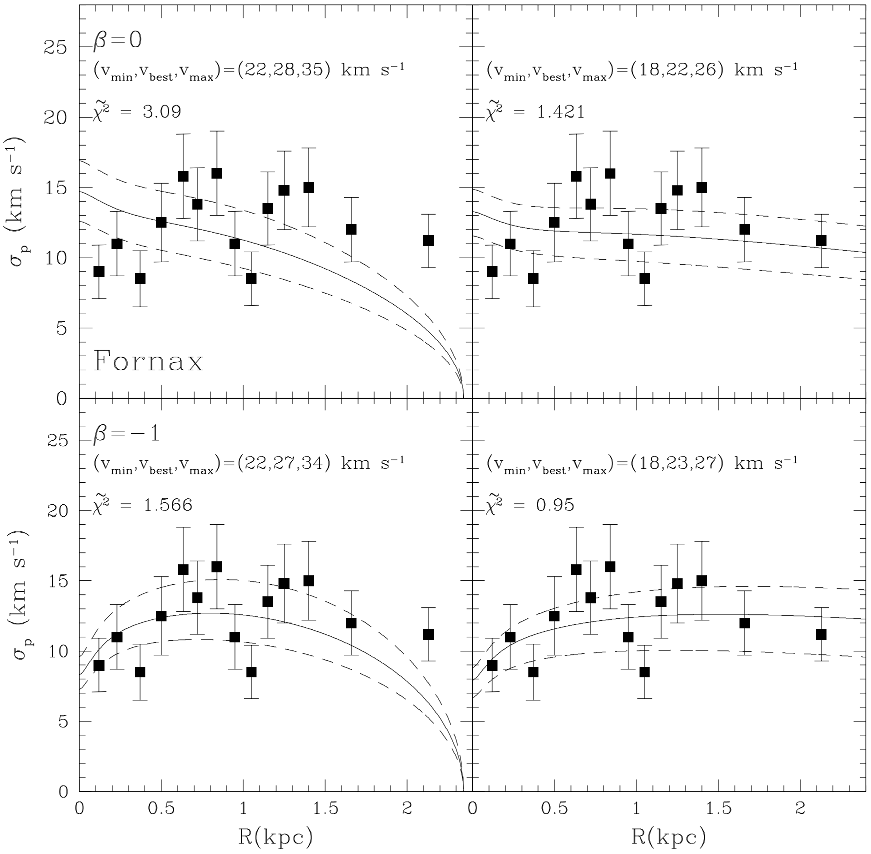

Figure 5.9: Same as Figure 5.8, but for the dSph Fornax. Similarly to the case of Draco, subhalos with $V_{\rm max}$ in the range $20-30$ km s^{-1} provide the best fit to the data (solid lines), while $V_{\rm max} > 35$ km s^{-1} are 3σ (dashed lines) or more away from the best fit.

Determining the absolute best fit to the data requires fitting more parameters, which is clearly outside the scope of the present chapter (however, see Lokas 2002). In general, the degree of anisotropy can be a function of radius instead of being simply a constant parameter. In models in which the dSphs are formed by the tidal stirring and transformation of disk-like systems similar to present-day dwarf irregular galaxies (Mayer et al. 2001a; Mayer et al. 2001b), the remnant is a triaxial system whose velocity anisotropy depends on the radius. The remnants produced in those simulations can be fitted by either an exponential or a King profile, similar to the observed dSphs. Although there is considerable scatter in their structural properties (Mayer et al. 2001b), in general the stellar orbits are tangentially anisotropic in the central regions (at distances equivalent to the core radii of Draco and Fornax) and become nearly isotropic or slightly radially anisotropic in the outer regions, where they are partially flattened by rotation. The interesting point is that values of β ranging from -0.5 to -1.3 are typical in the region where most of their bound mass is. This result is confirmed by recent gas-dynamical simulations with radiative cooling and heating and star formation (L. Mayer et al. 2004, in preparation; Mayer & Wadsley 2003) and lends support to the results shown in Figure 5.7 for $\beta = -1$. Note that Zentner & Bullock (2003) suggested that a mild radial anisotropy for the dSphs equal to $\beta = 0.15$ should be expected because the latter value is typical of the central regions of simulated CDM halos, where the dwarfs actually reside. However, our results highlight that this is not necessarily the case. The tidally stirred stellar components develop a tangential anisotropy even though they evolve inside an initially isotropic dark matter halo because their evolution is governed by non-axisymmetric, bar/buckling instabilities (Mayer et al. 2001b).

We end by emphasizing that if the density profiles of the subhalos models are initially steeper than an NFW profile by either having intrinsically steeper inner slopes (as might be possible for some of the satellites in our cosmological runs; see § 5.3.2) or becoming steeper as a result of the adiabatic contraction following the collapse of baryons (Blumenthal et al. 1986), circular velocities even lower than the above values would be required to acceptably reproduce the observed data.

5.5 Discussion

The results presented in the previous sections indicate that the conversion between $\sigma_\star$ and $V_{\rm max}$ initially adopted by Moore et al. (1999) and Klypin et al. (1999) is reasonable. Low values of $V_{\rm max}$ are required if the dSphs are embedded in CDM halos. There is a second, phenomenological reason why the observed satellites should not reside in halos as massive as the ones postulated by S02. In this case, their baryonic components would lie within a very small region corresponding to only 1% of the virial radius of the object, posing a problem for structure formation scenarios. Indeed, in the prevailing galaxy formation paradigm (e.g., Fall & Efstathiou 1980; Mo et al. 1998), the baryons condense into a rotationally supported structure whose size is determined by the initial spin parameter λ and concentration c of the dark matter halo, and the fraction of mass and angular momentum of baryons relative to that of the halo. Assuming that the specific angular momentum of baryons is conserved during their infall and that the halo and baryons start with the same specific angular momentum (Mo et al. 1998), one can easily show that for a halo as massive as $V_{\rm vir} = 50\ {\rm km\,s^{-1}}$, a spin parameter equal to $\lambda < 0.01$ would have been needed for the baryons to collapse to the observed size of Draco. However, such a small value for the spin occurs in less than 1% of the cosmological halos (Warren et al. 1992; Lemson & Kauffmann 1999; Gardner 2001).

The distribution of spin parameters has been measured so far only for isolated halos and at mass scales larger than those of dwarf galaxies (e.g., Bullock et al. 2001b; Gardner 2001). Although a new systematic analysis overcoming the above limitations will be needed in the future, we made the first step forward in this direction and we measured the spin parameter λ for some of our subhalos. In particular, we selected ten isolated halos from the high resolution region of run R6 and six subhalos within the virial radius of the cluster in both runs R6 and R12. All halos are selected by mass ($M_{\rm vir} \simeq 6.3 \times 10^{10}\,h^{-1}{\rm M}_\odot$). The spin parameters are measured at a radius equal to $0.5\,r_{\rm vir}$ for the isolated halos, where $r_{\rm vir}$ denotes the halo virial radius, and at $0.7\,r_{\rm t}$ for the subhalos, where $r_{\rm t}$ denotes the subhalo tidal radius. The λ-values we found for both isolated halos and subhalos are between 0.024 and 0.12 and follow a log-normal distribution with $\overline{\lambda} = 0.039$ and $\sigma_\lambda = 0.55$ in agreement with previous studies using a much larger halo sample (e.g., Bullock et al. 2001b). This finding confirms our phenomenological argument that the dSph satellites could not be embedded in very massive halos. Finally, it is interesting to note that the comparison of the spin parameters of the same subhalos in runs R6 and R12 shows that they are independent of resolution. Removal of baryons from an initially more extended system by tidal stripping, by supernova feedback, or even by photoevaporation from the UV background cannot be invoked to reduce the size of the baryonic component of the dwarfs at a later stage, because the halo would have been massive enough to suppress all these mechanisms (Benson et al. 2002b). One then would have to rely on some catastrophic loss of angular momentum during baryonic collapse, but there is no obvious reason why this should have happened.

Recently, Kravtsov, Gnedin, & Klypin (2004) proposed a qualitatively different solution to the missing satellites problem. Using high resolution cosmological simulations of the formation of a Milky Way sized halo in a ΛCDM universe, these authors argued that the luminous dSphs in the Local Group can be identified with halos that had considerably higher masses and circular velocities when they formed at high redshift. Their model provide a convincing explanation as to why the dSphs could retain their gas and form stars after reionization and indicates that they are embedded in dark matter halos that suffered dramatic mass loss due to tidal stripping. We believe that the major difference between the subhalos' density structure found in our study and that claimed by S02 is due to resolution effects affecting the determination of the circular velocity. On the other hand, the reduced concentration that H03 find for their simulated satellites may be an artifact of non-equilibrium initial conditions combined with numerical resolution, rather than reflecting the influence of tidal shocks on the inner regions of the satellites. The evolution of the internal structure is expected to be dramatically different for models that are not self-consistent compared to models for which one considers carefully the exact dynamics. Regarding this issue, Kazantzidis et al. (2004) found that NFW satellites initialized using the Maxwellian approximation experience artificially accelerated mass loss and can completely disrupt in an external tidal field. The same satellites, however, survive in identical experiments once the exact self-consistent velocity distribution of the model is taken into account.

Of course, one cannot exclude that some dynamical mechanism other than tidal interactions might have been responsible for lowering the concentration of the subhalos. For example, if bars are effective in redistributing the angular momentum between the baryons and the halo (Weinberg & Katz 2002), then the dSphs could have been strongly affected by this mechanism if they originate from the morphological evolution of tidally stirred dwarf irregular galaxies. Indeed, tidal stirring always incorporates a strong bar instability phase. However, recent work suggests that the amount of angular momentum that a bar transfers to the halo is not enough to turn the inner cusp into a core (Sellwood 2003).

The results presented in this chapter argue that there is no simple solution to the substructure problem within CDM models. The kinematics of the dSphs are indeed a reasonable tracer of their dark halo potential wells. However, their kinematics can also be accurately reproduced with dark halo density profiles that are nearly flat in the center (see Figures 5.5 and 5.6). The latter fact illustrates the need to use better quality data and perhaps higher order moments of the velocity distribution to break this degeneracy and constrain the central cusp slopes (Lokas 2002). Our findings also have important implications for indirect dark matter detection experiments attempting to observe the resulting γ-ray flux from neutralino annihilation. The expected flux depends sensitively on the line-of-sight integral of the square of the mass density. This integral changes by more than one order of magnitude between the NFW and the much shallower density profiles found by S02, as pointed out by the same authors in a more recent paper (Stoehr et al. 2003). With such shallow density profiles, Air-Shower-Cerenkov telescopes like VERITAS and MAGIC might barely detect the emission from the Galactic center and would completely miss that coming from the dSphs. However, for dark matter particle candidates with properties consistent with some of the minimal supersymmetric models (Bergström et al. 1998) and with the persistently steep inner density profiles found in this work, the Galactic center would be easily detected and the dSph satellites still represent potentially valuable targets (Calcáneo–Roldán & Moore 2000).

5.6 Summary

We have investigated the structural evolution of substructure, using a set of high-resolution cosmological N-body simulations, coupled with simulations of the tidal stripping of individual satellites orbiting within a static host potential and employing up to $N = 10^7$ particles. Our main results and conclusions may be summarized as follows:

1. Cuspy satellite halos on eccentric orbits do not experience significant mass redistribution in their centers, and they retain the same steep inner density slope even after several strong pericentric tidal shocks. This result is valid for our high-resolution cosmological simulations, in which the satellites evolve within a time-dependent cosmological tidal field, and for our simulations of individual subhalos orbiting within a massive host system modeled as a fixed potential.

2. Convergence in the circular velocity profiles occurs much more slowly than that of the density profiles. This is due to the fact that low central resolution propagates to larger radii on account of the cumulative nature of the former quantity. This discourages any attempt to use circular velocities of simulated satellites to derive their structural properties.

3. The density structure of tidally stripped cuspy halos can be well approximated by a simple fitting function (eq. [5]), comprising an unmodified power-law central slope and an exponential cutoff, that describes the satellite's boundary imposed by the tides.

4. The predicted kinematics of the dSph galaxies Fornax and Draco, assuming that they are embedded in the potential wells of our tidally stripped satellites, were compared to the observed stellar velocity dispersion profiles. Adopting isotropic and tangentially anisotropic models for the stellar component, we find that dark matter halos with maximum circular velocities in the range $V_{\rm max} \sim 20 - 35\ {\rm km\,s^{-1}}$ fit the data better, whereas models with $V_{\rm max} \gtrsim 40\ {\rm km\,s^{-1}}$ are at least at the 3σ level from the best fit values. If the initial central density slopes of the simulated subhalos were steeper than the ones adopted here, even lower values of $V_{\rm max}$ would be required to fit the data. Tidal interactions do not provide the mechanism for embedding the luminous dwarf galaxies of the Milky Way within the most massive subhalos in a ΛCDM universe, and, therefore, for reconciling the overabundance of Galactic satellites with CDM predictions.

5. Models with a mild tangential anisotropy of stellar orbits reproduce better the shape of the observed velocity dispersion profiles of both Fornax and Draco, whereas radially anisotropic models overestimate the central stellar velocity dispersion by a

factor of ~ 2. Such a tangential anisotropy is expected in scenarios in which the dSphs result from the tidal stirring of systems similar to present-day dwarf irregular galaxies.

5.7 Acknowledgments

We would like to thank Francisco Prada for organizing the La Palma Cosmology Conference "Satellites and Tidal Streams" (2003) which motivated some of this work. Stimulating discussions with Andrey Kravtsov and Simon White are acknowledged. We are also grateful to Rocco Piffaretti for assistance with the statistical analysis and to the Swiss Center for Scientific Computing (CSCS), where the generation of the initial conditions for the cosmological runs was performed. The numerical simulations presented in chapter were carried out on the zBox supercomputer[2] and on LeMieux at the Pittsburgh Supercomputing Center.

---

[2] See http://www-theorie.physik.unizh.ch/~stadel/

Chapter 6

Concluding remarks and future prospects

In this thesis, I have studied a number of related aspects on the evolution and interactions of dwarf galaxies in high density environments modeled according to a ΛCDM scenario.

The large dynamical range in mass between the main host halo and the subhalo population makes even the highest resolution pure cosmological simulations inadequate to study the internal dynamical evolution of satellites, which has to be resolved on subkiloparsec scales.

We have therefore decided to investigate the evolution of satellites by performing high resolution N-body and hydrodynamical simulations of multicomponent galaxy models built in accordance with the predictions of ΛCDM simulations. Dwarf galaxy models are evolved in isolation, in cluster and galactic environments. The environment is reproduced using spherically symmetric external potentials, live galaxy models and cosmological cluster simulations, where the hierarchical growth and galaxy harassment are modeled self-consistently.

An overabundance of disks and irregular galaxies and an underabundance of early type galaxies in high redshift clusters is likely to be interpreted as a consequence of environmental effects which strongly influence the dynamical evolution of galaxies within the cluster. The effect of these interactions should be higher in the low luminosity cluster population. In Chapter 2 we investigated the morphological and kinematic transformation of disk dwarf galaxies. A particular effort which characterized this work consists in analyzing the simulations results with observational techniques, in order to obtain a more realistic comparison with the observed photometric and spectroscopic data.

High speed gravitational interactions could also account for the kinematically decoupled cores observed in dEs in group environments (de Rijcke et al. 2005). The tidal forces during a flyby interaction between a dwarf elliptical or its disky progenitor and a massive galaxy exert a torque on the dwarf galaxy that, according to analytical estimates, transfers enough angular momentum to its stellar envelope to explain the observed peculiar kinematics. I am currently performing new high resolution collisionless and hydrodynamical simulations in order to reproduce the formation of ellipticals with peculiar central kinematics.

In Chapters 3, 4 and 5 we investigated galaxy evolution in a different context, the halo of the Milky Way. The Milky Way environment and, more generally, the Local

Group, offers an excellent laboratory for near-field cosmology by permitting us to resolve its constituent galaxies into individual stars, studying the evolutionary history of their host galaxies at a level of detail and accuracy that is unmatched by any more distant galaxy, where only the integrated light can be studied. The resolved stellar content of nearby satellites can be used as probes of galaxy formation and evolution, which in turns is an important means for testing cosmological models of hierarchical structure formation.

Chapter 3 in particular is dedicated to the largest satellite of the Milky Way, the Large Magellanic Cloud. The Milky Way – Magellanic system provides us with a close up view of a complex ongoing galaxy interaction. The recent discovery of the Leading Arm stressed the importance of gravitational tides and questioned the role of ram-pressure stripping. However, the separation between gaseous and stellar feature, absence of stars in the Magellanic Bridge and in the Stream, filamentary structures in the Small Magellanic Cloud and the head-tail structures in the Magellanic Stream show that also hydrodynamical forces like ram-pressure gas stripping have acted here. The work presented here studies for the first time the simultaneous effect of gravitational and hydrodynamical forces acting on the Large Magellanic Cloud as it moves in the Galactic halo and underlines the effect of ram-pressure mechanisms by a low density hot gaseous halo.

Chapters 4 and 5 are dedicated to the least massive, yet most numerous type of galaxies in the Local Group, the dwarf spheroidal galaxies (dSphs). The Local Group is characterized by velocity dispersions much smaller than those characteristic of a cluster environment, permitting the slow, strong interactions normally associated with field galaxies. Since structures form hierarchically, we expect that interactions in infalling group environments represent a preprocessing step in the evolution of cluster galaxies. Moreover, galaxies and groups are older than galaxy clusters, which allows more time for tidal forces to transform disks to dSphs. In Chapter 5 we studied the evolution of substructures in ΛCDM models combining cosmological simulations and high resolution individual subhalos models orbiting in a static spherical potential. We found that the density profile of the dark matter component is not substantially modified by tidal forces, concluding that dSphs in the Local Group are embedded in dark matter halos with maximum circular velocities in the range $20 - 35$ km s^{-1}. The fate of the baryonic component was investigated in Chapter 4, where dwarf galaxy satellites orbiting within a Milky Way halo are subjected to the combined effect of tidal and hydrodynamical forces.

A further natural step in the context of this analysis is to study the evolution of dwarf galaxies in a cosmological ΛCDM Milky Way sized halo, in order to take in account the effects induced by the triaxiality of the main halo, encounters with substructures and hierarchical growth. In particular, according to Knebe 2005, we expect that the interactions are more prominent in younger, unvirialized systems, when compared to older more relaxed systems, due to the increased number of encounters a satellite experiences. Therefore it appears essential to study the transformation of satellites at different states of virialisation of the main halo, starting in the early stages of the Milky Way collapse. With this purpose I recently adopted a replacement technique similar to that exposed in Dubinski (1998) and in Moore et al. (1999) and replaced the subhalos population of a cosmological Milky Way sized galaxy with high resolution multicomponent systems. Each subhalo is replaced at the moment it enters in the main system, before the Galaxy has been fully assembled (Fig. 6.1). The mass of the galaxy models varies according to the mass of the original dark matter halo, while the baryonic fraction is kept constant and chosen in order to reproduce the low central surface brightness of dwarf galaxies in the

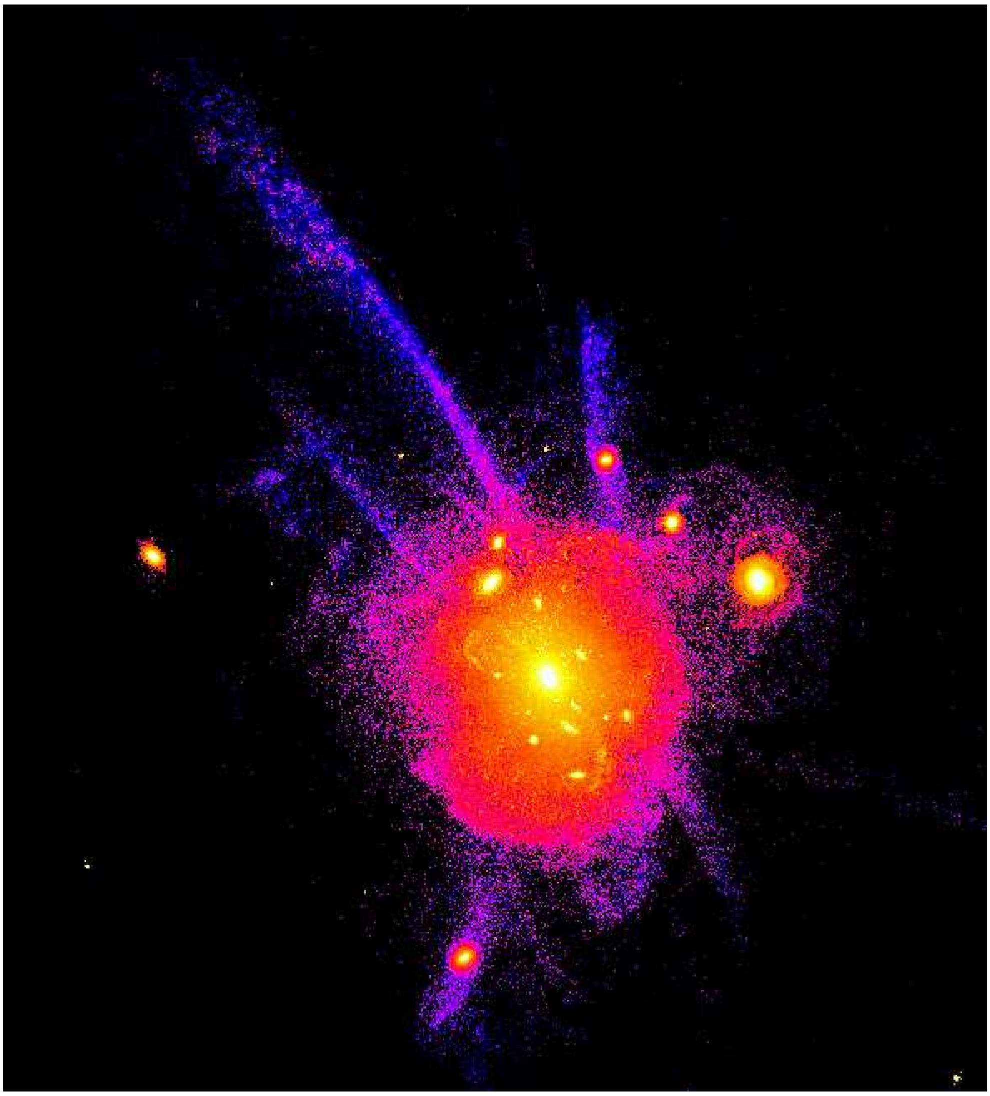

Figure 6.1: Dwarf galaxy models orbiting in a Milky Way sized cosmological halo at $z = 0$.

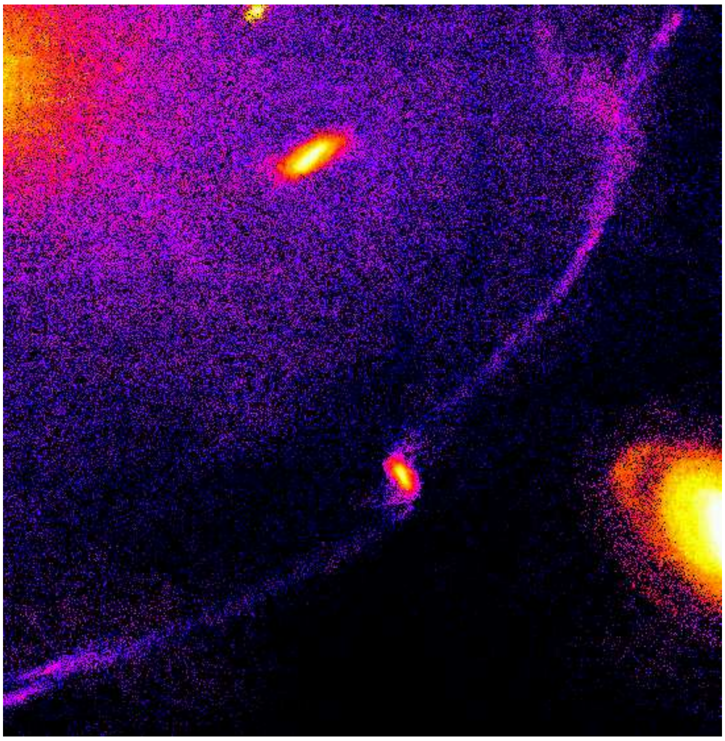

Figure 6.2: Stars stripped from a disk form a dynamically cold stream.

Local Group.

While in a cluster harassment accounts for $\sim 30\%$ of the total tidal perturbation suffered by a satellite, in a lower mass environment like a group or a Milky Way sized galaxy, this fraction increases since the strength of the interaction with the host potential diminishes. At the same time, hydrodynamical interactions generated by a low density Galactic corona or Local Group medium are less effective respect to those produced by the hot ICM. The combination of ram-pressure and tidal stripping should not operate so efficiently as in the case of clusters, where they strip off tidal debris and sweep clean any diffuse cold gas in the tidal tails. Therefore groups are an excellent environment to follow the fate of the stripped baryons and the evolution of tidal tails, which should survive as dynamically cold elongated features at the edge of the main system while both the presence of substructures and a non-spherical host potential contribute to heat them in the more central regions. My ongoing work in this area includes the study of morphological and kinematic characteristic of stellar streams in the Local Group and a detailed comparison with observations, which could provide informations about the distribution of substructures and the shape of the Milky Way halo (Fig. 6.2).

Bibliography

Aarseth, S.J. 1984, in Methods of computational Physics, eds. J.U.Brackhill, B.J.Cohen (Academic, New York)

Abraham, R. G., van den Bergh, S., Glazebrook, K., Ellis, R. S., Santiago, B. X., Surma, P., & Griffiths, R. E. 1996, ApJS, 107, 1

Aharony, O., Gubser, S. S., Maldacena, J. M., Ooguri, H., Oz, Y. 2000 Phys. Rept. 323, 183

Abadi, M. G., Moore, B., Bower, R. G. 1999, MNRAS, 308, 947

Athanassoula, E., & Bosma, A. 1985, ARA&A, 23, 147

Avila-Reese, V., Colín, P., Valenzuela, O., D'Onghia, E., & Firmani, C. 2001, ApJ, 559, 516

Bahcall, N. A., et al. 2003, ApJ, 585, 182

Balogh, M. L., Christlein, D., Zabludoff, A. I., & Zaritsky, D. 2001, ApJ, 557, 117

Balogh, M., Bower, R. G., Smail, I., Ziegler, B. L., Davies, R. L., Gaztelu, A., & Fritz, A. 2002, MNRAS, 337, 256

Balsara, D.S., 1995, J.Comp. Phys.,121, 357

Barazza, F. D., Binggeli, B., Jerjen, H. 2002, A&A, 391, 823

Barazza, F. D., Binggeli, B., Jerjen, H. 2003, A&Ap, 407, 121

Barkana, R., & Loeb, A., 1999, ApJ, 523, 54

Barnes, J., and Hut, P. 1986, Nature, 324, 446

Barnes, J. E. 1988, ApJ, 331, 699

Barnes, J. E. 1990, Nature, 344,379

Barnes, J. E., & Hernquist, L. E. 1991, ApJL, 370, L65

Barnes, J. E. 1989, Nature, 338, 123

Barnes, J. E. 1992, ApJ, 393, 484

Barnes, J. E., & Hernquist, L. E.1992, Ann. Rev, 30, 705

Barnes, J. E., & Hernquist, L. 1996, ApJ, 471, 115

Bekki, K., Couch, W. J., & Shioya, Y. 2002, ApJ, 577, 651

Bekki, K., Chiba, M. 2005, MNRAS, 356, 680

Bender, R., Nieto, J. L. 1990, A&A, 239, 97

Benson, A. J., Lacey, C. G., Baugh, C. M., Cole, S., & Frenk, C. S. 2002a, MNRAS, 333, 156B

Benson, A. J., Frenk, C. S., Lacey, C. G., Baugh, C. M., & Cole, S. 2002b, MNRAS, 333, 177B

Bergström, L., Ullio, P., Buckley, J. H., 1998, Astroparticle Physics, 9, 137

Bertschinger, E. 2001, ApJS, 137, 1

Binney, J. 1978, MNRAS, 183, 501

Binney, J., & Mamon, G. A. 1982, MNRAS, 200, 361

Binney, J., & Tremaine, S. 1987, Galactic Dynamics (Princeton: Princeton University Press)

Binney, J., & Evans, N. W. 2001, MNRAS, 327, L27

Blitz, L., Robishaw, T. 2000, ApJ, 541, 675

Blumenthal, G. R., Faber, S. M., Flores, R., & Primack, J. R. 1986, ApJ, 301, 27

Bode, P., Ostriker, J. P., & Turok, N. 2001, ApJ, 556, 93

Bœhm, C., Riazuelo, A., Hansen, S. H., & Schaeffer, R. 2002, Phys. Rev. D, 66, 083505

Braun, R., Thilker, D. A. 2004, A&A, 417, 421

Brueck, M. T., Hawkins, M. R. S. 1983, A&A, 124, 216

Brüns, C., et al. 2005, A&A, 432, 45

Bullock, J. S., Kravtsov, A. V., & Weinberg, D. H. 2000, ApJ, 539, 517

———.2001, ApJ, 548, 33

Bullock, J. S., Kolatt, T. S., Sigad, Y., Somerville, R. S., Kravtsov, A. V., Klypin, A., Primack, J. R., & Dekel, A. 2001a, MNRAS, 321, 559

Bullock, J.S., Dekel, A., Kolatt, T.S., Kravtsov, A.V., Klypin, A.A., Porciani, C., & Primack, J.R. 2001b, ApJ, 555, 240

Burkert, A. 1995, ApJ, 447, L25

Butcher, H., & Oemler, A. 1978, ApJ, 226, 559

Calcáneo-Roldán, C., & Moore, B. 2000, Phys. Rev. D, 62, 123005

Calcáneo-Roldán, C. , Moore, B. , Bland-Hawthorn, J., Malin, D., & Sadler, E. M. 2000, MNRAS, 314, 324

Colín, P., Klypin, A., Valenzuela, O., & Gottlöber, S. 2003, ApJ, submitted (astro-ph/0308348)

Carlberg, R. G., Yee, H. K. C., Ellingson, E., Abraham, R., Gravel, P., Morris, S., & Pritchet, C. J. 1996, ApJ, 462, 32

Chandrasekhar, S. 1943, ApJ, 97, 255

Colpi, M., Mayer, L., Governato, F. 1999, ApJ, 525, 720

Connors, T. W., Kawata, D., Maddison, S. T., Gibson, B. K. 2004, Publications of the Astronomical Society of Australia, 21, 222

Conselice, C. J., Gallagher, J. S., Wyse, R. F. G. 2001, ApJ, 559, 791

Couch, W. J., Balogh, M. L., Bower, R. G., Smail, I., Glazebrook, K., & Taylor, M. 2001, ApJ, 549, 820

Couchman, H. M. P., Thomas, P. A., Pearce, F. R. 1995, ApJ, 452, 797

Courteau, S. 1997, AJ, 114, 2402

Cowie, L. L., McKee, C. F. 1977, ApJ, 211, 135

Cowie, L. L., & Songaila, A. 1977, Nature, 266, 501

Croft, R. A. C., Weinberg, D. H., Bolte, M., Burles, S., Hernquist, L., Katz, N., Kirman, D., & Tytler, D. 2002, ApJ, 581, 20

Debattista, V. P., & Sellwood, J. A. 2000, ApJ, 543, 704

de Blok, W. J. G., McGaugh, S. S., Bosma, A., & Rubin, V. C. 2001, ApJ, 552, L23

de Blok, W. J. G., McGaugh, S. S., & Rubin, V. C. 2001, AJ, 122, 2396

de Blok, W. J. G., & Bosma, A. 2002, A&A, 385, 816

Dehnen, W. 2000, ApJ, 536, 39

Dekel, A. 1997, Galaxy Scaling Relations: Origins, Evolution and Applications, 245

Dehnen, W., & Binney, J., 1998, MNRAS, 294, 429

Dekel, A., Silk,, J., 1986, ApJ, 303, 39

De Rijcke, S., Dejonghe, H., Zeilinger, W. W., Hau, G. K. T. 2001, ApJ, 559, L21

De Rijcke, S., Dejonghe, H., Zeilinger, W. W., Hau, G. K. T. 2003, A&A, 400, 119

Diemand, J., Moore, B., Stadel, J. 2004a, MNRAS, 353, 624

Diemand, J., Moore, B., Stadel, J. 20004b, MNRAS, 352, 535

Diemand, J., Moore, B., Stadel, J., & Kazantzidis, S. 2004, MNRAS, 348, 977

Dressler, A. 1980, ApJ, 236, 351

Dressler, A., & Gunn, J. E. 1983, ApJ, 270, 7

Dressler, A., Thompson, I. B., & Shectman, S. A. 1985, ApJ, 288, 481

Dressler, A., Oemler, A. J., Butcher, H. R., Gunn, J. E. 1994, ApJ, 430, 107

Dressler, A., et al. 1997, ApJ, 490, 577

Drinkwater, M. J., Jones, J. B., Gregg, M. D., & Phillipps, S. 2000, Publications of the Astronomical Society of Australia, 17, 227

Dubinski, J., 1998, ApJ, 502, 141

Eke, V. R., Cole, S., Frenk, C. S. 1996, MNRAS, 282, 263

Eke, V. R., Navarro, J. F., & Steinmetz, M. 2001, ApJ, 554, 114

Efstathiou, G., Lake, G., Negroponte, J. 1982, MNRAS, 199, 1069

Efstathiou, G., Davis, M., Frenk, C., & White, S.D.M. 1985, ApJS, 57, 241

Einasto, J., Saar, E., Kaasik, A., & Chemin, A.D., 1974, Nature, 252, 111

Evrard, A. E. 1988, MNRAS, 235, 911

Evrard, A. E. 1991, MNRAS, 248, 8P

Faber, S.M., & Lin, D.C.N., 1983, 266, L17

Fall, S. M., & Efstathiou, G. 1980, MNRAS, 193, 189

Farouki, R. T., & Shapiro, S. L. 1982, ApJ, 259, 103

Fasano, G., Poggianti, B. M., Couch, W. J., Bettoni, D., Kjærgaard, P., & Moles, M. 2000, ApJ, 542, 673

Ferguson, H. C., Sandage, A. 1991, AJ, 101, 765

Ferguson, H.C., & Binggeli, B., 1994, A&A Rev, 6, 57

Ferguson, H. C., Dickinson, M., & Williams, R. 2000, ARA&A, 38, 667

Ferrara, A., & Tolstoy, E., 2000, MNRAS, 313, 291

Finoguenov, A., Briel, U. G., & Henry, J. P. 2003, A&A, 410, 777

Flores, R. A., & Primack, J. R. 1994, ApJ, 427, L1

Freedman, W. L., *et al.* 2001, ApJ, 553, 47

Fujita, Y. 1998, ApJ, 509, 587

Fujita, Y. 2004, PASJ, 56, 29

Gallagher, J.S., Madsen, G.J., Reynolds, R.J., Grebel, E.K., & Smecker-Hane, T.A., ApJ, 2003, 588, 326

Gallart, C., Freedman, W.L., Aparicio, A., Betelli, G., & Chiosi, C., 1999, AJ,118, 2245

Gallart, C., Martinez-Delgad0, D., Gomez-Flechoso, M.A., & Mateo, M., 2001, AJ, 121, 2572

Gardiner, L. T., Sawa, T., Fujimoto, M. 1994, MNRAS, 266, 567

Gardiner L. T., Noguchi M. 1996, MNRAS, 278, 191

Gardner, J. P. 2001, ApJ, 557, 616

Gavazzi, G., Boselli, A., Mayer, L., Iglesias-Paramo, J., Vilchez, J.M., & Carrasco, L., 2001, ApJ, 563, L23

Gavazzi, G. *et al.*, astroph 0410228 Accepted to A&A

Geha, M., Guhathakurta, P., & van der Marel, R. P. 2002, AJ, 124, 3073

Geha, M., Guhathakurta, P., van der Marel, R. P. 2003, AJ, 126, 1794

Gerhard, O. E. 1981, MNRAS,197, 179

Gerhard, O. E. 1983, MNRAS, 202, 1159

Gerhard, O. E. 1983, MNRAS, 203, 19P

Ghigna, S., Moore, B., Governato, F., Lake, G., Quinn, T., & Stadel, J. 1998, MNRAS, 300, 146

Gill, S. P.D., Knebe, A., & Gibson, B., 2004, MNRAS, 351, 410

Gingold, R.A. & Monaghan, J.J. 1977, MNRAS, 181, 375

Gnedin, O. Y., Hernquist, L., & Ostriker, J. P. 1999, ApJ, 514, 109

Gnedin, O.Y. 2003, ApJ, 589, 752

Goldreich, P., & Lynden-Bell, D. 1965, MNRAS, 130, 125

Governato, F., Mayer, L., Wadsley, J., Gardner, J.P., Willman, B., Hayashi, E., Quinn, T., Stadel, J., & Lake, G., 2004, ApJ, 607, 688

Graham, A. W., Jerjen, H., Guzmán, R. 2003, AJ, 126, 1787

Grebel, E.K., Gallagher, J.S., & Herbeck, D., 2003, ApJ, 125, 1926

Grebel, E.K. & Gallagher, J.S., 2004, ApJ, 610, L89

Guhathakurta, P., Reitzel, D. B. 1998, ASP Conf. Ser. 136: Galactic Halos, 22

Gunn, J. E., Gott, J. R. I. 1972, ApJ, 176, 1

Haardt, F., & Madau, P., 1996, ApJ, 461, 20

Hamilton, A. J. S., & Tegmark, M. 2002, MNRAS, 330, 506

Hayashi, E., Navarro, J. F., Taylor, J. E., Stadel, J., & Quinn, T. 2003, ApJ, 584, 541 (H03)

Hardy, E., Suntzeff, N. B., Azzopardi, M. 1989, ApJ, 344, 210

Haynes, M. P., & Giovanelli, R. 1986, ApJ, 306, 466

Henon, M. 1970, A&A, 9, 24

Hernandez, X., Gilmore, G., & Valls-Gabaud, D. 2000, MNRAS, 317, 831

Hernquist, L. 1989, Nature, 340, 687

Hernquist, L. & Katz, N. 1989, ApJS, 70, 419

Hernquist, L., & Spergel, D. N. 1992, ApJ, 399, L117

Hernquist L. 1990, ApJ, 356, 359

Hernquist L. 1993, ApJS, 86, 389

Hibbard, J. E., & Mihos, J. C. 1995, AJ, 110, 140

Hibbard, J. E., van der Hulst, J. M., Barnes, J. E., & Rich, R. M. 2001, AJ, 122, 2969

Hinshaw, G., et al. 2003, ApJS, 148, 135

Hockney, R.W., & Eastwood, J.W. 1981, Computer Simulations using Particles, (Mc Graw-Hill)

Hogan, C.J., & Dalcanton, J.J., 2000, Phys. Rev. D., 62, 063511

Hut, P. and Makino, J. 1999, Science, 283, 501

Jaffe, A. H., et al. 2001, Phys. Rev. Lett., 86, 3475

Jerjen, H., Kalnajs, A. & Binggeli, B. 2000, A&A, 358, 845

Jimenez, R., Verde, L., & Oh, S. Peng, 2003, MNRAS, 339. 243

Kamionkowski, M., & Liddle, A. 2000, Phys. Rev. Lett., 84, 4525

Kauffmann, G., White, S. D. M., & Guiderdoni, B. 1993, MNRAS, 264, 201

Kazantzidis, S., Magorrian, J., & Moore, B. 2004, ApJ, 601, 37

Kim, D. W., Jura, M., Guhathakurta, P., Knapp, G. R., & van Gorkom, J. H. 1988 ApJ, 330, 684

Kim S., Staveley-Smith L., Dopita M. A., Freeman K. C., Sault R. J., Kesteven M. J., McConnell D. 1998, ApJ, 503, 674

King, I. 1962, AJ, 67, 471

Klessen, R. S., Grebel, E., & Harbeck, D. 2003, ApJ, 589, 798

Kleyna, J., Wilkinson, M. I., Evans, N. W., Gilmore, G., & Frayn, C. 2002, MNRAS, 330, 792

Klypin, A., Kravtsov, A. V., Valenzuela, O., & Prada, F. 1999, ApJ, 522, 82

Klypin, A., Zhao, H., & Somerville, R. S. 2002, ApJ, 573, 597

Knebe, A., Gill, S. P. D., & Gibson, B. K. 2004, Publications of the Astronomical Society of Australia, 21, 216

Knebe, A., Power, C., Gill, S. P. D., Gibson, B. K. 2005, submitted to MNRAS, astro-ph 0507380

Kochanek, C. S. 1996, ApJ, 457, 228

Kormendy, J., Freeman, K. C. 2004, IAU Symposium, 220, 377

Kravtsov, A. V., Gnedin, O. Y.,& Klypin, A. 2004, ApJ, in press (astro-ph/0401088)

Lake, G., Schommer, R. A., & van Gorkom, J.H. 1987, ApJ, 314, 57

Larson, R. B., Tinsley, B. M., & Caldwell, C. N. 1980, ApJ, 237, 692

Lemson, G., & Kauffmann, G. 1999, MNRAS, 302, 111

Lewis, I., et al. 2002, MNRAS, 334, 673

Irwin, M. J. 1991, IAU Symp. 148: The Magellanic Clouds, 148, 453

Lin, D. N. C., Lynden-Bell, D. 1977, MNRAS, 181, 59

Lin, D. N. C., Jones, B. F., & Klemola, A. R. 1995, ApJ, 439, 652

Lokas, E. L. 2002, MNRAS, 333, 697L

Lubin, L. M., Oke, J. B., & Postman, M. 2002, AJ, 124, 1905

Lucy, L. 1977, ApJ, 82, 1013

Lufkin, G, Quinn, T., Wadsley, J., Stadel, J., & Governato, F., 2004, MNRAS, 347, 421

Luks, T., Rohlfs,K. 1992, A&A, 263, 41

Majewski, S. R., Ostheimer, J. C., Kunkel, W. E., Johnston, K. V., Patterson, R. J., Palma, C. 1999, IAU Symp. 190: New Views of the Magellanic Clouds, 190, 508

Maller, A. H., Bullock, J. S. 2004, MNRAS, 355, 694

Marcolini, A., Brighenti, F., D'Ercole, A. 2004, MNRAS, 352, 363

Marcolini A., Brighenti F., D'Ercole A. 2004, submitted to MNRAS, astro-ph/0404502

Mashchenko, S., Carignan, C., & Bouchard A., 2004, MNRAS, 352, 168

Mastropietro, C., Moore, B., Mayer, L., Wadsley, J., & Stadel, J., 2005, MNRAS in press, astro-ph/0412312

Mateo, M. 1998, ARA&A, 36, 435

Mathewson, D. S., Ford, V. L., Schwarz, M. P., Murray, J. D. 1979, IAU Symp. 84: The Large-Scale Characteristics of the Galaxy, 84, 547

Mathewson, D. S., Wayte, S. R., Ford, V. L., Ruan, K. 1987, Proceedings of the Astronomical Society of Australia, 7, 19

Mayer, L., Governato, F., Colpi, M., Moore, B., Quinn, T., Wadsley, J., Stadel, J., & Lake, G. 2001a, ApJ, 547, L123

———.2001b, ApJ, 559, 754

Mayer, L., Moore, B., Quinn, T., Governato, F., & Stadel, J. 2002, MNRAS, 336, 119

Mayer, L., & Wadsley, J. 2003, in the Proceedings of the Conference "Satellite and Tidal Streams", La Palma 26-30 May 2003, Spain, ed. F. Prada, D. Martínez-Delgado, & T. Mahoney (astro-ph/0309073)

Mayer, L., 2004, Proceedings of Science, BDMH2004 (2004), 037, astro-ph//0411476

Mayer, L., & Moore, B., 2004, MNRAS, 354, 477

McGaugh, S. S., & de Blok, W. J. G. 1998, ApJ, 499, 41

McGaugh, S. S., Barker, M. K., & de Blok, W. J. G. 2003, ApJ, 584, 566

Meurer, G. R., Bicknell, G. V., Gingold, R. A. 1985, Proceedings of the Astronomical Society of Australia, 6, 195

Mihos, J. C., & Hernquist, L. 1994, 425, L13

Mihos, J. C. 1995, ApJ, 438, L75

Mihos, J. C., & Hernquist, L. 1996, ApJ, 464, 641

Mihos, J. C., McGaugh, S. S., & de Blok, W. J. G. 1997, ApJ, 477, L79

Miller, R. H., & Smith, B. F. 1980, ApJ, 235, 793

Mo, H. J., Mao, S., & White, S. D. M. 1998, MNRAS, 295, 319

Monaghan, J.J. 1992, ARA&A, 30, 543

Moore, B. 1994, Nature, 370, 629

Moore, B., Davis, M. 1994, MNRAS, 270, 209

Moore, B., Katz, N., & Lake, G. 1996, ApJ, 457, 455

Moore, B., Katz, N., Lake, G., Dressler, A., Oemler, A. 1996, Nature, 379, 613

Moore, B., Lake, G. & Katz, N. 1998, ApJ, 495, 139

Moore, B., Lake, G., Quinn, T. & Stadel, J. 1999, MNRAS, 304, 465

Moore, B., Ghigna, S., Governato, F., Lake, G., Quinn, T., Stadel, J., & Tozzi, P. 1999, ApJ, 524, L19

Moore, B., Calcáneo-Roldán, C., Stadel, J., Quinn, T., Lake, G., Sebastiano, G., & Governato, F. 2001, Phys. Rev. D, 64, 063508

Moore, B., Diemand, J., Stadel, J. 2004, IAU Colloq. 195: Outskirts of Galaxy Clusters: Intense Life in the Suburbs, 513

Mori, M., Burkert, A. 2000, ApJ, 538, 559

Mori, M., Ferrara, A., Madau, P., 2002, ApJ, 571, 40

Murai, T., Fujimoto, M. 1980, PASJ, 32, 581

Murali, C. 2000, ApJL, 529, L81

Murray, S. D., White, S. D. M., Blondin, J. M., Lin, D. N. C. 1993, ApJ, 407, 588

Navarro, J. F. 1990, MNRAS, 242, 311

Navarro J. F., Frenk C. S., White S. D. M. 1996, ApJ, 462, 563

Navarro J. F., Frenk C. S., White S. D. M. 1997, ApJ, 490, 493

Negroponte, J., & White, S. D. M. 1983, MNRAS, 205, 1009

Noguchi, M. 1988, A&A, 203, 259

Nulsen, P. E. J. 1982, MNRAS, 198, 1007

Odenkirchen, M., et al. 2001, AJ, 122, 2538

Olsen, K. A. G., Salyk, C. 2002, AJ, 124, 2045

Oemler, A. J. 1974, ApJ, 194, 1

O'Neil, K., Bothun, G. D., Impey, C. D. 1999, AJ, 118, 1618

Ostriker, J. P., & Tremaine, S. D. 1975, ApJL, 202, L113

Pedraz, S., Gorgas, J., Cardiel, N., Sánchez-Blázquez, P., Guzmán, R. 2002, MNRAS, 332, L59

Percival, W. J., et al. 2001, MNRAS, 327, 1297

Persic, M., Salucci, P. 1997, ASP Conf. Ser. 117: Dark and Visible Matter in Galaxies and Cosmological Implications,

Phillips, J., Weinberg, D. H., Croft, R. A. C., Hernquist, L., Katz, N., & Pettini, M. 2001, ApJ, 560, 15

Piatek, S., Pryor, C., Armandroff, T. E., & Olszewski, E. W. 2002, AJ, 123, 2511

Pimbblet, K. A., Smail, I., Kodama, T., Couch, W. J., Edge, A. C., Zabludoff, A. I., & O'Hely, E. 2002, MNRAS, 331, 333

Postman, M., & Geller, M. J. 1984, ApJ, 281, 95

Putman, M. E., Gibson, B., K., Staveley-Smith, L. 1998 IAU Symp.190, New Views of the Magellanic Clouds, eds. Chu et al.

Putman, M. E. et al. 1998, Nat, 394, 752

Putman, M. E., Staveley-Smith, L., Freeman, K. C., Gibson, B. K., Barnes, D. G. 2003, ApJ, 586, 170

Putman, M. E., Bland-Hawthorn, J., Veilleux, S., Gibson, B. K., Freeman, K. C., Maloney, P. R. 2003, ApJ, 597, 948

Quilis, V., Moore, B., Bower, R. 2000, Science, 288, 1617

Quilis, V., Moore, B. 2001, ApJL, 555, L95

Quinn, P. J. 1984, ApJ, 279, 596

Read, J.I & Gilmore, G., 2004, MNRAS, in press

Rhee, G., Klypin, A., & Valenzuela, O. 2003, ApJ, submitted (astro-ph/0311020)

Riess, A. G. 1998, Bulletin of the American Astronomical Society, 30, 843

Sand, D. J., Treu, T., & Ellis, R. S. 2002, ApJ, 574, L129

Sand, D. J., Treu, T., Smith, G. P., & Ellis, R. S. 2004, ApJ, 604, 88

Sarazin, C. L. 1986, Reviews of Modern Physics, 58, 1

Schulz, S., Struck, C. 2001, MNRAS, 328, 185

Schiminovich, D., van Gorkom, J. H., van der Hulst, J. M., & Kasow, S. 1994, ApJ, 423, L101

Schweizer, F. 1982, ApJ, 252, 455

Sellwood, J. A. 2003, ApJ, 587, 638

Sembach, K. R. 2003, preprint (astro-ph 0311089)

Sembach, K. R. et al. 2003, ApJS, 146, 165

Sigurdson, K., & Kamionkowski, M. 2003, Phys. Rev. Lett., submitted (astro-ph/0311486)

Shaviv, N.J., & Dekel, A., 2003, submitted to MNRAS, astro-ph/0305527

Simien, F., Prugniel, P. 2002, A&A, 384, 371

Simon, J. D., Bolatto, A. D., Leroy, A., & Blitz, L. 2003, ApJ, 596, 957

Smith, G. P. et al. 2005, submitted (astro-ph0403455)

Sofue, Y. 1994, PASJ, 46, 431

Somerville, R.S., 2002, ApJ, 572, L23

Sommer-Larsen, J., Gotz, M., & Portinari, L., 2003, ApJ, 596, 47

Sparke, L. S., Sellwood, J. A. 1987, MNRAS, 225, 653

Spergel, D. N., & Steinhardt, P. J. 2000, Phys. Rev. Lett., 84, 3760

Spergel, D. N., et al. 2003, ApJS, 148, 175

Springel V., White S. D. M. 1999, MNRAS, 307, 162

Springel, V., Yoshida, N., White, S.D.M. 2001, New A., 6, 79

Springel, V., & Hernquist, L., 2003, MNRAS, 339, 289

Sridhar, S., & Nityananda, R. 1990, MNRAS, 245, 713

Stadel, J. 2001, PhD thesis, University of Washington

Stanimirovic, S., Dickey, J. M, Krčo, M., Brooks, A., M. 2002, ApJ, 576, 773

Steinmetz, M. 1996, MNRAS, 278, 1005

Stoehr, F., White, S. D. M., Tormen, G., & Springel, V. 2002, MNRAS, 335, L84 (S02)

Stoehr, F., White, S. D. M., Springel, V., Tormen, G., & Yoshida, N. 2003, MNRAS, 345, 1313

Susa, H., & Umemura, M. 2004, ApJ, 600, 1

Taffoni, G., Mayer, L., Colpi, M., Governato, F. 2003, MNRAS, 341, 434

Terlevich, A. I., Caldwell, N., & Bower, R. G. 2001, MNRAS, 326, 1547

Thacker, R.J., & Couchman, H.M.P., 2000, ApJ, 545, 728

Terlevich, A. I., Caldwell, N., & Bower, R. G. 2001, MNRAS, 326, 1547

Thilker, D.A., Braun, R., Walterbros, A.M., Corbelli, E., Lockman, F.J., Murphy, E., & Maddalena, R., 2004, ApJ, 601, L39

Thoul, A.A., & Weinberg, D.H. 1996. ApJ, 466, 608

Tittley, E.R., Pearce, F.R., & Couchman, H.M.P., 2001, ApJ, 561, 69

Tonry, J. L., et al. 2003, ApJ, 594, 1

Toomre, A. 1964, ApJ, 139, 1217

Toomre, A., & Toomre, J. 1972, ApJ, 178, 623

Toomre, A. 1974, IAU Symp. 58: The Formation and Dynamics of Galaxies, 58, 347

Toomre, A. 1977, Evolution of Galaxies and Stellar Populations, 401

Toomre, A. 1978, IAU Symp. 79, The Large Scale Structure of the Universe (Dordrecht: Reidel), 109

Toomre, A. 1981, in The structure and evolution of normal galaxies, Cambridge University Press, 1981, p. 11

Tormen, G., Diaferio, A., & Syer, D. 1998, MNRAS, 299, 728

Tremaine, S.D. 1976, ApJ, 203, 345

Trentham, N., & Mobasher, B. 1998, MNRAS, 299, 488

Treu, T., Ellis, R. S., Kneib, J.-P., Dressler, A., Smail, I., Czoske, O., Oemler, A., & Natarajan, P. 2003, ApJ, 591, 53

Tully, R. B. 1988, in Nearby Galaxies Catalog, Cambridge University Press, 1988, p. 221

Valenzuela, O., & Klypin, A. 2003, MNRAS, 345, 406

Van den Bergh, S., 1996, ApJ, 428, 617

van der Marel, R. P. 2001, AJ, 122, 1827

van der Marel, R. P., Cioni, M. L. 2001, AJ, 122, 1807

van der Marel R. P., Alves D. R., Hardy E., Suntzeff N. B. 2002, AJ, 124, 2639

van Dokkum, P. G., Franx, M., Kelson, D. D., Illingworth, G. D., Fisher, D., & Fabricant, D. 1998, ApJ, 500, 714

van Dokkum, P. G., Franx, M., Fabricant, D., Illingworth, G. D., & Kelson, D. D. 2000, ApJ, 541

van Zee, L., Skillman, E. D., & Haynes, M. P. 2004, AJ, 128, 121

van Zee, L., Barton, E. J., Skillman, E. D., astroph 0409346 Accepted to AJ.

Verde, L., Oh, S. P., & Jimenez, R., 2002, MNRAS, 336, 541

Vollmer, B., Marcelin, M., Amram, P., Balkowski, C., Cayatte, V., & Garrido, O. 2000, A&A, 364, 532

Vollmer, B., Cayatte, V., Balkowski, C., Duschl, W. J. 2001, ApJ, 561, 708

Vollmer, B. 2003, A&A, 398, 525

Wadsley, J. W., Stadel, J., Quinn, T. 2004, New Astronomy, 9, 137

Wakker, B. P. 2001, ApJS, 136, 463

Warren, M. S., Quinn, P. J., Salmon, J. K., & Zurek, W. H. 1992, ApJ, 399, 405

Wechsler, R. H., Bullock, J. S., Primack, J. R., Kravtsov, A. V., & Dekel, A. 2002, ApJ, 568, 52

Weinberg, M. D. 1995, ApJL, 455, L31

Weinberg, M. D. 1998, MNRAS, 299, 499

Weinberg, M. D. 2000, ApJ, 532, 922

Weinberg, M. D., & Katz, N. 2002, ApJ, 580, 627

Weinberg, S. 1972, New York: Wiley, c1972

Weiner, B. J., Williams, T. B. 1996, AJ, 111, 1156

Wilkinson, M., Kleyna, J.T., Evans, W.N., Gilmore, G.F., Irwin, M.J., & Grebel, E.K., 2004, ApJ, 611, L21

White, S. D. M. 1978, MNRAS, 184, 185

White, S. D. M. 1979, MNRAS, 189, 831

White, S. D. M. 1983, IAU Symp. 100: Internal Kinematics and Dynamics of Galaxies, 100, 337

White, S. D. M. 1987, IAU Symp. 127: Structure and Dynamics of Elliptical Galaxies, 127, 339

Whitmore, B. C., Lucas, R. A., McElroy, D. B., Steiman-Cameron, T. Y., Sackett, P. D., & Olling, R. P. 1990, AJ, 100, 1489

Wright, A. E. 1972, MNRAS, 157, 309

Yoshizawa, A. M., Noguchi, M. 2003, MNRAS, 339, 1135

Zaritsky, D., Lin, D. N. C. 1997, AJ, 114, 2545

Zentner, A. R., & Bullock, J. S. 2002, Phys. Rev. D, 66, 043003

———.2003, ApJ, 598, 49

Zhao, H., Evans, N. W. 2000, ApJL, 545, L35

Acknowledgments

I would like to thank Ben Moore for giving me the opportunity to write this thesis, for his apparently infinite list of new ideas, his continuous support and for the very nice group he built up here at the University. I really enjoyed these years in Zurich and I'll remember with pleasure parties and barbecues as well as scientific meetings. Lucio Mayer contributed significantly to this work and I would like to acknowledge him for help and discussions even at late-time. Among the other night-birds especial thanks to Rocco Piffaretti and Stelios Kazantzidis for many hours spent drinking coffees and writing formulas at the blackboard. I am grateful to Andrea Macciò for his numerous suggestions, to Joachim Stadel and Doug Potter for designing and building zBox and zBox2. Finally, I would like to thank Juerg Diemand, Steen Hansen, Victor Debattista, Kim Vy Tran, Tobias Kaufmann, Luigi Mancini, Frank van der Bosh and Marco Miranda for the useful discussions.

Other people have also contributed to some of the projects presented in this work, their input is acknowledged at the end of the corresponding chapters.

CURRICULUM VITAE

Personal data

Name : Mastropietro
First name : Chiara
Date of birth : 02/01/1976
Place of origin: Milan IT
Nationality : Italian

Education

5/2002-10/2005: PhD in Physics, Dr. sc. nat., University of Zurich, Switzerland
PhD thesis: N-Body Simulations of Interacting Galaxies
Thesis supervisor: Prof. Ben Moore

10/1995-02/2002: M.S. in Physics, Laurea degree, Milan University, Italy
Diploma thesis: Heating of Intracluster Medium by AGNs
Thesis supervisor: Dr. Fabio Governato

09/1990-06/1995: Maturita classica, Liceo Classico S. Donato mil. MI, Italy

Teaching experience

2003: Teaching assistant for Physics laboratories,
University of Zurich.

2004: Teaching assistant for Introduction to Cosmology and Astrophysics,
University of Zurich.

2004: Teaching assistant for Thermodynamics,
University of Zurich.

Languages

Italian: Native language
English: Writing and speaking: good

RESEARCH STATUS

Publications:

1.) Kazantzidis, S., Mayer, L., Mastropietro, C., Diemand, J., Stadel, J., & Moore
J. Stadel, & B. Moore
Density Profiles of Cold Dark Matter Substructure:
Implications for the Missing Satellites Problem
ApJ 601 (2004) 37

2.) Mastropietro, C., Moore, B., Mayer L., Wadsley, J., & Stadel, J.
The gravitational and hydrodynamical interaction
between the LMC and the Galaxy
MNRAS in press, astro-ph 0412312

3.) Mastropietro, C., Moore, B, Mayer, L., Debattista, V. P., Piffaretti, R., Stadel, J.
Morphological evolution of disk galaxies in clusters
MNRAS in press, astro-ph 0411648

4.) Mayer L., Mastropietro C., Wadsley, J., Stadel, J., Moore, B.
Simultaneous ram pressure and tidal stripping:
how dwarf spheroidals lost their gas
submitted to MNRAS, astro-ph0504277

In preparation:

1.) S. Kazantzidis, B. Moore, & L. Mayer
Ram-pressure induced star formation in low density environments:
the E+A connection
MNRAS to be submitted

Conference proceedings:

1.) Mastropietro, C., Moore, B., Mayer, L., Stadel, J.
Ram pressure processes in the Galactic Halo
and the Formation of the Magellanic Stream
in: *Proceedings of Extra planar gas*
Dwingeloo, Netherlands, June 2004, ASP Conference, ed. R. Braun

2.) Mastropietro, C., Moore, B., Diemand, J., Mayer L., Stadel, J.:
Morphological evolution of cluster galaxies
in: *proceedings of "Morphological evolution of cluster galaxies: Intense Life in the Suburbs "*
IAU Colloquium No. 195, 2004, A. Diaferio ed.

3.) Mastropietro, C., Moore, B., Mayer, L., Stadel, J., Wadsley, J.
On the formation of the Magellanic Stream
in: *Proceedings of "Satellites and Tidal Streams"*
La Palma 2003, eds. F. Prada, D. Martinez-Delgado, T. Mahoney